NONEQUILIBRIUM FLUCTUATIONS AND PHASE TRANSITIONS IN HYBRID QUANTUM SYSTEMS

Dissertation
zur Erlangung des Doktorgrades
der Fakultät für Mathematik, Informatik und Naturwissenschaften,
Fachbereich Physik
der Universität Hamburg

vorgelegt von
Niklas Mann
aus Nordenham

Hamburg
2019

Gutachter der Dissertation:	Prof. Dr. Michael Thorwart Priv.-Doz. Dr. Axel Pelster
Zusammensetzung der Prüfungskommission:	Prof. Dr. Michael Thorwart Priv.-Doz. Dr. Axel Pelster Prof. Dr. Alexander Lichtenstein Prof. Dr. Roland Wiesendanger Prof. Dr. Michael Potthoff
Vorsitzender der Prüfungskommission:	Prof. Dr. Michael Potthoff
Datum der Disputation:	02.09.2019

Abstract

NONEQUILIBRIUM FLUCTUATIONS AND PHASE TRANSITIONS IN HYBRID QUANTUM SYSTEMS

by Niklas Mann

We investigate the impact of fluctuations on the dynamics of very different systems. Geometric fluctuations in dimer molecules cause symmetry breaking that can enable otherwise forbidden processes. We demonstrate that angular fluctuations in the dipolar arrangement of a non-chiral molecule are associated with chirality symmetry breaking. The linear chiral response which depends on the average geometry thus vanishes, yet certain 2D chiral optical signals are finite due to geometric fluctuations. The correlation time of these fluctuations can be experimentally revealed by the waiting time dependence of the 2D signal.

Further, we analyze the dynamics of a quantum two-state system affected by nonequilibrium quantum fluctuations. We find a nontrivial dependence of the relaxation and dephasing rates which is directly linked to the structure of the unperturbed central system. By means of Heisenberg–Langevin equations of motion, we calculate the correlation function of the nonequilibrium fluctuations and obtain a generalized nonequilibrium fluctuation relation which includes the equilibrium fluctuation-dissipation theorem.

In the following, we consider a hybrid quantum many-body system formed by a vibrational mode of a nanomembrane, which interacts optomechanically with light in a pumped cavity, and a distant ultracold atom gas in the optical lattice of the outcoupled light. The adiabatic elimination of the light field yields an effective coupling between atoms and membrane which can be realized in two ways.

First, the center-of-mass motion of the atom gas in the lattice can be coupled to the motion of the membrane. By changing the pump strength, the effective atom-membrane coupling can be tuned. Above a critical intensity, we find a second-order nonequilibrium quantum phase transition from a localized symmetric state of the atom cloud to a shifted symmetry-broken state, the energy of the lowest collective excitation vanishes, and a strong atom-membrane entanglement arises.

Second, the membrane can be coupled to a transition between two internal states of the atoms. We show that this coupling scheme allows for first- and second-order nonequilibrium quantum phase transitions. The emergent symmetry-broken phase is characterized by a sizeable occupation of the high-energy internal state and a displaced membrane. The order of this phase transition can be changed by tuning the transition frequency. In addition, we show that the mechanical mode can be squeezed by the back-action of internal excitations of the atoms in the gas. A Bogoliubov approach reveals that these internal excitations form a fluctuating environment of quasi-particle excitations for the mechanical mode with a gaped spectral density. Interestingly, mechanical squeezing is enhanced by atomic interactions.

Zusammenfassung

NICHTGLEICHGEWICHTS-FLUKTUATIONEN UND PHASENÜBERGÄNGE IN HYBRIDEN QUANTENSYSTEMEN

von Niklas Mann

Geometrische Fluktuationen in Dimeren führen zu einer Symmetriebrechung, die verbotene Prozesse ermöglichen kann. Wir zeigen, dass Winkelfluktuation in der dipolaren Anordnung eines nicht chiralen Moleküls zu einer chiralen Symmetriebrechung führen. Das lineare, chirale Signal verschwindet, während bestimmte chirale, optische 2D Signale, aufgrund geometrischer Fluktuationen, endlich sind. Wartezeitabhängige Messungen des 2D Signals erlauben eine experimentelle Bestimmung der Korrelationszeit der Fluktuationen.

Wir untersuchen die Dynamik eines Zwei-Zustands-Systems unter dem Effekt von Nichtgleichgewichtsfluktuationen. Wir finden eine nicht-triviale Abhängigkeit der Relaxations- und Dephasierungsraten, die mit der Struktur des ungestörten Systems zusammenhängt. Wir bestimmen die Korrelationsfunktion der Nichtgleichgewichtsfluktuationen und erhalten eine verallgemeinerte Nichtgleichgewichtsfluktuations-Relation, welche das Fluktuations-Dissipations-Theorem beinhaltet.

Im Anschluss betrachten wir ein hybrides Quanten-Vielteilchensystem, bestehend aus einer Vibrationsmode einer Nanomembrane, die optomechanisch mit dem Licht in einer Kavität wechselwirkt, und einem ultrakaltem atomaren Gas im optischen Gitter des ausgekoppelten Lichts. Eine adiabatische Eliminierung des Lichts ergibt eine effektive Wechselwirkung zwischen Atomen und Membran, die auf zwei Weisen realisiert werden kann.

Zunächst kann die Schwerpunktsbewegung der Atome im Gitter an die Vibration der Membran gekoppelt werden. Die effektive Wechselwirkung kann mithilfe der Lichtintensität variiert werden. Oberhalb einer kritischen Intensität finden wir einen kontinuierlichen Nichtgleichgewichts-Quantenphasenübergang von einem lokalisierten symmetrischen Zustand der Atomwolke zu einem versetzten, Symmetrie gebrochenen Zustand. Die Energie der niedrigsten kollektiven Anregungsmode verschwindet und eine starke Verschränkung zwischen Membran und Kondensat wird beobachtet.

Zudem kann ein interner Übergang zwischen zwei Zuständen der Atome an die Membran gekoppelt werden. In diesem Fall finden wir, dass sowohl ein Nichtgleichgewichts-Quantenphasenübergang zweiter Ordnung als auch einer erster Ordnung vorliegt. Die emergente, Symmetrie gebrochene Phase ist durch eine deutliche Besetzung des energetisch-höheren internen Zustands und einer verschobenen Membran charakterisiert. Die Ordnung kann beeinflusst werden, indem die atomare Übergangsfrequenz variiert wird. Weiterhin zeigen wir, dass die nanomechanische Mode durch die atomare Rückkopplung der internen Anregungen gequetscht werden kann. In einem Bogoliubov Ansatz zeigt sich, dass diese internen Anregungen eine fluktuierende Umgebung für die Membran formen.

Contents

List of Abbreviations

BEC	**B**ose–**E**instein **C**ondensate
BKT	**B**erezinsky–**K**osterlitz–**T**houless
ETH	**E**igenstate **T**hermalization **H**ypothesis
FDT	**F**luctuation **D**issipation **T**heorem
FT	**F**luctuation **T**heorem
FWHM	**F**ull **W**idth at **H**alf **M**aximum
GPE	**G**ross–**P**itaevskii **E**quation
NQPT	**N**onequilibrium **Q**uantum **P**hase **T**ransition
OTOC	**O**ut-of-**T**ime-**O**rder **C**orrelator
PBDA	**P**erylene **B**isimide **D**onator **A**cceptor
PBS	**P**olarization **B**eam **S**plitter
PT	**P**hase **T**ransition
QBA	**Q**uantum **B**ack **A**ction
QCP	**Q**uantum **C**ritical **P**oint
QPT	**Q**uantum **P**hase **T**ransition
QSDE	**Q**uantum **S**tochastic **D**ifferential **E**quation
QSSE	**Q**uantum **S**tochastic **S**chrödinger **E**quation
TEBD	**T**ime-**E**volving **B**lock-**D**ecimation

Chapter 1

Introduction and Overview

In 1827, the botanist Robert Brown noticed that tiny particles in water perform *jiggled*, irregular movements in a random manner. By that time, this discovery was the first observation of random processes and it took almost eighty years in order to come up with a theoretical description that had to go beyond the classical physics predicted by Newton's second law of motion. This first theoretical explanation was given by Einstein [1] in 1905 in which he explained the mechanism behind the irregular motion as a consequence of the molecular motion in the solvent. Almost at the same time, Smoluchowski (1906) and Langevin (1908) provided an alternative description for the phenomenon which is known as Brownian motion. They showed that the mean squared displacement of an initially resting particle grows linearly in time with the diffusion constant as the proportionality constant, recovering the original result found by Einstein.

Besides the random force on the Brownian particle that is caused by the irregular occurrence of collisions with the solvent molecules, these scattering processes give rise to a frictional force due to the impact on a moving particle. Even though such events appear randomly, a systematic result proportional to the particle velocity is produced. In fact, this means that there has to exist an internal relationship between the fluctuating force and the friction force, as both originate from the same process. This general concept is manifested in the fluctuation-dissipation theorem [2, 3] (FDT) which was originally formulated by Callen and Welton. Within the framework of linear response, Kubo determined the response of a system that is perturbed by an external force coupled to an arbitrary observable B. In particular, he showed that the linear response of any measured quantity A is directly connected to the symmetrized thermal correlator of these two observables A and B for the unperturbed system, which resulted in the celebrated FDT [2–5]. For instance, two direct applications of the FDT appear in the form of the Green–Kubo formula which relates the conductivity to the current fluctuations [4] or the Einstein–Smulochovski relation for the Brownian particle which provides a relation between its mobility and the diffusion constant [1].

While the FDT holds for classical, quantum and many-body systems alike, it connects the action of the spontaneous fluctuations at thermal equilibrium with the inevitable consequence of the appearance of dissipation. Since its derivation, it has acted as a decisive tool in order to investigate systems close to thermal equilibrium and is still. By relating the susceptibility to the quantum Fisher information, it has been shown that the FDT can be used to measure quantum entanglement for complex quantum systems at thermal equilibrium [6]

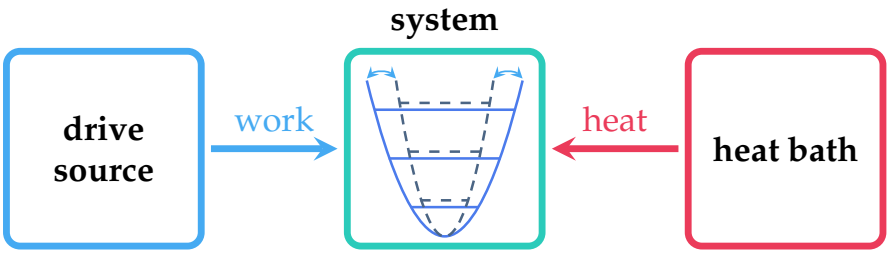

FIGURE 1.1: The sketch illustrates the setup of fluctuation theorems, in which a classical or quantum system is driven by an external force and connected to a heat bath. The drive source performs work on the system under the absorption of heat from the bath. This figure is adapted from reference [8].

and after a quantum quench [7].

The conceptuality of fluctuations goes far beyond dissipative dynamics in open classical or quantum systems, including thermal or vacuum noise. In fact, fluctuations play a key role in the field of phase transitions (PTs). For instance, thermal fluctuations at very high temperatures wipe out any correlation in the system, leading to very small correlation lengths. On the other hand, when the temperature is very low, thermal fluctuations are very small, which again results in very small correlation lengths. In between, when the thermal energy becomes comparable to the relevant energy scale of the system, the correlation lengths can become much larger, such that the inner disorder can be overcome, leading to a qualitative change of the physical properties of the system.

In the course of this chapter, we outline the individual problems that are addressed in this thesis. Throughout this work, we use natural units and will therefore consequently set $\hbar = k_B = c = 1$.

Fluctuations in Systems out of Thermal Equilibrium

Over the past three decades, the search for similar relations that hold for open and closed system away from thermal equilibrium alike has been intensified. This led to the discovery of exact fluctuation relations for classical and quantum systems. These relations reveal the fundamental properties of entropy production for systems under real nonequilibrium conditions as sketched in figure 1.1. Various relations have been obtained [9–17] which are collectively referred to as fluctuation theorems (FTs) [5, 18].

The earliest attempts dealt with the question of irreversible work and entropy fluctuations in a closed driven classical system. These investigations culminated in the discovery of the steady-state and transient FT for entropy production of classical systems in a nonequilibrium state [9, 10, 13, 19–21]. In contrast to the second law of (equilibrium) thermodynamics, it suggests that the entropy of an isolated system may decrease with a finite probability [22, 23]. In fact, the FT reproduces the second law of thermodynamics by taking the ensemble average. Other types of FTs are obtained for closed systems where the underlying dynamics is described by a time-dependent Hamiltonian. This analysis lead to the discovery of another prime example, the Jarzynski equality [11, 24] in the steady state limit and its later

found generalization in the form of the Crooks relation [12]. It implies that the free energy difference between the initial and final equilibrium state is obtained by measuring the work performed by the nonequilibrium drive [25, 26]. In form of a quantum fluctuation theorem, the quantum mechanical counterpart of the classical FT was later obtained by making use of the time-reversal symmetry for a unitary time evolution and the assumption that the heat bath is initially in a state given by the Gibbs distribution [8, 27, 28]. Still, the classical and quantum FTs alike are of experimental relevance and a decisive tool to study systems such as biological molecules [26, 29], molecular motors [30], colloidal particles [15], NMR systems [31], trapped ions [32] and superconducting qubits [33].

Another branch which has evolved in the recent years addresses the question, whether there exists a universal law for higher-order fluctuations in equilibrium systems, similar to the FDT. By considering the second moments of fluctuations and dissipation, operator sequences in the correlation function are introduced in a out-of-time-order. These out-of-time-order correlators (OTOCs) were first introduced by Larkin and Ovchinnikov [34] and are expected to be related to quantum chaos. Tsuji *et al*. [35–37] have shown that by considering OTOCs defined according to a bipartite statistical average, a generalization of the FDT is found. By including linear combinations of the Wigner-Yanase skew information [35, 38], a special form of the quantum Fisher information, an out-of-time-order FDT for the physical OTOCs with the usual thermal average is obtained. This generalized FDT connects the chaotic properties of the system to its nonlinear response and the information content of quantum fluctuations [35].

In chapter 2, we consider a similar type of system as the generic case depicted in figure 1.1. We determine the dynamical response of a quantum two-state system that is under the effect fluctuations provided by very different sources. We consider two specific systems in which fluctuations play an essential role. We investigate first a dimer molecule that is affected by thermal fluctuations and second, a mesoscopic system which is driven by nonequilibrium fluctuations induced by electron transport between two reservoir at different chemical potentials.

In the first setup, we study a quantum system in which the transfer of excitation energy between a donor and an acceptor molecule is forbidden in the static system configuration. The energy transfer only becomes possible when thermal fluctuations are at work, as these introduce geometry fluctuations of the dipole orientation in the considered perylene bisimide donor acceptor (PBDA) pair. They show a rather strong Förster resonant energy transfer [39] that is forbidden in the static average geometry [40] as the dipolar coupling vanishes. We demonstrate an analogous effect associated with the breaking of chirality symmetry. In its equilibrium geometry, this dimer is non-chiral, such that the linear chiral response vanishes. However, angular fluctuations clearly break this symmetry and result in a finite chirality. This can be quantified by the nonlinear spectroscopic signals, as it was proposed by Sanda *et al*. [41]. We apply this concept of chirality fluctuations to the particular case of the PBDA pair and determine the chiral signals by treating the slow angular fluctuations as an Ornstein–Uhlenbeck process. We calculate for a finite fixed angle a certain tensor component of the free induction decay for linearly polarized light. This yields

the information which is equivalent to the circular dichroism. We also study how the response changes when tuning the PBDA pair towards a homodimer. Such an arrangement, in particular, facilitates the investigation of the noise-induced energy transfer [40]. Then, we study the angle-averaged 2D chiral spectrum and its dependence on the waiting time. Most importantly, this allows us to determine the angle fluctuation correlation time and strength. We show quantitatively that the chirality fluctuations can be used to test the orthogonality of the (static) dipoles in the PBDA pair on an entirely independent footing.

In the second setup, we study the relaxation of a quantum two-state system and the action of nonequilibrium quantum fluctuations produced by a strong electron current. We provide an analysis in terms of lowest-order tunneling processes between the quantum dot and the leads. The coupling between the electronic level on the dot and the quantum two-state system can be arbitrarily large. The weak coupling of the tunneling to the fluctuations generates only a small broadening and a small energy shift of the system states such that the unperturbed energy spectrum is a good starting point. We employ the well established diagrammatic perturbation method [42, 43] formulated on the Keldysh contour to determine the real-time dynamics of the quantum two-state system under the action of a nonequilibrium charge current. The population of the central dot and the flowing charge current follow as well. This allows us to extract the relaxation and dephasing rate for the central two-state system and to explain their dependence on the various parameters in terms of the unperturbed energy spectrum. In addition, we use the Heisenberg-Langevin equation of motion to determine the autocorrelation function of the nonequilibrium fluctuations. For a static (DC) bias voltage between the two leads, we find a generalized nonequilibrium fluctuation relation which extends the well-known equilibrium fluctuation-dissipation theorem. The Fourier transform of the autocorrelation function includes Ohmic contributions as well as nontrivial Lorentzian terms. Due to its simple structure, the nonequilibrium fluctuation relation can be generalized to time-periodic (AC) transport voltages and leads us to a Floquet-fluctuation relation in terms of higher harmonics of the correlation function of the nonequilibrium noise.

Periodically Driven Closed Quantum Systems of Interacting Ultracold Atomic Gases

In open systems, the action of thermal and quantum fluctuations results in an equilibration dynamics such that the system eventually relaxes to a stationary state. In general, this process is not present in isolated many-body quantum systems. Yet, when the energy uncertainty in an initially prepared pure state is algebraically small in the Hilbert space dimension of the system Hamiltonian, the long-time average of a few-body observable can become time-independent. In fact, the magnitude of the expectation value then coincides with the prediction provided by a microcanonical average over the same energy window [44]. The conditions under which an expectation value *thermalizes* or not are summarized by the eigenstate thermalization hypothesis (ETH) [45, 46]. It has been shown that the ETH is satisfied by a large variety of nonintegrable quantum systems after a quantum quench [47–56]. In many-body quantum systems, the nonintegrability naturally arises due to finite particle interactions. Hence, interactions provide effects that otherwise only occur in open system

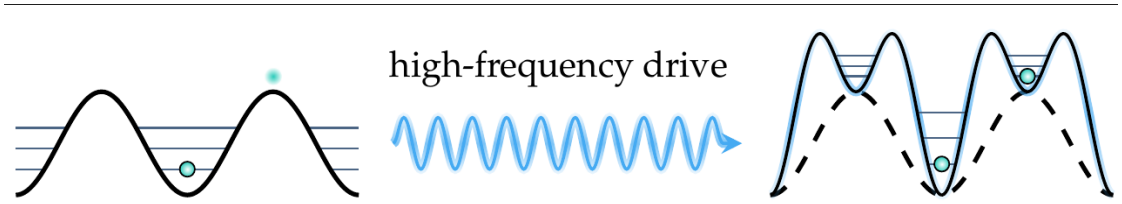

FIGURE 1.2: This sketch illustrates the application of a high-frequency periodic modulation of a static system Hamiltonian sketched on the left-hand side. Under certain circumstances, such a drive gives rise to an effective time-independent high-frequency Hamiltonian with renormalized parameters which is illustrated on the right-hand side. In a classical interpretation, an initially unstable equilibrium position (fading circle on the left-hand side) may be dynamically stabilized (see the right-hand side). A prominent example for such a scenario is a special inverted pendulum, namely the Kapitza's pendulum [90]. The figure is adapted from reference [60].

dynamics such as relaxation.

In addition to the ETH for a quantum quench, equivalent properties have been found for closed quantum systems under the effect of a periodic drive. In the long time limit, integrable systems relax to periodic states that are described by a generalized Gibbs ensemble [57, 58]. On the other hand, nonintegrable systems thermalize to a circular ensemble of random matrix theory, which can be interpreted as an infinite temperature state [59].

Moreover, strong external time-dependent driving is known to have pronounced implications for quantum many-body systems [60]. For instance, light can induce a collapse of long-range ordered charge-density-wave phases [61–64], deconstruct insulating phases [65–67], break Cooper pairs [68–71], or induce novel transient superconducting phases [72–78]. An interesting class of externally driven systems are parametric oscillators in which the characteristic frequency is periodically modulated. Already the classical Kapitza pendulum is known for its peculiar dynamics [79] which is stabilized by properly choosing the driving parameters. The parametric quantum harmonic oscillator has even a nonlinear Floquet spectrum [80, 81] with regimes of stable and unstable quantum dynamics.

Novel concepts of driven quantum many-body systems can be studied in atomic quantum gases, see references [82–86] for recent reviews. A trapped Bose-Einstein condensate (BEC) with weak interactions is well described by the mean-field Gross–Pitaevskii equation (GPE). In absence of any additional optical lattice, a homogeneous BEC in a time-dependent setup has been considered in different constellations for a long time. In an early work, Castin and Dum analytically studied a homogeneous BEC in a parametrically modulated harmonic trap [87]. They showed that the driving induces a parametric instability in the global motion of the condensate which gets depleted exponentially fast and non-condensed modes become dominantly populated due to this effective "heating". The effect of a parametrically driven trap potential was also studied in reference [88] within the Gross–Pitaevskii approach. It was shown that the dynamics of the condensate wave function is described by the classical Mathieu equation of a parametrically forced oscillator, by which one obtains stability criteria. In another mean-field study, the effect of a time-dependent scattering length on the collective motion of a BEC was studied in reference [89].

In the presence of an optical lattice, the BEC is described by the Bose–Hubbard model which is known to have the two distinct phases of a superfluid or a Mott insulator. Jaksch *et al*. [91] have investigated the case of a Bose–Hubbard model with a time-dependent lattice depth which leads to a variation of both the on-site interaction and the hopping amplitude. Starting out from the superfluid phase, the atoms are driven to the Mott insulator phase and converted there into molecules. Eventually, the melting of the molecular Mott insulating phase produces a molecular superfluid [91].

Furthermore, a periodically modulated local atomic interaction [92] can stabilize a Bose-Einstein condensate [93–95]. Moreover, the superfluid-Mott insulator transition can be controlled [96–99]. In the high-frequency limit, these time-dependent examples can be mapped onto effective, time-independent Hamiltonians in order to reveal the effects of the drive on the phase boundaries. In figure 1.2, such a scenario is illustrated. This technique is commonly referred to as Floquet engineering [86, 100] which can also be used to induce novel synthetic quantum matter [101]. Apart from this, anyonic statistics [102, 103] might be accessible [104] as well. Local modulations can coherently control the single-particle tunneling in shaken lattices [105], magnetic frustration [106], and effective magnetic fields [107]. Modulated local on-site Bose–Hubbard interactions can lead to correlated tunneling [108] and artificial gauge potentials, and thus to novel topological phases [109]. All these works commonly rely on the time-periodic modulation of local parameters.

An interesting regime which is less explored is realized when a strongly interacting gas in the Mott phase is exposed to a time-dependent external driving of the global trapping potential. When a system is driven parametrically, it exchanges energy with the driving field, and in principle can be heated to infinite temperature [59, 110, 111]. On the other hand, the parametric oscillator has regions of dynamical stability as well. So the natural question arises how does strong atomic interaction affect the stability of a globally parametrically driven quantum many-body system. Can strong short-range interaction stabilize a quantum gas in a parametric trap which would otherwise be unstable? In turn, can we obtain information on the atomic interaction by externally tuning the system to an unstable dynamical state?

In chapter 3, we show that a global parametric modulation of the trapping potential, which does not have to be tuned to local properties, can be used to control the stability of the interacting quantum gas in an optical lattice. In particular, the global dynamics of the quantum many-body system in a parametrically modulated trap can be stabilized or destabilized against equilibrium fluctuations by tuning the atomic interaction strength. Conversely, locating the onset of the instability can be used to determine the atomic interaction strength. To illustrate the mechanism, we investigate the parametrically driven Bose–Hubbard model with repulsive interaction in two regimes. First, we consider the regime of weakly interacting atoms in the lattice in the presence of a parametrically modulated global trap. This can be treated by a mean-field ansatz on the basis of the Gross–Pitaevskii equation (GPE) for the condensate wave function and is supported by a numerically exact treatment in terms of the time-evolving block-decimation (TEBD) method. Second, we aim to investigate the interplay of the strongly interacting quantum gas in the Mott regime with an additional

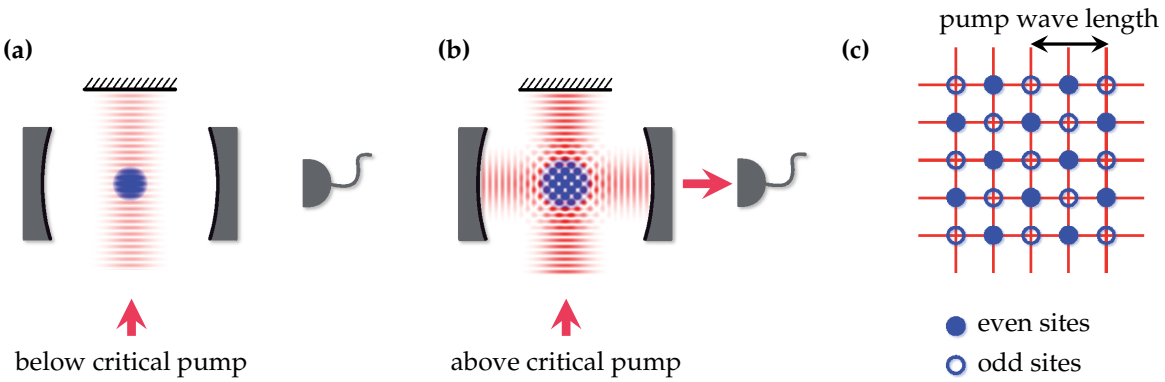

FIGURE 1.3: (a) An almost uniform gas of atoms is placed within a cavity resonator and orthogonally pumped by a laser with frequency close to the cavity resonance. (b) Above a critical pump power, photons scatter coherently into the cavity and a nonequilibrium quantum phase transition occurs. (c) Consequently, an optical lattice is formed, where the atoms spatially self-organize in a checkerboard pattern, such that the majority of atoms occupy either "even" or "odd" lattice sites. This figure is adapted from reference [115].

parametrically modulated trap. To this end, we have calculated the time-dependent dynamics in this regime numerically by the TEBD approach, taken from reference [112]. The parametric driving leads to a breathing of the width of a local central Mott region which becomes resonant at frequencies which are shifted as compared to the non-interacting case. In the Mott regime, energy absorption is increasingly suppressed due to the strongly reduced compressibility of the Mott region. After introducing the underlying driven Bose–Hubbard model, we present our mean-field analysis for the parametric resonance based on a discretized form of the GPE. To go beyond the weak-interacting regime, we compare our results to the case of strong interactions based on the exact numerical TEBD. The connection between periodically-driven harmonic trap and site-dependent hopping is clarified.

Nonequilibrium Quantum Phase Transitions in Hybrid Systems

Just as local particle-hole fluctuations drive the superfluid-Mott insulator quantum phase transition in the Bose–Hubbard model, global fluctuations may also induce a phase transition. For instance, these global fluctuations occur when a many-body system is collectively coupled to an external degree of freedom. Such systems often combine solid-state physics, quantum optics and atom physics in a single setup and are, therefore, usually termed quantum hybrid system. A prime example of this class is implemented in the form of a BEC in an optical lattice inside a transversely pumped optical cavity which is depicted in figure 1.3. In fact, this realization exhibits a quantum phase transition that is driven by global fluctuations of the intracavity photon number. By tuning the transverse laser pump strength above a critical value, a Dicke quantum phase transition between a normal phase and a self-organized superradiant phase occurs [113–117], as illustrated in 1.3 (a) and (b), respectively. Moreover, optical bistability [118, 119], a roton-type softening in the atomic dispersion relation [113, 120–122] and optomechanical Bloch oscillations [123] were uncovered. Similar effects occur also for polarizable and thermal particles in a cavity at finite temperature [124–126].

In the recent years, a new generation of hybrids has been experimentally realized. This class of systems merges state-of-the-art optomechanical systems with an atomic many-body quantum system into a single atom-optomechanical setup. In this way, as theoretically proposed [127, 128] and later experimentally realized [129–132], the vibrational motion of a nanomembrane in an optical cavity is coupled to the spatial motion of a distant cloud of cold ^{87}Rb atoms that reside in the optical lattice of the outcoupled light field. In order to overcome the resolved sideband cooling limit [133] and cool the nanomechanical oscillator close to its quantum mechanical ground state, the atom gas can be used as a coolant [128–130]. Recent approaches include active feedback cooling of the membrane oscillator to reach a minimal mode occupation number of $\langle n_{\mathrm{m}} \rangle \simeq 16$ [132], investigate collective effects in the quantum many-body system that lead to collective atomic motion with an instability [131], while other theoretical proposals suggest ways to induce robust atom-membrane entanglement, coherent quantum state transfer, teleportation and indirect measurement [127, 134–140].

Cutting-edge experiments in optomechanics demonstrate coherent state transfer [141] and entanglement between the cavity light and the mechanical resonator [134, 142, 143], macroscopic quantum coherence [144], as well as squeezed optical [145, 146] and mechanical [147–151] states. Besides, it is well known that squeezed states can be generated by nonlinearities [152, 153], such as, e.g., particle-particle interactions in an atomic condensate. Also engineering the environment of an optomechanical setup can produce a squeezed-vacuum reservoir and a transfer of squeezing to the movable mirror may occur [149]. Spin squeezed states of atoms can be induced by squeezed light [154–158], in which the squeezed state is transfered from the light to the atoms. Combining several of these elements in a single hybrid quantum system may be a key step to generate a robust squeezed mechanical state, that could be largely insusceptible to dissipative effects.

In chapter 4, we will first review the basics of classical phase transitions and their arising critical behavior. Most notably, the criticality appears in a universal manner which allows one to classify phase transitions by a set of very few numbers, the critical exponents. This feature is shortly outlined by summarizing Landau's theory of classical phase transitions. We give a formal definition of the quantum mechanical counterpart of the classical phase transition. While also quantum phase transitions show universal behavior, nonequilibrium conditions break this universality, giving rise to critical exponents which, for instance, depend on the structure and characteristics of the bath. A short overview about this aspect is given by revisiting the superradiant phase transition of the open Dicke quantum system, depicted in figure 1.3.

The chapter 5 is dedicated to the growing field of atom-optomechanical hybrid systems. Thereby, our focus is set on two explicit examples which are currently considered in literature, have been experimentally realized or are currently in development. These approaches allow to resonantly couple the motion of the membrane to either the spatial motion or internal degrees of freedom of the atomic gas. Hence, we distinguish between the *motional* and *internal* coupling scheme. The ingenuity of these examples grants access to resonant coupling over a large range of membrane frequencies. The principles of these realizations

are discussed and a profound derivation of the system Hamiltonian is provided within experimentally reasonable limits. In addition, we shortly summarize recent experimental and theoretical progress and applications.

In chapter 6, motivated by recent experimental progress [129, 131, 132], we study a hybrid atom-optomechanical setup in the *motional* coupling scheme [128–132, 137, 140]. Within the bad-cavity limit, we first adiabatically eliminate the light field in order to derive the effective equations of motion of the underlying dynamics. We include the full lattice potential and also the atomic interaction in the gas on the mean-field level. The numerical solution of the generalized Gross–Pitaevskii equation confirms the validity of an analytic approach based on a Gaussian condensate profile (see also chapter 3). Tuning the atom-membrane coupling by changing the laser intensity or cavity finesse, a nonequilibrium quantum phase transition (NQPT) occurs between a localized symmetric state and a symmetry-broken quantum many-body state with a shifted cloud-membrane configuration. It is fueled by the competition of the lattice, trying to localize the atoms at the minima, and the membrane displacement which tries to shake the atoms. In the regime of a deep lattice, it is revealed that the order of the NQPT is always continuous. Near the quantum critical point, the energy of the lowest collective excitation mode vanishes and the order parameter of the symmetry-broken state becomes non-zero, leading to a substantial atom-membrane entanglement. The mode-softening is accompanied by a roton-type bifurcation of the decay rate of the collective eigenmodes. Most importantly, the observed NQPT appears also when the light-mediated coupling between the atoms and the membrane is non-resonant. We further generalize the mean-field approach by including energetically higher excited states of the atomic condensate. This allows us to investigate the effects of thermal and light-field fluctuations. For white noise, we find critical exponents that differ from the usual mean-field exponents.

In chapter 7, we consider the *internal* coupling scheme. We show that this very coupling scheme also allows for a NQPT which can be readily tuned by changing the effective coupling strength. In contrast to the *motional* coupling scheme, both, a first- and a second-order NQPT can be realized in the same physical setup and this, by only changing a directly accessible parameter. We show this for the *membrane-in-the-middle-setup* [159] in which the light field is adiabatically eliminated and an effective coupling between the membrane and the transition between two states in the atom gas can be obtained. In a mean-field description, the atomic part is reduced to a single-site problem with a Gaussian ansatz for the condensate profile. Tuning the atom-membrane coupling by modifying the laser intensity, the system undergoes a NQPT. We provide simple analytical expressions for the critical point. Moreover, by tuning the atomic transition frequency, the order of the phase transition can be changed from second- to first-order and vice versa. In case of a discontinuous phase transition, the system exhibits hysteresis which can be detected by polarization measurements of the atom gas.

In chapter 8, we use the Bogoliubov approach to isolate the fundamental mode of the atomic condensate. This allows us to treat the quasi-particle excitations as fluctuations acting on the vibrational mode of the nanomembrane within in a system-bath picture. We

find an analytic expression for the bath spectral density of the quasi-particle modes in the zero-temperature limit, which depends on the atomic interaction strength. Hence, by tuning the atomic interaction, the effective environment of the optomechanical components can be engineered and the quantum state of the nanomechanical oscillator can be controlled. For weak atom-membrane coupling, the system becomes analytically solvable and we have direct access to thermodynamical observables of the membrane and atoms. Most interestingly, the variance of the mechanical displacement coordinate can be reduced to a squeezed nanomechanical state in a wide range of model parameters. In fact, squeezing is enhanced by a finite atom-atom interaction at finite temperatures.

Finally, in chapter 9, we provide a generalization of the mean-field ansatz discussed in chapter 7. Within a Bogoliubov prescription, we describe how the Gaussian ansatz can be used to estimate the spectrum of collective excitations of a binary BEC coupled to an additional degree of freedom. For instance, this allows us to include fluctuations and the study of the atom-membrane entanglement, as well as other effects beyond mean-field physics, such as correlations. In addition, we apply the Gaussian ansatz in a modified version to the Dicke model of figure 1.3. We reduce the generalized GPE to two coupled equations of motion describing the cavity photon amplitude and the atomic imbalance between even and odd sites.

Chapter 2

Fluctuations in and out of Equilibrium

A fundamental process in nature is symmetry breaking caused by thermal fluctuations induced by an equilibrium bath. This can enable processes that are otherwise forbidden. While a large amount of research has been devoted to the role of equilibrium quantum fluctuations, the impact of nonequilibrium quantum fluctuations remains not fully explored until today. In these fields fall the results obtained in the publications below which are presented in this chapter.

N. Mann, P. Nalbach, S. Mukamel, and M. Thorwart, "Probing chirality fluctuations in molecules by nonlinear optical spectroscopy", The Journal of Chemical Physics **141**, 234305 (2014).
N. Mann, J. Brüggemann, and M. Thorwart, "Dissipative dynamics of a quantum two-state system in presence of nonequilibrium quantum noise", The European Physical Journal B **89**, 279 (2016).

In many fields of quantum physics, the impact of fluctuations on a quantum system of interest is a fundamental problem. For instance, a quantum system, that is initially prepared in a pure state, loses its quantum coherence over time when brought in contact with thermal fluctuations. This matter has been in the focus of research since the early days of quantum mechanics [160–164]. Understanding the principles of quantum decoherence and dissipation is a key step to find an answer to the fundamental question how quantum mechanics is reconciled with the appearance of a classical world [165].

Fluctuations appear in different forms such as thermal fluctuations which are random deviations of a system from its equilibrium state or quantum fluctuations (or vacuum fluctuations) that are allowed by the uncertainty principle. An important physical principle valid for these two examples at thermal equilibrium is the fluctuation-dissipation theorem (FDT) [2, 4, 164, 166–168]. Connecting the action of fluctuations with the inevitable consequence of the appearance of dissipation, it holds for classical and quantum mechanical systems alike. Yet, this elegant concept is well known to be not applicable to nonequilibrium fluctuations. Up to now, efforts are made to find a general principle for those as well [169, 170].

During the course of this chapter, we present two examples of systems whose dynamics is under the impact of different types of fluctuations. First, we consider the molecule of a perylene bisimide donor acceptor (PBDA) pair that is affected by thermal noise, leading to fluctuations of the molecular geometry which affects its electronic structure. This molecule

has orthogonal transition dipole moments in its static configuration such that a direct Förster transfer is forbidden. Yet, geometric fluctuations induce a rather strong Förster resonant energy transfer as it has been shown by Nalbach *et al*. [40]. Here, we extend the same idea to chirality and show in general that a molecule which is achiral in its equilibrium state can show signatures of chirality when thermal fluctuations are included.

Second, we investigate the relaxation and dephasing dynamics of a quantum two-state system influenced by nonequilibrium quantum fluctuations which are provided by an electron current flowing between two non-interacting leads at different chemical potentials. To lowest-order in the tunneling process, we numerically determine the relaxation and dephasing rate of the two-state system and explain their dependence on various parameters. In addition, an analytical derivation of the autocorrelation function describing the nonequilibrium fluctuations is provided, which extends the FDT in the form of a generalized nonequilibrium fluctuation-dissipation relation for DC and AC bias voltages between the two leads.

2.1 Thermal Geometry Fluctuations in Dimer Molecules

The existence of chiral molecules in nature is by far no exception. In fact, almost all biological molecules are chiral. For instance, nuclear bases, sugars, and peptides exist in enantiomer pairs which are connected by a reflection symmetry. While most physical properties of these pairs are identical, chiral enantiomers exhibit large differences in their biological activity and chemical reactivity. As a consequence, the set of physical methods that are usable to study chirality is limited [171, 172]. For instance, the circular dichroism is a commonly used method which measures the difference between the absorption of σ_+ and σ_- circularly polarized light. However, chiral molecules often have more than just a single conformation and each of these has its own chiral response. At finite temperature, the different configurations become thermally accessible such that always the thermal average over all conformations is measured for an ensemble of chiral molecules [173]. Proposed in 2011, another possible candidate to measure chirality makes use of nonlinear optical signals. This method allows to study not only chiral molecules, but also molecules which are achiral in thermal equilibrium, yet exhibit a finite chirality when thermal fluctuations of their configuration break the spatial symmetry [41].

2.1.1 Geometric Setup of the Donor Acceptor Pair and Dipolar Interaction

In this section, we consider an orthogonally arranged perylene bisimide donor acceptor pair as depicted in figure 2.1. The excitonic energy transfer is induced by dipole-dipole interactions in the donor acceptor pair. Due to its orthogonally arranged dipole moments, the dipole-dipole interaction strength J is zero in its equilibrium position. A simplified sketch of the equilibrium scenario is given in figure 2.2(a), showing that not only the electric dipole moments $\boldsymbol{\mu}_1$, $\boldsymbol{\mu}_2$ are perpendicular, but also the connecting vector $\boldsymbol{R}$ is perpendicular to the donor electric dipole moment $\boldsymbol{\mu}_1$. In general, the dipole-dipole interaction strength is given

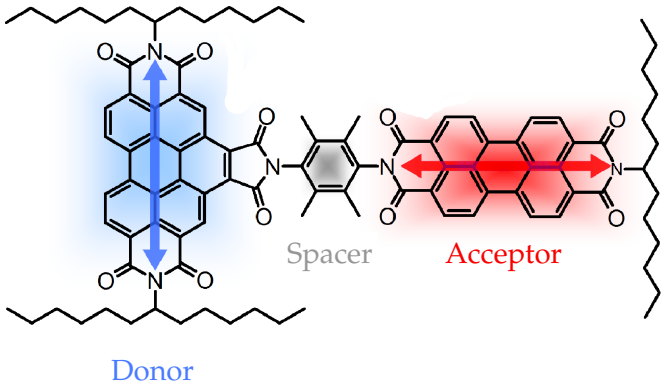

FIGURE 2.1: A sketch of the chemical structure of an orthogonally arranged PBDA pair is shown together with its transition dipole moments [174].

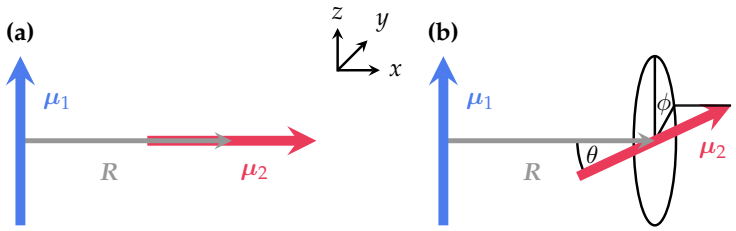

FIGURE 2.2: (a) A simplified sketch of the arrangement of the two transition dipole moments $\boldsymbol{\mu}_1$, $\boldsymbol{\mu}_2$ and the connecting vector $\boldsymbol{R}$ of the PBDA pair is shown for its non-chiral equilibrium orientation. (b) The sketch illustrates the angles ϕ and θ when $\boldsymbol{\mu}_1$ is not oriented along the x-axis.

by

$$J = \frac{\boldsymbol{\mu}_1\boldsymbol{\mu}_2 - 3(\boldsymbol{\mu}_1\boldsymbol{n})(\boldsymbol{\mu}_2\boldsymbol{n})}{R^3}, \tag{2.1}$$

where $\boldsymbol{n}$ is the unit vector in the direction of $\boldsymbol{R} = R\boldsymbol{n}$. Consequently, the interaction strength J vanishes when $\boldsymbol{n} \perp \boldsymbol{\mu}_1 \perp \boldsymbol{\mu}_2$.

For rigid molecules such as the donor and acceptor, any deviation from the orthogonal arrangement of the dipoles moments should arise from rotations around the positions of the chemical bonds between the donor and spacer molecule and between the acceptor and spacer molecule. In the following, we simplify the description by assuming that the connecting vector fixes the coordinate system and the two dipole moments may only rotate around their central positions. It follows that although rotations of the dipole moment $\boldsymbol{\mu}_1$ will result in a finite dipolar interaction, the PBDA will stay achiral. When $\boldsymbol{n} \parallel \boldsymbol{\mu}_2$, any additional vector will span a plane with the vector $\boldsymbol{n}$ (or $\boldsymbol{\mu}_2$), leaving the whole system planar. Hence, only when $\boldsymbol{\mu}_2$ rotates out of the plane formed by $\boldsymbol{\mu}_1$ and $\boldsymbol{n}$, a chiral signal can be obtained. In order to simplify the following calculation, we will consequently neglect rotations of the dipole moment $\boldsymbol{\mu}_1$. This step is justified, since for not too strong angular fluctuations, the results will remain qualitatively unchanged.

Any rotation of the dipole moment $\boldsymbol{\mu}_2$ can be described by the two angles θ and ϕ. These angles are introduced in figure 2.2(b). The first angle θ denotes the angle between $\boldsymbol{\mu}_2$ and the connecting vector $\boldsymbol{R}$, and the second angle ϕ measures the angle between the projection of $\boldsymbol{\mu}_2$ in the $y-z$ plane and the z-axis. Note that, although the complex is chiral for rotations with $\phi = \pi/2$, the dipole-dipole coupling vanishes. On the other hand, rotations with $\phi = 0$

induce a finite dipolar coupling while the complex remains achiral.

By using the formerly introduced angles, the dipole moments are parametrized according to

$$\boldsymbol{\mu}_1 = \Big(0,\, 0,\, \mu_1\Big)^T, \tag{2.2a}$$

$$\boldsymbol{\mu}_2 = \mu_2 \Big(\cos\theta,\, \sin\theta\sin\phi,\, \sin\theta\cos\phi\Big)^T. \tag{2.2b}$$

It follows that the dipolar coupling strength is a function of the two angles resulting in

$$J \equiv J(\theta,\phi) = J_0 \sin\theta\cos\phi\,. \tag{2.3}$$

Here, we have introduced $J_0 = \mu_1\mu_2/R^3$, which takes the value $J_0 \simeq 85\,\mathrm{cm}^{-1}$ for the particular PBDA pair studied here.

2.1.2 Slow Dynamics of the Angular Movement

A stochastic time evolution of the angles originates from fluctuations of the dipole moments around their equilibrium arrangement. This induces diffusive dynamics of the angles in a potential, which, in the simplest form, is harmonic. Here, we assume a harmonic potential for the angle θ with equilibrium position $\theta_0 = 0$ and a free rotation around ϕ. Moreover, we assume slow movements for the stochastic time evolution described by an Ornstein–Uhlenbeck process, which results in an equilibrium probability density

$$\rho_\theta^{\mathrm{eq}}(\theta) = \frac{1}{\sqrt{2\pi}\sigma_\theta} \exp\left(-\frac{\theta^2}{2\sigma_\theta^2}\right). \tag{2.4}$$

Furthermore, the probability to observe θ at time t when the angle at time $t = 0$ was initially θ' is given by the expression

$$\mathcal{P}_\theta(\theta,\theta',t) = \frac{1}{2\pi\sigma_\theta^2\sqrt{1-e^{-2Dt}}} \exp\left(-\frac{\theta^2+\theta'^2-2\theta\theta' e^{-Dt}}{2\sigma_\theta^2[1-e^{-2Dt}]}\right). \tag{2.5}$$

Here, the diffusion constant D is a measure for the inverse autocorrelation time of the fluctuations. In order to find an appropriate description of the PBDA pair, we further need to find a realistic value for the width of the angular probability distribution σ_θ. In reference [40], the angular reorganization energy was estimated to be $\lambda_\theta \simeq 1\mathrm{cm}^{-1}$. At high temperatures, the reorganization energy relates to the width σ_θ of the probability density via $\lambda_\theta = \langle J_0^2\theta^2\rangle/2k_BT$, where $\langle\theta^2\rangle = \int d\theta\,\theta^2\rho_\theta^{\mathrm{eq}}(\theta) = \sigma_\theta^2$. Under these considerations, we may estimate $\sigma_\theta \simeq 0.24$ for the PBDA pair at room temperature.

In addition, we assume a homogeneous equilibrium probability density $\rho_\phi^{\mathrm{eq}}(\phi) = (2\pi)^{-1}$ for the angle ϕ. The time evolution of ϕ is expected to occur in a similar form as the dynamics of the angle θ, however, with an infinitely large width $\sigma_\phi \to \infty$. The focus of our study is the diffusive angular dynamics occurring on the time scales of the diffusion constant D and

shorter such that we can also model the dynamics of ϕ by the form

$$\mathcal{P}_\phi(\phi,\phi',t) = \frac{1}{2\pi\sigma_\phi^2\sqrt{1-e^{-2Dt}}}\exp\left(-\frac{\phi^2+\phi'^2-2\phi\phi' e^{-Dt}}{2\sigma_\phi^2[1-e^{-2Dt}]}\right) \tag{2.6}$$

with the width $\sigma_\phi = 2\pi$.

2.1.3 System Hamiltonian of the PBDA pair and Light-Matter Interaction

In a reduced model of single excitations, we describe each monomer of the PBDA pair as a quantum two-level system with energy difference ϵ_j between ground and excited state. Then, the dimer is described by a Frenkel-exciton Hamiltonian given by

$$H = \frac{1}{2}\epsilon_1\sigma_z^{(1)} + \frac{1}{2}\epsilon_2\sigma_z^{(2)} + J(\theta,\phi)\sigma_x^{(1)}\sigma_x^{(2)}\,, \tag{2.7}$$

with the standard Pauli matrices $\sigma_{x,y,z}^{(j=1,2)}$. The Hamiltonian is readily diagonalized by the unitary transformation

$$T = \exp\left(\frac{i}{2}\alpha\sigma_y^{(1)}\sigma_x^{(2)} + \frac{i}{2}\beta\sigma_x^{(1)}\sigma_y^{(2)}\right) \tag{2.8}$$

with the angles α and β defined according to

$$\tan(\alpha+\beta) = -\frac{J(\theta,\phi)}{\epsilon} \quad \text{and} \quad \tan(\alpha-\beta) = -\frac{J(\theta,\phi)}{\delta\epsilon}\,, \tag{2.9}$$

where $\epsilon = (\epsilon_1+\epsilon_2)/2$ and $\delta\epsilon = (\epsilon_1-\epsilon_2)/2$. For the considered PBDA, we find $\delta\epsilon \simeq 2500\text{cm}^{-1}$. Applying the transformation T leads to two independent two-level systems with new Pauli matrices $\tau_z^{(\pm)}$ and energies $E_\pm(\theta,\phi) = \sqrt{\epsilon^2+J^2(\theta,\phi)} \pm \sqrt{\delta\epsilon^2+J^2(\theta,\phi)}$. Then, the Hamiltonian of the total system is simply given by the expression

$$H_d = THT^\dagger = \frac{1}{2}E_+(\theta,\phi)\tau_z^{(+)} + \frac{1}{2}E_-(\theta,\phi)\tau_z^{(-)}\,. \tag{2.10}$$

In the same way, the total dipole moment $\boldsymbol{\mu} = \boldsymbol{\mu}_1\sigma_x^{(1)} + \boldsymbol{\mu}_2\sigma_x^{(2)}$ of the heterodimer transforms according to

$$\boldsymbol{\mu} = \boldsymbol{\mu}_1\left[\cos(\alpha)\tau_x^{(+)} - \sin(\alpha)\tau_z^{(+)}\tau_x^{(-)}\right] + \boldsymbol{\mu}_2\left[\cos(\beta)\tau_x^{(-)} - \sin(\beta)\tau_x^{(+)}\tau_z^{(-)}\right]\,. \tag{2.11}$$

Spectroscopically, the decoupled two-level systems can be addressed individually. For this reason, it is sufficient to investigate the response of the $j = +,-$ systems, with the corresponding dipole components

$$\boldsymbol{\mu}_+ = \left[\boldsymbol{\mu}_1\cos(\alpha) + \boldsymbol{\mu}_2\sin(\beta)\right]\tau_x^{(+)}\,, \tag{2.12a}$$

$$\boldsymbol{\mu}_- = \left[-\boldsymbol{\mu}_1\sin(\alpha) + \boldsymbol{\mu}_2\cos(\beta)\right]\tau_x^{(-)}\,. \tag{2.12b}$$

For the PBDA pair, we have that $\epsilon \gg \delta\epsilon \gtrsim J_0 \simeq k_BT$ such that for the transformation angles $\alpha \simeq -\beta$ and $\tan(2\alpha) = -J(\theta,\phi)/\delta\epsilon$. Additionally, optical spectroscopic experiments

typically start with the system in the ground state. Under these considerations, the dipole moments can be further simplified to

$$\boldsymbol{\mu}_+ \simeq \begin{pmatrix} -\mu_2 \sin(\alpha)\cos(\theta) \\ -\mu_2 \sin(\alpha)\sin(\theta)\sin(\phi) \\ \mu_1 \cos(\alpha) - \mu_2 \sin(\alpha)\sin(\theta)\cos(\phi) \end{pmatrix} \tau_x^{(+)}, \tag{2.13a}$$

and similarly

$$\boldsymbol{\mu}_- \simeq \begin{pmatrix} -\mu_2 \cos(\alpha)\cos(\theta) \\ -\mu_2 \cos(\alpha)\sin(\theta)\sin(\phi) \\ -\mu_1 \sin(\alpha) + \mu_2 \cos(\alpha)\sin(\theta)\cos(\phi) \end{pmatrix} \tau_x^{(-)}. \tag{2.13b}$$

Let us note that the transformation angle $\alpha \equiv \alpha(\theta,\phi)$ depends on both geometric angles θ, ϕ. Moreover, we will use the shorthand notation $c_1(\theta,\phi) = \cos(\alpha) = J(\theta,\phi)/\mathcal{N}(\theta,\phi)$ and $c_2(\theta,\phi) = -\sin(\alpha) = (\sqrt{\delta\epsilon^2 + J^2(\theta,\phi)} - \delta\epsilon)/\mathcal{N}(\theta,\phi)$, with $\mathcal{N}^2(\theta,\phi) = J^2(\theta,\phi) + (\sqrt{\delta\epsilon^2 + J^2(\theta,\phi)} - \delta\epsilon)^2$. In order to not exaggerate dependences, we consequently omit the dependence on the two angle θ and ϕ from here on.

In the following, we are interested in the nonlinear optical response of the PBDA pair to a sequence of short lasers pulses. To that extent, we follow the description given in reference [41]. An expansion of the standard light-matter interaction Hamiltonian with the laser electric field generates effective magnetic dipole moments and electric quadrupoles which typically dominate over the real (intrinsic) contributions [175]. Therefore, we neglect the latter and combine the effective magnetic dipole moment $\boldsymbol{M}_\pm$ and the effective quadrupole tensor $\boldsymbol{Q}_\pm$ in the tensor

$$T_{\pm,\alpha\beta} = -iR_\alpha \mu_{\mp,\beta} = iQ_{\pm,\alpha\beta} - \sum_{\gamma=x,y,z} \epsilon_{\alpha\beta\gamma} M_{\pm,\gamma}/k. \tag{2.14}$$

Here, $R_{\alpha=x,y,z}$ are the components of the connecting vector $\boldsymbol{R}$ and k is the absolute value of the wave vector of the incident laser light. Moreover, we note that $Q_{\pm,\alpha\beta}$ is symmetric, while the contribution $\sum_\gamma \epsilon_{\alpha\beta\gamma} M_{\pm,\gamma}$ is antisymmetric in α and β. Inserting the electric dipole moments $\boldsymbol{\mu}_\pm$, we find

$$\boldsymbol{T}_- = -\frac{iR}{2} \begin{pmatrix} \mu_2 c_2 \cos\theta & 0 & 0 \\ \mu_2 c_2 \sin\theta \sin\phi & 0 & 0 \\ \mu_1 c_1 + \mu_2 c_2 \sin\theta\cos\phi & 0 & 0 \end{pmatrix}, \tag{2.15a}$$

$$\boldsymbol{T}_+ = -\frac{iR}{2} \begin{pmatrix} -\mu_2 c_1 \cos\theta & 0 & 0 \\ -\mu_2 c_1 \sin\theta \sin\phi & 0 & 0 \\ \mu_1 c_2 - \mu_2 c_1 \sin\theta\cos\phi & 0 & 0 \end{pmatrix}, \tag{2.15b}$$

from which we can reconstruct $\boldsymbol{Q}_\pm$ and $\boldsymbol{M}_\pm$. Consequently, the quadrupole tensors results in

$$\boldsymbol{Q}_- = -\frac{R}{4}\begin{pmatrix} 2\mu_2 c_2 \cos\theta & \mu_2 c_2 \sin\theta\sin\phi & \mu_1 c_1 + \mu_2 c_2 \sin\theta\cos\phi \\ \mu_2 c_2 \sin\theta\sin\phi & 0 & 0 \\ \mu_1 c_1 + \mu_2 c_2 \sin\theta\cos\phi & 0 & 0 \end{pmatrix}, \tag{2.16a}$$

$$\boldsymbol{Q}_+ = -\frac{R}{4}\begin{pmatrix} -2\mu_2 c_1 \cos\theta & -\mu_2 c_1 \sin\theta\sin\phi & \mu_1 c_2 - \mu_2 c_1 \sin\theta\cos\phi \\ -\mu_2 c_1 \sin\theta\sin\phi & 0 & 0 \\ \mu_1 c_2 - \mu_2 c_1 \sin\theta\cos\phi & 0 & 0 \end{pmatrix}. \tag{2.16b}$$

In addition, the magnetic dipole moments take the form

$$\boldsymbol{M}_- = \frac{ikR}{4}\left(0, \mu_1 c_1 + \mu_2 c_2 \sin\theta\cos\phi, -\mu_2 c_2 \sin\theta\sin\phi\right)^T, \tag{2.17a}$$

$$\boldsymbol{M}_+ = \frac{ikR}{4}\left(0, \mu_1 c_2 - \mu_2 c_1 \sin\theta\cos\phi, \mu_2 c_1 \sin\theta\sin\phi\right)^T. \tag{2.17b}$$

With the dimer in the rotating wave approximation, the light-matter interaction Hamiltonian with the classical laser field $\boldsymbol{F}(t)e^{i\boldsymbol{k}\boldsymbol{R}/2}$ to first order in the wave vector $\boldsymbol{k}$ reads

$$H_{\text{int}} = -\sum_{\alpha=x,y,z}\sum_{j=\pm} F_\alpha(t)\tau_+^{(j)}\left\{\mu_{j,\alpha} + i\sum_{\beta=x,y,z} k_\beta Q_{j,\alpha\beta} - \sum_{\beta,\gamma=x,y,z}\epsilon_{\alpha\beta\gamma}k_\beta M_{j,\gamma}\right\} + \text{H.c.}. \tag{2.18}$$

Here, $\tau_+^{(j)} = (\tau_x^{(j)} + i\tau_y^{(j)})/2$ is the operator which creates an excitation in the $j = \pm$ two-state subsystem.

2.1.4 Chiral Linear Response

In accordance with the assumption that the decoupled two-level systems with energies $E_\pm$ can be probed individually, we focus solely on the $j = +$ system. Then, the effective field-matter interaction Hamiltonian takes the simplified form $H_{\text{int}} = -\sum_\alpha F_\alpha(t)\mathcal{Y}_\alpha\tau_+ + \text{H.c.}$ with $\mathcal{Y}_\alpha = \mu_\alpha + \sum_\beta k_\beta T_{\alpha\beta} + \mathcal{O}(k^2)$, where we omitted the index $+$ and superscript $(+)$.

The linear optical response is given by the correlation function $I_{\alpha\beta}(t) = \langle\mathcal{Y}_\alpha(t)\mathcal{Y}_\beta(0)\rangle$. As a matter of fact, the response of a single molecule can rarely be resolved experimentally. Hence, we have to introduce instead an orientational average over the solid angle Ω in order to account for the statistical ensemble where each molecule has a different orientation in space. We denote this orientational averaging by $\langle\cdot\rangle_\Omega$, which leads to the averaged correlation function

$$I_{\alpha\beta}(t) = \frac{1}{3}\delta_{\alpha\beta}\sum_\gamma\langle\mu_\gamma^*(t)\mu_\gamma(0)\rangle_\Omega + \frac{1}{3}\sum_{\gamma,\delta}\epsilon_{\alpha\beta\gamma}k_\gamma\left[\langle M_\delta^*(t)\mu_\delta(0)\rangle_\Omega - \langle\mu_\delta^*(t)M_\delta(0)\rangle_\Omega\right]. \tag{2.19}$$

In this expression, only the second part is a chiral signal. Without loss of generality, we assume that the laser light is propagating along the x-direction with $k_\alpha = k\delta_{\alpha x}$ and measure

the signal

$$I_{yz}(t) \simeq \frac{2i}{3} \sum_{\alpha} \int d\theta \, \rho_{\theta}^{\mathrm{eq}}(\theta) \int \frac{d\phi}{2\pi} \, \mathrm{Im} \left\{ M_{\alpha}^{*}(\theta, \phi) \mu_{\alpha} \right\} e^{-\Gamma t} e^{-iE_{+}(\theta,\phi)t} \,, \tag{2.20}$$

in order to observe the chiral component. To arrive at this expression, we have assumed a slow variation of the angles with respect to the internal time scale such that we can set $\phi(t) \simeq \phi(0)$ and $\theta(t) \simeq \phi(0)$. Moreover, Γ is a phenomenological dephasing rate for which we assume $\Gamma = 50\mathrm{cm}^{-1}$, corresponding to a typical time scale of roughly ~ 100 fs. We obtain the linear chiral spectrum via a one-sided Fourier transformation with $I_{yz}(\omega) = \int d\theta d\phi \, J_{yz}(\omega, \theta, \phi)$, where the integrand is given by the expression

$$J_{yz}(\omega, \theta, \phi) = \frac{kR}{12\pi} \mu_1 \mu_2 \sin(\theta) \sin(\phi) \rho_{\theta}^{\mathrm{eq}}(\theta) \frac{\omega - E_{+} - i\Gamma}{[\omega - E_{+}]^2 + \Gamma^2} \,. \tag{2.21}$$

We observe that the integrand is antisymmetric in both angles θ and ϕ. As a consequence, each angle average individually leads to vanishing linear chiral response, i.e., $I_{yz}(\omega) \equiv 0$.

In figure 2.3, we show the real (a), (b), (c) and imaginary (d), (e), (f) part of the linear chiral signal $J_{yz}(\omega, \theta, \phi)$ as a function of the frequency ω and the angle ϕ. For all panels, the angle θ is fixed to $\pi/4$ and we have chosen $J_0 = 85\,\mathrm{cm}^{-1}$, $\Gamma = 50\,\mathrm{cm}^{-1}$ and the standard deviation $\sigma_\theta = 0.24$ for the angular fluctuations of the angle θ. These parameters have been chosen in order to mimic the real PBDA complex. From left to right, the energy difference increases from $\delta\epsilon = 25\,\mathrm{cm}^{-1}$ in (a), (d) to $\delta\epsilon = 85\,\mathrm{cm}^{-1}$ in (b), (e), and finally $\delta\epsilon = 2500\,\mathrm{cm}^{-1}$ in (c), (f), which corresponds to the PBDA pair. For $\phi = 0$, the molecular complex is achiral and the signal vanishes. When ϕ is finite, a double peak structure in the real signal emerges with opposite sign and a single peak in the imaginary part for varying frequency ω. For the PBDA complex in (c) and (f), a double peak structure is also observed when ϕ is varied, while ω is kept fixed. By decreasing the energy difference $\delta\epsilon$, the ellipsoid shape of the peak (in the imaginary part) changes toward a *heart* shape which exhibits two positive peaks followed by two negative peaks at some ω. We note that the case of small $\delta\epsilon$ is closer to a homodimer. Moreover, similar results can be expected, if the structure fluctuates around different chiral equilibrium positions at $\phi \neq 0$ and $\theta \neq 0$. With these results, it is possible to determine the geometric structure of such complexes.

2.1.5 Two-dimensional Chiral Spectrum

In order to measure a non-vanishing orientation averaged chiral signal, we focus on the two-dimensional chiral spectrum. Hence, we determine the three-pulse photon echo signal which is given by the four-point correlation function [176]

$$\mathcal{R}_{\alpha\beta\gamma\delta} = \langle \mathcal{Y}_{\alpha}^{*}(\tau_3) \mathcal{Y}_{\beta}(\tau_2) \mathcal{Y}_{\gamma}(\tau_1) \mathcal{Y}_{\delta}^{*}(0) \rangle_{\Omega} \,, \tag{2.22}$$

with the earlier defined $\mathcal{Y}_{\alpha} = \mu_{\alpha} + \sum_{\beta} k_{\beta} T_{\alpha\beta} + \mathcal{O}(k^2)$. Here, the arrival times of the three pulses are given by 0, τ_1 and τ_2, while the signal is detected at time τ_3. In particular, we

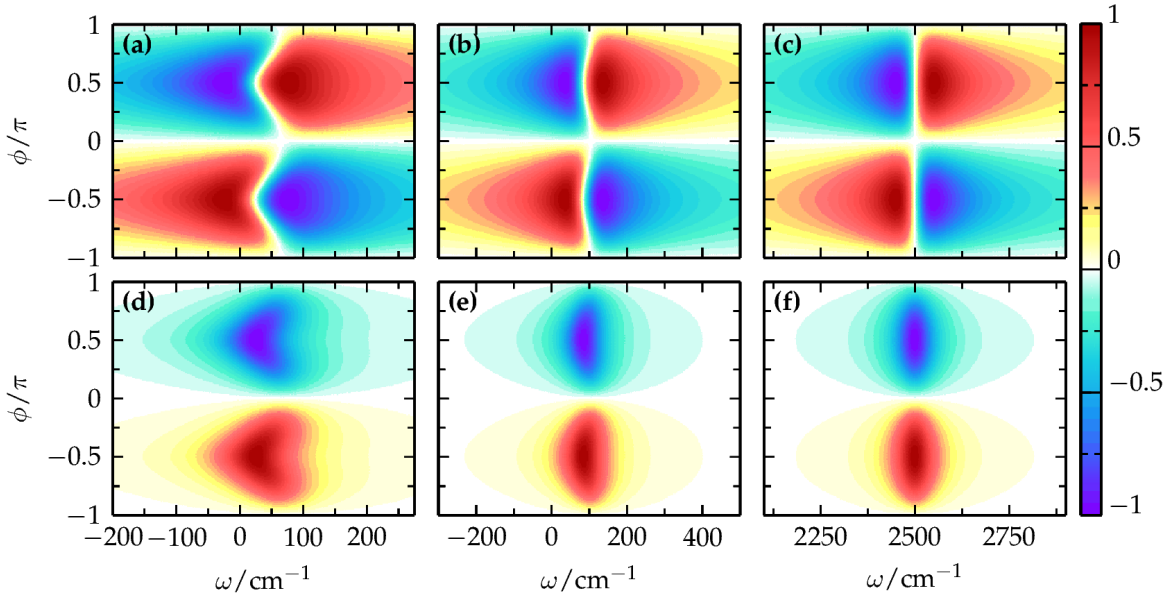

FIGURE 2.3: The real (a), (b), (c) and imaginary part (d), (e), (f) of the integrand of the chiral linear spectrum $J_{yz}(\omega, \theta, \phi)$ is shown as a function of the frequency ω and angle ϕ at fixed $\theta = \pi/4$. In each column, a different energy difference is considered with $\delta\epsilon = 25\,\mathrm{cm}^{-1}$ in (a), (d), $\delta\epsilon = 85\,\mathrm{cm}^{-1}$ in (b), (e) and $\delta\epsilon = 2500\,\mathrm{cm}^{-1}$ in (c), (f). The other parameters were chosen according to $J_0 = 85\,\mathrm{cm}^{-1}$, $\Gamma = 50\,\mathrm{cm}^{-1}$ and $\sigma_\theta = 0.24$. For a better comparison, each signal is normalized to its individual maximum.

estimate a certain combination of the four-point correlation functions [41], given by the expression

$$\mathcal{R}_c = \mathcal{R}^{xx}_{[yz][yz]} + 2\mathcal{R}^{zx}_{[xy][yz]}\,, \tag{2.23}$$

which yields a purely chiral two-dimensional signal. In this definition, the superscripts of the term $\mathcal{R}^{zx}$ represent the response in a setup where the first two pulses propagate in x-direction, while the third pulse and the detection is along the z-direction. Likewise, the superscripts of the term $\mathcal{R}^{xx}$ represents a collinear arrangement, where all pulses and the detection are along the x-direction. Besides, the subscripts denote the polarization direction of the corresponding pulses, where the bracket notation indicates the antisymmetrization of the tensors with respect to the parenthesized indices, i.e.,

$$\mathcal{R}^{zx}_{[xy][yz]} = \mathcal{R}^{zx}_{xyyz} - \mathcal{R}^{zx}_{yxyz} - \mathcal{R}^{zx}_{xyzy} + \mathcal{R}^{zx}_{yxzy}\,, \tag{2.24a}$$

$$\mathcal{R}^{xx}_{[yz][yz]} = \mathcal{R}^{xx}_{yzyz} - \mathcal{R}^{xx}_{zyyz} - \mathcal{R}^{xx}_{yzzy} + \mathcal{R}^{xx}_{zyzy}\,. \tag{2.24b}$$

We note that optical signals, that are associated to chirality exchange, result from the two-time correlation of the pseudo-scalar $\boldsymbol{\mu M}$. In general, these signals are weak as they scale with $\sim (kR)^2$. In fact, it can be shown that contributions in $\mathcal{R}_c$ to linear order in kR vanish after the orientational averaging [41]. For the same reason, contributions to zeroth order in kR coming from $\mathcal{R}^{zx}_{[xy][yz]}$ vanish. Yet, we may consider

$$\mathcal{R}^{xx}_{[yz][yz]} \sim \langle \mathcal{Y}^*_\alpha(\tau_3)\mathcal{Y}_\beta(\tau_2)\mathcal{Y}_\alpha(\tau_1)\mathcal{Y}^*_\beta(0)\rangle_\Omega - \langle \mathcal{Y}^*_\alpha(\tau_3)\mathcal{Y}_\beta(\tau_2)\mathcal{Y}_\beta(\tau_1)\mathcal{Y}^*_\alpha(0)\rangle_\Omega\,. \tag{2.25}$$

When angular fluctuations occur on a very fast time scale, the average over θ and ϕ can be performed at all times τ_i separately, which would lead to a vanishing signal $\mathcal{R}^{xx}_{[yz][yz]}$. However, this angular motion of the heavy nuclei is typically slow when compared to the time scale of the internal system[1]. In fact, a significant signal strength is only experimentally observed at coherence times $\tau = \tau_1$ and $t = \tau_3 - \tau_2$, which are much smaller than the inverse of the angular diffusion constant D^{-1}. Hence, the angles do not change significantly during these time intervals. On the other hand, the delay time $T = \tau_2 - \tau_1$ is usually varied over much longer times in experiments. Only during this time interval, the angular motion has to be taken into account, such that we can set $\theta(\tau_3) = \theta(\tau_2)$, $\theta(\tau_1) = \theta(0)$ and $\phi(\tau_3) = \phi(\tau_2)$, $\phi(\tau_1) = \phi(0)$. In addition, the probability densities introduced in equations (2.5) and (2.6) have to be explicitly included. This is done by performing the orientational averaging according to

$$\begin{aligned}\langle \mathcal{Y}^*_\alpha(\tau_3)\mathcal{Y}_\beta(\tau_2)\mathcal{Y}_\gamma(\tau_1)\mathcal{Y}^*_\delta(0)\rangle_\Omega =& e^{-\Gamma(t+\tau)}\int d\theta \int d\theta' \int d\phi \int d\phi' \mathcal{P}_\theta(\theta,\theta',T)\mathcal{P}_\phi(\phi,\phi',T) \\ &\times \mathcal{Y}^*_\alpha(\theta,\phi)\mathcal{Y}_\beta(\theta,\phi)\mathcal{Y}_\gamma(\theta',\phi')\mathcal{Y}^*_\delta(\theta',\phi')e^{-iE_+t}e^{iE'_+\tau}\,.\end{aligned} \tag{2.26}$$

Here, we have again used the shorthand notation $E_+ \equiv E_+(\theta,\phi)$ and $E'_+ \equiv E_+(\theta',\phi')$. With this expression, we find that the zeroth order contribution in the signal $\mathcal{R}^{xx}_{[yz][yz]}$ vanishes and, consequently, $\mathcal{R}_c$ yields no contributions to zeroth and first-order in kR. Thus, the two-dimensional chiral signal $\mathcal{R}_c$ is at least quadratic in kR.

Following the description in reference [41], the chiral signal can be written in the compact form

$$\mathcal{R}_c(t,T,\tau) = -\frac{2k^2}{3}\sum_{\alpha\beta\gamma}\Big(\langle X_{\alpha\beta\gamma\gamma\beta\alpha}\rangle_\Omega + 2\langle X_{\alpha\beta\gamma\beta\alpha\gamma}\rangle_\Omega\Big)\,, \tag{2.27}$$

by defining

$$X_{\alpha\beta\gamma\delta\epsilon\zeta} = \mathrm{Im}\big\{T_{\alpha\beta}(\tau_2)\mu^*_\gamma(\tau_2) - T_{\gamma\beta}(\tau_2)\mu^*_\alpha(\tau_2)\big\}\mathrm{Im}\big\{T_{\delta\epsilon}(0)\mu^*_\zeta(0) - T_{\zeta\epsilon}(0)\mu^*_\delta(0)\big\}\,. \tag{2.28}$$

Evaluating the expression for the PBDA dimer, we find

$$\sum_{\alpha\beta\gamma}\langle X_{\alpha\beta\gamma\gamma\beta\alpha}\rangle_\Omega = -\frac{R^2}{2}\mu_1^2\mu_2^2\langle\cos(\theta)\cos(\theta') + \sin(\theta)\sin(\phi)\sin(\theta')\sin(\phi')\rangle_\Omega\,, \tag{2.29a}$$

$$\sum_{\alpha\beta\gamma}\langle X_{\alpha\beta\gamma\beta\alpha\gamma}\rangle_\Omega = \frac{R^2}{4}\mu_1^2\mu_2^2\langle\cos(\theta)\cos(\theta')\rangle_\Omega\,, \tag{2.29b}$$

where the primed and unprimed angles indicate the initial orientation at time 0 and final orientation at time τ_2, respectively. After a one-sided Fourier transformation with respect to

[1] We note, however, that in order to treat the case where the angular motion occurs on the same time scale as the internal system time scale $E_\pm^{-1}$, a full quantum mechanical treatment is required.

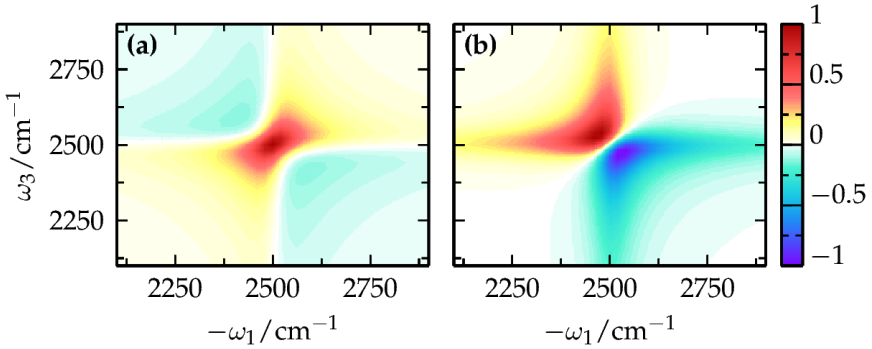

FIGURE 2.4: The real (a) and imaginary part (b) of the 2D chiral spectrum $\mathcal{R}_c(\omega_3, T, \omega_1)$ are shown for the very short waiting time $DT = 10^{-5}$ for the PBDA pair with $\delta\epsilon = 2500\,\mathrm{cm}^{-1}$, $J_0 = 85\,\mathrm{cm}^{-1}$, $\sigma_\phi = 2\pi$ and $\sigma_\theta = 0.24$. The real and imaginary part of the signal have been normalized to their individual maximum.

the coherence times $\tau = \tau_1$ and $t = \tau_3 - \tau_2$, we obtain the two-dimensional chiral signal

$$\mathcal{R}_c(\omega_3, T, \omega_1) = \frac{(kR)^2}{3}\mu_1^2\mu_2^2 \int d\theta d\theta' d\phi d\phi' \, \mathcal{P}_\theta(\theta, \theta', T)\mathcal{P}_\phi(\phi, \phi', T)F(\theta, \phi, \theta', \phi')\,, \tag{2.30}$$

with the function

$$F(\theta, \phi, \theta', \phi') = \sin(\theta)\sin(\phi)\sin(\theta')\sin(\phi')\frac{\Gamma + i(\omega_3 - E_+)}{\Gamma^2 + (\omega_3 - E_+)^2}\frac{\Gamma + i(\omega_1 + E'_+)}{\Gamma^2 + (\omega_1 + E'_+)^2}\,. \tag{2.31}$$

The angular conformations that dominantly contribute to the chiral signal are determined by the integrand $F(\theta, \phi, \theta', \phi')$. Accordingly to our previous discussion, these are the chiral configurations for which both angles are different from zero. The contributions exhibit a maximum when $\boldsymbol{\mu}_2$ is perpendicular to the plane that is spanned by $\boldsymbol{\mu}_1$ and $\boldsymbol{R}$, or, in other words, when $|\phi| = |\theta| = \pi/2$.

For the parameters of the PBDA complex given above, we show the two-dimensional chiral signal $\mathcal{R}_c(\omega_3, T, \omega_1)$ in figure 2.4 for the very short waiting time $DT = 10^{-5}$. Here, panel (a) depicts the real part, whereas the imaginary part is depicted in panel (b). Our assumption of an exponential decay with a fixed rate Γ of the dephasing dynamics corresponds to Markovian dephasing dynamics which is reflected in the peak shape. In general, the measured nonlinear chiral signals are rather weak as they scale with $(kR)^2$, which is typically of the order 10^{-6}.

As the diffusive angular dynamics occur on a time scale of the autocorrelation time D^{-1}, the probability densities progressively tend to their corresponding equilibrium densities as the waiting time T is increased. It is then expected that the strength of the nonlinear chiral signal strongly decreases when T is of similar order as the autocorrelation time. This effect is shown in figure 2.5 by measuring the relative maximum of the chiral signal $R(T)/R(T_0)$ with $R(T) = \max_{\omega_1,\omega_3} \mathrm{Re}\,\{\mathcal{R}_c(\omega_3, T, \omega_1)\}$ and $DT_0 = 10^{-5}$. In fact, by tracking the peak maximum of the nonlinear signal $R(T)$, it is possible to experimentally measure the autocorrelation time of the angular fluctuations. We note that for our considerations, the maximum is always located at the frequency $\omega_3 = -\omega_1 = \delta\epsilon$.

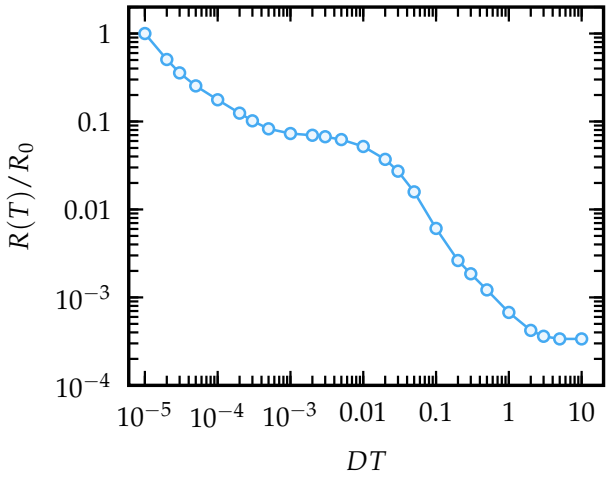

FIGURE 2.5: The maximal amplitude of the real part $R(T) = \max_{\omega_1,\omega_3} \mathrm{Re}\{\mathcal{R}_c(\omega_3, T, \omega_1)\}$ is shown in dependence of the waiting time T. The amplitude is scaled to the value $R_0 = R(T_0)$ at $DT_0 = 10^{-5}$. The other parameters are the same as in figure 2.4.

With this example, the striking impact of equilibrium fluctuations on the chiral properties of a dimer molecule is revealed. In the following section, we go beyond the equilibrium case of thermal fluctuations and consider an example in which nonequilibrium quantum fluctuations occur.

2.2 Nonequilibrium Fluctuations in a Mesoscopic Quantum System

In order to find a theoretical description of relaxation and decoherence processes, quantum statistical fluctuations need to be included in the modeling of the dynamics of a quantum system [160, 164]. In the style of classical mechanics, a quantum mechanical form of the Langevin equation can be derived. However, an often favored and more general approach is to consider an infinite set of uncoupled harmonic oscillators which are held at thermal equilibrium and coupled to the quantum system of interest. These harmonic oscillators act as a thermal bath (also bosonic environment) and induce fluctuations for the central system, leading to decoherence and relaxation effects. The minimal model as a central system that allows to study these questions is a two-state model or, in other words, spin-one-half model. This spin-boson model allows to study dephasing of the two states, while transitions lead to dissipation [161, 162]. In contrast to the minimalist approach, the spin-boson model does not only act as a simple toy model, but rather forms a cornerstone of quantum statistical physics. For more than thirty years, it has served as a key model for the development of various fundamental analytical and numerical techniques to describe open quantum systems. Outstanding examples among these methods utilize a real-time path integral formulation [161, 162, 177] which allows to obtain analytical results for the spin-boson model in certain limits. For instance, the non-interacting blip approximation treats transitions between the two states perturbatively, for which mainly incoherent decay of the population and coherence [161, 162, 178] are revealed.

The action of nonequilibrium quantum fluctuations to a coherent quantum two-state

system is however more complex. So far, there exists no closed exact expression for the relaxation and dephasing rates in general. A simple model to study the influence of nonequilibrium quantum statistical fluctuations appears in the form of a quantum two-state system which is coupled to the energy level of a single spinless non-interacting electron on a quantum dot. The quantum dot is connected to reservoirs of non-interacting electrons held at constant temperature, such that the electron can tunnel from or into these reservoirs. The minimal nonequilibrium condition requires at least two reservoirs (leads), between which an electric voltage is applied. As a consequence of a finite difference of the chemical potentials of the leads, a finite current between the two leads occurs. It follows that this charge transport induces nonequilibrium quantum fluctuations to the quantum two-state system coupled to the dot. This system very much resembles the equilibrium spin-boson model, such that it is also often entitled as the nonequilibrium spin-boson model, despite the fact that the statistical nature of the reservoirs actually is fermionic.

In order to model the nonequilibrium fluctuations generated by the flowing electron current through the dot, we consider the system-bath Hamiltonian in the form

$$H = H_S + H_B + H_T \,. \tag{2.32}$$

Here, the quantum two-state system is included in the dot Hamiltonian H_S. We denote the two quantum states of interest by $|\uparrow\rangle$ and $|\downarrow\rangle$ and couple these to the population of spinless electrons on the dot. The corresponding fermionic annihilation and creation operators are denoted as d and $d^\dagger$. To be specific, we consider the system Hamiltonian

$$H_S = \frac{B}{2}\sigma_z + \frac{\Delta}{2}\sigma_x + \frac{J}{2}d^\dagger d\sigma_z \,, \tag{2.33}$$

where $\sigma_{j=x,y,z}$ are the Pauli matrices. The energy difference between the two states $|\uparrow\rangle$ and $|\downarrow\rangle$ is given by B and we further allow a finite transition with the rate Δ. The effective spin-1/2 system is coupled to the electronic occupation number $n = d^\dagger d$ of the dot with the coupling constant J. The Hilbert space of the Hamiltonian H_S is then spanned by the vector basis $\{|\sigma, n\rangle\}$, where $\sigma \in \{\uparrow, \downarrow\}$ and $n \in \{0, 1\}$ is the number of electrons on the dot. By expanding the system Hamiltonian in its eigenbasis $H_S|\pm, n\rangle = \epsilon_{\pm,n}|\pm n\rangle$, we find the eigenenergies $\epsilon_{\pm,n} = \pm\sqrt{\Delta^2 + (B + nJ)^2}/2$. Here, $+(-)$ corresponds to an (anti-)symmetric linear superposition of the two spin states.

The nonequilibrium bath is composed of two non-interacting reservoirs of spinless electrons with energies $\epsilon_{k\alpha}$ described by the Hamiltonian

$$H_B = \sum_{k\alpha}(\epsilon_{k\alpha} - \mu_\alpha)c^\dagger_{k\alpha}c_{k\alpha} \,, \tag{2.34}$$

with the reservoir index $\alpha \in \{L, R\}$ which denotes the *left* and *right* lead. Provided that the reservoirs are large enough such that the interaction with the system has almost no back action on the fermions in the leads, we can commonly assume that the two baths are thermalized at all times at the same temperature $T = \beta^{-1}$, but with different chemical potentials μ_α. Here, we assume a symmetric voltage bias between the two reservoirs according to

$\mu_L - \mu_R = eV$.

The electron transport through the quantum dot is described by a coupling Hamiltonian given by

$$H_T = \sum_{k\alpha} \left(t_{k\alpha} d^\dagger c_{k\alpha} + \text{H.c.} \right) , \tag{2.35}$$

with tunneling amplitude $t_{k\alpha}$. The electronic operators d and $c_{k\alpha}$ obey the standard algebra of fermionic operators.

The nonequilibrium quantum two-state model has been addressed in reference [179] on the basis of a NIBA-like approximation. In the case of vanishing off-diagonal coupling in the quantum two-state system, i.e., $\Delta \to 0$, the full problem becomes exactly solvable. Hence, it is reasonable to study the effect of Δ perturbatively. Under the additional assumption of not too strong system-bath coupling J, an expansion of the noise correlators up to third order in J can be used. Then, the frequency-dependent spin-relaxation rates, the frequency-dependent fluctuation-dissipation ratio and an effective frequency-dependent nonequilibrium "*temperature*" could be determined [179].

A further extended analysis of the regime of small Δ characterized by a golden rule rate for the transitions between the two energy eigenstates proportional to Δ^2 has been carried out in reference [180]. The intermediate time domain has been carefully addressed for the full parameter regime of weak to strong system-bath coupling J at zero (or very low) temperature. A Marcus-like nonequilibrium quantum relaxation rate has been derived. Interestingly, a simple mapping between the equilibrium temperature and bias voltage has been shown not to exist. Different decay characteristics in different time regimes involve algebraic as well as exponential decays of the correlation function. In addition, going beyond the lowest order in Δ, it has been shown that a Coulomb gas description in terms of a power series in Δ is suggested to be valid, since the first few orders up to the contribution $\sim \Delta^6$ agree with the numerically calculated exact result. Yet, a complete analysis to all orders in Δ, but for linear order in J at finite temperature remained open.

2.2.1 Nonequilibrium Spin Dynamics and Electron Current

Before turning our focus on the fluctuations explicitly, we determine the system dynamics when subject to nonequilibrium fluctuations. This is done by using the well established diagrammatic perturbation method in Keldysh space [42, 43]. The evolution of the expectation value of an arbitrary operator A can be formulated in terms of a time-ordered integration along the Keldysh contour $\mathcal{C}$ according to

$$\langle A(t) \rangle = \text{tr} \left[\rho_0 \mathcal{T}_\mathcal{C} \exp\left(-i \int_\mathcal{C} d\tau \, H_T(\tau)_I \right) A(t)_I \right] , \tag{2.36}$$

with the time-ordering operator $\mathcal{T}_\mathcal{C}$ along the Keldysh contour. The subscript I indicates that the time dependence of all operators on the right-hand side is meant as the time evolution in the interaction picture. By the assumption that the initial density operator of the total system ρ_0 at time t_0 factorizes into a system and a bath part, equation (2.36) allows us to perform

a systematic expansion organized in orders of the tunneling Hamiltonian. Choosing the operator A to be the projection operator $|i\rangle\langle j|$, the time evolution of the reduced system density operator $\boldsymbol{P}$ can be derived. In practice, it is convenient to choose each state $|i\rangle$ to represent a different eigenstate of H_S, e.g., $|1\rangle = |-,0\rangle$, $|2\rangle = |+,0\rangle$, $|3\rangle = |-,1\rangle$ and $|4\rangle = |+,1\rangle$. Inserting the projection operator in equation (2.36) and differentiating with respect to time, the equation of motion for the reduced density operator is obtained

$$\partial_t P_j^i(t) = \sum_{kl} \int_{t_0}^{t} dt' \, K_{jl}^{ik}(t,t') P_l^k(t') \,, \tag{2.37}$$

with $\langle i|\boldsymbol{P}(t)|j\rangle = P_j^i(t)$. The correlation functions to all orders in H_T are included in the kernel $\boldsymbol{K}(t,t')$. By employing a tensor-matrix multiplication notation, the result may be rewritten in the compact form

$$\partial_t \boldsymbol{P}(t) = \int_{t_0}^{t} dt' \, \boldsymbol{K}(t,t') \boldsymbol{P}(t') \,. \tag{2.38}$$

In the following, we focus on the regime of sequential tunneling of electrons. In this limit, we are able to apply a Born–Markov approximation and replace $\boldsymbol{P}(t')$ with $\boldsymbol{P}(t)$ on the right-hand side of equation (2.38). Thus, we assume the coupling between the quantum dot (including the electronic level and the effective spin-1/2) and the electronic leads to be weak in comparison to the typical energy scales of both parts. In addition, we assume the correlation time of the electronic bath to be much smaller than the relaxation time of the central system, such that the integral limits can be extended to infinity. To be specific, we replace the time variable t' by $\tau = t - t'$. Then, the integral runs from zero to $-t_0$ and we can set $t_0 = -\infty$. It follows that the time evolution equation becomes local in time and the memory kernel turns into a time independent super-operator $\boldsymbol{W}$. Finally, equation (2.38) reduces to

$$\partial_t \boldsymbol{P} = \boldsymbol{W}\boldsymbol{P} \,. \tag{2.39}$$

Here, the coherences of the reduced density operator due to internal coherent coupling between the electronic and the spin-1/2 are completely included in the equation of motion.

Another important quantity, especially from an experimental point of view as it is directly accessible, is the tunnel current $I = e\partial_t(N_L - N_R)$, where N_α is the total number of electrons in the lead α. In a fashion similar to the preceding discussion, an expression for the stationary current can be derived, which leads to the expression

$$I = \frac{e}{2}\langle \boldsymbol{W}^I \rangle_{\mathrm{st}} \,, \tag{2.40}$$

where the mean has to be taken with respect to the stationary solution of equation (2.39). The operator $\boldsymbol{W}^I$ is very similar to $\boldsymbol{W}$ and can be determined, in general, to all orders in H_T by using the diagrammatic approach formulated in references [42, 43].

In order to find an expression for the super operator $\boldsymbol{W}$ (or $\boldsymbol{W}^I$, analogously), we expand the perturbation series (2.38). As the total number of electrons in the leads is conserved, only

even orders in the tunneling constant $t_{k\alpha}$ contribute. In the sequential tunneling approximation, we consider only the lowest order terms, which are to second order in $t_{k\alpha}$. It is, then, useful to encode the tunneling strengths in the parameter $\Gamma_\alpha = 2\pi \sum_k |t_{k\alpha}|^2 \delta(E_{F,\alpha} - \epsilon_{k\alpha})$, where $E_{F,\alpha}$ is the Fermi energy of lead α. In the following, we set our focus on the symmetric tunneling regime, where we set $\Gamma = \Gamma_L = \Gamma_R$. In addition, we apply the standard wide-band limit, which corresponds to an energy-independent tunneling amplitude in the vicinity of the Fermi energy.

Under these assumptions, we find that $\boldsymbol{W} = \boldsymbol{W}_0 + \boldsymbol{W}_N + \boldsymbol{W}_C$ decomposes into three parts. The first term $\boldsymbol{W}_0$ describes the free time evolution of the quantum dot according to

$$[\boldsymbol{W}_0]^{ik}_{jl} = -i(\epsilon_i - \epsilon_j)\delta_{ik}\delta_{jl}\,, \tag{2.41}$$

with the eigenenergies defined below equation (2.33). The second term $\boldsymbol{W}_N$ conserves the number of particles in the reduced system and reads

$$\begin{aligned}[\boldsymbol{W}_N]^{ik}_{jl} = -\frac{\Gamma}{2\pi}\sum_\alpha \sum_m \Big\{ &\langle i|d^\dagger|m\rangle\langle m|d|k\rangle [I^-_\alpha(\omega_{jm})]^* \delta_{jl} + \langle i|d|m\rangle\langle m|d^\dagger|k\rangle I^+_\alpha(\omega_{mj})\delta_{jl} \\ &+ \langle l|d|m\rangle\langle m|d^\dagger|j\rangle [I^+_\alpha(\omega_{mi})]^*\delta_{ik} + \langle l|d^\dagger|m\rangle\langle m|d|j\rangle I^-_\alpha(\omega_{im})\delta_{ik}\Big\}\,,\end{aligned} \tag{2.42}$$

where we have used the shorthand notation $\omega_{ij} = \epsilon_i - \epsilon_j$ and introduced the integral

$$I^\pm_\alpha(\omega) = i\int dE\, \frac{f^\pm_\alpha(E)}{\omega - E - i0^+}\,, \tag{2.43}$$

with the Fermi–Dirac distribution $f^\pm_\alpha(E) = [1 + e^{\pm\beta(E-\mu_\alpha)}]^{-1}$. Last, the third term $\boldsymbol{W}_C = \sum_\alpha \boldsymbol{W}_\alpha$ includes sequential tunneling processes, that induce a current between the lead α and the dot. The contributions read

$$[\boldsymbol{W}_\alpha]^{ik}_{jl} = \frac{\Gamma}{2\pi}\Big[\langle i|d^\dagger|k\rangle\langle l|d|j\rangle\big\{I^+_\alpha(\omega_{il}) + [I^+_\alpha(\omega_{jk})]^*\big\} + \langle i|d|k\rangle\langle l|d^\dagger|j\rangle\big\{I^-_\alpha(\omega_{kj}) + [I^-_\alpha(\omega_{li})]^*\big\}\Big]\,. \tag{2.44}$$

In fact, this part of the super-operator is closely related to the super-operator $\boldsymbol{W}^I$ which is required to estimate the stationary current. It involves a summation over parts of the operators $\boldsymbol{W}_\alpha$ and an additional minus sign in order to include the current direction. In particular, we have that $\boldsymbol{W}^I = \boldsymbol{W}^I_L - \boldsymbol{W}^I_R$ with

$$\begin{aligned}\big[\boldsymbol{W}^I_\alpha\big]^k_l = \frac{\Gamma}{2\pi}\sum_m \Big[&\langle m|d^\dagger|k\rangle\langle l|d|m\rangle\big\{I^+_\alpha(\omega_{ml}) + [I^+_\alpha(\omega_{mk})]^*\big\} \\ &- \langle m|d|k\rangle\langle l|d^\dagger|m\rangle\big\{I^-_\alpha(\omega_{km}) + [I^-_\alpha(\omega_{lm})]^*\big\}\Big]\,.\end{aligned} \tag{2.45}$$

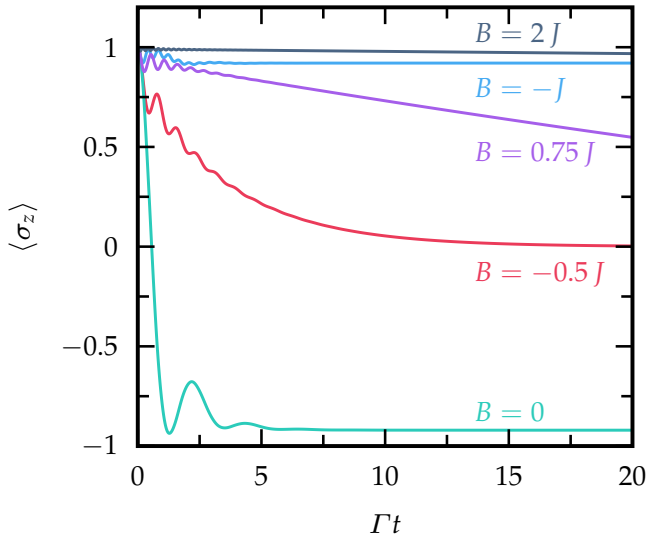

FIGURE 2.6: The time evolution of the quasi-spin occupation difference $\langle \sigma_z(t) \rangle$ is shown for different values of B as indicated in the figure. The dot is initially prepared in the pure state $\boldsymbol{P}(0) = |0\uparrow\rangle\langle 0\uparrow|$ and the other parameters are chosen as $J = 15\,\Gamma$, $\Delta = 3\,\Gamma$, $eV = 10\,\Gamma$ and $\beta = 0.7/\Gamma$. In units of the transition rate Δ, the chosen values of B fulfill $B = 2\,J = 10\,\Delta$, $B = -J = -5\,\Delta$, $B = -0.75\,J = 3.75\,\Delta$ and $B = -J/2 = 1.5\,\Delta$.

In practice, we perform the energy integration in equation (2.43) by hand and use the expression

$$I_\alpha^\pm(\omega) = -\pi f_\alpha^\pm(\omega) \pm i \log(\beta\omega_c/2\pi) \pm \frac{1}{2i}\left[\psi_0\left(\frac{1}{2} + \frac{i\beta}{2\pi}[\omega - \mu_\alpha]\right) + \psi_0\left(\frac{1}{2} - \frac{i\beta}{2\pi}[\omega - \mu_\alpha]\right)\right]. \tag{2.46}$$

Here, ω_c is a cut-off frequency which is equivalent to the band width of the leads and, therefore, considered to be very large compared to the characteristic frequencies of the system. In the appendix A, we show how this expression is obtained and why the digamma function $\psi_0(z)$ enters this formula.

2.2.1.1 Nonequilibrium Spin Relaxation and Dephasing

In the following, we investigate the relaxation and dephasing process of the quantum two-state system under the influence of a nonequilibrium current. By expanding the density operator $\boldsymbol{P}$ of the reduced system in terms of the right eigenvectors $\boldsymbol{r}^{(k)}$ of the non-Hermitian operator $\boldsymbol{W}$, we find that the solution of equation (2.39) takes the form

$$\boldsymbol{P}(t) = \sum_{k=0}^{4^2-1} c_k \boldsymbol{r}^{(k)} e^{-\Gamma_k t} e^{i\Omega_k t}. \tag{2.47}$$

Here, $\Lambda_k = i\Omega_k - \Gamma_k$ is k-th eigenvalue, satisfying $\boldsymbol{W}\boldsymbol{r}^{(k)} = \Lambda_k \boldsymbol{r}^{(k)}$. The stationary solution corresponds to the eigenvector $\boldsymbol{r}^{(0)}$ with eigenvalue $\Lambda_0 = 0$, which is the only eigenvector with a nonzero trace, i.e., $\mathrm{tr}\,\boldsymbol{r}^{(k)} = \delta_{k0}$. In addition, the asymptotic relaxation rate Γ_r of the system is given by the second largest real part of the eigenvalues, i.e., the smallest finite rate $\Gamma_k \neq 0$. The coefficients c_k are chosen such that equation (2.47) satisfies the initial condition $\boldsymbol{P}(0) = \sum_k c_k \boldsymbol{r}^{(k)}$, with $c_0 = 1$.

In figure 2.6, we show the time evolution of the mean value $\langle \sigma_z(t) \rangle$ of the quantum two-level system for different energy splittings B and universal coupling constants $\Delta = 3\,\Gamma$ and $J = 15\,\Gamma$. For the electronic reservoirs, we have chosen a universal temperature $\beta = 0.7/\Gamma$

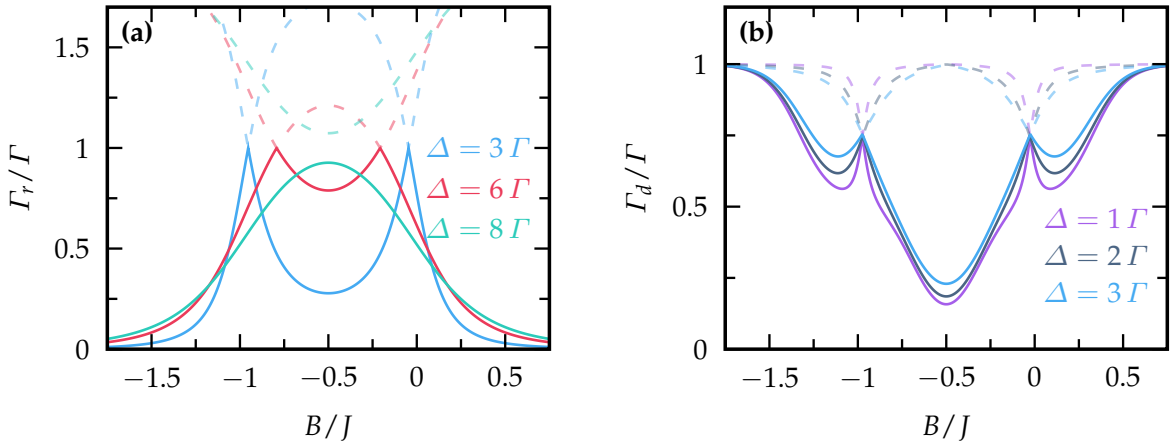

FIGURE 2.7: (a) The relaxation rate Γ_r is shown as a function of the energy splitting B for different values of Δ. The solid (dashed) curves show the smallest (second smallest) decay rate, obtained from the eigenspectrum of the Liouville super-operator $\boldsymbol{W}$. (b) The decoherence rate Γ_d is shown for various transition rates Δ as a function of B. The decoherence rate is minimal at resonance when $B = -J/2$ and grows up to a local maximum, when $B + J$ is one magnitude larger than Δ. The solid curves show the decoherence rate, whereas the dashed curves show the next largest rate. Due to a degeneracy of eigenvalues, exact crossings of the rates occur and the rates become ragged at these points. The other parameters have been chosen for both panels according to $J = 15\,\Gamma$, $eV = 10\,\Gamma$ and $\beta = 0.7/\Gamma$.

and the bias voltage $eV = 10\,\Gamma$. Under decaying oscillations in the transient dynamics, the spin relaxes in all five cases to its asymptotic steady state. However, for different values of B the relaxing behavior differs in several aspects, such as different relaxation rates, amplitudes and frequencies of the oscillations. A faster relaxation seemingly occurs, when the transition rate Δ is of the order of the energy difference B or $(B + J)$.

In order to systematically determine the relaxation rate Γ_r, we calculate the eigenspectrum of the super-operator $\boldsymbol{W}$[2] according to equation (2.47). As a function of the energy difference B, the results of this analysis are shown in figure 2.7(a) for different transition rates Δ. A comparison of the rates for different voltages eV and temperatures $T = 1/\beta$ shows that the relaxation process is essentially independent of T and eV. Consequently, the nonequilibrium relaxation rate Γ_r of the effective spin-1/2 is only a function of its internal parameters B, J, Δ and the tunneling rate Γ. On the one hand, for small $\Delta \sim \Gamma$, the relaxation rate is peaked at $B = 0$ and $B = -J$ and shows a local minimum at $B = -J/2$. But on the other hand, the local maxima disappear and a global maximum arises at $B = -J/2$ for transition rates Δ of comparable size. The particular ragged behavior at the local maxima with $B \neq -J/2$ is due to a degeneracy of two eigenvalues of the super-operator $\boldsymbol{W}$. Although each eigenvalue depends smoothly on the energy splitting B, the appearance of exact crossings at certain values of B is triggered, when the rates exchange their role as minimal ones. In addition, this smooth behavior is indicated by showing the next largest decay

[2] In addition to this analysis, a direct way to determine the relaxation rate from the dynamics shown in figure 2.6 is via a Fourier transformation of the polarization $\langle\sigma_z\rangle(\omega) = \int_0^\infty dt\, e^{i\omega t}\langle\sigma_z\rangle(t)$. The width of the peak at $\omega = 0$ determines the relaxation rate, which can be evaluated by a Lorentzian fit. Both methods result in identical rates. Note that this also applies to the determination of the decoherence rate.

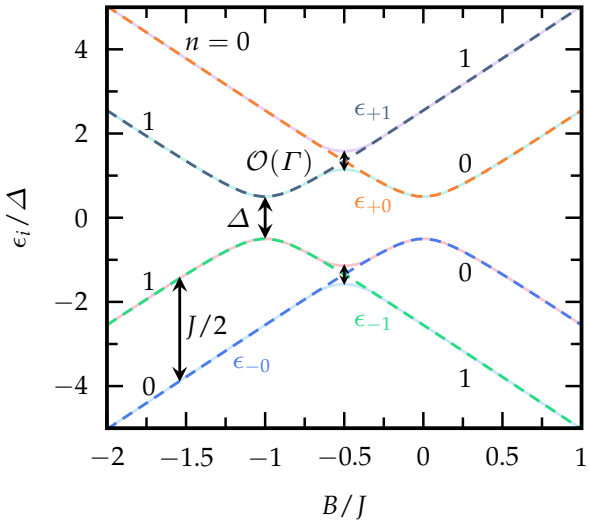

FIGURE 2.8: The energy spectrum of the isolated quantum dot $\epsilon_{\pm n} = \pm\sqrt{\Delta^2 + (B + nJ)^2}/2$ is shown. Here, $n = 0, 1$ is the electron occupation number and $J = 5\,\Delta$ was chosen.

rate via the curves in figure 2.7(a).

To explain this behavior, it is necessary to understand the spectrum of the quantum dot Hamiltonian. Thus, we show the eigenvalues ϵ_i as a function of the energy splitting B in figure 2.8 for the case $J = 5\,\Delta$ which corresponds to the case $\Delta = 3\,\Gamma$ in figure 2.7. The two pairs of energy levels correspond to the two possible electron occupation numbers n. Two avoided energy crossings occur at $B = -J/2$ with a gap that is determined by the tunneling rate Γ. These avoided crossings lead to a mixing of the two spin states with a different electron occupation. The low and high energy states, i.e., ϵ_{+n} and ϵ_{-n} are separated by $J/2$. In addition, the two families of eigenstates with different n are separated by $J/2$ far away from the avoided energy crossings. Two additional avoided crossings appear as a consequence of a finite transition rate Δ. These avoided crossings appear when either $B = 0$ or $B = -J$. In the first case, the two spin states with electron occupation $n = 0$ are mixed, while in the latter case, the states with $n = 1$ are mixed. The energy gaps of these avoided crossing are given by the transition rate Δ.

With the visualization of the energy spectrum, we can now understand the behavior of the relaxation rate depicted in figure 2.7(a). For the case $\Delta = 3\,\Gamma$, the two avoided energy crossings with the same electron number at $B = 0$ for $n = 0$ and $B = -J$ for $n = 1$ give rise to the two local serrated maxima. In the vicinity of these positions, the dot occupation number is stable and thus the fluctuations are very efficient in relaxing the spin. At the position of the other avoided crossings at $B = -J/2$, on the other hand, states with different electron occupation numbers are mixed, which renders the fluctuations around the already undetermined dot state inefficient. As a consequence, the relaxation rate becomes minimal.

By increasing the transition strength Δ, the energy gaps at $B = 0$ and $B = -J$ become larger, while they progressively approach each other. Finally, the four avoided energy crossings are very close to each other around $B = -J/2$. Then, these avoided crossings can no longer be resolved and the two local maxima in the relaxation rate merge to a single maximum at $B = -J/2$.

While the spin exhibits only pure relaxation dynamics in the long time regime, it also features decaying oscillatory dynamics in the transient regime, as shown in figure 2.6. This

spin dephasing is characterized by a frequency $\Omega_k \neq 0$ and the corresponding rate Γ_k, given by the eigenvalues of the Liouvillian $\boldsymbol{W}$. In the following, we consider the decoherence rate Γ_d given by the largest real part of the eigenvalue Λ_k with a nonzero imaginary part $\Omega_k \neq 0$.

In figure 2.7(b), we show the decoherence rate in dependence of the energy splitting B for different transition rates Δ. In the same manner as before, the underlying spectrum of the system Hamiltonian is the foundation to understand the behavior of the dephasing rate Γ_d. As a consequence of the absence of any resonance for $|2B + J| \gg \Delta$, we find a constant and comparably large decoherence Γ_d which leads to a rather fast decay of the oscillations. On the contrary, at the resonance $B = -J/2$, where two pairs of almost degenerate energy eigenstates exist, the decoherence rate is globally minimized which leads to a dynamics robust against dephasing. Away from the energy crossings, the decoherence rate is almost independent of Δ, as the off-diagonal elements of H_S are negligible to B for B, $B + J \gg \Delta$. Then, corrections in Γ_d are only of second-order in the transition rate Δ and the dephasing process is solely determined by the parametric coupling of the spin operator σ_z to the number of electrons n on the dot. Thus, the total Hamiltonian appears diagonal and the nonequilibrium fluctuations only induce dephasing with a rate dominated by the tunneling rate Γ.

At this point, let us emphasize again that the relaxation and dephasing describe true nonequilibrium processes which occur under the action of a strong nonequilibrium environment.

2.2.1.2 Electron Current and Differential Conductance

For the sake of completeness, we study the stationary current I between the leads which is given by equation (2.40). Thus, we show in figure 2.9 the current-voltage characteristics. Here, (a) shows the current coded in colors versus the voltage eV and energy splitting B, whereas (b) considers a constant $B = -5\,\Gamma$ and shows the current I only as a function of eV. The behavior of the current can be clearly divided into three different regions.

In the first region I of small voltages, no current flows. This region extends until the voltage becomes large enough such that the first transport channel opens. This occurs at $eV = 2|\epsilon_{\pm 0} - \epsilon_{\pm 1}|$, when the voltage is large enough to induce the first transition between the unoccupied and occupied eigenstates. Hence, at the point $B = -J/2$, where a crossing of two eigenenergies of the uncoupled dot Hamiltonian happens, an infinitesimally small bias voltage is enough to open the first transport channel and induce a finite electron transport.

In region II, the current reaches another plateau whose height depends on the parameters B, J, Δ. On the basis of an analysis of the matrix $\boldsymbol{W}^I$, the current can be determined. Under the assumption that each allowed transition has an identical probability, we calculate the trace of $\boldsymbol{W}^I$ for sharp steps of the Fermi function and weight everything with a factor $1/4$. By this, we arrive at the expression

$$I^{\mathrm{II}} = \frac{e\Gamma}{4}\left[1 + \frac{\Delta^2 + B(B+J)}{\sqrt{(\Delta^2 + B^2)(\Delta^2 + [B+J]^2)}}\right]. \tag{2.48}$$

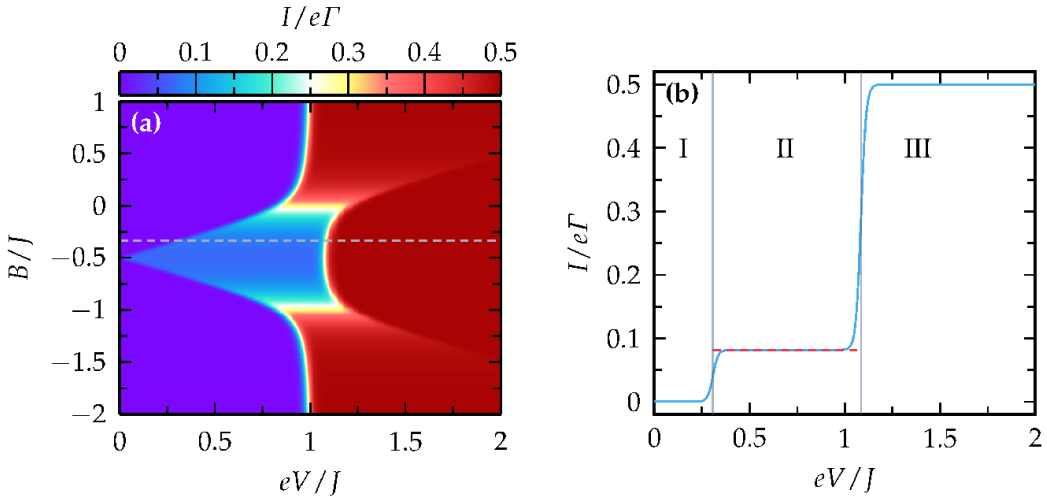

FIGURE 2.9: (a) The stationary current I is shown color coded versus the bias voltage eV and the level energy splitting B. The reservoir temperature and dot parameters have been chosen as $\beta = 10/\Gamma$, $J = 15\,\Gamma$ and $\Delta = 3\,\Gamma$. (b) A horizontal cut of the stationary current I, indicated by the dashed line in (a), is shown for the energy splitting $B = -5\,\Gamma$. Both plots can be divided into three regions. In these regions, there are either no (I), one (II) or two (III) energy level transitions of the dot in the energy window spanned by the voltage eV. In the region I the current is constantly zero, while it is maximized to $I = 0.5\,e\Gamma$ in region III. In the intermediate region II, the current follows equation (2.48) which is indicated by the dashed line in (b).

Equation (2.48) is shown by the dashed red line in figure 2.9(b), for which a good agreement with the numerically calculated current in this region is found.

In the last region III, an additional transport channel becomes available when the bias voltage is large enough to change the spin quantum number from $-$ to $+$. Consequently, the current is maximized to $I^{\mathrm{III}} = e\Gamma/2$ in the sequential tunneling regime for voltages larger than $eV = 2(\epsilon_{+0} - \epsilon_{-1})$. For finite temperatures, the behavior is smoothened out, whereas perfect steps would occur for zero temperature.

The classification into different regions is best visualized by the differential conductance $(\partial I/\partial V)$ shown in figure 2.10(a) color coded versus eV and B and a cut along constant $B = -5\,\Gamma$ in (b). In the vicinity of the resonance $B = -J/2$, two different curves, on which the differential conductance is significantly different from zero, appear. These curves divide the diagram into the three regions I, II, III and correspond to the points at which either $eV = 2(\epsilon_{-0} - \epsilon_{-1})$ or $eV = 2(\epsilon_{+0} - \epsilon_{-1})$. When increasing or decreasing the energy bias B away from the resonance, the separatrix I-II becomes more pronounced, while the separatrix II-III fades out. This becomes clear when looking at the current in region II. Under the assumption $B(B + J) > 0$, the current I^{II} to lowest order in Δ takes the form

$$I^{\mathrm{II}} \simeq \frac{e\Gamma}{2}\left[1 - \frac{1}{4}\left(\frac{\Delta}{B}\right)^2\right]. \tag{2.49}$$

Thus, away from the resonance, the current jumps almost directly to its maximal value at the border between regions I and II. Consequently, the differential conductance at the separatrix II-III is only of the order $(\Delta/B)^2$. On the other hand, in the regime $-J \lesssim B \lesssim 0$, the current

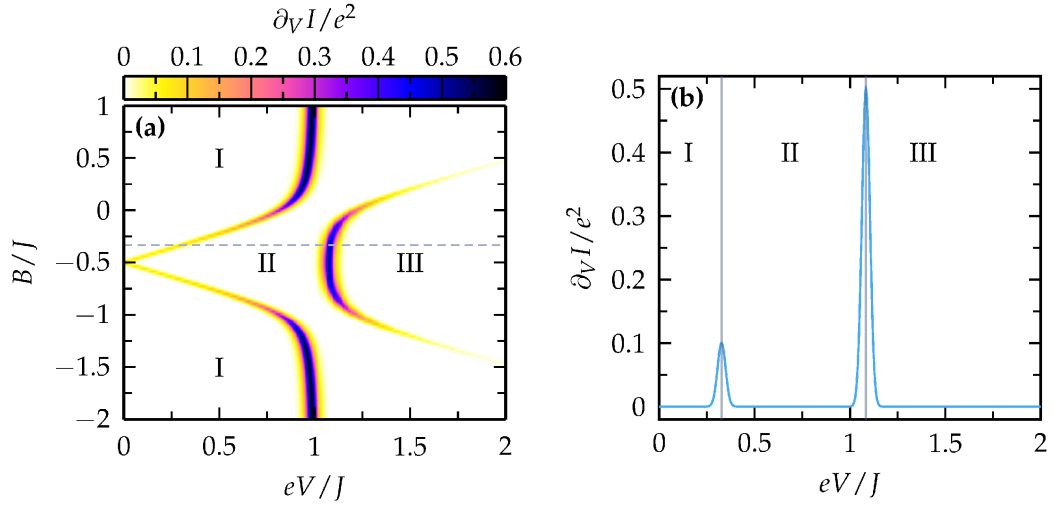

FIGURE 2.10: (a) The differential conductance $(\partial I/\partial V)$ is shown as a function of the bias voltage eV and the internal energy difference B. The dashed horizontal line indicates the value $B = -5\,\Gamma$. (b) For this very energy splitting B, the differential conductance is shown as a function of eV. The other parameters have been chosen as in figure 2.9.

jump at the first separatrix is only to a small level (compare also figure 2.9). Consequently, $(\partial I/\partial V)$ is more pronounced at the second separatrix.

2.2.2 Correlation Function of the Nonequilibrium Fluctuations

It is of foremost interest to know the features of the fluctuations which lead to a relaxation process to some stationary or thermal equilibrium state of the system that is subject to these fluctuations. For instance, their spectral distribution determines the relaxation and dephasing rates. At thermal equilibrium and for a Gaussian environment, the fluctuations are composed of a sum over harmonic thermal fluctuations with spectral weight that is determined by the spectral density of the bath [161]. When the system is subject to nonequilibrium fluctuations, such simple features are not known up to present. Here, we can readily evaluate the correlation properties of the nonequilibrium noise which acts on the two-state system.

In the presence of the coupling to the electronic occupation number, the Heisenberg equation of motion for the effective spin-1/2 system is given by

$$\partial_t \sigma_x = -B\sigma_y - Jd^\dagger d\sigma_y\,, \tag{2.50a}$$

$$\partial_t \sigma_y = B\sigma_x - \Delta\sigma_z + Jd^\dagger d\sigma_x\,, \tag{2.50b}$$

$$\partial_t \sigma_z = \Delta\sigma_y\,. \tag{2.50c}$$

Then, the tunneling coupling to the reservoirs induces fluctuations of the dot occupation whose correlation properties will be determined in the following. In order to estimate the dynamics of the fluctuations, we derive the equations of motion for the fermionic ladder

operators on the dot and in the leads as

$$i\partial_t d = \frac{J}{2}\sigma_z d + \sum_{k\alpha} t_{k\alpha} c_{k\alpha}\,, \tag{2.51a}$$

$$i\partial_t c_{k\alpha} = \epsilon_{k\alpha} c_{k\alpha} - t_{k\alpha} d\,, \tag{2.51b}$$

respectively. We note that these equations follow after neglecting terms that are at least cubic in the destruction and creation operators. This approximation is consistent with the Markov approximation that we applied in the preceding section. In addition, the latter equation also only includes sequential tunneling events between the leads and quantum dot. Next, we solve the inhomogeneous linear differential equation of the bath operators (2.51b) to find

$$c_{k\alpha}(t) = e^{-i\epsilon_{k\alpha}(t-t_0)}\left[c_{k\alpha} - it_{k\alpha}\int_{t_0}^{t} ds\, d(s) e^{i\epsilon_{k\alpha}(s-t_0)}\right]\,, \tag{2.52}$$

with $c_{k\alpha} = c_{k\alpha}(t_0)$ and insert the solution in equation (2.51a). Under the assumption that the time scale, on which the continuous density of states of the reservoir thermalizes, is much smaller than the time scale on which the system dynamics occur, we can set $d(s) \equiv d(t)$. In other words, we apply the Born–Markov approximation. Then, the appearing integrals can be solved analytically. In summary, we then arrive at the equation of motion for the annihilation operator of a particle on the dot in the form

$$\dot{d} = -\frac{iJ}{2}\sigma_z d - \Gamma d + \xi(t)\,, \tag{2.53}$$

with the inhomogeneity

$$\xi(t) = -i\sum_{k\alpha} t_{k\alpha} e^{-i\epsilon_{k\alpha}(t-t_0)} c_{k\alpha}\,, \tag{2.54}$$

acting as a fluctuating force with vanishing mean value but a non-vanishing autocorrelation function. In fact, this fluctuating force leads to a damping with rate Γ of the dot occupation, which in turn is related to the autocorrelation function $\langle \xi^\dagger(t)\xi(0)\rangle$. Moreover, we have used once more the wide-band limit and set $\Gamma = (\Gamma_L + \Gamma_R)/2$.

With equation (2.53), the dynamics of the dot occupation number $n(t)$ can now be determined under the influence of the nonequilibrium fluctuating force $\xi(t)$. Due to the finite damping with rate Γ, the dynamics of the dot occupation number become independent of the spin dynamics in the limit of $t_0 \to -\infty$. It follows that the occupation number then is time-independent and is simply given by

$$n(t) \equiv n = \int_0^\infty ds ds'\, \xi^\dagger(s)\xi(s') e^{-\Gamma(s+s')}\,, \tag{2.55}$$

with $n(t) = d^\dagger(t)d(t)$.

2.2.2.1 Characteristics of the Nonequilibrium Noise

The characteristics of the nonequilibrium quantum statistical fluctuations is fully determined by equation (2.55). In the limit of symmetric tunneling, the mean value of the dot occupation readily follows as

$$\langle n(t)\rangle = \frac{1}{2}\,. \tag{2.56}$$

The autocorrelation function of the dot occupation number is now determined to be

$$L(t,s) = \langle n(t)n(s)\rangle - \langle n(t)\rangle\langle n(s)\rangle = \left[\gamma^{+}(t-s)\right]^2, \tag{2.57}$$

where we have defined the functions

$$\gamma_\alpha^{\pm}(t) = \frac{\Gamma_\alpha}{2\pi}\int dE\,\frac{f_\alpha^{\pm}(E)}{E^2+\Gamma^2}e^{iEt}\,, \tag{2.58}$$

with $\gamma^{\pm}(t) = \sum_\alpha \gamma_\alpha^{\pm}(t)$. Moreover, $f_\alpha^{\pm}(E) = [1+e^{\pm\beta(E-\mu_\alpha)}]^{-1}$ is the Fermi–Dirac distribution of lead α. We observe that the autocorrelation function is time-translational invariant such that we can further simplify our notation according to $L(t,s) = L(t-s,0) = L(t-s)$. The spectral density of the nonequilibrium quantum noise is now obtained via the Fourier transform $L(\omega) = \int dt\, L(t)e^{i\omega t}$, which is, in general, given by the convolution integral

$$L(\omega) = \sum_{\alpha\beta}\frac{\Gamma_\alpha\Gamma_\beta}{2\pi}\int dE\,\frac{f_\alpha^{+}(E)f_\beta^{+}(\omega-E)}{(E^2+\Gamma^2)([\omega-E]^2+\Gamma^2)}\,. \tag{2.59}$$

In the limit of either zero[3] or infinite temperature, simple expressions for $L(\omega)$ can be derived. In the case of infinite temperature, the autocorrelation function results in a Lorentzian

$$\lim_{\beta\to 0} L(\omega) = \frac{1}{2}\frac{2\Gamma}{\omega^2+4\Gamma^2}\,. \tag{2.60}$$

Hence, the autocorrelation function becomes independent of the applied bias voltage, since all possible transitions become thermally accessible with unified probability. For compactness, we present the result of the zero temperature limit only for $\Gamma = \Gamma_L = \Gamma_R$, which can be written as

$$\lim_{\beta\to\infty} L(\omega) = \frac{1}{2}\frac{2\Gamma}{\omega^2+4\Gamma^2}\left[\mathcal{C}(\omega,eV/2)+\mathcal{C}(\omega,-eV/2)\right], \tag{2.61}$$

by defining the function

$$\mathcal{C}(\omega,\mu) = \frac{1}{\pi}\left[\theta(\omega)+\theta(\omega-2\mu)\right]\left[\tan^{-1}\left(\frac{\omega-\mu}{\Gamma}\right)-\tan^{-1}\left(\frac{\mu}{\Gamma}\right)+\frac{\Gamma}{\omega}\log\left(\frac{\Gamma^2+(\omega+\mu)^2}{\Gamma^2+\mu^2}\right)\right]. \tag{2.62}$$

By studying the zero temperature limit, we observe that for large voltages $eV \gg \Gamma$, the zero and infinite temperature results are identical, i.e., $\lim_{\beta\to 0} L(\omega) = \lim_{eV\to\infty}\lim_{\beta\to\infty} L(\omega)$. For different values of the bias voltage, we show the zero temperature autocorrelation function

[3] Strictly speaking, in the limit of zero temperature also quantum effects such as coherent tunneling can play an essential role such that this result has to be taken with care.

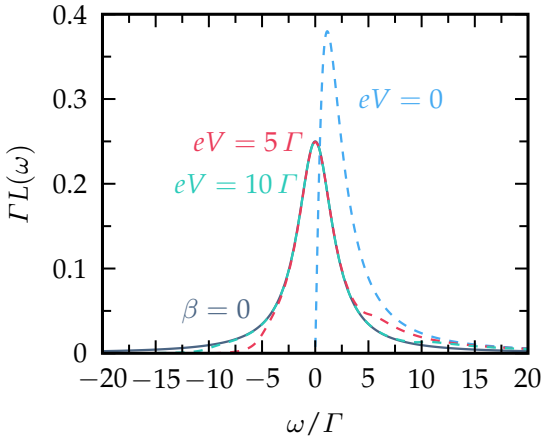

FIGURE 2.11: The autocorrelation function $L(\omega)$ is shown in the infinite temperature limit (solid) and zero temperature limit (dashed) for three different voltages.

(dashed) in addition to the case of infinite temperature (solid) in figure 2.11. In all cases, the spectral resolution of the nonequilbrium noise correlation function is dominated by a Lorentzian peak that is centered at zero frequency. The zero temperature limit features the appearance of a shoulder close to $\omega = eV$, wheres the spectral noise function $L(\omega)$ is reduced at the opposite position $\omega = -eV$.

Besides these two limits, the exact expression of the correlation function $L(\omega)$ at arbitrary temperature involves in general sums over fermionic Matsubara frequencies $\nu_n = (2n + 1)\pi/\beta$, which cannot be evaluated in a closed analytic expression. Yet, these sums generate peaks in the spectral weight at $\omega = \pm eV/2$ and $\omega = \pm eV$ with temperature dependent widths.

2.2.2.2 Nonequilibrium Fluctuation Relation

According to the fluctuation-dissipation theorem valid at quantum statistical equilibrium, an equilibrium correlation function $L_0(t)$ satisfies the relation $L_0(t - i\beta) = L_0^*(t)$. In order to check this relation for the nonequilibrium occupation correlation $L(t)$, we first look at the functions $\gamma_\alpha^\pm(t)$ for which we find

$$\gamma_\alpha^+(t - i\beta) = e^{\beta\mu_\alpha}\gamma_\alpha^-(t) \tag{2.63}$$

and

$$\gamma_L^+(t) = \left[\gamma_R^-(t)\right]^* . \tag{2.64}$$

By using these two identities, we estimate the final expression

$$L(t - i\beta) = L^*(t) - \sum_\alpha \left(1 - e^{-2\beta\mu_\alpha}\right) \left[\gamma_\alpha^+(t)\right]^* \left[\gamma_\alpha^+(t)\right]^* \tag{2.65}$$

which extends the equilibrium FDT to the nonequilibrium case. By taking the limit of vanishing voltage $\mu_\alpha = 0$, we note that the equilibrium FDT is recovered.

2.2.2.3 Time Dependent AC-Voltage

The results in the preceding part can be readily generalized to the case of AC-driven leads for which similar results are obtained. The AC-drive is explicitly included in the eigenenergies of the reservoir modes with $\epsilon_{k\alpha}(t) = \epsilon_{k\alpha} + eV_\alpha \cos(\Omega t)$. By using the unitary transformation $U(t) = e^{-i\sum_{k\alpha}\phi_\alpha(t)n_{k\alpha}}$ with $\phi_\alpha(t) = eV_\alpha \int_{t_0}^{t} ds\, \cos(\Omega s)$, the time dependence of the single particle energies $\epsilon_{k\alpha}(t)$ is transfered to the tunnel amplitudes $t_{k\alpha}(t) = t_{k\alpha}e^{i\phi_\alpha(t)}$. Thus, by making use of the Jacobi–Anger identity

$$e^{iz\sin\theta} = \sum_{n=-\infty}^{\infty} \mathcal{J}_n(z)e^{in\theta}\,, \tag{2.66}$$

the appearing exponential can be expanded in terms of Bessel functions $\mathcal{J}_n(z)$. Thus, we can follow the same calculus as before and obtain for the AC-driven correlation function

$$\bar{L}(t,s) = \sum_{klmn} \gamma^{+}_{kl}(t-s)\gamma^{+}_{mn}(t-s)e^{i(k+m)\Omega t}e^{-i(l+s)\Omega s}\,, \tag{2.67}$$

which however is no longer time-translational invariant. In analogy to the DC-driven case, we have defined

$$\gamma^{\pm}_{kl\alpha}(t) = \frac{\Gamma_\alpha}{2\pi}\mathcal{J}_k\left(\frac{eV_\alpha}{\Omega}\right)\mathcal{J}_l\left(\frac{eV_\alpha}{\Omega}\right)\int dE\, \frac{f^{\pm}_\alpha(E)e^{iEt}}{\Gamma^2 + (E+k\Omega)(E+l\Omega) + i(k+l)\Omega\Gamma}\,, \tag{2.68}$$

and again $\gamma^{\pm}_{kl}(t) = \sum_\alpha \gamma^{\pm}_{kl\alpha}(t)$. By evaluating the average over a single period $T = 2\pi\Omega^{-1}$, the time-translational invariance is regained, such that we investigate in the following the autocorrelation function

$$L(t-s) = \frac{1}{T}\int_0^T d\tau\, \bar{L}(t+\tau, s+\tau) = \sum_{klm} \gamma^{+}_{(k-m)l}(t-s)\gamma^{+}_{m(k-l)}(t-s)e^{ik\Omega(t-s)}\,. \tag{2.69}$$

In order to check the FDT, we use the relations

$$\gamma^{+}_{kl\alpha}(t-i\beta) = e^{\beta(\mu_\alpha - k\Omega)}\gamma^{-}_{kl\alpha}(t) \tag{2.70}$$

and

$$\sum_{kl}\gamma^{+}_{klR}(t) = \sum_{kl}\left[\gamma^{-}_{klL}(t)\right]^*\,. \tag{2.71}$$

Equipped with these identities, we find the relation

$$L(t-i\beta) = L^*(t) - \sum_\alpha\sum_{klm}\left(1-e^{-2\beta\mu_\alpha}\right)\left[\gamma^{+}_{(k-m)l\alpha}(t)\right]^*\left[\gamma^{+}_{m(k-l)\alpha}(t)\right]^* e^{-ik\Omega t}\,, \tag{2.72}$$

which generalizes the fluctuation-dissipation theorem to the periodically AC-driven case. Moreover, we note that in the non-driven regime with either $V_\alpha = 0$ or $\Omega = 0$, the DC result

is recovered by making use of the relations $\mathcal{J}_k(0) = \delta_{k0}$,

$$\sum_{k=-\infty}^{\infty} [\mathcal{J}_k(x)]^2 = 1\,, \qquad \text{and} \qquad \mathcal{J}_n(x+y) = \sum_{k=-\infty}^{\infty} \mathcal{J}_k(x)\mathcal{J}_{n-k}(y)\,. \tag{2.73}$$

Most interestingly, even in the AC-driven regime, the relation (2.72) can coincide with the equilibrium FDT by choosing the constant bias voltage $\mu_\alpha = 0$, even though $eV_\alpha, \Omega \neq 0$. This is plausible as we have averaged the autocorrelation function over a single period T such that the nonequilibrium condition is all together averaged to zero.

The system here studied illustrates the impact of nonequilibrium quantum statistical fluctuations on the dynamics of a two-level system. The relaxation and dephasing process yields nontrivial rates that are directly obtained from the spectrum of Liouville superoperator. In addition, fluctuation relations can be obtained which recover the normal the usual FDT under the equilibrium condition $eV \to 0$ and $eV_\alpha \to 0$.

In the next chapter, we will study an isolated quantum many-body system that is periodically driven. In this example, local particle interactions can provide the means to *thermalize* the system as summarized by the eigenstate thermalization hypothesis. Thus, similar effects as in open system dynamics can be observed.

CHAPTER 3

Parametric Resonance in a Driven Bose–Hubbard Model

The impact of the atomic interaction on the dynamical stability of the driven quantum many-body state in a parametrically driven harmonic potential is revealed in the regime of weak interaction. Analyzing a discretized Gross-Pitaevskii equation within a Gaussian variational ansatz yields a Mathieu equation for the condensate width. The parametric resonance condition is shown to be modified by the atom interaction strength. In this chapter, the main results presented in the following reference are summarized:

N. Mann, M. Reza Bakhtiari, F. Massel, A. Pelster, and M. Thorwart, "Driven Bose–Hubbard model with a parametrically modulated harmonic trap", Physical Review A **95**, 043604 (2017).

The eigenstate thermalization hypothesis characterizes whether observables of a closed quantum system can be accurately described by equilibrium thermodynamics in the form of a microcanonical ensemble. A prerequisite for such a system is the presence of nonintegrability. In this chapter, we consider a one-dimensional Bose–Hubbard model, where the nonintegrability is provided by local particle interactions. Against this background, we investigate the impact of finite interactions on the resonance condition of the system when it is affected by a parametric drive.

A weakly interacting Bose–Einstein condensate in a parametrically modulated harmonic trap has been studied in reference [87]. Within an analytic approach, the dynamical instability has been determined, which is accompanied by an exponentially fast depletion of the condensate. Later, it has been shown that the motion of the condensate is described by a nonlinear Mathieu equation [88]. Here, we include a global harmonic trapping potential in a one-dimensional Bose–Hubbard model.

The time-averaged potential curvature V_0 is parametrically modulated with the strength δV and the frequency Ω according to $V(t) = V_0 + \delta V \sin(\Omega t)$. The system Hamiltonian is given by

$$H(t) = -J \sum_{j=1}^{L-1} \left(b_{j+1}^\dagger b_j + \text{H.c.} \right) + \frac{U}{2} \sum_{j=1}^{L} n_j (n_j - 1) + V(t) \sum_{j=1}^{L} (j - j_0)^2 n_j \,, \tag{3.1}$$

where $j_0 = (L-1)/2$ is the lattice center, b_j ($b_j^\dagger$) are the bosonic annihilation (creation) operators at site j and $n_j = b_j^\dagger b_j$ denotes the local occupation number operator. Moreover, J is the nearest-neighbor hopping rate and U the on-site interaction strength. Here, we consider a lattice with L sites that is loaded with a fixed number of N bosonic atoms.

In an earlier work [112], we estimated the transient quantum many-body dynamics of the strongly interacting gas on a lattice in the presence of the parametrically modulated harmonic potential. By using the time-evolving block-decimation (TEBD) method[1], a resonant behavior was found.

For a more rigorous analysis of the resonant behavior and the instability condition, we establish an analytic mean-field approach and determine the resonance condition. In addition to this, the results of both approaches are compared with each other.

3.1 Quantum Many-Body Parametric Resonance in the Mean-Field Regime

In the limit of non-interacting particles, the system can be exactly mapped onto a discretized version of the quantum harmonic oscillator with the eigenfrequency $\omega_0 = 2\sqrt{JV_0}$. Applying the parametric drive, regions of dynamical instability [80, 81] are produced in the parameter space, which are characterized by diverging position and momentum variances. Here, the parametric resonance for the displacement mode is at

$$n\Omega = 2\omega_0\,, \tag{3.2}$$

with $n \in \mathbb{N} \setminus \{0\}$, or the condensate breathing mode according to $n\Omega = 4\omega_0$, equivalently. By considering the mean-field regime, we elucidate the impact of quantum many-body interactions on the resonance condition. At the same time, the formalism of the time-dependent variational theory will be formulated of which we will make use in subsequent chapters.

In the mean-field regime, the dynamics of a dilute, weakly interacting atomic condensate at zero temperature is described by the Lagrangian

$$\mathcal{L} = \frac{1}{N}\sum_j \left[\frac{i}{2}(\psi_j^*\partial_t\psi_j - \psi_j\partial_t\psi_j^*) + J(\psi_j^*\psi_{j+1} + \text{c.c.}) - V(t)(j-j_0)^2\psi_j^*\psi_j - \frac{U}{2}\psi_j^*\psi_j^*\psi_j\psi_j\right], \tag{3.3}$$

which is readily obtained from the Hamiltonian (3.1) by making the mean-field ansatz $|\psi\rangle = \sum_j \psi_j b_j^\dagger|0\rangle$. Here, $|0\rangle$ is the vacuum state with no particles occupying the lattice and by extremizing the Lagrangian with respect to the expansion coefficients ψ_j, a discretized form of the Gross–Pitaevskii equation can be derived. In order to find an approximative, analytic description for the time evolution of the bosonic condensate, we make a Gaussian ansatz for

[1] The TEBD method is a variant of the time-dependent density matrix renormalization group [181–183], which makes use of a clever expansion of the wave function. By expanding the wave function in terms of matrix product states, a numerical time evolution of any state can be formulated straightforwardly. Benefiting from a low entanglement in many one-dimensional lattice systems, the dimension of the generators of the matrix product state can be chosen quite small, resulting in one of the nowadays most efficient computational algorithms.

the wave function [95, 184]

$$\psi_j(t) = \left(\frac{N^2}{\pi\sigma(t)^2}\right)^{1/4} \exp\left(-\frac{[j-j_0]^2}{2\sigma(t)^2} + i\eta(t)[j-j_0]^2\right), \tag{3.4}$$

with real and time-dependent variational parameters including the width $\sigma(t)$ and the corresponding phase $\eta(t)$. The condensate width is measured in number lattice sites.

In order to drastically simplify our description, we consider a parameter regime where the atom gas is extended over many sites with $\sigma(t) \gg 1$ for all times. In a static picture, this is satisfied by making the assumption that the atomic hopping rate is much larger than the static potential curvature, i.e., $J \gg V_0$. Then, the summation over the lattice sites j can be converted into a continuous integration for which we extend the limits to $\pm\infty$[2]. Within this limit, the Lagrangian takes the form

$$\mathcal{L} = 2J\exp\left(-\frac{1}{4\sigma^2} - \eta^2\sigma^2\right) - \left[\dot{\eta} + V(t)\right]\frac{\sigma^2}{2} - \frac{NU}{\sqrt{8\pi}\sigma}. \tag{3.5}$$

The equations of motion for the condensate width and phase are provided by the Euler-Lagrange equations $\partial_y\mathcal{L} = \frac{d}{dt}\partial_{\dot{y}}\mathcal{L}$ with $y \in \{\sigma, \eta\}$. The dynamics is readily obtained via $\dot{\sigma} = 4J_\gamma\sigma\eta$ and

$$\ddot{\sigma} + \dot{\gamma}\dot{\sigma} + 4J_\gamma V(t)\sigma = 4J_\gamma\left[\frac{J_\gamma}{\sigma^3} + \frac{NU}{\sqrt{8\pi}\sigma^2}\right], \tag{3.6}$$

where $\gamma = (1/4\sigma^2) + \eta^2\sigma^2$ and $J_\gamma = Je^{-\gamma}$.

In the following, we aim at a linear stability analysis by expanding the condensate width $\sigma(t) = \sigma_0 + \delta\sigma(t)$ in terms of small deviations $\delta\sigma(t)$ around its equilibrium width σ_0. Hence, we assume $|\delta\sigma| \ll \sigma_0$ and linearize the equations of motion with respect to $\delta\sigma(t)$ and $\delta\eta(t)$. Here, we take into account that the stationary part of the phase $\eta(t) = \eta_0 + \delta\eta(t)$ satisfies $\eta_0 = 0$, which follows from $\dot{\sigma}_0 = 4J_\gamma\sigma_0\eta_0 = 0$. Then, the stationary solution of the condensate width is implicitly defined by the equation

$$V_0\sigma_0^4 = Je^{-1/4\sigma_0^2} + \frac{NU}{\sqrt{8\pi}}\sigma_0. \tag{3.7}$$

On the other hand, the dynamics of the deviation $\delta\sigma$ is determined by the generalized Mathieu equation

$$\delta\ddot{\sigma} + 4J'\left[V' + \delta V'\sin\Omega t\right]\delta\sigma = -4J'\delta V\sigma_0\sin\Omega t \tag{3.8}$$

which involves an additional linear driving term on the right-hand side. Moreover, the hopping $J' = Je^{-1/4\sigma_0^2}$ and the driving strength $\delta V' = \delta V(1 + 1/2\sigma_0^2)$ are renormalized by the stationary condensate width, whereas the hopping rate and the atom-atom interaction

[2] In order to send the limits to $\pm\infty$, the number of lattice sites L has to be much larger than the spatial expansion of the Bose gas. Then, a smooth transition to zero for the condensate wave function is guaranteed, rather than a sudden cut-off at a certain lattice site to zero. Hence, we have to assume that $\sigma \ll L$.

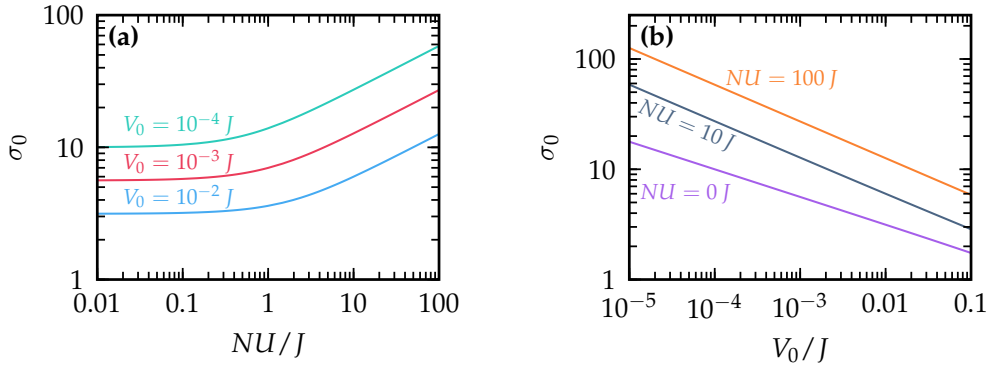

FIGURE 3.1: (a) The stationary width σ_0 of the density profile is shown as a function of the interaction strength NU for different mean potential curvatures. As indicated in the plot, different colors correspond to a different V_0. (b) The stationary condensate width σ_0 is displayed in dependence of the mean potential curvature V_0 for different atom-atom interactions NU, showing an algebraic behavior.

renormalize the potential curvature according to

$$V' = V_0\left(1+\frac{1}{2\sigma_0^2}\right)+\frac{3J'}{\sigma_0^4}\left(1-\frac{1}{3\sigma_0^2}\right)+\frac{NU}{\sqrt{2\pi}\sigma_0^3}\left(1-\frac{1}{4\sigma_0^2}\right). \tag{3.9}$$

Equation (3.8) describes breathing of the atomic condensate with the breathing mode frequency $\omega = 2\sqrt{J'V'}$. The resonance frequency ranges from $\omega \simeq 4\sqrt{JV_0} \equiv 2\omega_0$ in the non-interacting limit ($U = 0$) to $\omega \simeq 2\sqrt{3JV_0}$ in the Thomas–Fermi limit ($NU \gg J$), when the kinetic term can be neglected. Moreover, we note that the inhomogeneity of equation (3.8) does not influence the parametric resonance condition [95]. Hence, the system exhibits a parametric resonant behavior for $\delta V' \ll V'$ when the resonance condition $n\Omega = 2\omega$ is fulfilled.

3.1.1 Static Trap Potential

In order to validate the behavior of the resonance frequency and determine the behavior in the intermediate regime $NU \sim J$, we first calculate the stationary condensate width σ_0. That said, we assume a time-independent potential curvature, i.e., $\delta V = 0$. Shown in figure 3.1(a) as a function of the interaction strength NU for different potential curvatures V_0, we find that the width $\sigma_0 \simeq (J/V_0)^{1/4}$ is mainly determined by the static curvature V_0 and only gradually increases with NU in the regime below $NU \lesssim J$. On the other hand, when the interaction becomes comparable to the atomic tunneling, i.e., $NU \sim J$, the growth in σ_0 becomes steeper, which turns into an algebraic behavior $\sigma_0 \sim (NU)^{1/3}$ in the Thomas–Fermi limit. These proportionalities are directly obtained from equation (3.7) by neglecting either the interaction term (and setting $e^{-1/4\sigma_0^2} \simeq 1$) or the kinetic term, respectively.

In addition, the equilibrium condensate width is estimated as a function of V_0 and shown in figure 3.1(b) for different atom-atom interactions. Each case shows an algebraic decrease of $\sigma_0 \sim V_0^{-1/m}$ with V_0, where $3 \leq m \leq 4$. Again, $m = 4$ is obtained in the non-interacting limit, whereas the strongly interacting limit is dominated by $m = 3$.

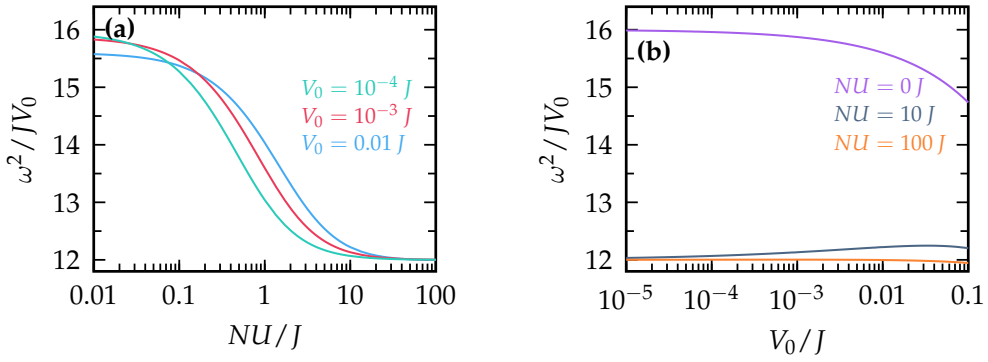

FIGURE 3.2: The square of the breathing mode frequency ω of the Bose gas is shown as (a) a function of the interaction strength NU for different mean potential curvatures and (b) in dependence of the mean potential curvature V_0 for different atom-atom interactions. The differently chosen parameters are indicated in both panels.

In accordance with the earlier discussion, the breathing mode frequency ω is displayed in figure 3.2(a) in dependence of the interaction strength NU. For comparative reasons, we show the square of ω scaled to $JV_0 = (\omega_0/4)^2$. In the strong interaction regime $NU \gg J$, the resonance frequency approaches $\omega \simeq 2\sqrt{3JV_0}$, where $J \simeq J'$ is satisfied, and becomes independent of the interaction NU. In contrast to that, $J \simeq J'$ is not satisfied *per se* in the opposite limit, when atomic interactions are negligible and the condensate is only extended over several sites. As an artifact of our ansatz, this can lead to a decreasing ratio ω/ω_0, since the resonance frequency is given by the expression $\omega \simeq 4\sqrt{JV_0}\sqrt{1+1/2\sigma_0^2}e^{-1/8\sigma_0^2}$ within this limit. In figure 3.2(b), we depict the resonance frequency as a function of the static potential steepness V_0 for different atom-atom interactions. An opposite behavior is found for small and large enough interaction strengths. While ω^2/JV_0 monotonically decreases with V_0 for non-interacting atoms $NU = 0$, it first increases weakly with V_0 for large enough NU and then decreases again, when the static potential curvature is the leading term in the primed potential curvature of equation (3.9).

3.1.2 Parametrically Driven Trap

In order to get information about the condensate stability inside the parametrically modulated trap, we rewrite the equation of motion (3.8) in terms of a set of coupled first-order linear differential equations. By defining the vector $\boldsymbol{x} = (\delta\sigma, \delta\dot{\sigma}, \tau, \dot{\tau})^T$, with $\tau = \sin\Omega t$, equation (3.8) can be written as $\dot{\boldsymbol{x}} = \boldsymbol{A}(t)\boldsymbol{x}$, with the matrix

$$\boldsymbol{A}(t) = \begin{pmatrix} 0 & 1 & 0 & 0 \\ -4J'(V' + \delta V' \sin\Omega t) & 0 & -4J'\delta V\sigma_0 & 0 \\ 0 & 0 & 0 & 1 \\ 0 & 0 & -\Omega^2 & 0 \end{pmatrix}. \tag{3.10}$$

The linear operator $\boldsymbol{A}(t)$ is periodic in time, i.e., $\boldsymbol{A}(t+T) = \boldsymbol{A}(t)$, with periodicity $T = 2\pi/\Omega$. By employing the Floquet theorem [185], it is possible to determine whether

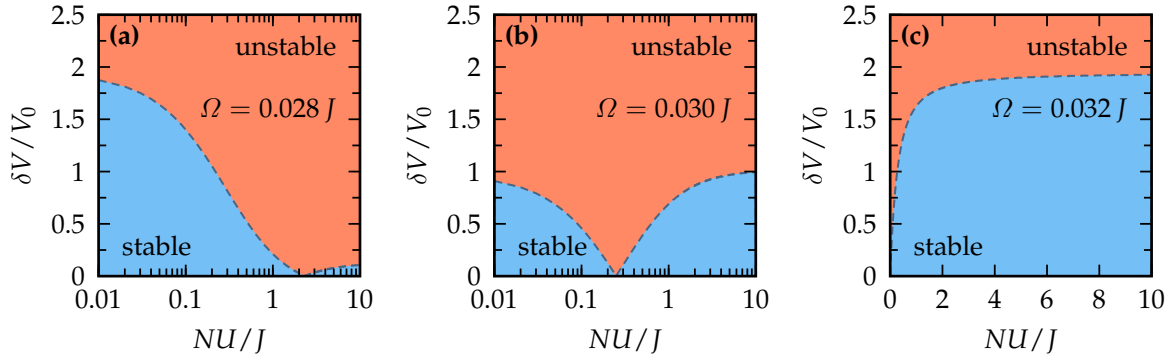

FIGURE 3.3: The stability diagram of the parametrically driven BEC for the first parametric resonance $n = 1$ is shown for (a) $\Omega = 0.028\,J$, (b) $\Omega = 0.030\,J$ and (c) $\Omega = 0.032\,J$. The horizontal and vertical axes indicate the interaction strength NU and the driving strength δV for $V_0 = 1.6 \times 10^{-5}\,J$, respectively. The system becomes unstable in the red colored regions, while in the blue colored regions all solutions are stable.

the solution for a given set of parameters is stable or not. The concept of Floquet analysis involves the evaluation of the fundamental solution $\boldsymbol{\Phi}(t)$ over a single period. Whether the system is behaving in a stable manner or becomes unstable can be characterized by the eigenvalues λ_i of the monodromy matrix $\boldsymbol{B} = \boldsymbol{\Phi}^{-1}(0)\boldsymbol{\Phi}(T)$. These eigenvalue are connected to the Floquet exponents ν_i according to $\lambda_i = e^{\nu_i T}$. Hence, when the modulus of all eigenvalues satisfies $|\lambda_i| \leq 1$, each Floquet exponent has a real part that is smaller or equal to zero and the solution is stable. However, if only a single eigenvalue does not satisfy this relation, meaning there exists an i_0 for which $|\lambda_{i_0}| > 1$, the system eventually destabilizes and expands exponentially fast.

The resulting stability diagram is visualized in figure 3.3 as a function of the atom interaction NU and the driving strength δV. Here, we consider a fixed static potential curvature $V_0 = 1.6 \times 10^{-5}\,J$, but different driving frequencies Ω for each plot. The dashed curves divide the parameter space in regions of stable and unstable behavior, while the blue regions indicate that the system is stable, the system becomes dynamically unstable in the red regions. At resonance $n\Omega = 2\omega$, an infinitesimal small driving strength δV is sufficient to destabilize the system. Finite particle interactions shift this resonance to smaller driving frequencies. While for $NU = 0\,J$ in figure 3.3(c), the first resonance is at $\Omega = 0.032\,J$, the resonance frequency is consecutively lowered, when increasing NU/J, see in figure 3.3(a) and (b).

By modifying the resonance condition, the atom interactions can be exploited to stabilize a condensate of bosonic atoms in a parametrically driven harmonic trap potential. Interestingly, locating the onset of the instability allows, in principle, to determine the atom interaction strength. Thus, dynamically probing a quantum many-body system with a periodic modulation of the harmonic confinement provides a diagnostic tool, which warrants an experimental realization in the realm of ultracold Bose gases.

3.1.3 Floquet Engineering and Artificial Gauge Fields

In addition to the parametric resonance, a periodic drive can also be used to Floquet engineer artificial gauge fields [186], which for instance can realize an atomic spin-orbit-like coupling [187, 188]. Here, the parametric driving of the global trap can be used to create a spatially varying hopping strength. Via a time-dependent unitary transformation $U(t) = e^{i\delta V \sin(\Omega t)\sum_j (j-j_0)^2 n_j/\Omega}$, the time dependence of the potential can be converted to a time- and site-dependent hopping amplitude. With this, the ladder operator transforms as

$$U(t) b_j U^\dagger(t) = b_j e^{-i\delta V \sin(\Omega t)(j-j_0)^2/\Omega} . \tag{3.11}$$

By absorbing the exponential into the hopping amplitude, a complex tunnel coupling is defined with a time- and site-dependent phase according to

$$J_j(t) = J e^{i\delta V \sin(\Omega t)[2(j-j_0)+1]/\Omega} = J \sum_k \mathcal{J}_k \left(\delta V [2(j-j_0)+1]/\Omega\right) e^{-ik\Omega t} . \tag{3.12}$$

Here, the second equality follows by making use of the Jacobi–Anger identity which expands the exponential in terms of Bessel functions of first kind $\mathcal{J}_k(x)$ (see equation (2.66)). Thus, for a large enough driving frequency Ω, the time average yields an effective local hopping rate $J_j^{\text{eff}} = J\mathcal{J}_0(\delta V[2(j-j_0)+1]/\Omega)$, where the spatial dependence is imprinted by the Bessel function $\mathcal{J}_0(x)$.

3.2 Transient Dynamics and Many-Body Resonance for Strongly Interacting Atoms

Let us first consider the static case $\delta V = 0$, and compare the ground states of the Hamiltonian (3.1) found by the mean-field ansatz and the numerically exact one of the TEBD method. From the condensate profile $\langle n_j \rangle$, we extract the full width at half maximum (FWHM), which coincides only in the non-interacting limit with the Gaussian width σ_0. The comparison as a function of the interaction strength U is shown in figure 3.4 for a half-filled lattice with $L = 32$ sites in a harmonic potential with $V_0 = 0.0922\,J$. In addition, the corresponding distributions $\psi_j^* \psi_j$ and $\langle n_j \rangle$ for certain U are shown in the inset. While for $U = 0$, a perfect match between both approaches is found, deviations grow with increasing interaction U. By increasing the local interaction, quantum fluctuations become more important, leading to a broadening of the atom distribution and a local formation of Mott insulating states. This formation of the Mott regions is the main reason for the deviations. In the inset of figure 3.4, this is indicated by a *wedding-cake* structure of the density profile with plateau-like Mott regions at the border for $U = 7\,J$. These Mott regions, where the local occupation is constantly one, cannot be reproduced by the Gaussian variational ansatz. Indeed, the condensate width predicted by the TEBD is systematically larger than the width of the variational mean-field approach. Moreover, the step-like increase of the FWHM around $U \simeq 7\,J$, is accompanied by the formation of the Mott plateau, which is a signature of the

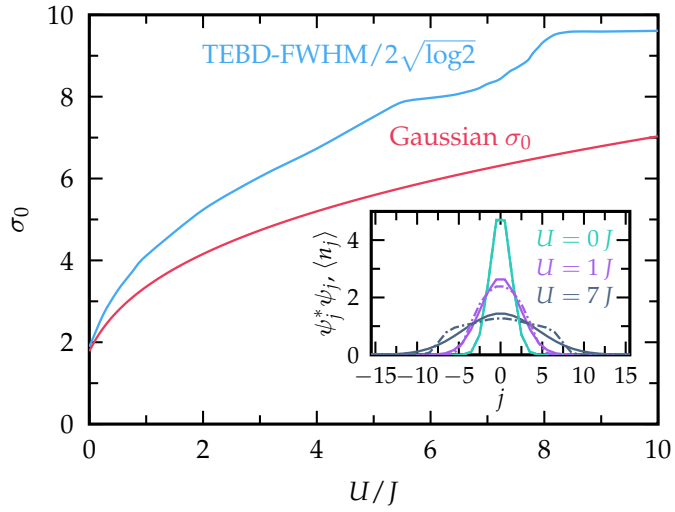

FIGURE 3.4: The main plot shows a comparison of the condensate width determined by the FWHM of the TEBD solution (blue) and the variational mean-field width σ_0 (red). The width is determined as a function of the interaction strength U/J with the static potential curvature $V_0 = 0.0922\,J$, $L = 32$ sites and $N = 16$ atoms. The step in the TEBD-FWHM indicates the BKT quantum phase transition. In addition, the inset shows a comparison between the local occupation number $\langle n_j \rangle$ and the condensate profile $\psi_j^* \psi_j$. Here, the dashed curves show the TEBD results and the solid curves show those of the Gaussian ansatz.

Berezinsky–Kosterlitz–Thouless (BKT) quantum phase transition (QPT). It has been shown that this QPT occurs between $U = 7.5\,J$ and $U = 8\,J$ for the $\langle n \rangle = 1$ Mott lobe [189, 190].

In addition to the static case, we set our focus next on the transient dynamics of the condensate in the parametrically modulated trap. Initially, we prepare the Bose gas in the ground state $|\psi_0\rangle$ of the Hamiltonian $H(0)$ at time $t = 0$. The time evolution of the total energy difference $\Delta E = E(t) - E(0)$ is shown figure 3.5(a) as a function of the time t and driving frequency Ω. Here, $E(t) = \langle H(t) \rangle_{\psi(t)} = \langle \psi(t)|H(t)|\psi(t)\rangle$ is the mean energy and $|\psi(t)\rangle = \mathcal{T} \exp\{-i \int_0^t ds\, H(s)\}|\psi_0\rangle$ is the state at time t. Moreover, $E(0) = \langle \psi_0|H(0)|\psi_0\rangle$ is the ground state energy of the initial Hamiltonian $H(0)$. In order to compare these results to the previous analysis, we scale the driving frequency Ω to the breathing mode frequency $\omega = 2\sqrt{J'V'}$ of the variational mean-field ansatz. Hence, a resonant behavior is expected to occur in the vicinity of $\Omega/\omega = 2/n$. A clear evidence for the two-photon resonance $n = 2$ is found, which is manifested in a monotonic growth of the total energy after each period. The resonance appears to be slightly shifted to larger driving frequencies due to effects of the atom interaction that are not included in the mean-field description. A signature of the $n = 1$ resonance is, however, not observed in the transient dynamics, but is expected to be pronounced for larger times. In the case of an off-resonant modulation, the energy simply oscillates with the driving frequency, involving only small variations in the amplitude. These two effects are illustrated by studying cuts along the Ω-lines as exemplary shown in figure 3.5(b) for $\Omega = 1.31\,\omega$ and $\Omega = 2.34\,\omega$.

In order to quantify the resonance in the transient dynamics, we introduce the energy absorption over a certain number of m periods according to

$$\langle E \rangle = \frac{\Omega}{2\pi m} \int_0^{2\pi m/\Omega} dt\, \Delta E(t)\,. \tag{3.13}$$

The time window for the calculated dynamics in 3.5(a) encompasses up to $m = 7$ periods over which we average the total energy and show the result in figure 3.5(c). Here, the dashed

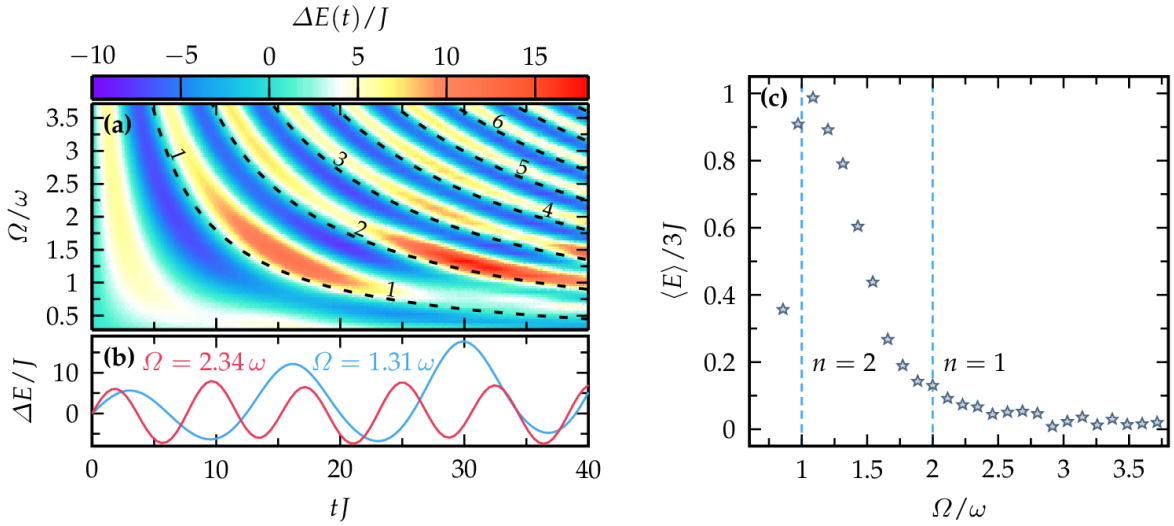

FIGURE 3.5: (a) The time evolution of the total energy $\Delta E(t) = \langle H(t)\rangle_{\psi(t)} - \langle H(0)\rangle_{\psi_0}$ is shown as a function of the driving frequency Ω. The dashed lines indicate times at which $t = 2\pi n/\Omega$. (b) A cut along constant Ω-lines is shown. (c) The total energy of (a) is averaged over up to 7 periods and shown as a function of Ω. Here, the parameters are $L = 64$, $N = 32$, $V_0 = 0.01\,J$, $\delta V = 0.002\,J$ and $U = 8\,J$. The raw data have been taken from reference [112].

vertical lines indicate the points where the parametric resonance is expected to occur according to the Gaussian mean-field ansatz. The second resonance around $\Omega \simeq \omega$ is indicated by a rather broad peak which is slightly shifted, whereas the first resonance $\Omega = 2\omega$ is only slightly visible at the flank of the peak. By taking longer times into account, the rise of the first resonance $\Omega \simeq 2\omega$ and the slight oscillations at the flank are expected to enhance and vanish, respectively.

Nevertheless, we have found a rather good agreement in the resonance condition between the numerical exact and the Gaussian variational ansatz. In the following chapters, we will again make use of this rather simple and computationally cheap but accurate method by applying it to a very different type of quantum systems.

Chapter 4

Phase Transitions and Critical Phenomena

The phase of a thermodynamic system is characterized by its uniform physical properties and the state of matter in which the system resides depends on the external conditions. The most prominent example of phases are the liquid, solid and gaseous states of matter. For instance, by lowering the temperature, a gas can condensate to a liquid. This change of phase, commonly referred to as a phase transition, is described by the van der Waals theory. Originally published in 1873, van der Waals generalized the 'ideal gas' by introducing an additional two-particle interaction potential. A treatment of the interaction on the mean-field level provided one of the first theoretical explanations of critical phenomena.

In the years following after van der Waals' explanation of the gas-fluid phase transition, similar behaviors in different materials were discovered. For instance, ferromagnetic iron was found to show also such a critical phenomenon at a certain temperature. Discovered by Pierre Curie in 1895, this temperature is also known as the Curie temperature or Curie point. It determines above which temperature iron loses its ferromagnetic features. Later, this behavior was explained by Weiss. In his molecular-field theory of ferromagnetism, Weiss introduced a hypothetical molecular mean field in analogy to the van der Waals theory.

The critical phenomena [191, 192] of these two examples show the same universal behavior and belong to same universality class, the class of mean-field phase transitions. This universality class is described by an algebraic behavior of the particle density difference between liquid and gas or the magnetization according to $\sim (T - T_c)^\beta$ for the gas or ferromagnet, respectively. Here, T_c is the critical temperature at which the phase transition occurs. For the class of mean-field phase transitions, the critical exponent β is predicted to be always $1/2$. On the basis of general symmetry arguments given by Landau in his work on the theory of phase transitions in 1937, it is suggested that mean-field theory is essentially exact. In contradiction to these arguments, Guggenheim showed in 1945 that the coexistence curve of the gas to liquid phase transition is actually not parabolic [193], indicating $\beta \neq 1/2$. Nowadays, it is known that mean-field theory does not provide the actual critical exponents. However, the Landau theory is still an invaluable tool in order to study phase transitions and investigate critical phenomena.

4.1 Landau Theory of Phase Transitions

The definition of an appropriate, so-called order parameter is one possible approach in order to investigate a phase transition and its universal behavior. The order parameter is defined such that it is only different from zero in one of the two phases. A first general description of universality goes back to Landau in which he derived the free enthalpy G in the critical region as a function of the order parameter [194]

$$\varphi = \int_V d^3x\, \psi(\boldsymbol{x}) \begin{cases} = 0 & \text{for } T > T_\mathrm{c}\,, \\ \neq 0 & \text{for } T < T_\mathrm{c}\,, \end{cases} \tag{4.1}$$

with its density $\psi(\boldsymbol{x})$ and volume V. For the ferromagnet for instance, φ corresponds to the total magnetization, while $\psi(\boldsymbol{x})$ is the local magnetization. As the temperature $T < T_\mathrm{c}$ tends towards the critical temperature, ψ decreases to zero and the expansion of the free enthalpy[1] can be written as

$$G(T;\varphi) = \int_V d^3x\, \left[g_0(\boldsymbol{x}) - \pi(\boldsymbol{x})\psi(\boldsymbol{x}) + a(T)\psi^2(\boldsymbol{x}) + b(T)\psi^4(\boldsymbol{x}) + c(T)\big(\nabla\psi(\boldsymbol{x})\big)^2 \right] . \tag{4.2}$$

Here, $\pi(\boldsymbol{x})$ is a force conjugate to the order parameter density $\psi(\boldsymbol{x})$, as for instance the magnetic induction for the ferromagnet. Moreover, the enthalpy density at vanishing order parameter is denoted by $g_0(\boldsymbol{x})$ and the expansion coefficients a, b, c are assumed to behave smoothly as a function of temperature.

For a given temperature T, the equilibrium value of the order parameter φ is fixed by the condition that $G(T;\varphi)$ is minimal. By reasons of symmetry, the free enthalpy $G(T;\varphi)$ should not vary when $\psi(\boldsymbol{x})$ and $\pi(\boldsymbol{x})$ simultaneously change their sign. Hence, the expansion only contains terms that are of even order in the order parameter density $\psi(\boldsymbol{x})$.

An important special case is the position-independent case, i.e., when $\psi(\boldsymbol{x}) \equiv \varphi/V$ and $\pi(\boldsymbol{x}) \equiv \pi$. Then, the expansion (4.2) simplifies to

$$G(T;\varphi) = G(T;0) - \pi\varphi + \frac{1}{V}a(T)\varphi^2 + \frac{1}{V^3}b(T)\varphi^4\,, \tag{4.3}$$

where $G(T;0) = \int_V d^3x\, g_0(x)$. When $\pi = 0$, the order parameter φ should vanish for $T > T_\mathrm{c}$, whereas it should be finite for $T < T_\mathrm{c}$. In general, the equilibrium value of φ has to minimize the free enthalpy, and consequently the first derivative has to be zero:

$$\left(\frac{\partial G}{\partial \varphi}\right)_T \stackrel{!}{=} 0 = \frac{2}{V}a(T)\varphi + \frac{4}{V^3}b(T)\varphi^3\,, \tag{4.4}$$

which has the three possible solutions

$$\varphi_0 = 0 \quad \wedge \quad \varphi_0 = \pm V\sqrt{-\frac{a(t)}{2b(T)}}\,. \tag{4.5}$$

[1] Here, we are only interested in the free enthalpy as a function of temperature, i.e., we fix the pressure and omit the pressure dependence.

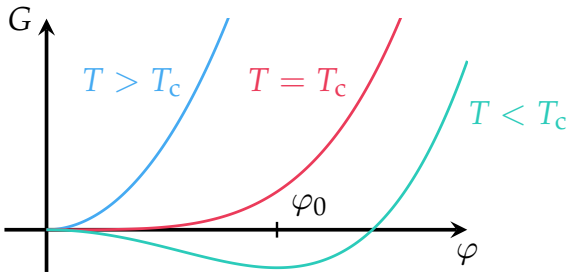

FIGURE 4.1: The schematic behavior of the free enthalpy G is shown as a function of the order parameter for three different temperatures.

In the high-temperature regime ($T > T_c$), the first solution $\varphi = 0$ should minimize $G(T;0)$, such that the second derivative has to fulfill the minimum requirement

$$\left(\frac{\partial^2 G}{\partial \varphi^2}\right)_T (\varphi = 0) = \frac{2}{V} a(T) \overset{!}{>} 0\,. \tag{4.6}$$

Thus, one finds that the first coefficient has to fulfill $a(T) > 0$ for $T > T_c$. On the other hand, below the critical temperature $T < T_c$, the order parameter should be given by the second solution $\psi \neq 0$ of equation (4.5). In addition, the minimization requirement reads

$$a(T) + \frac{6}{V^2} b(T) \varphi_0^2 = -2a(T) \overset{!}{>} 0\,, \tag{4.7}$$

such that $a(T) < 0$ and $b(T) > 0$ for $T < T_c$. The schematic behavior of the free enthalpy is shown in figure 4.1.

In combination, the expansion coefficient $a(T)$ has to change its sign at the critical temperature such that it suggests the ansatz

$$a(T) = a_0 (T - T_c)\,, \tag{4.8}$$

where $a_0 > 0$. Moreover, it can be shown that including higher, odd powers of $(T - T_c)$ would lead to contradictions [194]. In addition, the fourth order expansion coefficient $b(T)$ at the critical temperature has to fulfill $b(T_c) > 0$, which in the vicinity of the phase transition can be approximated $b(T) \simeq b(T_c) \equiv b_0$. Consequently, the free enthalpy takes the approximate form

$$G(T;\varphi) \simeq G(T;0) + \frac{a_0}{V}(T - T_c)\varphi^2 + \frac{b_0}{V^3}\varphi^4\,. \tag{4.9}$$

In the case $b(T_c) \leq 0$, an expansion of the Gibbs enthalpy to fourth order in the order parameter is no longer sufficient and higher orders have to be included. In fact, it can be shown by simple algebra that then the continuous behavior of φ in the vicinity of the critical temperature turns into a discontinuous one. The behavior of the order parameter at the critical point is a possible way to classify a phase transition.

4.2 Classification and Universality

Already earlier to Landau's theory, Ehrenfest (1933) introduced a classification scheme by ascribing an order to the phase transition. He defined the order of a phase transition by order

heat capacities: α, α'	$C_H \sim (-\tau)^{-\alpha'}$ $C_H \sim \tau^{-\alpha}$	$T < T_c$, $B_0 = 0$ $T > T_c$, $B_0 = 0$
order parameter: β	$M \sim (-\tau)^{\beta}$	$B_0 = 0$
susceptibilities: γ, γ'	$\chi_T \sim (-\tau)^{-\gamma'}$ $\chi_T \sim \tau^{-\gamma}$	$T < T_c$, $B_0 = 0$ $T > T_c$, $B_0 = 0$
critical isotherm: δ	$M \sim B_0^{1/\delta}$	$T = T_c$
correlation length: ν, ν'	$\xi \sim (-\tau)^{-\nu'}$ $\xi \sim \tau^{-\nu}$	$T < T_c$, $B_0 = 0$ $T > T_c$, $B_0 = 0$

TABLE 4.1: The critical exponents are summarized for a ferromagnet with an external magnetic field of strength B_0, taken from reference [194].

of the lowest derivative of the thermodynamical potential that exhibits a discontinuity at the transition point. For instance, the Landau expansion of the free enthalpy in equation (4.9) describes a second-order phase transition, as the first derivative of the order parameter $\varphi = (\partial G/\partial \pi)_T$ with respect to T, i.e., the second derivative of the Gibbs energy $(\partial^2 G/\partial T \partial \pi)$, is discontinuous at $T = T_c$.

Yet, the physical differences between the phases, coexisting at the transition point, become progressively insignificant as the order of the phase transition increases. In practice, only the lowest orders are of relevance and we distinguish between discontinuous, and continuous phase transitions, corresponding to first-order, and second- or higher-order phase transitions, respectively.

A characteristic feature of any continuous phase transition is the already mentioned universal behavior. In the vicinity of the transition point, many physical quantities exhibit a behavior that can be characterized by universal critical exponents which, for instance, are independent of the atomic constituents in the case of the van der Waals gas. Indeed, a power law behavior in the critical region for a physical quantity X according to

$$X \sim |\tau|^{\vartheta} \tag{4.10}$$

is very often observed, where $\tau = (T - T_c)/T_c$ is the reduced temperature. Moreover, this power law behavior can, in principle, be different below and above the critical temperature, leading to different critical exponents ϑ whether the critical point is approached from $\tau < 0$ or $\tau > 0$.

A finite set of these critical exponents exists and they are attributed to the power law behavior of the order parameter, heat capacity, susceptibility, and correlation length. A list of these critical exponents is summarized for the example of a ferromagnet in table 4.1.

Coming back to the previous example, the Landau theory of equation (4.9) predicts a power law behavior of the order parameter according to

$$\varphi_0 = \pm V \sqrt{\frac{a_0}{2b}} (T_c - T)^{1/2} \tag{4.11}$$

universality class	α	β	γ	δ	ν
Landau theory	0	1/2	1	3	1/2
2D Ising	0	1/8	7/4	15	1
3D Ising	0.1096(5)	0.32653(10)	1.2373(2)	4.7893(8)	0.63012(16)

TABLE 4.2: The critical exponents of the Landau theory are summarized and exemplary compared to those of the two-dimensional and three-dimensional Ising universality class [195].

with the critical exponent $\beta = 1/2$. Hence, the Landau theory belongs to the mean field universality class for which the critical exponents are independent of the systems spatial dimension. For many other physical systems, such as the two-dimensional or three-dimensional Ising universality class, the critical exponents can become very different depending on the dimensionality. A comparison of the different values of the critical exponents is given in table 4.2.

4.3 Equilibrium Quantum Phase Transitions

In the last decades, the interest in the quantum mechanical equivalent of a classical phase transition steadily grew. With the realization of a Bose–Einstein condensate in 1995 [196, 197], which was rewarded with the Nobel prize in 2001, systems of ultracold atoms with almost no defects and high controllability could be established for the very first time. Nowadays, ultracold atoms are routinely combined with standing wave laser fields, generating an optical lattice. By this, lattice models such as the Bose–Hubbard model (see chapter 3) or Fermi–Hubbard model are realized, which are well-known for their rich phase diagrams.

In analogy to the definition of a classical phase transition, the quantum phase transition (QPT) is defined by a non-analytical point in the ground state energy. In order to describe the principles of the QPT, we consider a Hamiltonian of the form

$$H = H_0 + \lambda H_1 \,, \tag{4.12}$$

with a dimensionless coupling constant λ.

For a finite Hilbert space dimension spanned by the eigenvectors of the Hamiltonian H, the ground state energy is usually a smooth function of the control parameter λ. The only exception arises when λ couples to a conserved quantity for which $[H_0, H_1] = 0$. Hence, both operators H_0 and H_1 can be simultaneously diagonalized. Consequently, the eigenvectors have to be independent of the coupling constant, while the energy spectrum exhibits a level crossing at a certain critical coupling $\lambda = \lambda_c$ where an excited level becomes the ground state. As a consequence, the first derivative of the ground state energy with respect to λ is not defined at λ_c, which is the definition of a first-order phase transition according to the Ehrenfest classification. This behavior is schematically shown in figure 4.2(a).

The other possibility is that both operators do not commute with each other, $[H_0, H_1] \neq 0$. In the energy spectrum, an avoided energy crossing appears at the critical coupling $\lambda =$

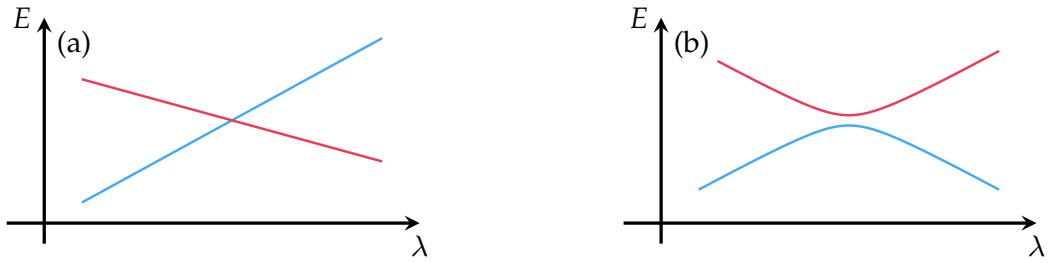

FIGURE 4.2: The two possible scenarios for the behavior of the two lowest eigenenergies is depicted as a function of the control parameter λ. In plot (a), the case $[H_0, H_1] = 0$ is schematically visualized, while the other case with $[H_0, H_1] \neq 0$ is shown in plot (b).

λ_c, which is indicated in figure 4.2(b). As the Hilbert space dimension grows, the avoided level crossing becomes progressively sharper, which leads to non-analytical point in the limit of infinite Hilbert space dimension.

In the following, we will focus on quantum phase transitions that are continuous, corresponding to the latter case. As the quantum critical point λ_c is approached, the typical energy scale of fluctuations Δ above the ground state vanishes according to the universal behavior

$$\Delta \sim |\lambda - \lambda_c|^{z\nu} . \tag{4.13}$$

For a gapped spectrum, the energy scale Δ corresponds to the energy difference between ground and first excited state. On the other hand, for a gapless system, Δ is the energy scale at which a qualitative change in the nature of the energy spectrum in comparison to its low energy behavior occurs. In addition, Δ defines a time scale $t_c \sim 1/\Delta$ on which spatial correlations of the order parameter decay. At the critical point, these spatial correlations ξ of the order parameter become long-ranged and diverge with an algebraic behavior $\xi \sim t_c^{1/z} \sim |\lambda - \lambda_c|^{-\nu}$. Here, z is the dynamical critical exponent which relates the correlation time to the correlation length.

Strictly speaking, a quantum phase transition occurs only at temperature $T = 0$ as it is formally defined by a non-analytical point in the ground state energy. Essentially, any phase transition occurring at some finite temperature T will become 'classical'. This happens as soon as the typical energy of the long-distance order parameter fluctuations becomes less than the thermal energy $\Delta < T^{1/z\nu}$. However, while thermal fluctuations control the critical behavior and dominate on a macroscopic scale, quantum mechanics can still be important on a microscopic level. Only at $T = 0$, the behavior is always dominated by quantum fluctuations.

For many systems[2], this behavior leads to a phase diagram that can be divided into four regions. It is depicted in figure 4.3. Here, the inverse control parameter λ^{-1} is represented by the horizontal axis, such that the ordered phase, where the order parameter is different from zero, is in the region $\lambda^{-1} < \lambda_c^{-1}$. The vertical axis represents temperature T. Upon variation of the control parameter and temperature, the long-range order is destroyed and the phase

[2] In some exception, order persists only for $T = 0$, which is for example the case for two-dimensional magnets with a $SU(2)$ symmetry. Here, the Mermin–Wagner theorem forbids order at finite temperature.

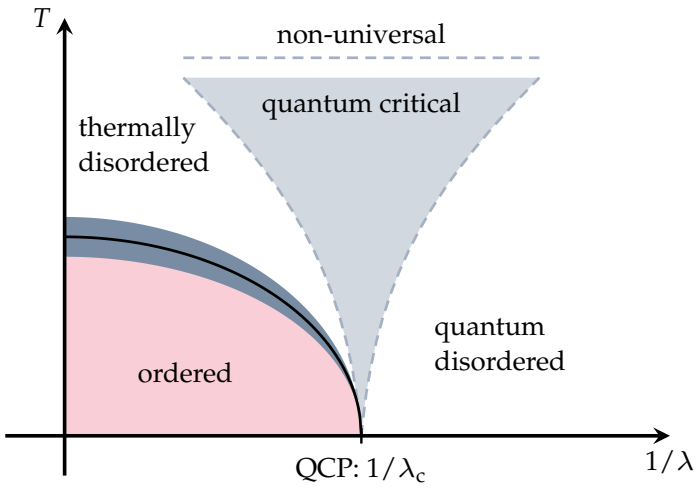

FIGURE 4.3: The phase diagram is shown in the vicinity of the quantum critical point (QCP) as a function of the control parameter λ and temperature T. The phase diagram is divided into four different regions. The solid curve indicates the boundary between ordered and disordered phase. In the vicinity of this border, the critical behavior is classical. In the region above the ordered phase, thermal fluctuations destroy the long-range order, while in the region $\lambda < \lambda_c$, quantum fluctuations wipe out any long-range order. In between these two regions, the quantum critical region, the system exhibits unusual finite temperature behavior. The figure is adapted from [192].

transition occurs, indicated by the solid curve. Around the phase boundary, the system exhibits a critical behavior that is classical. This region progressively narrows as the quantum critical point (QCP) is approached. In addition, the region of the disordered phase can be divided into two regions. Within these regions, the physics is dominated by either thermal fluctuations or quantum fluctuations. In between these regions, both types of fluctuations become important. This induces an unconventional finite temperature behavior, which is characterized by thermal excitations of the quantum critical ground state and the absence of conventional quasi-particle-like excitations. As soon as the thermal energy exceeds the characteristic microscopic energy scale, this quantum critical behavior is cut-off.

In addition to classical phase transitions, also quantum phase transitions can be grouped in universality classes. A prominent example is the superfluid to Mott insulator phase transition in the one-dimensional Bose–Hubbard model given in equation (3.1) with $V(t) = 0$, which exhibits a universal behavior. This QPT falls into the BKT universality class to which also the classical two-dimensional XY model belongs. On the other hand, as soon as a dissipative channel is included, novel critical phenomena are observed. These nonequilibrium phase transitions exhibit critical exponents that can be very different from their non-dissipative counterpart, even in the mean field regime [120, 198–200].

4.4 The Nonequilibrium Dicke Phase Transition

A well-studied example for a system that exhibits a nonequilibrium quantum phase transition (NQPT) is the hybrid system sketched in figure 4.4(a) (see also figure 1.3). A BEC is placed in a high-finesse cavity which is driven by a transversal laser pump field [116, 117,

201]. A strong enough driving field leads to a phase transition from the normal phase to the superradiant phase which is characterized by a spatial self-organization of the atomic gas in a checkerboard pattern. In a semiclassical picture, 90 degree scattering of the photons into the cavity mode is forbidden by the Bragg condition. Only finite density fluctuations of the uniformly distributed condensate allow a finite number of photons to be incoherently scattered into the cavity and superpose constructively. Above a certain pump field strength, these density fluctuations are sufficient, such that a significant number of photons enter the cavity. This is followed by an exponential instability for which the intracavity light intensity is strongly enhanced. Consequently, the atoms self-organize in the formed optical lattice and the Bragg condition for orthogonal scattering becomes fulfilled.

In summary, this phase transition is triggered by atomic density fluctuations induced by a light field mediated long-range interaction potential. Moreover, the cavity decay induces vacuum fluctuations in the light field leading to a steady state which is fundamentally different from the ground state and exhibits increased density fluctuations. In the mean field regime, the dynamics of this hybrid quantum system in one dimension is described by the set of coupled differential equations [113, 114]

$$i\partial_t\alpha = \left[-\Delta_C + NU_0\int dz\, \cos^2(z)|\psi(z)|^2 - i\kappa\right]\alpha + \sqrt{N}\eta\int dz\, \cos(z)|\psi(z)|^2\,, \tag{4.14a}$$

$$i\partial_t\psi(z) = \left[-\omega_R\partial_z^2 + NU_0|\alpha|^2\cos^2(z) + \sqrt{N}\eta(\alpha+\alpha^*)\cos(z) + Ng|\psi(z)|^2\right]\psi(z)\,. \tag{4.14b}$$

The cavity mode amplitude α is constantly driven by a transverse laser with strength η at a finite cavity detuning Δ_C. By means of atom-photon scattering, photons may enter the cavity at a finite life time κ^{-1}. These photons induce an optical potential with amplitude $NU_0|\alpha|^2$ for the atomic ensemble, whose spatial distribution is described by the condensate profile $\psi(z)$. Here, $\langle a^\dagger a\rangle = N|\alpha|^2$ is the total number of photons in the cavity and N is the number of atoms. Moreover, ω_R is the atomic recoil frequency and g is the local atomic interaction strength. Note that the potential has a 2π-periodicity, such that the problem can be reduced to a single site problem within the definition interval $z \in \{-\pi, \pi\}$ by assuming periodic boundary conditions.

4.4.1 Steady-State Solution

It has been shown that the steady-state solution (α_0, ψ_0) of equation (4.14) exhibits a nonequilibrium quantum phase transition for $\Delta_C < 0$ at a certain, critical pump amplitude $\eta = \eta_c$ different from zero [113]. This NQPT is characterized by an abrupt change of the photon number in the cavity mode and a self-organization of the atomic condensate. Below η_c, the photon number is constantly zero, $\alpha_0 = 0$, and the atomic condensate is homogeneously distributed with $\psi_0(z) = (2\pi)^{-1/2}$. When η is increased above η_c, this symmetry is spontaneously broken. Consequently, photons enter the cavity and the atoms arrange in the formed optical lattice with a two-fold steady state. This two-fold steady state has either a positive ($\alpha_0 > 0$) or negative photon quadrature ($\alpha_0 < 0$), and the atoms favor to locate around either even or odd lattice sites at $z = n\pi$ or $z = (2n+1)\pi/2$ with $n \in \mathbb{Z}$, respectively.

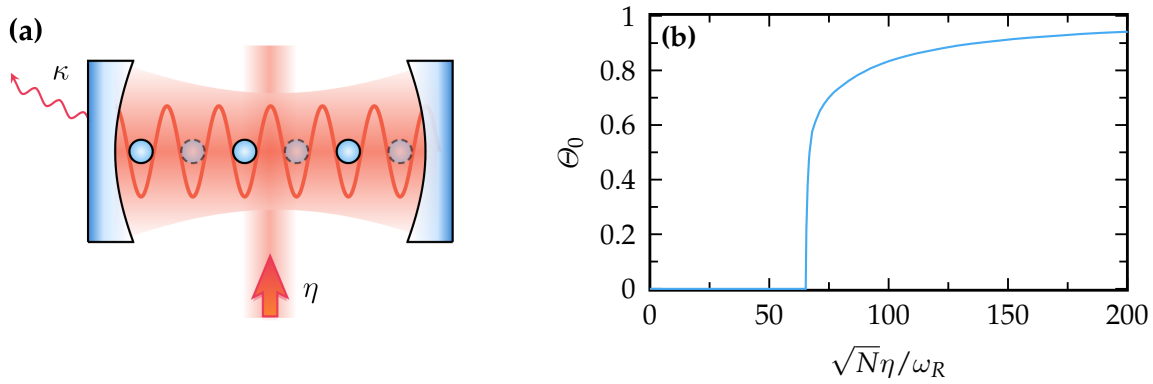

FIGURE 4.4: (a) An atomic gas ensemble is placed in a high-finesse cavity and transversely driven by a coherent laser field with driving amplitude η. An optical lattice is generated by photons that are scattered into the cavity mode with a finite life time κ^{-1}. (b) The steady state value of the atomic order parameter Θ_0 is shown as a function of the pump amplitude η. Below the critical atom-photon coupling η_c, the order parameter is constantly zero and shows a square root behavior just above η_c which saturates to $\Theta_0 = 1$ for large η. The data were taken from reference [113] for the parameters $NU_0 = -100\,\omega_R$, $Ng = 2\pi \times 10\,\omega_R$, $\Delta_C = -300\,\omega_R$, and $\kappa = 200\,\omega_R$.

In order to estimate the critical pump rate η_c, a stabilization analysis can be performed. For this, a small deviation $\epsilon \ll 1$ from the condensate steady state below η_c in the form $\psi = (1 + \epsilon \cos z)/\sqrt{2\pi}$ is assumed. Within this ansatz, the cavity photon amplitude is given by $\alpha_0 = \sqrt{N}\eta\epsilon/(\Delta_C - NU_0/2 + i\kappa)$ to lowest order in ϵ. By performing a single time evolution step in imaginary time $t = i\tau$ and comparing the decay rates of the homogeneous part and the perturbation $\cos z$, the critical pump rate is estimated to

$$\sqrt{N}\eta_c = \sqrt{\frac{(\Delta_C - NU_0/2)^2 + \kappa^2}{NU_0 - 2\Delta_C}}\sqrt{\omega_R + \frac{Ng}{\pi}}\,. \tag{4.15}$$

Apart from the photon amplitude α_0, the phase transition can be tracked by the atomic imbalance $\Theta_0 = \int dz\, \cos z |\psi_0(z)|^2$ between odd and even sites, which is also a suitable measure for the order parameter. Shown in figure 4.4(b) as a function of the pump amplitude, the order parameter Θ_0 is constantly zero in the homogeneously distributed phase below the critical coupling rate. It exhibits a square root behavior $\Theta_0 \sim (\eta - \eta_c)^{1/2}$ just above the critical point, which is characteristic for the mean-field phase transition. Far above the critical pump rate, the order parameter saturates to 1.

4.4.2 Critical Exponents for Steady State and Ground State

In addition to the mean-field description, Nagy *et al.* [199, 202] have established a Bogoliubov-like treatment of the open system dynamics for white noise and a non-Markovian bath, including excitations of the atomic subsystem out of the mean-field steady state. For non-interacting atoms, they have applied a two mode ansatz for the atomic field operators in the form

$$\Psi(z) = \frac{c_0}{\sqrt{2\pi}} + \frac{c_1}{\sqrt{\pi}}\cos z\,, \tag{4.16}$$

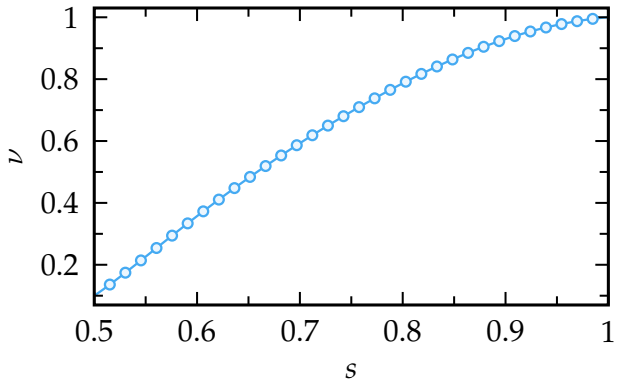

FIGURE 4.5: The critical exponent ν is estimated as a function of the sub-Ohmic bath exponent s. The parameter were chosen as $\omega_b = 0.5\,\omega_a$, $\kappa = \omega_a$, and $\gamma = 0.25\,\omega_a$. The data points are taken from reference [199].

with bosonic annihilation operators c_0, c_1. Via a Holstein–Primakoff transformation in the normal phase and the limit $N \to \infty$, the system can be mapped onto a system of two bilinearly coupled harmonic oscillators with the Hamiltonian

$$H = \omega_a a^\dagger a + \omega_b b^\dagger b + \frac{\lambda}{2}(a^\dagger + a)(b^\dagger + b)\,, \tag{4.17}$$

where a is the annihilation operator of the photon mode and b corresponds to the atomic mode which describes excitations out of the mean-field ground state $\psi(z) = \sqrt{N/2\pi}$. In other words, $\langle b^\dagger b\rangle$ is a direct measure for the atomic depletion. Both operators, a and b, follow the usual bosonic commutation relations, i.e., $\left[a, a^\dagger\right] = \left[b, b^\dagger\right] = 1$. Here, λ is the atom-photon mode coupling which is directly proportional to the pump strength η. The finite lifetime of the photons in the cavity is modeled by zero temperature white noise with a decay rate κ. For a BEC, it is well known that Beliaev coupling between collective excitation modes leads to a transfer of energy between energetically higher- and lower-lying excitation modes [203]. During this process, a single higher-lying energy excitation is converted into two quanta of lower-lying energy modes. The theoretical treatment of such a process on the microscopic level is complicated. Hence, the damping of the atomic mode is phenomenologically modelled by a sub-Ohmic bath at zero temperature with the spectral density

$$J(\omega) = \theta(\omega)\frac{\gamma}{\pi}\frac{(\omega/\omega_b)^s}{1 + (\omega/\omega_c)^2}\,, \tag{4.18}$$

where $0 < s \leq 1$. Here, ω_c is a cutoff frequency and γ is the dissipation strength.

Within a path-integral formalism, the steady-state mean occupation numbers $\langle a^\dagger a\rangle$ and $\langle b^\dagger b\rangle$ of the photon and atomic mode, respectively, are evaluated. By splitting the path into a classical path and quantum mechanical fluctuations, the path integral for the two harmonic oscillators can be evaluated in a closed analytic expression (see appendix E).

In the vicinity of the critical point $\lambda = \lambda_c$ the correlation function $\langle a^\dagger a\rangle \sim (\lambda - \lambda_c)^{-\nu}$ follows an algebraic power law with a critical exponent ν. This critical exponent is shown in figure 4.5 as a function of the sub-Ohmic bath exponent s. For a sub-Ohmic bath, the critical exponent decreases below 1 and is monotonically growing in dependence of the exponent s. For the Ohmic case at $s = 1$, the critical exponent ν becomes 1, being the same result as for sole Markovian white noise with $\gamma = 0$ [120, 198, 200]. In contrast to the ground state, where

it is always $\nu = 1/2$, the critical exponent strongly depends on the type of dissipation.

In the following, we will study a different hybrid quantum system motivated by recent experiments [129, 131]. In this process, we will first introduce the system and discuss the different coupling mechanisms that allow to couple an atomic condensate to the motion of nanomechanical oscillator. This system is another example for a hybrid system that exhibits a nonequilibrium quantum phase transition.

CHAPTER 5

Coupling a Nanomechanical Membrane to an Atomic Gas

The dipolar interaction between atoms and a light field induces a position dependent AC-Stark shift on the electronic levels of the atoms. By this, the standing wave patterns of reflected laser beams create optical lattices for ultracold atoms [204]. These periodic potentials can be used to realize the Hubbard model for bosonic or fermionic atoms in the laboratory. State-of-the-art experiments benefit from the high fidelity that has been established over the last decade. Consequently, various *unwanted* effects are avoided which include, for instance, the back-action of the atomic motion on the laser field or thermal vibrations of the mirror that reflects the light field.

On the other hand, optomechanics [205–207] is nowadays able to realize nanoscale mechanical oscillators close to their quantum regime in form of semi-transparent dielectric slabs, also membranes, or micrometer-sized mirrors. The combination of these two types of systems has led to a new generation of quantum hybrid systems in which an additional quantum degree of freedom is included by the vibrational motion of the mirror.

This new type of quantum hybrid systems exhibits many intriguing features and experimental realizations are thinkable in various setups. Though the coupling scheme for each presented system can be very different, the interaction between the atomic gas and the vibrational mode is always mediated by an external laser drive. Hence, the prototypical system Hamiltonian can be written as a sum of five consecutive terms

$$H = H_{\mathrm{a}} + H_{\mathrm{m}} + H_{\mathrm{l}} + H_{\mathrm{a-l}} + H_{\mathrm{m-l}}\,, \tag{5.1}$$

where the atomic part is described by H_{a}, the mechanical degree of freedom by H_{m} and the light field by H_{l}. The atom-light field and membrane-light field interactions are included in $H_{\mathrm{a-l}}$ and $H_{\mathrm{m-l}}$, respectively.

In this chapter, we will present different possible realizations of this atom - optomechanical hybrid system, explain their essential coupling mechanisms and outline distinct advantages, features, non-trivial effects as well as useful applications.

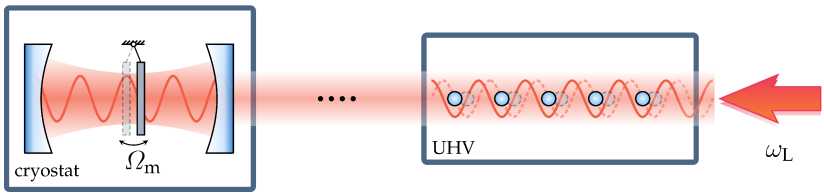

FIGURE 5.1: A nanomechanical membrane inside an optical cavity is coupled to the vibrational motion of a distant atomic ensemble.

5.1 The Distant Motional Coupling Scheme

In order to achieve a strong and coherent coupling between the motion of atoms in the lattice and a micromechanical oscillator, one faces the challenge that the effective coupling strength scales with the mass ratio $\sqrt{m/M} \sim 10^{-7} - 10^{-4}$ of the atom mass m and membrane mass M [208]. It has been shown that a strong coupling can still be reached by placing the combined system inside an optical cavity. This leads to an additional scaling in the coupling rate with the cavity finesse $\mathcal{F}$ [127, 209]. Due to different environmental requirements[1], the cavity-enhanced coupling between the mechanical oscillator and the atoms is best realized by placing the oscillator inside the cavity, while the atoms are located outside the cavity.

In this section, we consider a setup in which the vibrational mode is realized by a dielectric slab placed inside an optical cavity, the "membrane-in-the-middle" setup [128, 209]. The outcoupled light of the cavity forms an optical lattice for the atoms in a distant location. In a quasistatic picture, a finite displacement of the membrane leads to a change of the position of the lattice sites. This generates a linear displacement force on the atoms which, in turn, pushes the atoms away from their equilibrium position. On the other hand, a backaction of the atomic motion on the membrane is induced by a finite atomic center-of-mass displacement [210]. Hence, the atoms start to oscillate around the potential well minima with a universal phase. As a consequence of the arising dipole force, which is proportional to the spatial derivative of the lattice potential, the photons in the propagating beams are redistributed by absorption and stimulated emission. A sketch of the system is provided in figure 5.1.

We consider one well separated vibrational mode of the membrane which is modeled as a single harmonic oscillator

$$H_m = \Omega_m a^\dagger a \,, \tag{5.2}$$

with mechanical frequency Ω_m and bosonic annihilation (creation) operator a ($a^\dagger$) which follow the usual bosonic algebra $\left[a, a^\dagger\right] = 1$. The atomic ensemble (without optical lattice) is modeled by a one-dimensional many-body Hamiltonian in second quantization

$$H_a = -\frac{1}{2m}\int dz\, \Psi^\dagger(z)\partial_z^2\Psi(z) + \frac{g}{2}\int dz\, \Psi^\dagger(z)\Psi^\dagger(z)\Psi(z)\Psi(z)\,, \tag{5.3}$$

with bosonic field operators $\Psi(z)$ and $\Psi^\dagger(z)$, obeying $\left[\Psi(z), \Psi^\dagger(z')\right] = \delta(z - z')$. The local atom-atom interaction with strength g is due to s-wave collisions and m is the mass of one atom. The light modes are included over a bandwidth 2θ around the laser frequency ω_L with

[1] In order to reach the quantum regime, the oscillator has to be placed in a cryogenic environment, whereas the ultracold atoms require ultrahigh vacuum.

the Hamiltonian

$$H_{\mathrm{l}} = \int_{\omega_L-\theta}^{\omega_L+\theta} d\omega\, \omega b_\omega^\dagger b_\omega\,, \tag{5.4}$$

where the mode operators obey $\left[b_\omega, b_{\omega'}^\dagger\right] = \delta(\omega-\omega')$.

In order to describe the light field accurately, we have to distinguish between the light field outside and inside of the cavity. Thus, we have to explicitly include the mode functions $u_\omega(z)$ associated to b_ω. To do so, we define the electrical field operator [211]

$$E^+(z) = i\int d\omega\, \mathcal{E}_\omega u_\omega(z) b_\omega\,, \tag{5.5}$$

with the normalization constants $\mathcal{E}_\omega = \sqrt{\omega/\pi\mathcal{A}}$, where $\mathcal{A}$ is the beam cross-sectional area. The mode functions can be divided into three regions: first, the region outside the cavity; second, the region between the right side-end mirror of the cavity and the membrane; and third, the region between the membrane and the left side-end mirror.

In the first region, the mode functions take the form $u_\omega(z) = e^{i\phi_\omega}\sin(\omega z+\phi_\omega)$, where ϕ_ω is the phase accumulated during the propagation inside the cavity. This leads to a shift in the standing wave pattern outside of the cavity. In the second region, the mode functions are given by $u_\omega(z) = |T_\omega A_\omega^{-1}|e^{i\phi_\omega}\sin(\omega z+\phi'_\omega)$. The coefficients A_ω, T_ω are defined according to

$$A_\omega = \frac{t_{\mathrm{m}} e^{-i\omega d_{\mathrm{m}}}}{1-r_{\mathrm{m}}e^{2i\omega\ell}} \equiv |A_\omega| e^{i\phi'_\omega}, \tag{5.6}$$

$$T_\omega = A_\omega \frac{te^{-i\omega d}}{1-re^{2i(\omega L+\phi'_\omega)}} \equiv |T_\omega| e^{i\phi_\omega}, \tag{5.7}$$

where r_{m} (r) and t_{m} (t) are the reflection and transmission coefficients of the membrane (cavity side-end mirror), respectively. Further, ℓ is the position of the semi-transparent membrane with thickness d_{m}, L is the cavity length, and d is the thickness of the cavity side-end mirror. Finally, the mode functions in the third region are $u_\omega(z) = e^{i\phi_\omega}|T_\omega|\sin(\omega z)$.

In the case of an empty cavity ($r_{\mathrm{m}} \to 0$), the resonance frequencies $\omega_j = j\pi/L$ with $j \in \mathbb{N}\setminus\{0\}$ are well-defined and the coefficients $|T_\omega|^2$ can be approximated around the nearest resonance by a Lorentzian with width κ. In summary, we have

$$u_\omega(z) = \begin{cases} |T_\omega|\sin(\omega z) & \text{if } 0 < z < \ell\,, \\ |T_\omega A_\omega^{-1}|\sin(\omega z+\phi'_\omega) & \text{if } \ell + d_{\mathrm{m}} < z < L\,, \\ \sin(\omega z+\phi_\omega) & \text{if } L+d < z\,, \end{cases} \tag{5.8}$$

where the additional phase factor $e^{i\phi_\omega}$ can be absorbed in the mode operators b_ω.

Here, the membrane is modeled as a dielectric slab with refractive index n_{m}. Then, the radiation pressure of the light field inside the cavity on the membrane is given by $P_{\mathrm{l}} = (n_{\mathrm{m}}^2-1)\left[E^-(\ell+d_{\mathrm{m}})E^+(\ell+d_{\mathrm{m}}) - E^-(\ell)E^+(\ell)\right]/2$ [212]. Consequently, the coupling between the membrane and the light field for a small membrane displacement $z_{\mathrm{m}} = (a+a^\dagger)/\sqrt{2M\Omega_{\mathrm{m}}}$

takes the form

$$H_{\mathrm{m-l}} = P_{\mathrm{l}}\mathcal{A}z_{\mathrm{m}} = \frac{(n_{\mathrm{m}}^2-1)\mathcal{A}}{2}\left[E^-(\ell+d_{\mathrm{m}})E^+(\ell+d_{\mathrm{m}}) - E^-(\ell)E^+(\ell)\right]z_{\mathrm{m}}\,. \tag{5.9}$$

In contrast to the radiation pressure force, the dipolar interaction of the atoms with the light field induces an AC-Stark shift of the electronic levels of the atoms. Assuming a large detuning $|\Delta| \gg \theta$ from the closest atomic transition frequency, the atom-light field coupling is given by

$$H_{\mathrm{a-l}} = \frac{\mu_{\mathrm{a}}^2}{\Delta}\int dz\, E^-(z)E^+(z)\Psi^\dagger(z)\Psi(z)\,, \tag{5.10}$$

where μ_{a} is the atomic transition dipole moment.

5.1.1 Linearization in the Photon Field

Before evaluating the electrical field operators in (5.9) and (5.10), we have to explicitly include the laser drive in this model. The coherent laser drive is provided by a linear replacement for the light field operator at the laser frequency, i.e.,

$$b_\omega \to b_\omega + \alpha_L\delta(\omega-\omega_L)e^{-i\omega_L t}\,. \tag{5.11}$$

The amplitude α_L is directly related to the running power of the laser $P = \omega_L\alpha_L^2/2\pi$. In order to linearize the atom- and membrane-light field interaction in the mode operators b_ω, we will assume that $\alpha_L \gg 1$.

Inserting the expression for the mode functions of (5.8) in (5.9) with (5.11) yields the membrane-light field coupling in linearized form

$$\begin{aligned} H_{\mathrm{m-l}}^{\mathrm{lin}} =& \frac{\alpha_L(n_{\mathrm{m}}^2-1)\mathcal{A}}{2}\int d\omega\, \mathcal{E}_{\omega_L}\mathcal{E}_\omega[u_{\omega_L}(l+d_{\mathrm{m}})u_\omega(l+d_{\mathrm{m}}) - u_{\omega_L}(l)u_\omega(l)] \\ &\times\left[b_\omega e^{i\omega_L t} + b_\omega^\dagger e^{-i\omega_L t}\right]z_{\mathrm{m}}\,. \end{aligned} \tag{5.12}$$

Here, the coupling term quadratic in α_L leads to a constant linear force on the membrane, which only alters its equilibrium position. This can be accounted for, by a simple redefinition of the zero-point position and will, therefore, be omitted from hereon.

For further simplifications of the expressions in (5.12), we assume that the cavity resonance frequencies are not much influenced by the presence of the membrane, which holds for a membrane of small reflectivity $|r_{\mathrm{m}}| \ll 1$. Furthermore, we assume the optical cavity to be in the bad cavity regime. That is, the photon loss rate κ is much larger than the membrane frequency Ω_{m}, i.e., $\kappa \gg \Omega_{\mathrm{m}}$. In addition, we will also have to enforce a similar relation for the relevant atomic excitations. For our purpose, it is sufficient to assume the atomic side bands to be in between the membrane side bands. An exemplary depiction of the response profile of such an optical cavity is given in figure 5.2. Under these assumptions, the response

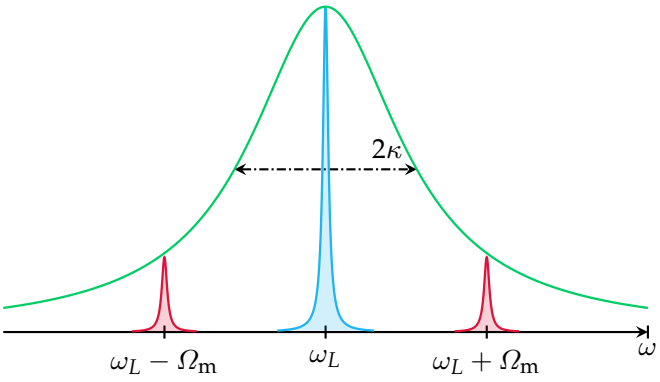

FIGURE 5.2: The green envelope indicates the response profile of the cavity and its width is directly related to the photon loss rate κ. In the bad cavity limit $\kappa \gg \Omega_{\rm m}$, both sideband photons $\omega_L \pm \Omega_{\rm m}$ are well accommodated.

coefficients $|T_\omega| \simeq |T_{\omega_L}|$ are approximately

$$|T_\omega|^2\big|_{\omega\simeq\omega_L} \simeq \frac{2\mathcal{F}}{\pi}\frac{\kappa^2}{(\omega-\omega_L)^2+\kappa^2} \simeq \frac{2\mathcal{F}}{\pi}\,, \tag{5.13}$$

with the cavity finesse $\mathcal{F} = \pi/2\kappa L$, such that $u_\omega(z) \simeq u_{\omega_L}(z)$. In the limit of a thin membrane $\omega_L d_{\rm m} \ll 1$, we may rewrite $|u_{\omega_L}(\ell+d_{\rm m})|^2 - |u_{\omega_L}(\ell)|^2 = d_{\rm m}\partial_\ell|u_{\omega_L}(\ell)|^2$. Then, with the field amplitudes $\mathcal{E}_\omega \simeq \mathcal{E}_{\omega_L}$, we arrive at

$$H^{\rm lin}_{\rm m-l} = \lambda_{\rm m}(a+a^\dagger)\int\frac{d\omega}{\sqrt{2\pi}}\left(b_\omega e^{i\omega_L t} + b_\omega^\dagger e^{-i\omega_L t}\right), \tag{5.14}$$

with the membrane-light field coupling strength

$$\lambda_{\rm m} = \frac{\alpha_L|r_{\rm m}|\omega_L}{\sqrt{\Omega_{\rm m}M}}\sin(2\omega_L\ell)\frac{2\mathcal{F}}{\pi^{3/2}}\,, \tag{5.15}$$

for which we assumed the membrane reflectivity $|r_{\rm m}| = (n_{\rm m}^2-1)\omega_L d_{\rm m}/2$. The optimal membrane-light field interaction is achieved, when the membrane is placed on the slope of the light intensity, i.e., $\sin(2\omega_L\ell) = 1$. Here, we have used that the derivative is given by $\partial_\ell|u_{\omega_L}(\ell)|^2 = 2\mathcal{F}\omega_L\sin(2\omega_L\ell)/\pi$.

In the same manner, we linearize the atom-light field interaction. Here, however, the term which is quadratic in the amplitude α_L is essential and provides the optical lattice potential $V(z) = V\sin^2(\omega_L z+\phi_{\omega_L})$ for the atomic ensemble, with the lattice depth $V = \alpha_L^2\mu_{\rm a}^2\mathcal{E}_{\omega_L}^2/\Delta$. In addition, the lattice depth defines the relevant atomic excitation frequency in the motional coupling scheme. The phase shift ϕ_{ω_L} can be directly included by the replacement $z \to z' = z - \phi_{\omega_L}/\omega_L$. Inserting the electric field operator and the linear displacement (5.11), the atom-light field coupling Hamiltonian to linear order in α_L reads

$$H^{\rm lin}_{\rm a-l} = \lambda_{\rm a}\int\frac{d\omega}{\sqrt{2\pi}}\left(b_\omega e^{i\omega_L t} + b_\omega^\dagger e^{-i\omega_L t}\right)\int dz\,\Psi^\dagger(z)\sin(\omega_L z)\sin(\omega z+\Delta\phi_\omega)\Psi(z)\,, \tag{5.16}$$

with the phase shift $\Delta\phi_\omega = \phi_\omega - \phi_{\omega_L}\omega/\omega_L \simeq \phi_\omega - \phi_{\omega_L}$ and the atom-light field interaction strength

$$\lambda_{\rm a} = \sqrt{2\pi}\alpha_L\mu_{\rm a}^2\mathcal{E}_{\omega_L}^2/\Delta\,. \tag{5.17}$$

Finally, in the frame rotating with the laser frequency (without the rotating wave approximation), the linearized Hamiltonian is given by

$$\begin{aligned} H_{\mathrm{msc}}^{\mathrm{lin}} =& \Omega_{\mathrm{m}} a^\dagger a + \int d\omega\, \Delta_\omega b_\omega^\dagger b_\omega + \int dz\, \Psi^\dagger(z) \left[V \sin^2(\omega_L z) - \frac{\partial_z^2}{2m} + \frac{g}{2}\Psi^\dagger(z)\Psi(z) \right] \Psi(z) \\ &+ \lambda_{\mathrm{a}} \int \frac{d\omega}{\sqrt{2\pi}} \left(b_\omega + b_\omega^\dagger \right) \int dz\, \Psi^\dagger(z) \sin(\omega_L z) \sin(\omega z + \Delta\phi_\omega) \Psi(z) \\ &+ \lambda_{\mathrm{m}} (a + a^\dagger) \int \frac{d\omega}{\sqrt{2\pi}} \left(b_\omega + b_\omega^\dagger \right) , \end{aligned} \tag{5.18}$$

with the detuning $\Delta_\omega = \omega - \omega_L$. This concludes the linearization procedure. In (5.18), we can see that the cavity response affects the coupling in two ways. First, the cavity finesse $\mathcal{F} \sim |T_{\omega_L}|^2$ enters the membrane-light field coupling λ_{m}, which directly enhances the coupling strength, and, second, the atom-light field coupling is affected via the phase shift $\Delta\phi_\omega = \arg(T_\omega) - \arg(T_{\omega_L})$.

5.1.2 The Harmonic Approximation

First investigated in the context of sympathetic membrane cooling [128, 209], the authors assumed a non-interacting atomic gas within the limit of a deep optical lattice. In this regime, the motion of the j-th atom can be expanded around its equilibrium position $\bar{z}_j$ with quantum fluctuations $z_j = (d_j + d_j^\dagger)/\sqrt{2m\Omega_{\mathrm{a}}}$, where $\left[d_j, d_k^\dagger\right] = \delta_{jk}$. This yields a harmonic potential with trap frequency

$$\Omega_{\mathrm{a}} = 2\sqrt{V\omega_R}\,, \tag{5.19}$$

where $\omega_R = {\omega_L}^2/2m$ is the atomic recoil frequency. Accordingly, an expansion of the atom-light field coupling yields a bilinear coupling and the linearized Hamiltonian becomes

$$\begin{aligned} H =& \Omega_{\mathrm{m}} a^\dagger a + \int d\omega\, \Delta_\omega b_\omega^\dagger b_\omega + \Omega_{\mathrm{a}} d^\dagger d + \lambda_{\mathrm{m}} (a + a^\dagger) \int \frac{d\omega}{\sqrt{2\pi}} \left(b_\omega + b_\omega^\dagger \right) \\ &+ \sqrt{N}\lambda_{\mathrm{a}}' (d + d^\dagger) \int \frac{d\omega}{\sqrt{2\pi}} \sin(\Delta_\omega \bar{z} + \Delta\phi_\omega) \left(b_\omega + b_\omega^\dagger \right) , \end{aligned} \tag{5.20}$$

with the atom-light field coupling strength

$$\lambda_{\mathrm{a}}' = \frac{\sqrt{m\pi\Omega_{\mathrm{a}}^3}}{2\alpha_L \omega_L}\,, \tag{5.21}$$

and the center-of-mass mode $d = \sum_j d_j/\sqrt{N}$. In this form, the atom-light field coupling is enhanced by a factor $\sqrt{N}$.

In the derivation of the linearized Hamiltonian of Eq. (5.18) and (5.20), a cavity damping was assumed that is much larger than the dominant time scales of the atomic and mechanical part, i.e. $\kappa \gg \Omega_{\mathrm{m}}, \Omega_{\mathrm{a}}$. Consequently, the strong photon dissipation allows to adiabatically eliminate the light field in a Born–Markov approximation and an effective description for the atom-mechanical hybrid system is found. In order to avoid retardation effects within the effective description, the propagation time τ of the light field between cavity and atom

gas has to be small in comparison to the system timescales Ω_{m}^{-1}, Ω_{a}^{-1}. In total, the hierarchy of time scales [128]

$$\Delta \gg \theta \gg \tau^{-1}, \kappa \gg \Omega_{\mathrm{m}}, \Omega_{\mathrm{a}} \gg N\lambda_{\mathrm{a}}'^2, \lambda_{\mathrm{m}}^2, \sqrt{N}\lambda_{\mathrm{a}}'\lambda_{\mathrm{m}} \tag{5.22}$$

has been assumed for the following calculation.

To obtain the effective description for the atom-membrane coupling, the idea is the following. First, the Heisenberg equations for the field operators are derived to be

$$i\partial_t a = \Omega_{\mathrm{m}} a + \lambda_{\mathrm{m}} \int \frac{d\omega}{\sqrt{2\pi}} \left(b_\omega + b_\omega^\dagger\right) , \tag{5.23a}$$

$$i\partial_t d = \Omega_{\mathrm{a}} d + \sqrt{N}\lambda_{\mathrm{a}}' \int \frac{d\omega}{\sqrt{2\pi}} \sin(\Delta_\omega \bar{z} + \Delta\phi_\omega) \left(b_\omega + b_\omega^\dagger\right) , \tag{5.23b}$$

$$i\partial_t b_\omega = \Delta_\omega b_\omega + \frac{\lambda_{\mathrm{m}}}{\sqrt{2\pi}}(a + a^\dagger) + \frac{\sqrt{N}\lambda_{\mathrm{a}}'}{\sqrt{2\pi}} \sin(\Delta_\omega \bar{z} + \Delta\phi_\omega)(d + d^\dagger) . \tag{5.23c}$$

The formal solution of the Heisenberg equation of motion for the light field modes (5.23c) is

$$\begin{aligned} b_\omega(t) =& e^{-i\Delta_\omega t} b_\omega - \frac{i\lambda_{\mathrm{m}}}{\sqrt{2\pi}} \int_0^t ds\, e^{-i\Delta_\omega (t-s)} [a(s) + a^\dagger(s)] \\ & - \frac{i\sqrt{N}\lambda_{\mathrm{a}}}{\sqrt{2\pi}} \sin(\Delta_\omega \bar{z} + \Delta\phi_\omega) \int_0^t ds\, e^{-i\Delta_\omega (t-s)} [d(s) + d^\dagger(s)] , \end{aligned} \tag{5.24}$$

with the shorthand notation $b_\omega(0) = b_\omega$ and the initial time set to 0. In a second step, this solution is inserted in the equation of motion for the mechanical and atomic operators a and d. The emergent integration over the field modes ω is of the form $\int_{-\theta}^{\theta} d\omega\, e^{i\omega t} \simeq 2\pi\delta(t)$, which leads to advanced and retarded terms in the equation of motion. Finally, neglecting the advanced terms and the retardation time, the effective quantum Langevin equations of motion are obtained

$$i\partial_t a(t) = \Omega_{\mathrm{m}} a(t) - \sqrt{N}\lambda \left[d(t) + d^\dagger(t)\right] - \xi_{\mathrm{m}}(t) , \tag{5.25a}$$

$$i\partial_t d(t) = \Omega_{\mathrm{a}} d(t) - \sqrt{N}\lambda \left[a(t) + a^\dagger(t)\right] , \tag{5.25b}$$

with the effective atom-membrane coupling $\lambda = \lambda_{\mathrm{m}}\lambda_{\mathrm{a}}'$. The light field fluctuations are included by the radiation pressure noise $\xi_{\mathrm{m}}(t)$ on the membrane in Eq. (5.25a). This stochastic force is given by

$$\xi_{\mathrm{m}}(t) = \sqrt{\frac{\Gamma_{\mathrm{m}}}{2}} \int_{\omega_L - \theta}^{\omega_L + \theta} \frac{d\omega}{\sqrt{2\pi}} \left(b_\omega e^{-i\Delta_\omega t} + b_\omega^\dagger e^{i\Delta_\omega t}\right) \tag{5.26}$$

with the associated diffusion rate $\Gamma_{\mathrm{m}} = 2\lambda_{\mathrm{m}}^2$. Under the assumption that the light field modes b_ω are initially in a vacuum state with $\langle b_\omega b_{\omega'}^\dagger \rangle = \delta(\omega - \omega')$, the noise $\xi_{\mathrm{m}}(t)$ is characterized by the white noise autocorrelation function

$$\langle \xi_{\mathrm{m}}(t)\xi_{\mathrm{m}}(s) \rangle = \frac{\Gamma_{\mathrm{m}}}{2} \delta_\theta(t - s) . \tag{5.27}$$

Here, $\delta_\theta(t) = \int_{-\theta}^{\theta} d\omega\, e^{i\omega t} = \sin(\theta t)/\pi t$ is a delta sequence that is peaked with a width of $1/\theta$. Thus, assuming that the timescale on which the reduced system evolves is much slower than $1/\theta$, the limit $\theta \to \infty$ can be taken, such that

$$\lim_{\theta\to\infty} \delta_\theta(t) = \lim_{\theta\to\infty} \frac{\sin(\theta t)}{\pi t} = \delta(t)\,. \tag{5.28}$$

5.1.2.1 Atom Momentum Diffusion and Mechanical Damping

In order to describe a realistic experimental setup and determine a regime in parameter space where sympathetic cooling is possible, damping (and heating) effects and atom momentum diffusion have to be included properly.

Atoms in an optical lattice undergo light-induced momentum diffusion processes. As an artifact of the one-dimensional treatment, this diffusion process has dropped out in the above calculation [128]. As shown in [213], the atom momentum diffusion in a trapping potential is determined by the diffusion constant $\Gamma_\mathrm{a} = \gamma_\mathrm{se}\Omega_\mathrm{a}/2\Delta$, with the natural linewidth of the transition γ_se.

On the other hand, placing the membrane in a cryogenic environment leads to a cooling of the vibrational mode and also to clamping losses due to the membrane support, such that also here appropriate noise terms have to be included. The thermal decoherence is characterized by the damping rate $\Gamma_\mathrm{th}N_\mathrm{m} \simeq T_0/Q_\mathrm{m}$, where Q_m is the mechanical quality factor, T_0 and N_m are the environment temperature and mode occupation number, respectively. Simultaneously, absorption of the laser photons leads to an additional heating of the membrane. This heating effect can be included by the definition of an effective bath temperature $T_\mathrm{eff} = T_0 + P_\mathrm{abs}/K_\mathrm{th}$ and its corresponding occupation number $\overline{N}_\mathrm{m} = T_\mathrm{eff}/\Omega_\mathrm{m} = N_\mathrm{m} + \delta N$. The absorbed laser power $P_\mathrm{abs} = 4a_\mathrm{m}^2\mathcal{F}P/\pi$ with the thermal link K_th leads to an effectively raised environment occupation by $\delta N = P_\mathrm{abs}/K_\mathrm{th}\Omega_\mathrm{m}$. Here, $a_\mathrm{m}^2 = 1 - t_\mathrm{m}^2 - r_\mathrm{m}^2$ is the power absorption coefficient and the thermal link is a measure that quantifies the heat transport from the absorption area to the frame support of the membrane. It depends on the geometry of the membrane and intracavity beam waist, as well as the thermal conductivity of the membrane[2].

With these considerations, the quantum Langevin equations become

$$i\partial_t a = \left[\Omega_\mathrm{m} - i\frac{\Gamma_\mathrm{th}}{2}\right] a - \sqrt{N}\lambda\left[d + d^\dagger\right] - \xi_\mathrm{m} + i\xi_\mathrm{th}\,, \tag{5.29a}$$

$$i\partial_t d = \Omega_\mathrm{a} d - \sqrt{N}\lambda\left[a + a^\dagger\right] - \xi_\mathrm{a}\,. \tag{5.29b}$$

The thermal stochastic force operator ξ_th is a bosonic operator which is characterized by the commutator $\left[\xi_\mathrm{th}(t), \xi_\mathrm{th}^\dagger(s)\right] = \Gamma_\mathrm{th}\delta(t-s)$. In addition, the thermal noise is δ-correlated with $\langle\xi_\mathrm{th}^\dagger(t)\xi_\mathrm{th}(s)\rangle = \overline{N}_\mathrm{m}\Gamma_\mathrm{th}\delta(t-s)$ and the atomic stochastic operator satisfies $\langle\xi_\mathrm{a}(t)\xi_\mathrm{a}(s)\rangle = \Gamma_\mathrm{a}\delta(t-s)/2$.

[2] For more details see the appendix of reference [128], where a thorough calculation on this matter is given by solving the heat equation for an ultrathin, circular membrane.

Q_m	10^7	Γ_m	$0.024\,\Omega_\mathrm{m}$	Ω_a	Ω_m
$\mathcal{F}$	450	Γ_a	$0.0032\,\Omega_\mathrm{m}$	N	10^8
N_m	83 300	$\overline{N}_\mathrm{m}\Gamma_\mathrm{th}$	$0.029\,\Omega_\mathrm{m}$	$\sqrt{N}\lambda$	$0.085\,\Omega_\mathrm{m}$
δN	208 000			$\mathcal{C}_0$	43

TABLE 5.1: The optimized parameters are based on the analysis in reference [128]. The left column shows the parameters of the optomechanical part, the central column the decoherence rates and the right column the atomic parameters and atom-membrane coupling.

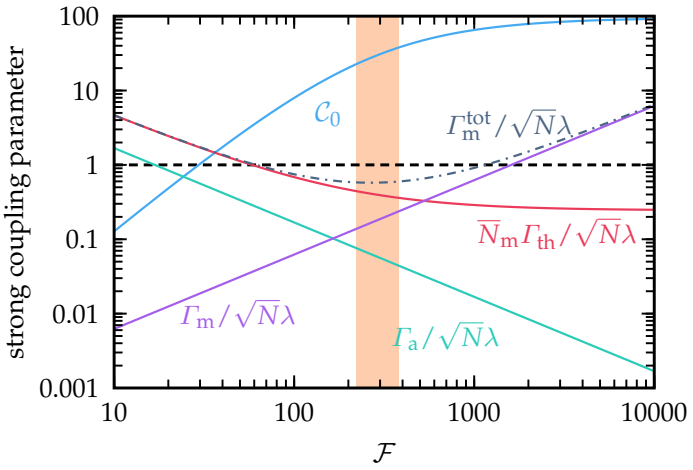

FIGURE 5.3: The cooperativity $\mathcal{C}_0$ and strong coupling condition are shown as a function of the cavity finesse $\mathcal{F}$. The orange shaded area indicates the optimal coupling regime. Other parameters than the finesse are taken from table 5.1.

With the aim to obtain a coherent state transfer, which, for instance, is essential to set up a cooling mechanism, the atom-membrane coupling has to exceed the individual decoherence rates. This strong coupling limit is expressed by

$$\sqrt{N}\lambda \gg \overline{N}_\mathrm{m}\Gamma_\mathrm{th},\, \Gamma_\mathrm{m},\, \Gamma_\mathrm{a}\,. \tag{5.30}$$

A measure that is directly connected to this condition is the cooperativity

$$\mathcal{C}_0 = \frac{N\lambda^2}{\Gamma_\mathrm{m}^\mathrm{tot}\Gamma_\mathrm{a}}\,, \tag{5.31}$$

with $\Gamma_\mathrm{m}^\mathrm{tot} = \overline{N}_\mathrm{m}\Gamma_\mathrm{th} + \Gamma_\mathrm{m}$. The cooperativity $\mathcal{C}_0$ is shown in figure 5.3 as a function of the cavity finesse $\mathcal{F}$ for realistic parameters taken from reference [128] and summarized in table 5.1. For a small finesse, $\mathcal{C}_0$ grows quadratically and eventually saturates. In analogy, this behavior is observed in the different ratios of the decoherence rates and atom-membrane coupling strength. While the atomic diffusion rate does not depend on the finesse, the momentum diffusion of the membrane grows quadratically in the finesse, leading to a linear behavior $\Gamma_\mathrm{m}/\sqrt{N}\lambda \sim \mathcal{F}$. On the other hand, the thermal decoherence rate $\overline{N}_\mathrm{m}\Gamma_\mathrm{th}$ is first dominated by the finesse-independent thermal environment of the support and then outmatched by the heating effect of the absorbed light field which scales linearly with the finesse. The optimal coupling regime is reached in the vicinity around $\mathcal{F} \simeq 300$, where $\mathcal{C}_0 > 1$ and the membrane decoherence rate satisfies $\Gamma_\mathrm{m}^\mathrm{tot} < \sqrt{N}\lambda$.

5.1.2.2 Sympathetic Cooling Scheme

An atomic gas loaded in an optical lattice is a well-controllable and clean system, which can be perturbed in various ways. By means of laser cooling, the atomic motion can be cooled by using, for instance, optical molasses [214]. In combination with the resonant excitation exchange, it can be used to introduce a sympathetic cooling scheme. The atomic cooling with rate $\Gamma_{\rm ac}$ is included via

$$i\partial_t d = \left[\Omega_{\rm a} - i\frac{\Gamma_{\rm ac}}{2}\right] d - \sqrt{N}\lambda\left[a + a^\dagger\right] - \xi_{\rm a} + i\xi_{\rm ac}\,, \tag{5.32}$$

where $\xi_{\rm ac}$ is a bosonic vacuum noise operator. This noise is characterized by the two-point correlator $\langle \xi_{\rm ac}(t)\xi_{\rm ac}^\dagger(s)\rangle = \Gamma_{\rm ac}\delta(t-s)$. By defining the vector $\boldsymbol{x} = (a, d, a^\dagger, d^\dagger)^t$, the quantum Langevin equation can be written in the form $\partial_t \boldsymbol{x} = -i\boldsymbol{M}\boldsymbol{x} + \boldsymbol{\xi}$, with the dissipation vector

$$\boldsymbol{\xi} = (i\xi_{\rm m} + \xi_{\rm th}, i\xi_{\rm a} + \xi_{\rm ac}, -i\xi_{\rm m} + \xi_{\rm th}^\dagger, -i\xi_{\rm a} + \xi_{\rm ac}^\dagger)^t \tag{5.33}$$

and the linear stability matrix

$$\boldsymbol{M} = \begin{pmatrix} \Omega_{\rm m} - i\Gamma_{\rm th}/2 & -\sqrt{N}\lambda & 0 & -\sqrt{N}\lambda \\ -\sqrt{N}\lambda & \Omega_{\rm a} - i\Gamma_{\rm ac}/2 & -\sqrt{N}\lambda & 0 \\ 0 & \sqrt{N}\lambda & -\Omega_{\rm m} - i\Gamma_{\rm th}/2 & \sqrt{N}\lambda \\ \sqrt{N}\lambda & 0 & \sqrt{N}\lambda & -\Omega_{\rm a} - i\Gamma_{\rm ac}/2 \end{pmatrix}. \tag{5.34}$$

Due to the present dissipation channels, the combined system may eventually equilibrate to a steady state. The system stabilizes when each eigenvalue m_i of the matrix $\boldsymbol{M}$ satisfies $\mathrm{Im}(m_i) < 0$. In this case, the steady state is characterized by the equation $\boldsymbol{x} = \lim_{t\to\infty}\int_0^t ds\, e^{-i\boldsymbol{M}(t-s)}\boldsymbol{\xi}(s)$. Expanding the vector $\boldsymbol{x}$ in the eigenmodes of $\boldsymbol{M}$, the correlations can be calculated according to

$$\langle x_{i_1} x_{i_2}\rangle = -\sum_{j_1,j_2}\sum_{k_1,k_2}\frac{i\Xi_{k_1k_2}}{m_{j_1}+m_{j_2}} R_{i_1j_1}R_{i_2j_2}L_{j_1k_1}L_{j_2k_2}\,, \tag{5.35}$$

with the matrices of left and right eigenvectors $\boldsymbol{L}$ and $\boldsymbol{R}$ of $\boldsymbol{M}$[3]. Further, $\boldsymbol{\Xi}$ is the noise correlation matrix whose components are defined according to $\langle \xi_i(t)\xi_j(s)\rangle = \Xi_{ij}\delta(t-s)$, where $\xi_i(t)$ is the i-th entry of the noise vector $\boldsymbol{\xi}$.

Within the rotating frame approximation, the anti-diagonal coupling terms of the stability matrix are neglected, and the matrix can be diagonalized analytically, yielding the complex eigenvalues

$$m_{1,2} = \frac{\Omega_{\rm m}+\Omega_{\rm a}}{2} - i\frac{\Gamma_{\rm th}+\Gamma_{\rm ac}}{4} \pm \frac{1}{2}\sqrt{\left(\Omega_{\rm m}-\Omega_{\rm a} - i\frac{\Gamma_{\rm th}-\Gamma_{\rm ac}}{2}\right)^2 + 4N\lambda^2}\,, \tag{5.36}$$

[3]For a more detailed discussion on the derivation of the solution in terms of left and right eigenvectors see appendix B.

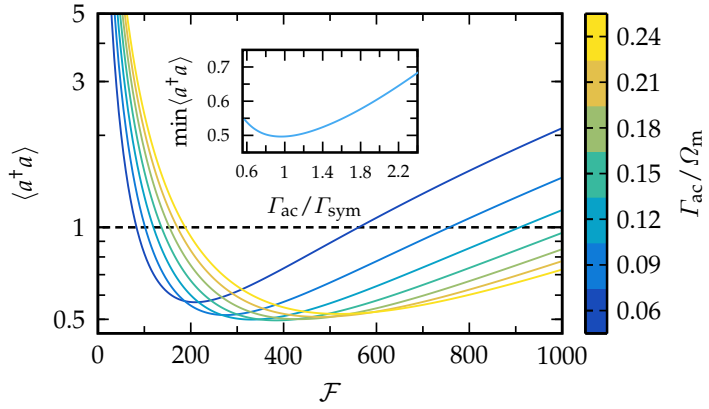

FIGURE 5.4: The membrane occupation $\langle a^\dagger a \rangle$ is shown as a function of the cavity finesse $\mathcal{F}$ for different atomic cooling rates Γ_{ac}. The inset shows the membrane occupation number minimized with respect to $\mathcal{F}$. Other parameters than the finesse are taken from table 5.1.

and $m_{3,4} = -m_{1,2}^*$. By estimating the imaginary parts of the eigenvalues, one can define a sympathetic cooling rate of the membrane[4]

$$\Gamma_{sym} \simeq \frac{4N\lambda^2\Gamma_{ac}}{\Gamma_{ac}^2 + 4(\Omega_m - \Omega_a)^2}, \tag{5.37}$$

with $\sqrt{N}\lambda, \Gamma_{th} \ll \Gamma_{ac}$.

In order to characterize a sympathetic cooling regime, the steady state occupation number of excitations $\langle x_3 x_1 \rangle = \langle a^\dagger a \rangle$ is a suitable figure of merit. In figure 5.4, the number of excitations on the membrane is shown as a function of the cavity finesse. As indicated by the color bar, different atomic cooling rates Γ_{ac} have been considered. In the weak coupling regime ($\mathcal{F} \lesssim 100$), the membrane is strongly affected by thermal effects of the apparatus. On the other hand, the optical heating caused by laser photon absorption becomes stronger as the finesse $\mathcal{F}$ is increased. The competition between both heating effects and sympathetic cooling leads to a minimized membrane occupancy around $\mathcal{F} \simeq 400$.

The position and the value of the minimum depend on the atomic cooling rate Γ_{ac} which is visualized in the inset of figure 5.4. Here, the membrane occupancy for a fixed Γ_{ac} is minimized with respect to the cavity finesse. In order to reach the strong coupling regime with inclusion of the atomic cooling, the atom-membrane coupling strength has to exceed Γ_{ac}. In combination with optical heating, a global minimum is found at $\Gamma_{ac} \simeq \Gamma_{sym}$.

5.1.3 Experimental Realization

On the basis of theoretical studies [128, 209], first experimental realizations have investigated the sympathetic cooling scheme [129, 215]. In combination with cryogenic precooling of the membrane and optical feedback cooling[5] [130, 132], it has been shown that the quantum mechanical regime of a low-frequency oscillator can be reached.

In their experimental setup, Jöckel *et al.* [129] placed a 42 nm thin Si_3N_4 membrane in a low-finesse cavity (here, $\mathcal{F} = 140$) and measured its displacement spectrum with and without utilization of the atomic coolant. An effective temperature of the vibrational mode was

[4] The same sympathetic cooling rate is found within a classical decription [215].

[5] Optical feedback cooling is achieved by applying engineered radiation pressure of a dedicated laser beam [216].

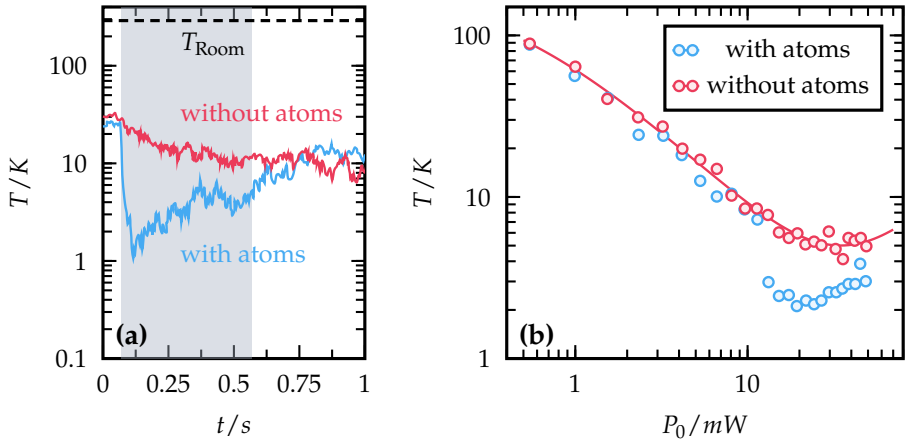

FIGURE 5.5: (a) The membrane temperature is shown in the three-step sequence with (blue) and without (red) sympathetic cooling. The dashed line indicates the room temperature $T_{\mathrm{Room}} = 20°C$. (b) The minimal temperature of the membrane is determined from the three-sequence experiment and shown as a function of the laser power P_0 in the second step. When the resonance condition $\Omega_{\mathrm{a}} \simeq \Omega_{\mathrm{m}}$ is met, sympathetic cooling becomes possible, which leads to a substantially decreased membrane temperature. The solid curve shows a fit [217] with the function $T(P_0) = (a + bP_0^2)/(1 + cP_0)$ which follows from the theory of optical cooling. The data were taken from reference [129].

estimated from the integral of the mechanical displacement spectrum. An exemplary measurement is shown in figure 5.5 (a). Without precooling of the membrane, the experiment was carried out in a time-resolved three-step sequence, with off-resonant atom-membrane coupling only in the first step. By tuning the laser power in the second step (shaded region), the resonant coupling regime $\Omega_{\mathrm{a}} \simeq \Omega_{\mathrm{m}}$ is reached. In the presence of the atomic coolant (blue curve), a substantial reduction of the membrane temperature is observed. On the other hand, in the presence of only cavity optomechanical cooling (without atoms, red curve), the membrane equilibrates to a temperature that is about one order of magnitude larger. In the last step, the atomic cooling is turned off.

In addition, the minimal temperature is tracked as function of the power of the coupling beam P_0, which is shown with and without atoms in figure 5.5 (b). By increasing the coupling laser power, not only the atom-membrane coupling is enhanced, but also the optical lattice becomes deeper, i.e., the atomic frequency Ω_{a} is increased. As a consequence, sympathetic cooling is abruptly turned on around $P_0 \simeq 14\,\mathrm{mW}$. The data points without the atoms are well described by the fit function $T(P_0) = (a + bP_0^2)/(1 + cP_0)$, which originates from the theory of cavity optical cooling [207, 217].

In addition, the same three-step measurements have been repeated with a modified cavity of $\mathcal{F} = 300$, which results in a lower temperature minimum of $650 \pm 230\,\mathrm{mK}$, corresponding to a phonon number of $\langle a^\dagger a \rangle \simeq (4.9 \pm 1.7) \times 10^4$. By combining this technique with optical feedback cooling, it has been shown that phonon numbers of $\langle a^\dagger a \rangle \simeq 16 \pm 1$ can be reached [132]. Here, the main cooling part is achieved by optical feedback cooling. Yet, sympathetic cooling allows to further reduce the temperature of the mechanical oscillator by some percents. Most interestingly, this combined method is capable of creating a strongly coupled quantum hybrid system where the vibration mode is in the quantum

ground state and the atom gas in a quantum many-body state.

Another feature of the state of a quantum hybrid system is its collective nature. Mediated long-range interaction in the atom gas due to the coupling to the optomechanical system can lead to a collective atomic motion in the optical lattice and an instability at large atom numbers [131].

Despite its attractive simple concept, a large disadvantage of the motional coupling scheme is the lack of tunability. While a regime where near resonant coupling between atoms and the membrane becomes possible is desirable, the frequency of the nanooscillator is limited to feasible trap frequencies in the optical lattice. This limits the nanooscilator to the sub-MHz regime. Another limiting factor to achieve strong coupling is the scaling of the atom-membrane interaction with $\lambda \sim \sqrt{m/M}$. An eligible candidate to circumvent these problems will be discussed in the following section.

5.2 The Distant Internal State Coupling Scheme

Rather than coupling the vibration of a nanomembrane to the center-of-mass motion of the atomic ensemble in an optical lattice, a transition in the internal state structure of the atoms may also be utilized to achieve an effective atom-membrane coupling mechanism [159]. By coupling the membrane to the internal atomic states, both subsystems can be brought much easier into resonance, because the atomic energy splitting involved in the transition can be easily tuned, e.g., by an external magnetic field. For instance, by addressing a transition between Zeeman-sublevels, the atoms can be resonantly coupled to a membrane in the MHz regime, while the utilization of hyperfine ground states would allow a resonant coupling in the GHz regime.

In this section, we consider a cloud of ^{87}Rb atoms placed in an external optical potential as depicted in figure 5.6. The internal states of the atoms, labeled by $\tau \in \{-, +, \mathrm{e}\}$, are arranged in Λ-type scheme. The energy separation between the two lowest states is denoted by Ω_a. A σ_- polarized laser constantly drives the transition between the states $|+\rangle$ and $|\mathrm{e}\rangle$ at a finite detuning Δ. The passing beam is directed to a polarization beam splitter (PBS) which splits the circularly polarized light into linearly polarized light on two arms of equal length. The light field in the upper path is reflected back onto the PBS by a fixed mirror. The light in the left path is directed into a low-finesse optical cavity in which a semitransparent nanomechanical membrane is placed. The outcoupled light field is returned back to the PBS. In a quasistatic picture, a finite displacement of the membrane induces a relative phase shift $\Delta\phi$ between the propagating $\pi_y \to \pi_y e^{i\Delta\phi}$ beam in the cavity and propagating vertical $\pi_x \to \pi_x$ beam. This relative phase shift is translated to a polarization rotation in the PBS. Then, the emergent σ_+ polarized photon impinges on an atom and may induce a two-photon transition between the states $|-\rangle$ and $|+\rangle$. The back-action of the atoms on the membrane is triggered by an internal transition between the two states $|+\rangle$ and $|-\rangle$. The emission of the additional σ_+ photon alters the radiation pressure on the membrane.

The optomechanical part of the system is described in a fashion similar to the distant motional coupling scheme. The nanomembrane is modeled as a single vibrational mode by

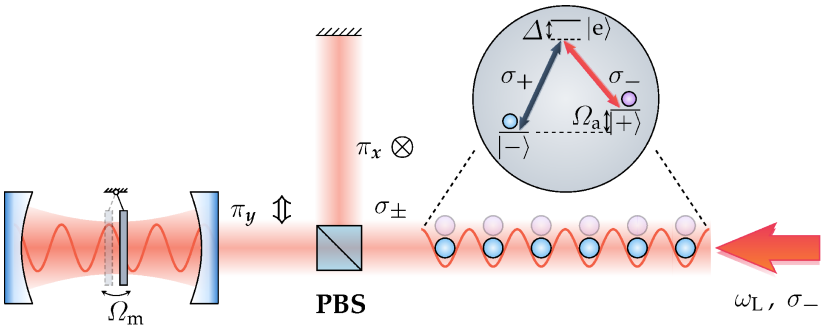

FIGURE 5.6: A nanomechanical membrane in an optical cavity is coupled to the internal states of a distant atomic ensemble that is trapped in an optical lattice. The internal states of the atoms are arranged in a Λ-type scheme according to the inset. The figure is adapted from reference [159].

the Hamiltonian of equation (5.2). The two optical polarizations are included as two light fields over a bandwidth 2θ around the laser frequency ω_L via

$$H_l = \sum_{\mu=\pm} \int_{\omega_L-\theta}^{\omega_L+\theta} d\omega\, \omega b^\dagger_{\mu,\omega} b_{\mu,\omega}\,. \tag{5.38}$$

The mode operators obey bosonic commutation relations $\left[b_{\mu,\omega}, b^\dagger_{\mu',\omega'}\right] = \delta_{\mu\mu'}\delta(\omega-\omega')$. The field operators $b_{-,\omega}$ and $b_{+,\omega}$ correspond to the different circular polarizations σ_- and σ_+, respectively. The atomic gas is modeled by the standard many-body Hamiltonian

$$H_a = \sum_\tau \int dz\, \Psi^\dagger_\tau(z) \left[\epsilon_\tau + V_\tau(z) - \frac{\partial_z^2}{2m}\right] \Psi_\tau(z) + \frac{1}{2}\sum_{\tau,\tau'} g_{\tau\tau'} \int dz\, \Psi^\dagger_\tau(z)\Psi^\dagger_{\tau'}(z)\Psi_{\tau'}(z)\Psi_\tau(z)\,, \tag{5.39}$$

with the internal state energies $\epsilon_\pm = \pm\Omega_a/2$, $\epsilon_e = \omega_L + \Delta$, the optical potential $V_\tau(z)$ and a state-dependent local particle interaction with strength $g_{\tau\tau'}$.

In accordance with the previous section, the non-linearized membrane-light field interaction takes the form of equation (5.9), with the exception that both polarizations have to be included. This is done by taking the electric field operator of the π_y polarized light which is given by

$$E^+_{\pi_y} = \sum_{\mu=\pm} \frac{i}{\sqrt{2}} \int d\omega\, \mathcal{E}_\omega u_\omega(z) b_{\mu,\omega}\,. \tag{5.40}$$

The external pumping laser has a σ_- polarization, such that the drive is included by the linear replacement at the laser frequency ω_L

$$b_{\mu,\omega} \to b_{\mu,\omega} + \alpha_L \delta_{\mu,-}\delta(\omega-\omega_L)e^{-i\omega_L t}\,. \tag{5.41}$$

With this in mind, the linearized form of the membrane-light field interaction is given by the expression

$$H^{\rm lin}_{\rm m-l} = \sum_{\mu=\pm} \lambda_m (a + a^\dagger) \int \frac{d\omega}{\sqrt{2\pi}} \left(b_{\mu,\omega} e^{i\omega_L t} + b^\dagger_{\mu,\omega} e^{-i\omega_L t}\right)\,, \tag{5.42}$$

with the same membrane-light coupling constant λ_m defined in equation (5.15).

Assuming a rather large laser detuning $\Delta \gg \mu_+ \alpha_L \mathcal{E}_{\omega_L}$, the excited state $|\mathrm{e}\rangle$ can be eliminated. Here, μ_+ is the atomic transition dipole matrix element for the internal state transition from the state $|+\rangle$ to $|\mathrm{e}\rangle$. Then, the effective atom-light field interaction takes the form

$$\begin{aligned} H_{\mathrm{a-l}} = &\sum_{\tau=\pm} \frac{\mu_\tau^2}{\Delta} \int dz\, E^-_{\sigma_{-\tau}}(z) E^+_{\sigma_{-\tau}}(z) \Psi^\dagger_\tau(z) \Psi_\tau(z) \\ &+ \frac{\mu_+ \mu_-}{\Delta} \int dz \left[E^-_{\sigma_-}(z) E^+_{\sigma_+}(z) \Psi^\dagger_-(z) \Psi_+(z) + \mathrm{H.c.} \right], \end{aligned} \tag{5.43}$$

with the atomic dipole moments μ_τ of the corresponding internal state transition and the electric field operators outside of the cavity as

$$E^+_{\sigma_\mu}(z) = \int d\omega\, \mathcal{E}_\omega u_\omega(z) b_{\mu,\omega}\,. \tag{5.44}$$

Here, the relevant mode functions are the same as in the motional coupling scheme of equation (5.8). After a linearizing procedure in the light field operators analogous to the motional coupling scheme, we arrive at the atom-light field coupling Hamiltonian

$$\begin{aligned} H^{\mathrm{lin}}_{\mathrm{a-l}} = &\lambda_{\mathrm{a}} \int \frac{d\omega}{\sqrt{2\pi}} \left(b_{-,\omega} e^{i\omega_L t} + b^\dagger_{-,\omega} e^{-i\omega_L t} \right) \int dz\, \Psi^\dagger_+(z) \sin(\omega_L z) \sin(\omega z + \Delta\phi_\omega) \Psi_+(z) \\ &+ \lambda_\pm \int \frac{d\omega}{\sqrt{2\pi}} \int dz\, \sin(\omega_L z) \sin(\omega z + \Delta\phi_\omega) \left[\Psi^\dagger_+(z) \Psi_-(z) b_{+,\omega} e^{i\omega_L t} + \mathrm{H.c.} \right], \end{aligned} \tag{5.45}$$

with the coupling constants $\lambda_{\mathrm{a}} = \sqrt{2\pi}\alpha_L \mu_+^2 \mathcal{E}^2_{\omega_L}/\Delta$ and $\lambda_\pm = \sqrt{2\pi}\alpha_L \mu_+ \mu_- \mathcal{E}^2_{\omega_L}/\Delta$. In contrast to the motional coupling scheme, the atom-light field coupling terms in this section involve two different processes. The first term in equation (5.45) couples the atoms in the internal state $|+\rangle$ to the photon field quadrature in a similar manner as in the motional coupling scheme. We will later see that this particular term breaks the coupling symmetry. On the other hand, the terms in the second line induce transitions of the atoms between the different internal states under the creation (annihilation) of a σ_+ polarized photon. Moreover, an optical lattice for the atoms in the internal state $|+\rangle$ is provided by the quadratic term in the field amplitude α_L. The lattice potential takes the form $V(z) = \Omega_{\mathrm{ol}} \sin^2(\omega_L z)$ with the depth $\Omega_{\mathrm{ol}} = \alpha_L^2 \mu_+^2 \mathcal{E}^2_{\omega_L}/\Delta$ of the optical lattice.

5.2.1 Specifying the External Lattice Potential

In order to simplify the linearized atom-light field coupling, the external lattice potential $V_\tau(z)$ can be chosen such that the atoms are positioned around the lattice sites z_j with $\sin(2\omega_L z) = 1$. An additional potential for the atoms in the state $|+\rangle$ has to be provided in order to cancel the lattice potential generated by the driving laser. This leads to a constant term which redefines the atomic transition frequency $\Omega_{\mathrm{a}} \to \Omega_{\mathrm{a}} + \Omega_{\mathrm{ol}}$. Overall, we choose the optical potential according to $V_\tau(z) = -V \sin(2\omega_L z)/2$.

In a rotating frame around the laser frequency (without the rotating frame approximation), we arrive at the linearized Hamiltonian in its final form

$$\begin{aligned} H_{\mathrm{isc}}^{\mathrm{lin}} =& \Omega_{\mathrm{m}} a^\dagger a + \sum_{\tau=\pm} \int dz\, \Psi_\tau^\dagger \left[\tau \frac{\Omega_{\mathrm{a}}}{2} - \frac{\partial_z^2}{2m} - \frac{V}{2} \sin(2\omega_L z) + \frac{1}{2} \sum_{\tau'=\pm} g_{\tau\tau'} \Psi_{\tau'}^\dagger \Psi_{\tau'} \right] \Psi_\tau \\ &+ \sum_{\mu=\pm} \int d\omega\, \Delta_\omega b_{\mu,\omega}^\dagger b_{\mu,\omega} + \sum_{\mu=\pm} \lambda_{\mathrm{m}} \left(a + a^\dagger \right) \int \frac{d\omega}{\sqrt{2\pi}} \left(b_{\mu,\omega} + b_{\mu,\omega}^\dagger \right) \\ &+ \int \frac{d\omega}{\sqrt{2\pi}} \int dz\, \sin(\omega_L z) \sin(\omega z + \Delta\phi_\omega) \left[\lambda_\pm b_{+,\omega} \Psi_+^\dagger \Psi_- + \lambda_{\mathrm{a}} b_{-,\omega} \Psi_+^\dagger \Psi_+ + \mathrm{H.c.} \right], \end{aligned} \tag{5.46}$$

where the position dependence in the atomic field operators has been omitted.

This system has been originally proposed by Vogell *et al.* [159] with slight modifications. By disregarding the atom-atom interaction, the system was investigated in the context of sympathetic cooling and compared to the previously proposed cooling scheme which involved the motional coupling. By tuning the atomic transition frequency on resonance with the membrane frequency $\Omega_{\mathrm{a}} \simeq \Omega_{\mathrm{m}}$ and simultaneous atom cooling, the coupling term which couples the light field to the number of atoms in the state $|+\rangle$ can be neglected.

By means of adiabatic elimination of the light field, an effective description of the atom-membrane system is found using the master equation in Lindblad form

$$\dot{\rho} = -i\,[H, \rho] + \frac{\gamma_{\mathrm{m}}}{2} \mathcal{D}\left[a + a^\dagger \right] \rho\,, \tag{5.47}$$

with the Lindblad operator $\mathcal{D}[x]\rho = x\rho x^\dagger - \left\{ x^\dagger x, \rho \right\}/2$ and the mechanical diffusion rate $\gamma_{\mathrm{m}} = 2\lambda_{\mathrm{m}}^2$. By employing a single-mode approximation $\Psi_\pm(z) = d_\pm \psi(z)$ with a complex mode function $\psi(z)$ and bosonic ladder operators $d_\pm$, the effective Hamiltonian in the limit of vanishing atom-atom interactions $g = 0$ is given by

$$H = \Omega_{\mathrm{m}} a^\dagger a + \Omega_{\mathrm{a}}' S_z - \lambda (a + a^\dagger) S_x \tag{5.48}$$

with the effective spin operators $S_z = (d_+^\dagger d_+ - d_-^\dagger d_-)/2$ and $S_x = (d_+^\dagger d_- + d_-^\dagger d_+)/2$ and the effective atom-membrane coupling rate $\lambda = \lambda_\pm \lambda_{\mathrm{m}}$.

5.2.2 Realization of a Negative Mass Spin Oscillator

An intriguing feature of the atomic-"spin" ensemble is the realization of a negative mass oscillator. This idea involves an optical pump of the atoms in order to generate a population inversion between the energetically inverted spin states $|+\rangle$ and $|-\rangle$. For this purpose, we utilize a spin description in terms of a collective spin of the atomic ensemble with the effective spin operators $S_j = \sum_{\tau,\tau'} d_\tau^\dagger \left(\sigma_j\right)_{\tau\tau'} d_{\tau'}/2$, bosonic annihilation operators d_τ in the corresponding internal state, $j \in \{x, y, z\}$, and the Pauli matrices σ_j. We note that the eigenvalues of the operators S_j range between $-N/2$ and $N/2$. Now, the driving induces a large fraction of atoms to occupy the energetically higher internal state $|+\rangle$, such that the mean

value of the spin operator $\boldsymbol{S} = (S_x, S_y, S_z)^T$ is $\langle \boldsymbol{S} \rangle \simeq (0, 0, s_0)$. Here, $s_0 \gg 1$ is a large number close to the maximally polarized state with $\langle S_z \rangle = N/2$. Next, we define normalized spin components $q_\mathrm{a} = S_x/\sqrt{s_0}$, $p_\mathrm{a} = S_y/\sqrt{s_0}$ that fulfill the canonical commutation relation

$$[q_\mathrm{a}, p_\mathrm{a}] = i\frac{S_z}{s_0} \simeq i, \tag{5.49}$$

in the Holstein–Primakoff approximation. In addition, we make use of the relation $S_z \simeq \sqrt{s_0(s_0+1)} - (q_\mathrm{a}^2 + p_\mathrm{a}^2)/2$, such that the collective-spin Hamiltonian results in

$$H_\mathrm{a} = \Omega_\mathrm{a}' S_z \simeq \Omega_\mathrm{a}' s_0 - \frac{\Omega_\mathrm{a}'}{2}\left(q_\mathrm{a}^2 + p_\mathrm{a}^2\right), \tag{5.50}$$

where the first term is only a constant and the second part realizes the harmonic oscillator with negative mass.

In combination with a regular, positive mass harmonic oscillator, such a realization can be utilized to unite quantum back-action (QBA) evading measurements[6], quantum nondemolition measurements and quantum noise cancellation [220]. In addition, entanglement between two atomic samples mimicking the macroscopic spins has been induced earlier in reference [221], which in turn can be used to enhance quantum measurements [222].

An experimental setup similar to that shown in figure 5.6 has been realized recently, in which the vibrational motion of a mechanical membrane placed in a high-finesse optical cavity implements the harmonic oscillator with positive mass [223]. On the other hand, the negative mass harmonic oscillator is included by a far distant thermal cloud of caesium atoms. In their work, the authors have shown that this setup is capable of QBA evading measurements which enables a high displacement sensitivity. Let us note that the use of a high-finesse cavity requires a description beyond the effective time-evolution of the Lindblad equation (5.47) with (5.48), because retardation effects become progressively more important. In fact, it is more closely related to a different type of coupling scheme, namely the high-finesse coupling scheme which we will shortly summarize in the following section.

5.3 The High-Finesse Coupling Scheme

An alternative possible realization of a system that combines an optomechanical system with an ensemble of bosonic atoms [138, 224, 225] is very closely related to the Dicke model sketched in figure 4.4(a). This system consists of an atomic ensemble of N atoms that is placed inside a transversely driven high-finesse optical cavity. The transverse pump coherently drives the atoms with a strength η and is chosen to be far-detuned from the closest atomic transition in order to ensure low electronic excitations and suppress spontaneous photon emission. Yet, the laser frequency is nearly resonant with the cavity frequency ω_C, such that the cavity resonance detuning $\Delta_C = \omega_L - \omega_C$ is close to the cavity line width

[6] The continuous observation of the membrane position imposes a quantum back-action perturbation on its momentun. In accordance with the Heisenberg uncertainty, the randomness of this back-action accumulates to an uncertainty on the measurement of motion [218, 219], which puts a limitation on the precision of measurements.

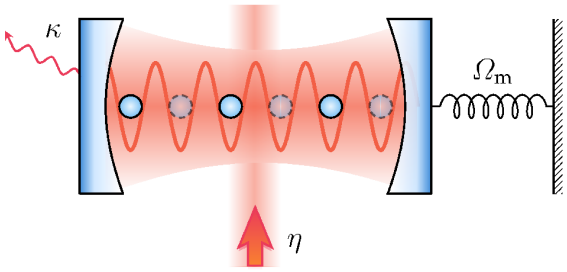

FIGURE 5.7: A Bose–Einstein condensate is trapped in an optomechanical cavity with a vibrating side-end mirror. The atomic condensate is coherently driven by a far-detuned, transverse pump laser.

$\kappa \simeq \Delta_C$. Hence, the scattering process of photons into the cavity occurs quasi-resonantly. In addition, the radiation pressure on the side-end mirrors leads to excitations of its vibrational mode with the mechanical frequency Ω_m, giving rise to an additional dissipation channel. For simplicity, let us consider only a single vibrational mode of the right-hand side mirror, while the left mirror is kept fixed. Then, a finite displacement of the vibrating mirror is associated with a shift of the cavity frequency according to

$$\omega_C' = \frac{\omega_C}{1 + (b + b^\dagger)/L\sqrt{2M\Omega_\mathrm{m}}} \simeq \omega_C - \lambda_\mathrm{m}(b + b^\dagger)\,, \tag{5.51}$$

where M is the mirror mass and L the cavity length. The effective optomechanical coupling constant $\lambda_\mathrm{m} = \omega_C/L\sqrt{2M\Omega_\mathrm{m}}$ follows by linearizing the fraction with respect to the mirror displacement. A simplified sketch of the system is presented in figure 5.7. Note that due to the similarities to the system without the vibrational degree of freedom, this system also exhibits a nonequilibrium quantum phase transition with similar characteristics as discussed in section 4.4.

In the rotating wave and electric-dipole approximation [114], the dynamics of the system in the mean field regime is determined by the set of coupled equations of motion

$$i\partial_t\beta = (\Omega_\mathrm{m} - i\Gamma_\mathrm{m})\,\beta - \sqrt{N}\lambda_\mathrm{m}|\alpha|^2\,, \tag{5.52a}$$

$$i\partial_t\alpha = \left[-\Delta_C + NU_0\int dz\,\cos^2(z)|\psi|^2 - \sqrt{N}\lambda(\beta+\beta^*) - i\kappa\right]\alpha + \sqrt{N}\eta\int dz\,\cos(z)|\psi|^2\,, \tag{5.52b}$$

$$i\partial_t\psi = \left[-\omega_R\partial_z^2 + NU_0|\alpha|^2\cos^2(z) + \sqrt{N}\eta(\alpha+\alpha^*)\cos(z) + Ng|\psi|^2\right]\psi\,, \tag{5.52c}$$

for a one-dimensional Bose gas elongated along the cavity axis. Here, we have introduced a phenomenological damping of the mechanical and cavity mode with rates Γ_m and κ, respectively. The first equation describes the motion of the membrane with the ansatz $\langle b\rangle = \sqrt{N}\beta$. Analogously to the set of equations (4.14), the second and third equation describe the motion of the cavity photon amplitude α and the atomic condensate wave function ψ in the cavity.

Due to the non-bilinear coupling between cavity amplitude α and vibrational amplitude β, i.e., $\sim \lambda_\mathrm{m}|\alpha|^2(\beta+\beta^*)$, the critical coupling rate at which the phase transition occurs is unchanged. In other words, the long-range order of the atoms happens when the driving amplitude satisfies $\eta \geq \eta_\mathrm{c}$, where η_c is given in equation (4.15). However what is affected is the amplitude of the order parameter $\Theta = \int dz\cos(z)|\psi|^2$ in the superradiant phase as

shown in [226]. In addition, it gives rise to a dynamical unstable phase at $\eta \geq \eta_c$ in the ground state phase diagram [227, 228], since the phonon-photon coupling is of parametric nature $\sim |\alpha|^2$.

In the next chapter, we will investigate the system in the motional coupling scheme. We will adiabatically eliminate the light field beyond the assumption of a deep lattice (see equation (5.25)) and then show that the system exhibits a phase transition.

CHAPTER 6

Nonequilibrium Quantum Phase Transition in the Motional Coupling Scheme

By altering the laser intensity in the atom-optomechanical hybrid quantum system, a nonequilibrium quantum phase transition occurs between a localized symmetric state and a symmetry-broken quantum many-body state with a shifted atom cloud-membrane configuration. The results presented in this chapter have been partially published in:

N. Mann, M. Reza Bakhtiari, A. Pelster, and M. Thorwart, "Nonequilibrium quantum phase transition in a hybrid atom-optomechanical system", Physical Review Letters **120**, 063605 (2018).

The effective atom-membrane coupling can be derived in various approaches. In section 5.1.2, the effective description was derived by solving the Heisenberg equations of motion for the field operators b_ω. In this chapter, we will follow an alternative way. On the basis of a quantum stochastic Schrödinger equation (QSSE) approach, an effective quantum master equation in Lindblad form for the reduced system can be derived [159, 211]. On the basis of the analytical mean-field Gross–Pitaevskii approach developed in chapter 3, we analyze the emerging equations of motion.

6.1 Adiabatic Light Field Elimination

Here, we start with the linearized Hamiltonian (5.18) in the interaction picture with respect to the free time evolution of the photon field. The operators in the interaction picture are denoted by a subscript I next to the time variable. Hence, the only operators transforming are the light field operators which have to be replaced by $b_\omega(t)_I = b_\omega e^{-i\Delta_\omega t}$. The formal solution of the Schrödinger equation for an initial state $|\psi(t_0)\rangle$ reads

$$|\psi(t)\rangle = \mathcal{T} \exp\left\{-i \int_{t_0}^{t} ds\, H_{\mathrm{msc}}^{\mathrm{lin}}(s)_I\right\} |\psi(t_0)\rangle\,, \tag{6.1}$$

where $\mathcal{T}$ is the time-ordering operator. Next, we expand this equation for small time steps δt. Up to second-order, the relevant terms read

$$|\psi(t_0+\delta t)\rangle \simeq \left\{1 - i\int_{t_0}^{t_0+\delta t} dt\, H^{\text{lin}}_{\text{msc}}(t)_I - \int_{t_0}^{t_0+\delta t} dt \int_{t_0}^{t} ds\, H^{\text{lin}}_{\text{msc}}(t)_I H^{\text{lin}}_{\text{msc}}(s)_I\right\} |\psi(t_0)\rangle\,. \quad (6.2)$$

In addition, we assume that the initial state $|\psi(t_0)\rangle$ is in a product state of the form $|\psi(t_0)\rangle = |\psi(t_0)\rangle_{\text{a+m}} \otimes |\text{vac}\rangle_{\text{l}}$, with the vacuum state of the light field $|\text{vac}\rangle_{\text{l}}$ and $|\psi(t_0)\rangle_{\text{a+m}}$ referring to a state acting on the atom-membrane subspace. In other words, we assume $b_\omega(t)_I|\psi(t_0)\rangle = 0$ and $b_\omega(t)_I b^\dagger_\omega(t')_I|\psi(t_0)\rangle = \left[b_\omega(t)_I, b^\dagger_\omega(t')_I\right]|\psi(t_0)\rangle$.

Equipped with these relations, we evaluate the terms in equation (6.2) and keep only terms up to first order in δt. Then, the second term on the right-hand side becomes

$$-i\left\{H_{\text{msc},0}\delta t + \lambda_{\text{m}}(a+a^\dagger)\delta B^\dagger(t_0) + \lambda_{\text{a}}\int dz\, \Psi^\dagger(z)\Psi(z)\delta C^\dagger(t_0,z)\right\}|\psi(t_0)\rangle\,, \quad (6.3)$$

where we have defined the noise-increment operators $\delta B(t) = B(t+\delta t) - B(t)$ and $\delta C(t,z) = C(t+\delta t,z) - C(t,z)$ with

$$B(t) = \int_{t_0}^{t} ds \int \frac{d\omega}{\sqrt{2\pi}}\, b_\omega(s)_I\,, \quad (6.4a)$$

$$C(t,z) = \int_{t_0}^{t} ds \int \frac{d\omega}{\sqrt{2\pi}}\, \sin(\omega_L z)\sin(\omega z + \Delta\phi_\omega) b_\omega(s)_I\,. \quad (6.4b)$$

Moreover, we have defined the free Hamiltonian of the reduced system $H_{\text{msc},0} = H_{\text{m}} + H_{\text{a}} + V\int dz\, \Psi^\dagger(z)\sin^2(\omega_L z)\Psi(z)$. By keeping only the terms to lowest order in the time delay δt, the third term in equation (6.2) has the only contributions

$$\begin{aligned} -i\Big\{&-\lambda(a+a^\dagger)\int dz\, \Psi^\dagger(z)\sin(2\omega_L z)\Psi(z) - i2\lambda(a+a^\dagger)\int dz\, \Psi^\dagger(z)\sin^2(\omega_L z)\Psi(z) \\ &-i\frac{\lambda_{\text{m}}^2}{2}(a+a^\dagger)^2 + \frac{\lambda_{\text{a}}^2}{4}\int dz dz'\, \Psi^\dagger(z)\Psi(z)\mathcal{G}(z,z')\Psi^\dagger(z')\Psi(z')\Big\}\delta t|\psi(t_0)\rangle\,, \end{aligned} \quad (6.5)$$

with the effective atom-membrane coupling strength $\lambda = \lambda_{\text{m}}\lambda_{\text{a}}/2$. The adiabatic elimination of the light field introduces a spatial long-range interaction in the atomic ensemble with the complex interaction potential

$$\mathcal{G}(z,z') = \sin(\omega_L z)\sin(\omega_L z')\left[\sin(\omega_L|z-z'|) - \sin(\omega_L[z+z']) - 2i\sin(\omega_L z)\sin(\omega_L z')\right]\,. \quad (6.6)$$

In the limit $\delta t \to 0$, the QSSE is found. To this extent, we assume that each time step does not depend on an earlier time step. This is equivalent to the weak-coupling assumption or Markov approximation, as we had assumed that the system state $|\psi(t)\rangle$ always factorizes. Additionally, we assume that the evolution of the reduced system happens on a much slower time scale than the travel time of the light in the system. In this case, we may neglect

retardations in the equation of motion. The QSSE in Ito form follows according to

$$\begin{aligned} d|\psi(t)\rangle = &\left\{ -iH_{\mathrm{msc}}^{\mathrm{eff}} - \frac{1}{2}\left[\lambda_{\mathrm{m}}(a+a^\dagger) + \lambda_{\mathrm{a}}\int dz\, \Psi^\dagger(z)\sin^2(\omega_L z)\Psi(z)\right]^2 \right\} dt|\psi(t)\rangle \\ &- i\left\{ \lambda_{\mathrm{m}}(a+a^\dagger)dB^\dagger(t) + \lambda_{\mathrm{a}}\int dz\, \Psi^\dagger(z)\Psi(z)dC^\dagger(t,z)\right\}|\psi(t)\rangle\,, \end{aligned} \tag{6.7}$$

where the effective Hamiltonian has been defined as

$$\begin{aligned} H_{\mathrm{msc}}^{\mathrm{eff}} =& \Omega_{\mathrm{m}} a^\dagger a + \int dz\, \Psi^\dagger(z)\left[V\sin^2(\omega_L z) - \frac{\partial_z^2}{2m} - \lambda(a+a^\dagger)\sin(2\omega_L z) + \frac{g}{2}\Psi^\dagger(z)\Psi(z)\right]\Psi(z) \\ &+ \frac{\lambda_{\mathrm{a}}^2}{4}\int dz dz'\, \mathrm{Re}[\mathcal{G}(z,z')]\Psi^\dagger(z')\Psi(z')\Psi^\dagger(z)\Psi(z)\,. \end{aligned} \tag{6.8}$$

In the same way as above, the differential noise increment operators are defined via $dB(t) = \lim_{\delta t\to 0} B(t+\delta t) - B(t)$, and likewise $dC(t,z) = \lim_{\delta t\to 0} C(t+\delta t,z) - C(t,z)$.

On a first glance, the quantum stochastic differential equation (QSDE) (6.7) seems to produce a non-unitary time evolution for the wave function. However, this is not the case, as the terms to second-order in the differential noise operators follow the Ito rules [211]

$$\begin{aligned} dB(t)dB^\dagger(t) =& dt\,, \\ dC(t,z)dC^\dagger(t,z') =& \sin^2(\omega_L z)\sin^2(\omega_L z')dt\,, \\ dB(t)dC^\dagger(t,z) = dC(t,z)dB^\dagger(t) =& \sin^2(\omega_L z)dt\,, \end{aligned} \tag{6.9}$$

while other quadratic terms are zero. In fact, it can be shown that the time evolution operator $U(t)$ for the stochastic form of the Schrödinger equation satisfies

$$U(t,t_0) = T\exp\left\{ -i\int_{t_0}^{t}\left(H_{\mathrm{msc}}^{\mathrm{eff}}ds + \lambda_{\mathrm{m}}(a+a^\dagger)[dB+dB^\dagger] + \lambda_{\mathrm{a}}\int dz\, \Psi^\dagger\Psi[dC+dC^\dagger]\right)\right\}, \tag{6.10}$$

which indeed is unitary.

6.1.1 Quantum Langevin Equation

Rather than describing the system dynamics via a QSDE of the wave function, in some cases it is more appropriate to derive the quantum Langevin equations for a closed set of operators. In the Heisenberg picture, the time evolution of an arbitrary operator O is given by $O(t) = U^\dagger(t,0)OU(t,0)$. With this, a stochastic form of the quantum Langevin equation is found according to

$$da = -i\left[a, H_{\mathrm{msc}}^{\mathrm{eff}}\right]dt - i\lambda_{\mathrm{m}}(dB+dB^\dagger)\,, \tag{6.11a}$$

$$d\Psi(z) = -i\left[\Psi(z), H_{\mathrm{msc}}^{\mathrm{eff}}\right]dt - i\lambda_{\mathrm{a}}\sin^2(\omega_L z)\Psi(z)(dB+dB^\dagger)\,. \tag{6.11b}$$

Here, we have made the replacement $dC(z) = \sin^2(\omega_L z)dB$, which is satisfying the Ito rules (6.9) and complies with the nature of the stochastic force. Note that the additional

field operator $\Psi(z)$ in front of the stochastic term is needed to conserve the particle number. Moreover, the last term in (6.11b) describes fluctuations of the lattice potential depth, which can lead to excitations of the atoms to higher motional bands in the optical lattice.

By interpreting the terms $(dB + dB^\dagger)$ as white noise operators, we arrive at the quantum Langevin equations

$$i\partial_t a = \left[a, H_{\text{msc}}^{\text{eff}}\right] - \lambda_{\text{m}}\xi_{\text{l}}\,, \tag{6.12a}$$

$$i\partial_t \Psi(z) = \left[\Psi(z), H_{\text{msc}}^{\text{eff}}\right] - \lambda_{\text{a}}\sin^2(\omega_L z)\Psi(z)\xi_{\text{l}}\,, \tag{6.12b}$$

where the quantum Langevin equation for the membrane mode is in accordance with equation (5.25a). The autocorrelation function of the field fluctuations satisfies $\langle\xi_{\text{l}}(t)\xi_{\text{l}}(s)\rangle = \delta(t-s)$.

6.1.2 Master Equation

While the practicality of the QSSE is that it only involves the time evolution of the wave function, without loss of the light field fluctuations and the effective atom-membrane coupling, it comes with a disadvantage. Without question, it is numerically advantageous to evolve only a wave function in time. However, due to the stochastic description, the time evolution has to be done over and over again until the result is satisfyingly converged. On the other hand, the QSSE also provides the appropriate quantum master equation in Lindblad form for the reduced density operator. Assuming that we start in the pure state $|\psi(t)\rangle$, we can define the stochastic density operator $W(t) = |\psi(t)\rangle\langle\psi(t)|$ and the equation of motion is found via the three contributions

$$dW(t) = d|\psi(t)\rangle\langle\psi(t)| + |\psi(t)\rangle d\langle\psi(t)| + d|\psi(t)\rangle d\langle\psi(t)|\,. \tag{6.13}$$

If we now average over the light field degrees of freedom, we can derive the master equation for the reduced density operator $\rho(t) = \text{Tr}_{\text{l}}W(t)$, which is no longer stochastic. By using the relations of equation (6.9), we find the master equation

$$\partial_t\rho = i\left[\rho, H_{\text{msc}}^{\text{eff}}\right] + \sum_{ij=\text{a,m}}\left[L_i\rho L_j^\dagger - \frac{1}{2}\left\{L_i^\dagger L_j, \rho\right\}\right], \tag{6.14}$$

with the Lindblad operators

$$L_{\text{a}} = \lambda_{\text{a}}\int dz\,\Psi^\dagger(z)\sin^2(\omega_L z)\Psi(z)\,, \tag{6.15a}$$

$$L_{\text{m}} = \lambda_{\text{m}}(a + a^\dagger)\,. \tag{6.15b}$$

6.2 Nonequilibrium Quantum Phase Transition

By the scaling of the space coordinate $z \to z/\omega_L$, the equations of motion can be written in the compact form

$$i\partial_t a = [\Omega_\mathrm{m} - i\Gamma_\mathrm{m}]\, a - \lambda \int dz\, \Psi^\dagger(z) \sin(2z) \Psi(z) - \lambda_\mathrm{m}\xi_\mathrm{l} + i\xi_\mathrm{th}\,, \tag{6.16a}$$

$$i\partial_t \Psi = \left[V \sin^2(z) - \omega_R \partial_z^2 + g\Psi^\dagger\Psi - \lambda(a + a^\dagger)\sin(2z)\right]\Psi - \lambda_\mathrm{a} \sin^2(z)\Psi\xi_\mathrm{l}\,, \tag{6.16b}$$

where we have introduced a thermal damping of the membrane with damping rate Γ_m and the bosonic thermal noise operator ξ_th. For the thermal noise operator, we assume that it satisfies the autocorrelation functions $\langle \xi_\mathrm{th}(t)\xi_\mathrm{th}^\dagger(s)\rangle = 2\Gamma_\mathrm{m}\delta(t-s)$ and $\langle \xi_\mathrm{th}^\dagger(t)\xi_\mathrm{th}(s)\rangle = \langle \xi_\mathrm{th}(t)\xi_\mathrm{th}(s)\rangle = \langle \xi_\mathrm{th}^\dagger(t)\xi_\mathrm{th}^\dagger(s)\rangle = 0$, corresponding to zero temperature noise. Moreover, we have assumed a large detuning Δ such that the long-range interaction potential induced by the photon field can be neglected.

6.2.1 The Extended Gross–Pitaevskii Equation

In the condensate regime, a large fraction of the atoms occupy the ground state. By considering weakly interacting atoms which, in addition, are only weakly coupled to the vibrational oscillator, the quantum Langevin equations (6.12) can be drastically simplified. In other words, when $g, \lambda \ll \Omega_\mathrm{m}, \omega_R$, the field operators $\Psi(z)$ can be approximated by a complex function $\psi(z)$ according to $\Psi(z) \simeq \sqrt{N}\psi(z)$, with the number of atoms N. In the same manner, the membrane operator a can be replaced by its mean value $\langle a\rangle = \sqrt{N}\alpha$. In this limit, the system dynamics is determined by two coupled differential equations, the extended Gross–Pitaevskii equation (GPE),

$$i\partial_t \alpha = [\Omega_\mathrm{m} - i\Gamma_\mathrm{m}]\,\alpha - \sqrt{N}\lambda \int dz\, \sin(2z)|\psi|^2\,, \tag{6.17a}$$

$$i\partial_t \psi = \left[V\sin^2(z) - \omega_R\partial_z^2 + Ng|\psi|^2 - \sqrt{N}\lambda(\alpha + \alpha^*)\sin(2z)\right]\psi\,. \tag{6.17b}$$

We observe that the condensate equation of motion exhibits a π-periodicity in space. This fact will also be reflected in the condensate wave function, such that $\psi(t, z+\pi) = \psi(t,z)$. Hence, we can restrict ourselves to the space interval $[-\pi/2, \pi/2]$ and use periodic boundary conditions[1].

The set of equations is very similar in structure to that of equations (4.14) for a BEC in an optical cavity with transversal pumping. There, the competition between the kinetic energy of the atomic ensemble and the energy of the cavity field lead to a nonequilibrium quantum phase transition from a non-localized, translational invariant condensate state to a self-organized state [113]. From the equations (6.17), we see a similar competition. Here, the two potential contributions $V\sin^2(z)$ and $\sqrt{N}\lambda(\alpha+\alpha^*)\sin(2z)$ can dynamically compete with each other. This competition depends on the back-action of the membrane on the atoms

[1] In order to numerically evaluate the steady-state solution of the combined equations of motion, we use a Crank–Nicolson scheme in imaginary time. For details about this scheme see the appendix C.

and consequently on the collective behavior of the atoms. Eventually, this may lead to the formation of two different stable phases, one with $\alpha = 0$ and the other with $\alpha \neq 0$.

Due to the damping of the membrane, the combined system will eventually relax to a steady state. This state is characterized by the membrane amplitude α_0 and the condensate function $\psi(t,z) = e^{-i\mu t}\psi_0(z)$, with the chemical potential μ. By using equations (6.17), the steady state satisfies

$$\alpha_0 = \frac{\sqrt{N}\lambda}{\Omega_\mathrm{m} - i\Gamma_\mathrm{m}} \int dz\, \sin(2z){\psi_0}^2\,, \tag{6.18a}$$

$$\mu\psi_0 = \left[V\sin^2(z) - \omega_R\partial_z^2 + Ng\psi_0^2 - \sqrt{N}\lambda(\alpha_0 + \alpha_0^*)\sin(2z)\right]\psi_0\,, \tag{6.18b}$$

where we have chosen ψ_0 to be real without loss of generality.

The dynamical competition of the potential terms is included in the steady state behavior. In order to gain further insight and quantify the steady state, we consider the deep optical lattice regime, i.e., $V \gg \omega_R, Ng$. In this limit, the condensate wave function is very closely centered around each lattice minimum and the sine functions can be expanded to lowest order in the position variable z. From the equation (6.18a), the relation $\alpha_0 = 2\sqrt{N}\lambda z_0/(\Omega_\mathrm{m} - i\Gamma_\mathrm{m})$ is found, where $z_0 = \int dz\, z\psi_0^2$ is the center-of-mass position of the condensate. On the other hand, the center-of-mass position according to equation (6.18b) satisfies $z_0 = \sqrt{N}\lambda(\alpha_0 + \alpha_0^*)/V$[2]. By comparison of these two relations, we see that below the atom-membrane coupling constant

$$\sqrt{N}\lambda_V = \sqrt{\frac{V}{4}}\sqrt{\Omega_\mathrm{m} + \frac{\Gamma_\mathrm{m}^2}{\Omega_\mathrm{m}}}\,, \tag{6.19}$$

the only possible solutions is $z_0 = \alpha_0 = 0$, whereas the relation with $z_0, \alpha_0 \neq 0$ is only satisfied at $\lambda = \lambda_V$. Eventually, the expansion of the sine to lowest order in z breaks down above this coupling rate, being a first indicator for the presence of a nonequilibrium quantum phase transition which is manifested in an abrupt change of the steady state.

On the other hand, in the zero potential limit, i.e., $V = 0$, the condensate wave function at zero atom-membrane coupling is translational invariant. For a finite atom-membrane coupling, this translational invariance is broken and the condensate profile adopts the shape of the coupling potential $\sin(2z)$. Hence, we make the ansatz [113]

$$\psi_0(z) = \pi^{-1/2}\left[1 + \epsilon\sin(2z)\right]\,, \tag{6.20}$$

and find $\alpha_0 = \sqrt{N}\lambda\epsilon/(\Omega_\mathrm{m} - i\Gamma_\mathrm{m})$. This ansatz is inserted in equation (6.17b) and one evolution step in imaginary time is carried out to find

$$\frac{\delta\psi}{\delta\tau} = -\frac{Ng}{\pi}\pi^{-1/2} - \left[4\omega_R + \frac{3Ng}{\pi} - 2N\lambda^2\frac{\Omega_\mathrm{m}}{\Omega_\mathrm{m}^2 + \Gamma_\mathrm{m}^2}\right]\pi^{-1/2}\epsilon\sin(2z)\,. \tag{6.21}$$

[2]This relation is found via the expansion of the potential terms in the GPE (6.18b) according to $V\sin^2(z) - \sqrt{N}\lambda(\alpha_0 + \alpha_0^*)\sin(2z) \simeq Vz^2 - 2\sqrt{N}\lambda(\alpha_0 + \alpha_0^*)z = V(z - z_0)^2 - Vz_0^2$.

The first and the remaining terms produce decays with different rates. Equating these two rates allows us to find the critical coupling rate at which both decay rates are identical. This happens when

$$\sqrt{N}\lambda_{\text{free}} = \sqrt{2\omega_R + \frac{Ng}{\pi}}\sqrt{\Omega_{\text{m}} + \frac{\Gamma_{\text{m}}^2}{\Omega_{\text{m}}}}\,, \tag{6.22}$$

and the homogeneous mode function $1/\sqrt{\pi}$ of (6.20) decays faster than the $\epsilon\sin(2z)/\sqrt{\pi}$ mode function if $\sqrt{N}\lambda > \sqrt{N}\lambda_{\text{free}}$. In order to verify this behavior, we numerically calculate the steady state as a function of the atom-membrane coupling strength $\sqrt{N}\lambda$. In figure 6.1(a), we show the stationary membrane displacement $\text{Re}(\alpha_0)$ as a function of the atom-membrane coupling strength $\sqrt{N}\lambda$ for different lattice depths V. Here, the membrane displacement can act as an order parameter equivalent to the center-of-mass position of the atomic ensemble. It shows that below a certain atom-membrane coupling, the membrane displacement vanishes and the atomic condensate is located symmetrically around the lattice site at $z = 0$. Tuning the coupling strength above this critical coupling, the stationary membrane displacement takes one of two possible states with either $\text{Re}(\alpha_0) > 0$ or $\text{Re}(\alpha_0) < 0$. This spontaneous symmetry-breaking is a second indicator for a phase transition. Eventually, it goes over into a linear proportionality $|\alpha_0| \sim \sqrt{N}\lambda$. In the linear region, the atom gas is located around newly formed lattice sites by the $\sin(2z)$ potential at $z = \pm\pi/2$, corresponding to either the positive or negative branch of the membrane displacement.

From the value at which the symmetry-breaking in figure 6.1(a) occurs, we extract the critical coupling rate $\sqrt{N}\lambda_c$ and compare it to the analytical results of the critical coupling rate. This comparison is shown in figure 6.1(b) as a function of the lattice depth for a non-interacting ($Ng = 0$) and a strongly interacting ($Ng = 100\,\omega_R$) condensate in black and blue, respectively. In both cases, the offset at $V = 0$ is very well described by equation (6.22) as indicated by the dashed horizontal lines. The behavior in the deep lattice limit is well approximated by the green dashed line resulting from equation (6.19).

Examples of the condensate wave function are given in figure 6.2 for non-interacting atoms ($g = 0$). Considering an optical lattice depth of $V = 200\,\omega_R$, the shape is very well described by a Gaussian profile. At zero coupling (blue, solid), the atoms are centered around the equilibrium position of the optical potential $V\sin^2(z)$. For the coupling rate $\sqrt{N}\lambda = 0.85\,\Omega_{\text{m}}$, which is above the threshold $\sqrt{N}\lambda_{\text{c}}$, the atomic equilibrium position is shifted to the position $z = \tan^{-1}(2\sqrt{N}\lambda(\alpha_0 + \alpha_0^*)/V)$. Due to the twofold degenerate steady state, the atomic equilibrium position is either shifted to positive values (solid, green) or negative values (dashed, green).

In the following, we perform a rigorous analysis of the problem. By adapting the appropriate shape of the condensate profile to the present potential, the equations of motion can be drastically simplified. In figure 6.2, it has been shown that the wave function can be very well described by a single Gaussian with variable width and center-of-mass position, although the potential is given by a sum of trigonometric functions. In doing so, the partial differential equations (6.17) can be reduced to a rather simple set of coupled differential equations. We adapt the mean-field language of chapter 3 to this problem by including an additional variational parameter.

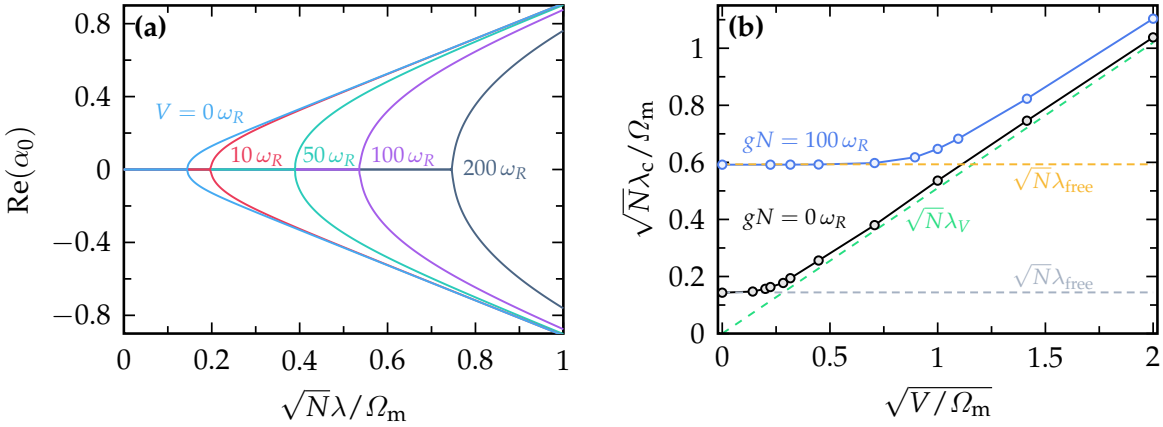

FIGURE 6.1: (a) The stationary value of the membrane displacement $\mathrm{Re}(\alpha_0)$ is shown as a function of the coupling rate $\sqrt{N}\lambda$ for a non-interacting condensate ($Ng = 0$). Curves with different colors correspond to the different lattice depths V which are indicated in the panel. (b) The critical coupling rate $\sqrt{N}\lambda_\mathrm{c}$ is extracted from (a) and shown as a function of the lattice depth V. Analogously, the critical coupling rate is estimated for an interacting condensate with $Ng = 100\,\omega_R$. The offset at $V = 0$ is very well reproduced by the free condensate limit of equation (6.22), indicated by the dashed horizontal lines. The green dashed line shows the critical coupling rate in the deep optical potential limit of equation (6.19). In both panels, we have used the membrane parameters $\Omega_\mathrm{m} = 100\,\omega_R$ and $\Gamma_\mathrm{m} = 20\,\omega_R$.

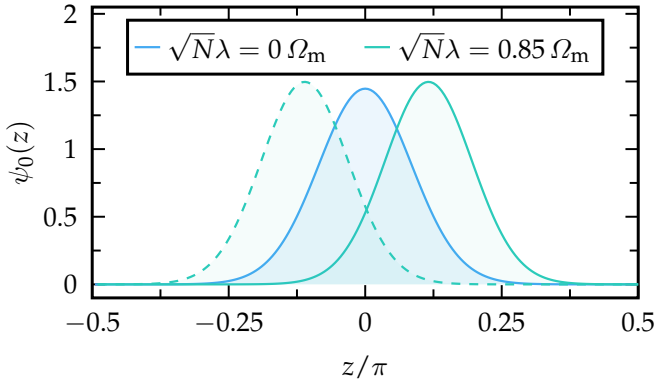

FIGURE 6.2: The condensate wave function is shown for two different atom-membrane coupling strength. Below the splitting point $\sqrt{N}\lambda_\mathrm{c}$, the atoms are symmetrically distributed around $z = 0$, while the atoms are located around either $z < 0$ (dashed) or $z > 0$ (solid) above the critical point for $\sqrt{N}\lambda = 0.85\,\Omega_\mathrm{m}$. The other parameters used are $V = 200\,\omega_R$, $g = 0$, $\Omega_\mathrm{m} = 100\,\omega_R$ and $\Gamma_\mathrm{m} = 20\,\omega_R$.

6.2.2 Cumulant Expansion of the Equation of Motion

In a rather deep optical lattice, i.e., $V \gg \omega_R$, the condensate profile is well described by a sum of Gaussian functions residing in the individual lattice wells. When the overlap of the wave function between neighboring sites is considerably small, the problem effectively reduces to a single site problem. In this regime, we describe the condensate profile by a single Gaussian

$$\psi(t,z) = \left(\frac{1}{\pi\sigma(t)^2}\right)^{1/4} \exp\left(-\frac{[z-\zeta(t)]^2}{2\sigma(t)^2} + i\kappa(t)z + i\eta(t)z^2\right), \tag{6.23}$$

with real, time-dependent variational parameters that include the condensate width $\sigma(t)$ and the center-of-mass position $\zeta(t)$. Moreover, we include a space- and time-dependent phase in the form $\kappa(t)z + \eta(t)z^2$. This is essential, as otherwise the condensate profile would be real-valued and no dynamical behavior would be obtained. For an accurate description, we consider lattice depths $V \gtrsim 10\,\omega_R$ and weak atomic interactions $Ng \ll V$.

In order to find the equations of motion for the variational parameters, we determine the lowest cumulants of the condensate probability distribution, whose dynamics is described by the extended GPE (6.17). Hence, by multiplying equation (6.17b) by $\psi^*(t,z)[z-\zeta(t)]$ and integrating over the space coordinate z, we find for the left-hand side (LHS)

$$\int dz\, \psi^*(t,z)[z-\zeta] \times [\,\text{LHS of (6.17b)}\,] = i\frac{\dot\zeta}{2} - \frac{\sigma^2}{2}(\dot\kappa + 2\dot\eta\zeta)\,, \tag{6.24}$$

and the right-hand side (RHS)

$$\begin{aligned}\int dz\, \psi^*(t,z)[z-\zeta] \times [\,\text{RHS of (6.17b)}\,] =& \omega_R(\kappa+2\eta\zeta)(i+2\eta\sigma^2) + \frac{V}{2}\sin(2\zeta)\sigma^2 e^{-\sigma^2} \\ &- \sqrt{N}\lambda(\alpha+\alpha^*)\cos(2\zeta)\sigma^2 e^{-\sigma^2}\,.\end{aligned} \tag{6.25}$$

In addition, we calculate the second cumulant by multiplying by $\psi^*(t,z)[\{z-\zeta(t)\}^2 - \sigma(t)^2/2]$ and integrating over z to find

$$\begin{aligned}i\frac{\sigma\dot\sigma}{2} - \frac{\dot\eta\sigma^4}{4} =& \omega_R\left[2\eta^2\sigma^4 - \frac{1}{2} + 2i\eta\sigma^2\right] + \frac{V}{2}\cos(2\zeta)\sigma^4 e^{-\sigma^2} - \frac{Ng\sigma}{4\sqrt{2\pi}} \\ &+ \sqrt{N}\lambda(\alpha+\alpha^*)\sin(2\zeta)\sigma^4 e^{-\sigma^2}\,.\end{aligned} \tag{6.26}$$

The imaginary part of the two cumulants yield the relations $\dot\zeta = 2\omega_R(\kappa+2\eta\zeta)$ and $\dot\sigma = 4\omega_R\eta\sigma$, which allows us to eliminate the auxiliary phases η and κ. With these, we find the equations of motion for the membrane amplitude α, the center-of-mass position ζ of the condensate and the condensate width σ in the compact form

$$\dot\alpha = -i\partial_{\alpha^*}E - \Gamma_\mathrm{m}\alpha\,, \tag{6.27a}$$

$$(2\omega_R)^{-1}\ddot\zeta = -\partial_\zeta E\,, \tag{6.27b}$$

$$(4\omega_R)^{-1}\ddot\sigma = -\partial_\sigma E\,, \tag{6.27c}$$

by defining the effective potential energy

$$E[\alpha,\mathcal{S},\sigma] = \Omega_{\mathrm{m}}|\alpha|^2 + \frac{\omega_R}{2\sigma^2} + \frac{Ng}{\sqrt{8\pi}\sigma} - \frac{V}{2}\sqrt{1-\mathcal{S}^2}e^{-\sigma^2} - \sqrt{N}\lambda(\alpha+\alpha^*)\mathcal{S}e^{-\sigma^2}\,. \tag{6.28}$$

Most importantly, we have defined the order parameter $\mathcal{S} = \sin(2\zeta)$ of the NQPT that is a different measure for the center-of-mass position of the atomic ensemble.

6.2.3 Quantum Phase Transition in the Mean-Field Regime

The steady-state value of the membrane is found by setting the corresponding time derivative to zero, such that we find $\alpha_0 = \sqrt{N}\lambda\mathcal{S}e^{-\sigma^2}/(\Omega_{\mathrm{m}} - i\Gamma_{\mathrm{m}})$. By inserting this expression in the potential energy E to solely express the energy functional as a function of the condensate parameters σ and $\mathcal{S}$. Then, the steady-state values of these two parameters are given by those values that globally minimize the energy functional[3]. Hence, to find the steady-state values, we have to solve the coupled equations

$$\sqrt{1-\mathcal{S}_0^2}\left[\omega_R + \frac{Ng}{\sqrt{8\pi}}\sigma_0\right] = V\sigma_0^4 e^{-\sigma_0^2}\,, \tag{6.29a}$$

$$\mathcal{S}_0\left[N\lambda^2\sqrt{1-\mathcal{S}_0^2} - N\lambda_V^2 e^{\sigma_0^2}\right] = 0\,. \tag{6.29b}$$

The second equation (6.29b) is solved by three possible values for the order parameter that are either

$$\mathcal{S}_0 = 0 \quad \text{or} \quad \mathcal{S}_0 = \pm\sqrt{1-(\lambda_V/\lambda)^4 e^{2\sigma_0^2}}\,. \tag{6.30}$$

The displaced solution $\mathcal{S}_0 \neq 0$ is imaginary for $\lambda \lesssim \lambda_V$ and the only physical solution which minimizes the energy functional $E[\alpha_0,\mathcal{S},\sigma]$ is $\mathcal{S}_0 = 0$. By increasing the atom-membrane coupling to $\lambda \gtrsim \lambda_V$, the displaced solution becomes real and the initial global minimum at $\mathcal{S}_0 = 0$ turns into a local maximum, which can be shown by a Landau expansion of the effective nonequilibrium energy functional, see equation (6.35b).

In order to gain a more profound understanding of the role of increasing the atom-membrane coupling strength λ, we expand the potential energy surface as a function of one of the variational parameters. For instance, the potential energy $E(\sigma) \equiv E[\alpha_0(\sigma),\mathcal{S}_0(\sigma),\sigma]$ exhibits only a single minimum for $\sigma > 0$. Via the normalized potential energy

$$\mathcal{E}(\sigma) = \frac{E(\sigma) - E(\sigma_0)}{\max_{\bar{\sigma}}\{E(\bar{\sigma}) - E(\sigma_0)\}}\,, \tag{6.31}$$

we show this behavior in figure 6.3(a) as a function of the condensate width σ and the atom-membrane coupling rate $\sqrt{N}\lambda$ for $V = 50\,\omega_R$, $Ng = 0$. The dashed curve marks the configuration of minimal potential energy $\mathcal{E}(\sigma_0) = 0$. Below the critical coupling rate λ_{c}, the

[3] We note that by directly minimizing the energy functional $E[\alpha,\mathcal{S},\sigma]$ of equation (6.28) with respect to α, $\mathcal{S}$, and σ, a different result will be found as the nonequilibrium condition is not included. In fact, this procedure will evaluate the ground state phases.

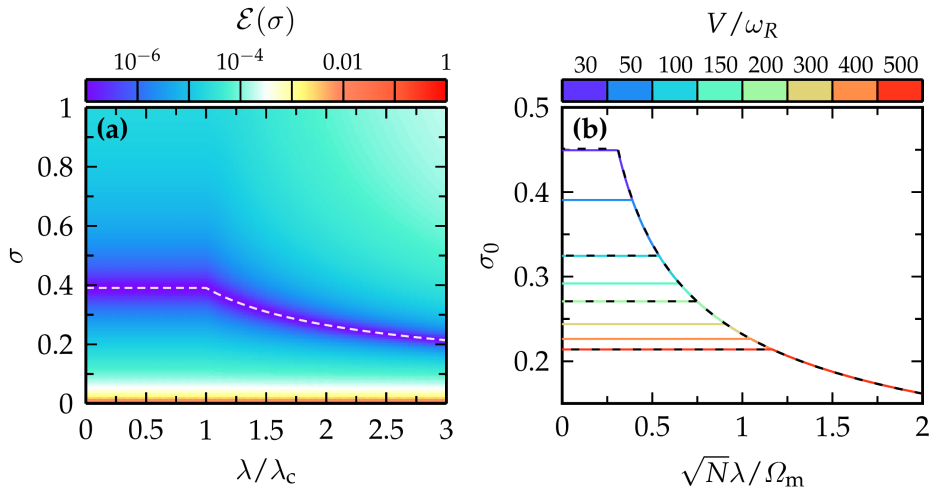

FIGURE 6.3: (a) Scaled energy potential as a function of the condensate width σ and the atom-membrane coupling λ for non-interacting atoms with $V = 50\,\omega_R$. For a fixed λ, the energy potential exhibits a global minimum which defines the steady state value σ_0 as indicated by the dashed curve. (b) Stationary condensate width σ_0 as a function of the coupling strength for various potential depths V, as indicated by the color bar. Other parameters used are $\Omega_m = 100\,\omega_R$, $\Gamma_m = 20\,\omega_R$ and $g = 0$.

stationary width σ_0 is constant, whereas it decreases to a good approximation as $\sim 1/\sqrt{\lambda}$ above λ_c.

Moreover, figure 6.3(b) shows the stationary condensate width σ_0 for various values of the potential depth V, which are indicated by the color bar. Here, the solid curves show the variational result of the cumulant expansion, whereas the dashed curves show the steady state width σ_0 calculated using the GPE (6.17) in imaginary time for four corresponding cases of V. Both results are in good agreement with each other, which validates the Gaussian ansatz[4]. The constant plateau is determined by equation (6.29a) with $\mathcal{S}_0 = 0$ and for non-interacting atoms approximately given by $\sigma_0 \simeq (\omega_R/V)^{1/4}$.

On the other hand, the normalized energy surface as a function of the order parameter $\mathcal{S}$ has either one stable state or two stable solutions. This is visualized by plotting $\mathcal{E}(\mathcal{S})$ as a function of the order parameter $\mathcal{S}$ and the atom-membrane coupling in figure 6.4(a). Again, the dashed curve indicates the configuration $\mathcal{S}_0$ at which the potential is minimized. For smaller values $\lambda \leq \lambda_c$, the energy potential surface forms a single potential well around $\mathcal{S} = 0$, whereas for $\lambda > \lambda_c$, it becomes a double well potential with a local maximum at $\mathcal{S} = 0$.

In addition, we show the stationary value of the order parameter $\mathcal{S}_0$ for different potential depths V. The variational results (solid curves) are consistent with the full numerical results (dashed curves). For small values of the atom-membrane coupling, the atomic condensate is symmetrically located around the lattice minima at $\zeta_0 = j\pi$, $j \in \mathbb{Z}$. Consequently, the order parameter $\mathcal{S}_0$ vanishes and the membrane amplitude α_0 equals zero. Then, the

[4] A comparison of the computational time consumption shows that the estimation via the analytical approach is of the order of seconds, while it is of the order of minutes for the estimation via the imaginary time evolution with the GPE.

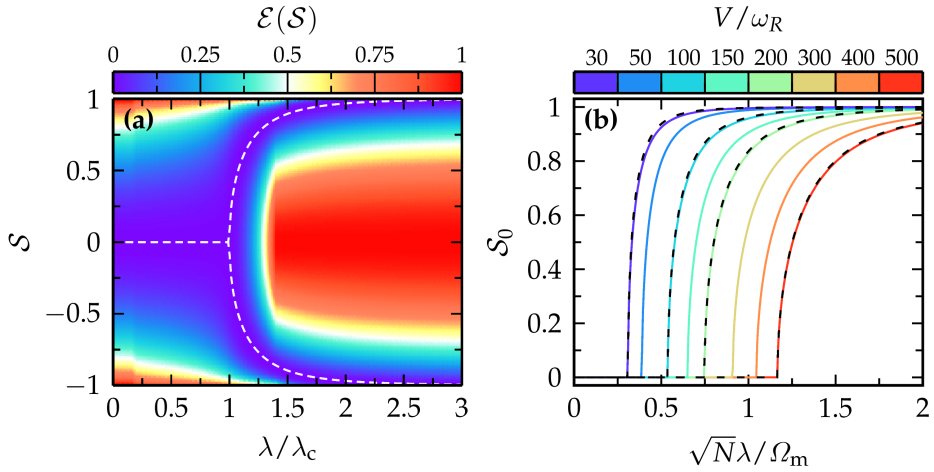

FIGURE 6.4: (a) Scaled energy potential as a function of the order parameter $\mathcal{S}$ and the atom-membrane coupling λ for non-interacting atoms with $V = 50\,\omega_R$. Below the critical coupling strength the potential surface exhibits a single minimum at $\mathcal{S} = 0$. At $\lambda = \lambda_c$, this minimum turns into a maximum and two new minima are formed at $\mathcal{S} \neq 0$. (b) Stationary value of the order parameter $\mathcal{S}_0$ as a function of the coupling strength for various potential depths V, as indicated by the color bar. Here, only the positive solution $\mathcal{S}_0 \geq 0$ is shown. Other parameters used are $\Omega_m = 100\,\omega_R$, $\Gamma_m = 20\,\omega_R$ and $g = 0$.

NQPT occurs at the critical coupling λ_c, which follows from solving the implicit equation[5]

$$\omega_R + \frac{Ng}{\sqrt{8\pi}}\sqrt{2\log\frac{\lambda_c}{\lambda_V}} = 4V\left(\frac{\lambda_V}{\lambda_c}\log\frac{\lambda_c}{\lambda_V}\right)^2 . \tag{6.32}$$

Above the critical coupling strength λ_c, the atoms begin to move away from their equilibrium positions $\zeta_0 = j\pi$ to the displaced lattice minima. In the vicinity of the phase transition, the order parameter is given by the expression $\mathcal{S}_0 \simeq \pm\theta(\lambda - \lambda_c)\sqrt{1-(\lambda_c/\lambda)^4}$. By expanding the order parameter around $\lambda = \lambda_c(1+\epsilon)$, we observe that it follows the universal scaling law $\mathcal{S}_0 = 2\epsilon^{1/2}$ with the critical exponent $\beta = 1/2$, which is the characteristic signature of the mean-field phase transition. By plotting the order parameter $\mathcal{S}_0$ as a function of ϵ, the different configurations collapse to a single curve, see figure 6.5. In accordance with an expansion of the energy surface with respect to the order parameter, all these observables show that the hybrid system undergoes a second-order nonequilibrium quantum phase transition.

In order to verify that the phase transition is always continuous, we do a Landau expansion of the energy functional around $\mathcal{S} = 0$, where

$$E[\mathcal{S}] = \frac{\omega_R}{2\sigma_0^2} + \frac{Ng}{\sqrt{8\pi}\sigma_0} - \frac{V}{2}\sqrt{1-\mathcal{S}^2}e^{-\sigma_0^2} - \frac{V}{4}\left(\frac{\lambda}{\lambda_V}\right)^2\mathcal{S}^2 e^{-2\sigma_0^2}, \tag{6.33}$$

[5]This equation is found by setting the bracket in equation (6.29b) to zero for $\mathcal{S}_0 = 0$. Hence, the solution for σ_0 can be inserted in equation (6.29a) to find the defining equation for λ_c.

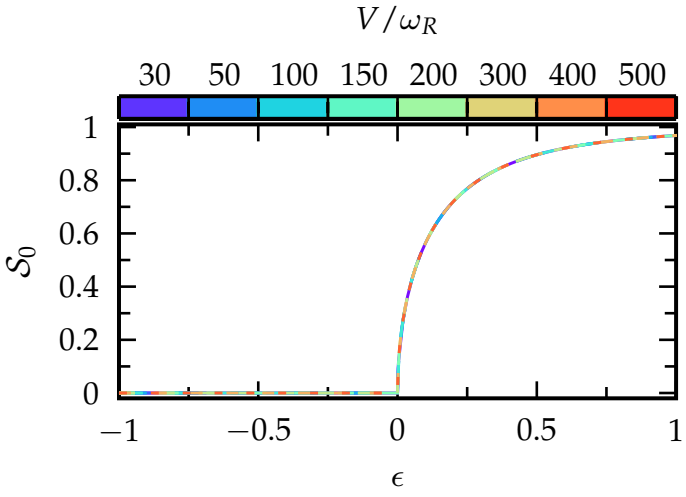

FIGURE 6.5: Universal behavior of the order parameter in the vicinity of the phase transition for various potential depths. Other parameters used are $Ng = 0$, $\Omega_\mathrm{m} = 100\,\omega_R$ and $\Gamma_\mathrm{m} = 20\,\omega_R$.

and $\sigma_0 \equiv \sigma_0(\mathcal{S})$ is a function of the order parameter. It is implicitly determined via the surface $F[\sigma_0, \mathcal{S}] = 0$. With the functional

$$F[\sigma, \mathcal{S}] = V\sqrt{1-\mathcal{S}^2}e^{-\sigma^2}\sigma + V\left(\frac{\lambda}{\lambda_V}\right)^2 \mathcal{S}^2 e^{-2\sigma^2}\sigma - \frac{\omega_R}{\sigma^3} - \frac{Ng}{\sqrt{8\pi}\sigma^2}\,. \tag{6.34}$$

Since the energy functional $E[\mathcal{S}]$ is symmetric in the order parameter $\mathcal{S}$, i.e., $E[-\mathcal{S}] = E[\mathcal{S}]$, the Landau expansion takes the form of equation (4.9) with $E[\mathcal{S}] = \sum_n a_{2n}\mathcal{S}^{2n}$. Up to fourth order, the Landau coefficients are given by

$$a_0 = \frac{\omega_R}{2\sigma_0^2} - \frac{V}{2}e^{-\sigma_0} + \frac{Ng}{\sqrt{8\pi}\sigma_0}\,, \tag{6.35a}$$

$$a_2 = \frac{V}{4}\left[1 - \left(\frac{\lambda}{\lambda_\mathrm{c}}\right)^2\right] e^{-\sigma_0^2}\,, \tag{6.35b}$$

$$a_4 = \frac{V}{16}\left[1 - 2\left(1 - 2\frac{\lambda^2}{\lambda_\mathrm{c}^2}\right)\sigma_0\sigma_0''\right] e^{-\sigma_0^2}\,. \tag{6.35c}$$

The derivative $\sigma_0'' = \partial_\mathcal{S}^2\sigma_0$ is implicitly defined via the functional $F[\sigma, \mathcal{S}]$. With the theorem of implicit functions, the first derivative follows $\sigma_0' = -(\partial_\mathcal{S}F)/(\partial_\sigma F)|_{\mathcal{S}=0,\sigma=\sigma_0} = 0$, whereas the second derivative is given by

$$\sigma_0'' = \left(\frac{\omega_\zeta}{\omega_\sigma}\right)^2 \left(1 - 2\frac{\lambda^2}{\lambda_\mathrm{c}^2}\right)\sigma_0\,. \tag{6.36}$$

Here, we have defined the frequency of the breathing mode of the atomic condensate

$$\omega_\sigma^2|_{\mathcal{S}=0} = 4\omega_R\left[\frac{3\omega_R}{\sigma_0^4} + V(1-2\sigma_0^2)e^{-\sigma_0^2} + \frac{Ng}{\sqrt{2\pi}\sigma_0^3}\right]\,, \tag{6.37}$$

and the harmonic excitation frequency in the lattice potential

$$\omega_\zeta^2|_{\mathcal{S}=0} = 4\omega_R V e^{-\sigma_0^2}\,. \tag{6.38}$$

This expression is consistent with the atomic frequency Ω_a defined in section 5.1.2. Here, the additional exponential factor includes effects of the finite elongation of the condensate in the sine trap potential.

Under the assumption that $a_4 > 0$, the second-order Landau coefficient $a_2 = 0$ defines the point of the continuous phase transition. In accordance with the prior discussion, this happens when $\lambda = \lambda_\mathrm{c}$. On the other hand, a first-order phase transition may occur if $a_4 < 0$. In this case, the Landau expansion to fourth order is no longer sufficient and higher orders have to be included. However, for our purpose, it is adequate to state that only if $a_2 = a_4 = 0$, the order of the phase transition (PT) can change from continuous to discontinuous. Hence, we look at the expression in the brackets of a_4 in equation (6.35c) for $\lambda = \lambda_\mathrm{c}$ which results in the relation

$$1 - 2\left(\frac{\omega_\zeta}{\omega_\sigma}\right)^2 \sigma_0^2 = 0 \quad \Leftrightarrow \quad \left(\frac{\omega_\zeta}{\omega_\sigma}\right)^2 = \frac{1}{2\sigma_0^2}\,. \tag{6.39}$$

For a strongly confined condensate with $\sigma_0 \ll 1$, the harmonic excitation frequency ω_ζ has to be much larger than the breathing mode frequency ω_σ, in order to fulfill the equality. Therefore, the effective potential given by the term in the brackets of equation (6.37) would have to become smaller than the actual lattice potential depth V. This, however, is not possible. Indeed, we have estimated for the Bose–Hubbard model with a harmonic trap potential that the breathing mode frequency ranges from $\omega_\sigma^2 \simeq 16\omega_R V$ (non-interacting limit[6]) to $\omega_\sigma^2 \simeq 12\omega_R V$ (Thomas-Fermi limit[7]), see also equation (3.9) and figure 3.2 for the replacement $J \leftrightarrow \omega_R$. Hence, the frequency ω_σ is always larger than the frequency of the displacement mode $\omega_\zeta \simeq \sqrt{4\omega_R V}$. Consequently, we can conclude that the NQPT is always continuous within the validity area of the analytical Gaussian ansatz.

6.2.4 Collective Excitation Spectrum and Ground State Entanglement

Solving the complete set of equations of motion (6.27), or even the extended GPE (6.17), is a challenging task, however, their linearized forms already provide insight into the collective behavior of the system. In order to determine the collective excitation frequencies and decay rates, we follow two different approaches. First, the spectrum of the collective excitations is evaluated within the cumulant expansion and, second, by considering small deviations from the steady state in the extended Gross–Pitaevskii equation (a third approach will be discussed in section 6.3).

6.2.4.1 Analytical Expressions of the Low-Energy Collective Spectrum

Here, we consider deviations from the stationary state $(\alpha_0, \zeta_0, \sigma_0)$ in the form of $\alpha(t) = \alpha_0 + \delta\alpha(t)$, $\zeta(t) = \zeta_0 + \sqrt{\omega_R/\omega_\zeta}[\delta\zeta(t) + \delta\zeta^*(t)]$ and $\sigma(t) = \sigma_0 + \sqrt{2\omega_R/\omega_\sigma}[\delta\sigma(t) + \delta\sigma^*(t)]$.

[6] In the deep lattice limit, the condensate width is given by $\sigma_0^4 \simeq \omega_R/V$, which results in $\omega_\sigma^2 \simeq 16\omega_R V$, when higher orders in the condensate width are neglected.

[7] In the Thomas-Fermi limit, the kinetic term is neglected and the condensate width is approximated by $\sigma_0^3 \simeq Ng/\sqrt{8\pi V}$, leading to the frequency of the breathing mode $\omega_\sigma^2 \simeq 12\omega_R V$.

Inserting this ansatz in the equations of motion (6.27) and the subsequent linearization with respect to these deviations, we find the linearized equations of motion

$$i\delta\dot{\alpha} = [\Omega_\mathrm{m} - i\Gamma_\mathrm{m}]\,\delta\alpha - \lambda_{\alpha\zeta}(\delta\zeta + \delta\zeta^*) + \lambda_{\alpha\sigma}(\delta\sigma + \delta\sigma^*)\,, \tag{6.40a}$$

$$i\delta\dot{\zeta} = \omega_\zeta\delta\zeta - \lambda_{\alpha\zeta}(\delta\alpha + \delta\alpha^*)\,, \tag{6.40b}$$

$$i\delta\dot{\sigma} = \omega_\sigma\delta\sigma + \lambda_{\alpha\sigma}(\delta\alpha + \delta\alpha^*)\,, \tag{6.40c}$$

with the bare frequencies

$$\omega_\zeta^2 = \frac{4\omega_R V e^{-\sigma_0^2}}{\sqrt{1-\mathcal{S}_0^2}}\,, \tag{6.41a}$$

$$\omega_\sigma^2 = 4\omega_R\left[\frac{3\omega_R}{\sigma_0^4} + \frac{V(1-2\sigma_0^2)}{\sqrt{1-\mathcal{S}_0^2}}e^{-\sigma_0^2} + \frac{Ng}{\sqrt{2\pi}\sigma_0^3}\right]. \tag{6.41b}$$

Here, the bare atomic displacement frequency ω_ζ is constant below the critical coupling with $\omega_\zeta^2 = 4\omega_R V e^{-\sigma_0^2}$ and increases linearly with the atom-membrane coupling strength above $\lambda > \lambda_\mathrm{c}$, according to $\omega_\zeta^2 = 4\omega_R V(\lambda/\lambda_V)^2 e^{-2\sigma_0^2}$. Moreover, we have defined the coupling constants

$$\lambda_{\alpha\zeta} = \sqrt{N}\lambda\sqrt{\frac{4\omega_R}{\omega_\zeta}}\sqrt{1-\mathcal{S}_0^2}e^{-\sigma_0^2}\,, \tag{6.42a}$$

$$\lambda_{\alpha\sigma} = \sqrt{N}\lambda\sqrt{\frac{8\omega_R}{\omega_\sigma}}\mathcal{S}_0\sigma_0 e^{-\sigma_0^2}\,. \tag{6.42b}$$

While the coupling $\lambda_{\alpha\sigma}$ between the membrane mode and the condensate breathing mode is zero in the non-displaced phase, the coupling $\lambda_{\alpha\zeta}$ between the condensate and membrane displacement mode increases linearly with λ, whereas it decreases with $\lambda_{\alpha\zeta} \sim \lambda^{-3/2}$ in the displaced phase. Consequently, the atomic displacement mode decouples in the limit $\lambda \to \infty$ from the two other modes.

In order to determine the collective excitation spectrum within the harmonic analysis, we arrange the deviations in a vector $\boldsymbol{\delta x} = (\delta\alpha, \delta\zeta, \delta\sigma, \delta\alpha^*, \delta\zeta^*, \delta\sigma^*)^T$, such that the differential equations (6.40) can be written in the short form $\boldsymbol{\delta\dot{x}} = -i\boldsymbol{M}\boldsymbol{\delta x}$, with the linear stability matrix

$$\boldsymbol{M} = \begin{pmatrix} \Omega_\mathrm{m} - i\Gamma_\mathrm{m} & -\lambda_{\alpha\zeta} & \lambda_{\alpha\sigma} & 0 & -\lambda_{\alpha\zeta} & \lambda_{\alpha\sigma} \\ -\lambda_{\alpha\zeta} & \omega_\zeta & 0 & -\lambda_{\alpha\zeta} & 0 & 0 \\ \lambda_{\alpha\sigma} & 0 & \omega_\sigma & \lambda_{\alpha\sigma} & 0 & 0 \\ 0 & \lambda_{\alpha\zeta} & -\lambda_{\alpha\sigma} & -\Omega_\mathrm{m} - i\Gamma_\mathrm{m} & \lambda_{\alpha\zeta} & -\lambda_{\alpha\sigma} \\ \lambda_{\alpha\zeta} & 0 & 0 & \lambda_{\alpha\zeta} & -\omega_\zeta & 0 \\ -\lambda_{\alpha\sigma} & 0 & 0 & -\lambda_{\alpha\sigma} & 0 & -\omega_\sigma \end{pmatrix}. \tag{6.43}$$

Below the critical coupling coupling, the stability matrix becomes block diagonal as $\lambda_{\alpha\sigma} = 0$. In the limit of zero mechanical damping $\Gamma_\mathrm{m} \to 0$, the problem reduces to an

analytically solvable eigenvalue problem for the matrix

$$\boldsymbol{M}|_{\alpha\zeta} = \begin{pmatrix} \Omega_{\mathrm{m}} & -\lambda_{\alpha\zeta} & 0 & -\lambda_{\alpha\zeta} \\ -\lambda_{\alpha\zeta} & \omega_\zeta & -\lambda_{\alpha\zeta} & 0 \\ 0 & \lambda_{\alpha\zeta} & -\Omega_{\mathrm{m}} & \lambda_{\alpha\zeta} \\ \lambda_{\alpha\zeta} & 0 & \lambda_{\alpha\zeta} & -\omega_\zeta \end{pmatrix} \tag{6.44}$$

acting on the subspace of the deviations in the ζ-α plane. The reduced linear stability matrix $\boldsymbol{M}|_{\alpha\zeta}$ has the four eigenvalues ν_i, satisfying

$$\nu^2 = \Omega_{\mathrm{m}}^2 + \omega_\zeta^2 \pm \sqrt{(\Omega_{\mathrm{m}}^2 - \omega_\zeta^2)^2 + 16\Omega_{\mathrm{m}}\omega_\zeta\lambda_{\alpha\zeta}^2}\,. \tag{6.45}$$

Hence, in the limit of off-resonant coupling $(\Omega_{\mathrm{m}}^2 - \omega_\zeta^2)^2 \gg \Omega_{\mathrm{m}}\omega_\zeta\lambda_{\alpha\zeta}^2$, the eigenvalues follow as

$$\begin{aligned} \nu_{1,\pm} &\simeq \pm\,\Omega_{\mathrm{m}}\sqrt{1 + (\lambda/\lambda_{\mathrm{c}})^2}\,, \\ \nu_{2,\pm} &\simeq \pm\,\omega_\zeta\sqrt{1 - (\lambda/\lambda_{\mathrm{c}})^2} = \pm\sqrt{4\omega_R V e^{-\sigma_0^2}}\sqrt{1 - (\lambda/\lambda_{\mathrm{c}})^2}\,, \end{aligned} \tag{6.46}$$

and the other two collective excitation frequencies $\nu_{3,\pm} = \pm\omega_\sigma$, which are exact.

6.2.4.2 Full Spectrum of Excitations

Similar to before, a harmonic analysis can also be carried out within the GPE approach. The collective excitation spectrum is found by considering deviations from the stationary state (α_0, ψ_0) in the form $\psi(z,t) = e^{-i\mu t}[\psi_0(z) + \delta\psi(t,z)]$ and $\alpha(t) = \alpha_0 + \delta\alpha(t)$. Without loss of generality, the mean-field steady state $\psi_0(z)$ can be chosen to be real valued. Then, linearizing the coupled equations of motion (6.17) with respect to the deviations, the Bogoliubov–de Gennes equations

$$i\partial_t\delta\alpha = [\Omega_{\mathrm{m}} - i\Gamma_{\mathrm{m}}]\delta\alpha - \sqrt{N}\lambda\mathcal{Q}\left[\delta\psi + \delta\psi^*\right]\,, \tag{6.47a}$$

$$i\partial_t\delta\psi(z) = \left[h_0(z) + Ng\psi_0^2(z)\right]\delta\psi(z) + Ng\psi_0^2(z)\delta\psi^*(z) - \sqrt{N}\lambda\sin(2z)\psi_0(z)[\delta\alpha + \delta\alpha^*]\,, \tag{6.47b}$$

are obtained. Here, we have defined the linear operators $\mathcal{Q}[f] = \int dz\,\psi_0(z)\sin(2z)f(z)$ and $h_0(z) = -\omega_R\partial_z^2 + V\sin^2(z) + Ng\psi_0^2(z) - \sqrt{N}\lambda(\alpha_0 + \alpha_0^*)\sin(2z) - \mu$.

The set of differential equations (6.47) couples the deviations to their complex conjugates. In that sense, the solutions are of the form $\delta\alpha(t) = \sum_k[e^{-i\nu_k t}\delta\alpha_{k+} + e^{i\nu_k^* t}\delta\alpha_{k-}^*]$ and $\delta\psi(t,z) = \sum_k[e^{-i\nu_k t}u_k(z) + e^{i\nu_k^* t}v_k^*(z)]$ with complex frequencies ν_k. Within this ansatz, the frequencies are determined by solving the eigenvalue problem

$$\nu_k\boldsymbol{y}_k = \boldsymbol{M}_{GP}(z)\boldsymbol{y}_k\,, \tag{6.48}$$

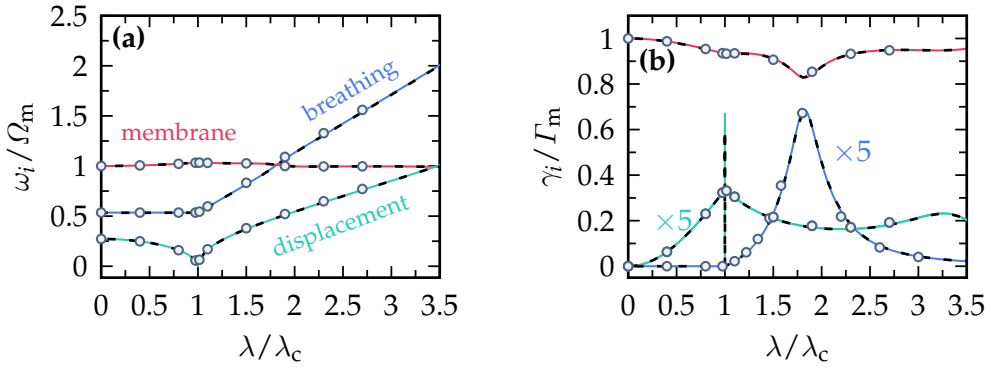

FIGURE 6.6: The three energetically lowest (a) collective excitation frequencies $\omega_i = \mathrm{Re}(\nu_i)$ and (b) corresponding decay rates $\gamma_i = -\mathrm{Im}(\nu_i)$ are shown as a function of the atom-membrane coupling. The different colors correspond to different eigenmodes. The dominant contributions for the curves red, blue and green are membrane amplitude, condensate width and condensate displacement excitation, respectively. Here, the solid curves are showing the eigenmode spectrum estimated within the cumulant expansion, whereas the dashed (black) curves are the corresponding values determined in the numerical GPE scheme. The circles show the excitation spectrum obtained within in the Bogoliubov ansatz of equation (6.59). For ease of comparison, the two smallest decay rates have been scaled by a factor of 5. The parameters used are $V = 200\,\omega_R$, $\Omega_m = 100\,\omega_R$, $\Gamma_m = 20\,\omega_R$, and $g = 0$.

with the vector $\boldsymbol{y}_k = (\delta\alpha_{k+}, u_k(z), \delta\alpha_{k-}, v_k(z))^T$ and the linear stability matrix

$$\boldsymbol{M}_{GP}(z) = \begin{pmatrix} \boldsymbol{X}(z) & \boldsymbol{Y}(z) \\ -\boldsymbol{Y}^*(z) & -\boldsymbol{X}^*(z) \end{pmatrix}, \tag{6.49}$$

where we have defined the matrices

$$\boldsymbol{X}(z) = \begin{pmatrix} \Omega_m - i\Gamma_m & -\sqrt{N}\lambda\mathcal{Q} \\ -\sqrt{N}\lambda\sin(2z)\psi_0(z) & h_0(z) + Ng\psi_0^2(z) \end{pmatrix}, \tag{6.50a}$$

$$\boldsymbol{Y}(z) = \begin{pmatrix} 0 & -\sqrt{N}\lambda\mathcal{Q} \\ -\sqrt{N}\lambda\sin(2z)\psi_0(z) & Ng\psi_0^2(z) \end{pmatrix}. \tag{6.50b}$$

The symmetry of $\boldsymbol{M}_{GP}(z)$ suggests that if ν_k is an eigenvalue, the negative complex conjugate $-\nu_k^*$ is also an eigenvalue.

6.2.4.3 Roton-type Spectrum in the Vicinity of the Critical Point

The eigenfrequencies of the collective excitations are shown in figure 6.6(a) as a function of the atom-membrane coupling constant $\sqrt{N}\lambda$. Here, the dashed curves show the frequencies found in the GPE approach, whereas the solid curves refer to the analytical results (the circles refer to another approach discussed below). As the atom-membrane coupling is approaching the critical point λ_c, the lowest excitation frequency decreases with a roton-type behavior according to equation (6.46). At the same time, the corresponding decay rate in figure 6.6(b) increases up to a maximum at $\lambda = \lambda_c$ and is followed by a bifurcation. This bifurcation in addition to the roton-type behavior is well-known from atomic condensates

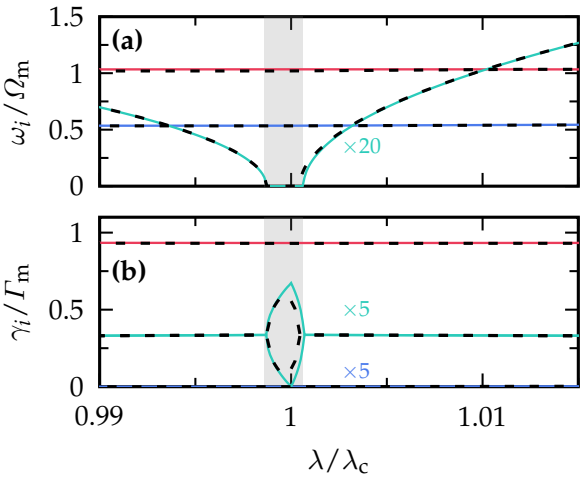

FIGURE 6.7: A zoom to the vicinity of the critical point shows the behavior of the (a) collective excitation frequencies and (b) decay rates. Within a certain area (shaded in grey), the lowest excitation frequency is constantly zero and the decay rate exhibits a bifurcation. The same parameters as in figure 6.6 have been used. Certain curves are scaled by the indicated factors.

with a long-range interaction [121, 122, 229, 230], which, in the present case, is mediated by the membrane mode. The vanishing excitation frequency at $\sqrt{N}\lambda_c$ corresponds to the Goldstone boson mode which is associated with the spontaneous symmetry breaking at the critical point. In fact, the appearance of a massless Goldstone boson is characteristic for a second-order phase transition

Moreover, we show in figure 6.7 a zoom of figure 6.6 around the critical point. In a narrow range around the critical point, a bifurcation of the decay rate can be observed, whereas the lowest excitation frequency is constantly zero in this region.

6.2.4.4 Covariance and Atom-Membrane Entanglement

In addition to the preceding analysis of the collective excitation spectrum, the eigenmodes can be used as a measure of quantum entanglement between the atomic condensate and the membrane. Here, we consider the case of zero damping ($\Gamma_m = 0$) and determine the ground state of the combined system within the Gaussian ansatz. In this case, the dynamics governed by $\boldsymbol{\delta\dot{x}} = -i\boldsymbol{M}\boldsymbol{\delta x}$ with the linear stability matrix of equation (6.43) is generated by the Hamiltonian

$$H = \Omega_m b_\alpha^\dagger b_\alpha + \omega_\zeta b_\zeta^\dagger b_\zeta + \omega_\sigma b_\sigma^\dagger b_\sigma - \lambda_{\alpha\zeta}(b_\alpha^\dagger + b_\alpha)(b_\zeta^\dagger + b_\zeta) + \lambda_{\alpha\sigma}(b_\alpha^\dagger + b_\alpha)(b_\sigma^\dagger + b_\sigma)\,, \quad (6.51)$$

with the bosonic algebra $\left[b_\mu, b_\nu^\dagger\right] = \delta_{\mu\nu}$, where $b_\mu = \delta\mu$ with $\mu \in \{\alpha, \sigma, \zeta\}$. The Hamiltonian (6.51) is diagonalized by the Bogoliubov transformation

$$b_\mu = \sum_{i=1}^{3}\left[u_\mu^i d_i + \left(v_\mu^i\right)^* d_i^\dagger\right]\,, \quad (6.52)$$

with the eigenfrequencies $\omega_i = \mathrm{Re}(\nu_i)$ and new bosonic ladder operators d_i, $d_i^\dagger$. In order to satisfy the bosonic commutation relation, the transformation coefficients have to be normalized according to

$$\sum_\mu\left[u_\mu^i\left(u_\mu^j\right)^* - v_\mu^i\left(v_\mu^j\right)^*\right] = \delta_{ij}\,. \quad (6.53)$$

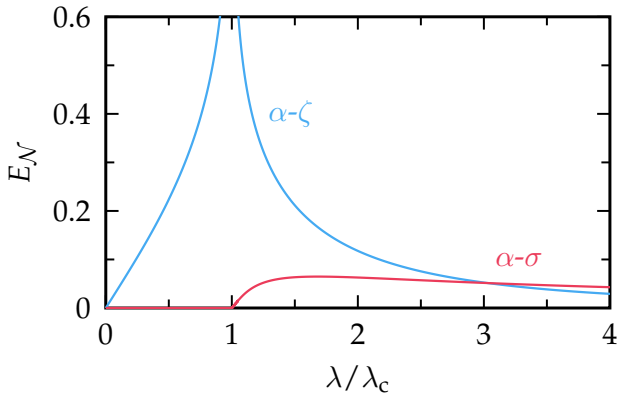

FIGURE 6.8: The logarithmic negativity $E_\mathcal{N}$ is shown as a function of the atom-membrane coupling λ. The blue (red) curve measures the entanglement between membrane displacement and condensate displacement (width) mode. The same parameters as in figure 6.6 have been used, but with $\Gamma_\mathrm{m} = 0$.

In order to determine the entanglement between the membrane and condensate, we calculate the logarithmic negativity $E_\mathcal{N}$ [198, 231, 232] from the ground state solution of (6.51). The logarithmic negativity is related to the smallest symplectic eigenvalue $\tilde{\nu}_-$ of the reduced covariance matrix of the quadratures according to

$$C_{kl} = \frac{1}{2}\langle x_k x_l + x_l x_k \rangle \,, \tag{6.54}$$

with the vector $\boldsymbol{x} = (q_\alpha, p_\alpha, q_\sigma, p_\sigma, q_\zeta, p_\zeta)^T$, where $q_\mu = (b_\mu + b_\mu^\dagger)/\sqrt{2}$ and $p_\mu = (b_\mu - b_\mu^\dagger)/\sqrt{2}i$. To describe the entanglement between two different modes, the reduced covariance matrix $\boldsymbol{C}'$ is obtained by neglecting the columns and rows of the irrelevant mode. Then, the reduced covariance takes the form

$$\boldsymbol{C}' = \begin{pmatrix} \boldsymbol{U} & \boldsymbol{V} \\ \boldsymbol{V}^T & \boldsymbol{W} \end{pmatrix} , \tag{6.55}$$

and the logarithmic negativity can be expressed as

$$E_\mathcal{N} = \max\{0, -\log(2\tilde{\nu}_-)\} \quad \text{with} \quad \tilde{\nu}_- = 2^{-1/2}\sqrt{\Sigma(\boldsymbol{C}') - \sqrt{\Sigma(\boldsymbol{C}')^2 - 4\det \boldsymbol{C}'}} \,, \tag{6.56}$$

where $\Sigma(\boldsymbol{C}') = \det \boldsymbol{U} + \det \boldsymbol{W} - 2\det \boldsymbol{V}$.

The ground state of the collective mode Hamiltonian (6.51) is a three-mode squeezed state, which generates a strong atom-membrane entanglement close to the critical coupling rate. This behavior is manifest in a rising logarithmic negativity, which is shown in figure 6.8 and results in a singularity. For $\Gamma_\mathrm{m} = 0$, this results in a singularity of the entanglement measure between the atom and membrane displacement modes at the critical point, indicating the strong entanglement. In order to study the case $\Gamma_\mathrm{m} \neq 0$, the thermal fluctuations have to be included, as otherwise the occupation of the collective modes will decay to zero. For instance, this has been studied in BEC-cavity setup by Nagy *et al.* [198], where it has been shown that the logarithmic negativity is peaked with a finite-valued global maximum in the vicinity of the phase transition, instead of a diverging logarithmic negativity. In the next section, we will discuss a possible approach to include the thermal and light field fluctuations in the Gaussian cumulant expansion.

6.3 Bogoliubov Prescription of the Phase Transition

In order to include the thermal and light field fluctuations in an appropriate manner, we make a Bogoliubov ansatz for the atomic field operator $\Psi(t,z)$. As we have seen in the preceding section, the ground state of the harmonic oscillator very well approximates the steady state of the condensate in the π-periodic optical lattice potential. Here, we make the three mode ansatz

$$\Psi(t,z) \simeq \left[\sqrt{N}\psi_0(z-\zeta_0) + d_\zeta(t)\psi_1(z-\zeta_0) + d_\sigma(t)\psi_2(z-\zeta_0)\right] e^{-i\mu t} \tag{6.57}$$

with the quasi-eigenstates

$$\psi_n(z) = \left(\frac{1}{\pi\sigma_0^2}\right)^{1/4} \frac{1}{\sqrt{2^n n!}} H_n(z/\sigma_0) \exp\left(-\frac{z^2}{2\sigma_0^2}\right) \tag{6.58}$$

and the n-th Hermite polynomial[8]. The spatial oscillations and breathing of the condensate are then totally encrypted in excitations to energetically higher oscillator orbitals $\psi_{n\geq 1}(z)$ via the ladder operators d_σ and d_ζ. These operators follow bosonic commutation relations. Moreover, $\psi_0(z-\zeta)$ is the mean-field steady state of equation (6.23).

For the membrane mode, we assume $a(t) = \sqrt{N}\alpha_0 + d_\alpha(t)$ with bosonic commutation relations, such that $\left[a, a^\dagger\right] = \left[d_\alpha, d_\alpha^\dagger\right] = 1$. The ansatz for the condensate field operator $\Psi(t,z)$ is inserted in equations (6.12). In the Bogoliubov ansatz, only the terms to linear order in the ladder operators are considered, such that we linearize these equations with respect to d_α, d_σ and d_ζ. The equations of motion for $d_\zeta(t)$ and $d_\sigma(t)$ are found in a similar manner as the cumulant expansion. However, here, we simply multiply by either $\psi_1(z-\zeta)$ or $\psi_2(z-\zeta)$ and integrate over the space coordinate z. Hence, we find the equations of motion[9]

$$i\partial_t d_\alpha = (\Omega_\mathrm{m} - i\Gamma_\mathrm{m})d_\alpha - \Lambda_{\alpha\zeta}(d_\zeta + d_\zeta^\dagger) + \Lambda_{\alpha\sigma}(d_\sigma + d_\sigma^\dagger) - \lambda_\mathrm{m}\xi_\mathrm{l} + i\xi_\mathrm{th}\,, \tag{6.59a}$$

$$i\partial_t d_\zeta = \Omega_\zeta d_\zeta + g_\zeta d_\zeta^\dagger - \Lambda_{\alpha\zeta}(d_\alpha + d_\alpha^\dagger) - \lambda_\zeta\xi_\mathrm{l}\,, \tag{6.59b}$$

$$i\partial_t d_\sigma = \Omega_\sigma d_\sigma + g_\sigma d_\sigma^\dagger + \Lambda_{\alpha\sigma}(d_\alpha + d_\alpha^\dagger) - \lambda_\sigma\xi_\mathrm{l}\,, \tag{6.59c}$$

with the bare frequencies

$$\Omega_\zeta = \frac{\omega_R}{\sigma_0^2} + V\sqrt{1-\mathcal{S}_0^2}\sigma_0^2 e^{-\sigma_0^2} + \frac{4N\lambda^2\Omega_\mathrm{m}}{\Omega_\mathrm{m}^2+\Gamma_\mathrm{m}^2}\mathcal{S}_0^2\sigma_0^2 e^{-2\sigma_0^2}\,, \tag{6.60a}$$

$$\Omega_\sigma = \frac{2\omega_R}{\sigma_0^2} + V\sqrt{1-\mathcal{S}_0^2}\left(2-\sigma_0^2\right)\sigma_0^2 e^{-\sigma_0^2} + \frac{4N\lambda^2\Omega_\mathrm{m}}{\Omega_\mathrm{m}^2+\Gamma_\mathrm{m}^2}\mathcal{S}_0^2\left(2-\sigma_0^2\right)\sigma_0^2 e^{-2\sigma_0^2} - \frac{Ng}{\sqrt{32\pi}\sigma_0}\,. \tag{6.60b}$$

[8] Here, we consider only the ground state as well as the first and second excited state of the harmonic oscillator. Hence, the relevant Hermite polynomials are $H_0(x) = 1$, $H_1(x) = 2x$ and $H_2(x) = 4x^2 - 2$.

[9] We note that in order to find these equations of motion, we have made use of the steady state equations (6.29).

Moreover, we have defined the coupling parameters

$$\Lambda_{\alpha\zeta} = \sqrt{2N}\lambda\sqrt{1-\mathcal{S}_0^2}\sigma_0 e^{-\sigma_0^2}, \tag{6.61a}$$

$$\Lambda_{\alpha\sigma} = \sqrt{2N}\lambda\mathcal{S}_0\sigma_0^2 e^{-\sigma_0^2}, \tag{6.61b}$$

the atomic interaction induced coupling $g_\zeta = Ng/\sqrt{8\pi}\sigma_0$, $g_\sigma = 3g_\zeta/2$ and the coupling to the light field fluctuations with $\lambda_\zeta = \sqrt{N}\lambda_a\mathcal{S}_0\sigma_0 e^{-\sigma_0^2}/\sqrt{2}$, $\lambda_\sigma = \sqrt{N}\lambda_a\sqrt{1-\mathcal{S}_0^2}\sigma_0^2 e^{-\sigma_0^2}/\sqrt{2}$.

By expanding the vector $\boldsymbol{x} = (d_\alpha, d_\zeta, d_\sigma, d_\alpha^\dagger, d_\zeta^\dagger, d_\sigma^\dagger)^T$ in the collective eigenmodes of the set of equations (6.59) , we determine the steady state via equation (B.5). The Bogoliubov eigenspectrum is very well reproduced by the collective spectrum in the Gaussian and numerical GPE ansatz of the previous section. In figure 6.6, the spectra are compared with each other, where the frequencies (decay rates) of the Bogoliubov prescription are depicted by the circles.

6.3.1 Without Light Field Fluctuations

A similar approach has been taken in the context of a BEC in an optical cavity [198]. In such a setup, the dominant source of noise is due to photon losses in the cavity, which is similar to the zero temperature fluctuations on the membrane that are considered here. In order to compare our system to the open-system description of the superradiant phase transition, let us first neglect the light field fluctuations ξ_l, such that the only present noise is ξ_{th}.

In order to observe the present NQPT in a real setup, one has to find observables which show different characteristic behaviors in both phases. Experimentally accessible quantities of the membrane are the phonon occupancy $\langle n_\alpha\rangle = \langle d_\alpha^\dagger d_\alpha\rangle$ and the position variance $\langle x_\alpha^2\rangle = \langle (d_\alpha + d_\alpha^\dagger)^2\rangle/2$. In figure 6.9(a), we show these two observables as a function of the atom-membrane coupling strength. For relatively small and large couplings, $\lambda \ll \lambda_c$ and $\lambda \gg \lambda_c$, the position variance is constantly one half, while it diverges at the critical point λ_c. Similarly, the membrane occupation is zero for coupling rates far below and above the critical point. It diverges at $\sqrt{N}\lambda = \sqrt{N}\lambda_c$ according to the power law behavior $\langle n_\alpha\rangle \sim |\lambda - \lambda_c|^{-\nu}$ with a critical exponent of $\nu = 1$ rather than the usual mean-field exponent (cf. table 4.1, where the critical exponent is predicted to be $\nu = 1/2$ according to Landau theory). The critical exponent is extracted by a log-log plot of the phonon number in the inset of figure 6.9(a).

Moreover, we show in figure 6.9(b) the quantum depletion of the atomic condensate $N_{qntm} = \langle d_\zeta^\dagger d_\zeta\rangle + \langle d_\sigma^\dagger d_\sigma\rangle$ and the occupation number of the two excited states. In contrast to the phonon number, the atomic condensate always exhibits excited particles for a finite atom-membrane coupling, even in the non-interacting regime $g = 0$. Below the critical coupling, only the ζ-mode has a finite occupation, whereas $\langle n_\sigma\rangle = \langle d_\sigma^\dagger d_\sigma\rangle$ is constantly zero as $\Lambda_{\alpha\sigma} \equiv 0$. In the vicinity of the phase transition, the condensate depletion diverges with the exponent -1, while N_{qntm} exhibits a global minimum above the critical point. Above the threshold λ_c, also the σ-mode couples to the membrane and, consequently, the thermal fluctuations lead to a finite occupation $\langle n_\sigma\rangle \neq 0$, while the occupation number $\langle n_\zeta\rangle$ is steadily

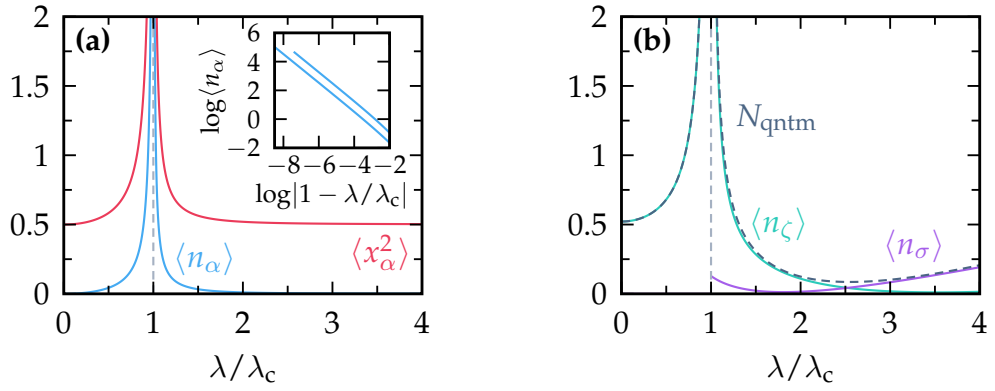

FIGURE 6.9: (a) The occupation number $\langle n_\alpha \rangle$ and the displacement variance of the membrane $\langle x_\alpha^2 \rangle$ are shown as a function of the atom-membrane coupling strength λ. The inset shows a log-log plot of the phonon occupation number. (b) The number of depleted atoms N_{qntm}, the occupation number of the first excited state $\langle n_\zeta \rangle$, and the second excited state $\langle n_\sigma \rangle$ are shown. The dashed vertical line indicates the critical point. Here, we have used the parameters $V = 200\,\omega_R$, $gN = 0$, $\Omega_{\mathrm{m}} = 100\,\omega_R$, and $\Gamma_{\mathrm{m}} = 20\,\omega_R$.

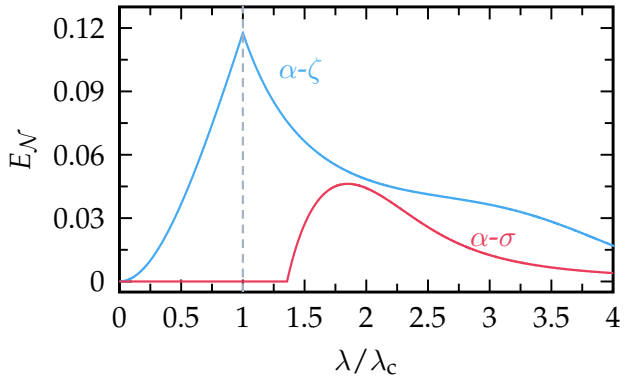

FIGURE 6.10: The logarithmic negativity $E_{\mathcal{N}}$ is shown as a function of the atom-membrane coupling λ. The blue (red) curve measures the entanglement between membrane displacement and condensate displacement (width) mode. The dashed vertical line indicates the critical coupling rate. The same parameters as in figure 6.9 have been used.

reduced to zero as the order parameter $\mathcal{S}_0$ is approaching unity. Consequently, the ζ-mode decouples from the other modes. The here found behavior is in accordance with the results of a BEC in a cavity [198].

On the other hand, we show the entanglement between atoms and membrane in figure 6.10. In contrast to the ground state entanglement, the present fluctuations strongly reduce the entanglement in the steady state. As a consequence, the singularity of $E_{\mathcal{N}}$ in figure 6.8 is reduced to a non-differentiable, global maximum at $\lambda = \lambda_c$. Above the critical coupling rate, the entanglement is progressively reduced as the atom-membrane interaction increases. This behavior intermediately flattens out in the region where the frequency of the low energy mode becomes comparable to the membrane frequency Ω_{m}, which is around $\lambda \simeq 3.5\lambda_c$. The entanglement between the membrane displacement and atomic breathing mode is shifted to larger coupling rates in comparison to the ground state entanglement. Moreover, it exhibits a maximum just in the vicinity where two of the collective excitation frequencies in figure 6.6(a) cross each other.

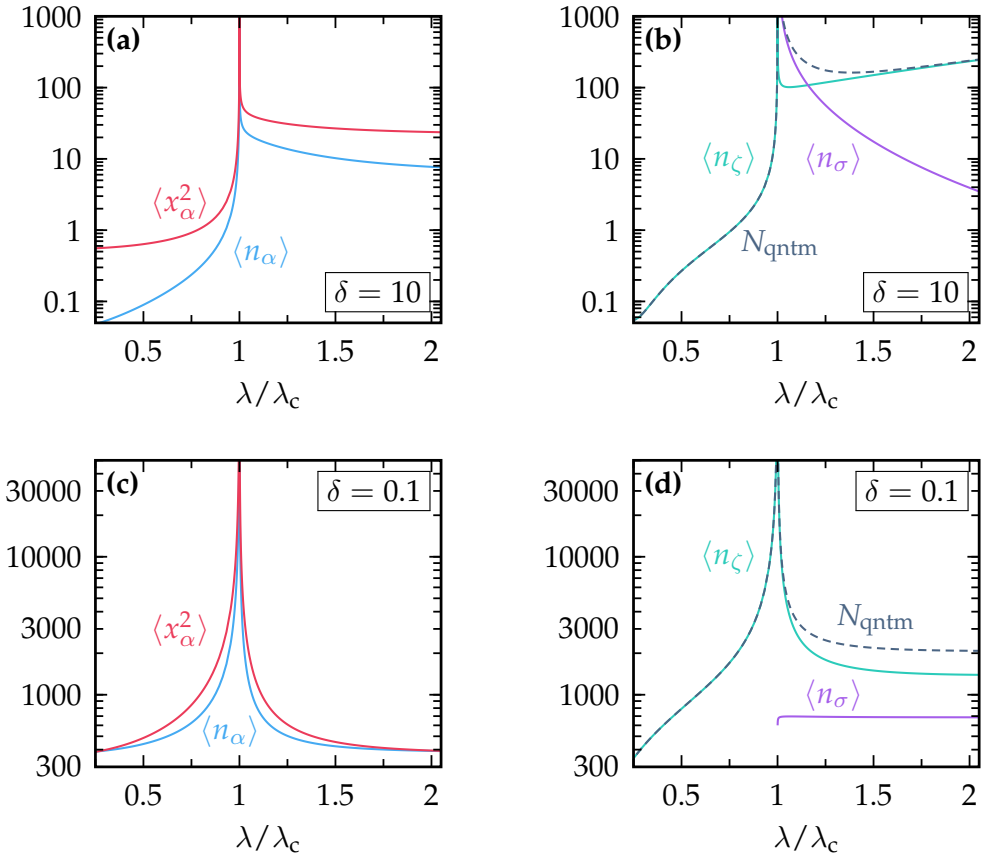

FIGURE 6.11: (a), (c) The occupation number $\langle n_\alpha \rangle$ and the position variance $\langle x_\alpha^2 \rangle$ of the membrane are shown as a function of the lattice depth V. (b), (d) The number of depleted atoms N_{qntm} and the occupation number of the first and second excited state, $\langle n_\zeta \rangle$ and $\langle n_\sigma \rangle$, are shown. Here, we have used the parameters $Ng = 0$, $\Omega_m = 100\,\omega_R$, and $\Gamma_m = 20\,\omega_R$. The atom-membrane coupling strength is chosen such that the phase transition is at $V = V_c = 200\,\omega_R$, namely $\sqrt{N}\lambda = 74.8\,\omega_R$. For the top panels (a) and (b) we have chosen $\delta = 10$, while for the bottom panels (c) and (d) $\delta = 0.1$ was chosen.

6.3.2 Light Field Fluctuations

When including the light field fluctuations in our description and studying the observables as a function of the coupling strength, one has to define the atom-light field and membrane-light field couplings individually, as the light field fluctuation couples differently to the atoms and the membrane with coupling strengths λ_a and λ_m, respectively. To circumvent this problem, we fix the atom-membrane coupling strength to $\sqrt{N}\lambda = \lambda_a\lambda_m/2 = 74.8\,\omega_R$ and study the effect of the light field fluctuations as a function of the lattice potential depth V. Then, for the parameters $\Omega_m = 100\,\omega_R$ and $\Gamma_m = 20\,\omega_R$ with $Ng = 0$, the phase transition happens at $V = V_c = 200\,\omega_R$. Moreover, we choose the parametrization $\sqrt{N}\lambda_a = \sqrt{2N\lambda}\delta$ and $\lambda_m = \sqrt{2\lambda}/\delta$.

In figure 6.11, we show the occupation numbers of the different modes in dependence of λ/λ_c for the cases $\delta = 10$ and $\delta = 1/10$ in (a), (b) and (c), (d), respectively. Here, the critical coupling $\lambda_c(V)$ is a function of the potential depth V according to equation (6.32), such that a modification of V alters λ_c. Consequently, the quotient λ/λ_c varies as a function of V

Ω_m	$2\pi \times 263.8\,\mathrm{kHz}$	ω_R	$2\pi \times 3.8\,\mathrm{kHz}$
Γ_m	$2\pi \times 24.4\,\mathrm{mHz}$	N	2×10^6
M	$9.7 \times 10^{-11}\,\mathrm{kg}$	m	$1.443 \times 10^{-25}\,\mathrm{kg}$
ω_L	$2\pi \times 384\,\mathrm{THz}$	$\omega_\perp$	$2\pi \times (62 \ldots 85)\,\mathrm{Hz}$
$\mathcal{F}$	50 to 120	g	$2\pi \times (11.6 \ldots 16.6)\, a_\mathrm{Bohr}\mathrm{kHz}$

TABLE 6.1: The relevant system parameters based on reference [130, 132] are summarized. The left column shows the parameters of the optomechanical subsystem and the right column those of the atomic condensate.

while the atom-membrane coupling rate is constantly fixed. We observe that the light field fluctuations lead to a significant increase of the occupation numbers in the displaced phase ($\lambda > \lambda_\mathrm{c}$) for $\delta = 10$ in (a) and (b). On the other hand, in the normal phase ($\lambda < \lambda_\mathrm{c}$), $\langle n_\alpha \rangle$ is two orders smaller. Here, the light field fluctuations do only indirectly couple to the ζ-mode via the membrane mode, as $\lambda_\zeta = 0$. For $\delta = 1/10$ in (c) and (d), this consequently leads to a larger influence even in the normal phase which results in higher occupation numbers.

Apart from the effects of the light field fluctuations on the excitations, a strong, negative effect on the atom-membrane entanglement is observed. Already the thermal fluctuations strongly reduce the steady-state entanglement, when compared to the ground state entanglement. By including the photon fluctuations, this entanglement is completely diminished as the relevant autocorrelator scales with the atom-membrane coupling strength. These fluctuations are, however, necessary in order to create an effective atom-membrane coupling as a coherent laser field is not able to mediate excitations between both subsystems.

6.4 Experimental Realization and the Role of Atom Interactions

On the basis of the existing setups [129, 130], an experimental observation is possible by including modest changes. Present optical lattices with potential depths $V \simeq 2000\,\omega_R$ readily achieve resonant coupling, i.e., $\omega_\zeta \simeq \Omega_\mathrm{m}$, with $\sqrt{N}\lambda \simeq 3\,\omega_R$ (the other parameters are summarized in table 6.1). The fact that the atom-membrane coupling does not have to be resonant in order to measure the phase transition facilitates a realization. For instance, by ramping down the lattice depth to $V \simeq 30\,\omega_R$, the critical coupling $\sqrt{N}\lambda_\mathrm{c}$ can be reached by altering the cavity finesse $\mathcal{F}$ or the laser power. In order to independently tune V and λ, a second laser has to be applied which is slightly misaligned to the coupling laser of the same frequency but shifted by $\pi/2$. By increasing the laser intensity of the second laser, the optical potential depth is effectively reduced, while the atom-membrane coupling strength is unaffected.

Apart from the displacement variance $\langle x_\alpha^2 \rangle$, a possible measure to track the phase transition is the membrane eigenfrequency which can be readily measured by spectroscopic means with a precision much below 1% [233]. Therefore, we show a zoom around the collective excitation frequency corresponding to the membrane mode in figure 6.12(a). The point of the phase transition exhibits a characteristic cusp which is clearly resolvable within the

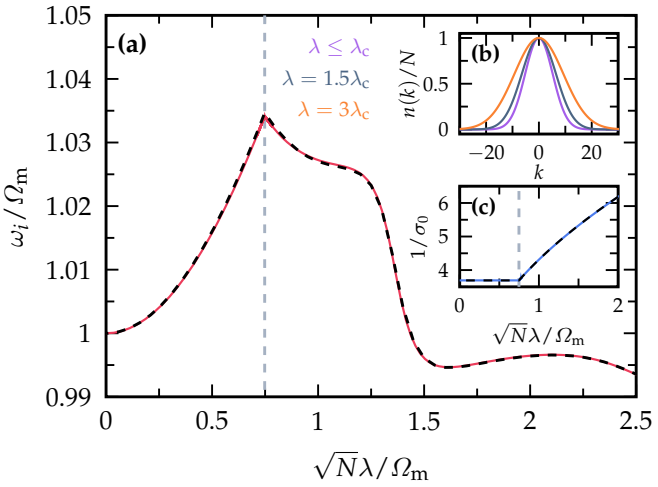

FIGURE 6.12: (a) The membrane excitation frequency and (b) the momentum distribution $|n(k)|$ of the atoms in a single well are shown. (c) The width of the momentum distribution $|n(k)|$ is shown as a function of the atom-membrane coupling. Here, the dashed vertical line indicates the critical point λ_c. The parameters are $V = 200\,\omega_R$, $\Omega_m = 100\,\omega_R$, $\Gamma_m = 20\,\omega_R$ and $g = 0$.

experimental fidelity. In addition, the nonequilibrium quantum phase transition can also be detected by looking at the momentum distribution of the atoms in a time-of-flight measurement. In figure 6.12(b), together with figure 6.12(c), we show the momentum distribution of the atoms

$$n(k) = N \int dz\, e^{ik(z-\zeta_0)} |\psi(z)|^2 = N e^{-(k\sigma_0/2)^2}\,, \tag{6.62}$$

and its width for various coupling constants λ. Below the critical point, the width is constant, while it grows monotonically with the square root of λ above the threshold λ_c.

In a real setup, the periodic character of the potential and condensate wave function has to be taken into account. Assuming a lattice with L occupied lattice wells, the momentum distribution $n_{lat}(k) = f(k)n(k)$ is modified by the form factor

$$|f(k)| = \frac{\sin(\pi L k/2)}{L \sin(\pi k/2)}\,, \tag{6.63}$$

where we considered the atomic density $n_{lat}(z) \simeq (N/L)\sum_{j=0}^{L-1} |\psi_0(z - j\pi)|^2$. A comparison of the momentum distribution for a single site lattice and a lattice with $L = 10$ sites is shown in figure 6.13(a). By fitting a Gaussian profile to the pronounced maxima of the lattice momentum distribution $n_{lat}(k)$, the condensate width can be extracted.

In the previous part, we have mainly shown the results for the case of non-interacting atoms. As shown in table 6.1, the effective one-dimensional interaction strength is, in fact, of the order $Ng \sim 1 - 10\,\omega_R$. This order of interaction strength is induced by application of a perpendicular harmonic confinement potential with frequency $\omega_\perp \sim 100$ Hz and assuming a number of $N/L = 10^4$ atoms per lattice site.

In figure 6.13(b) is shown the order parameter $\mathcal{S}_0(\lambda)$ for different atom-atom interactions. Qualitatively, no difference in the order parameter is found. While the curves are on top of each other for $Ng \ll V$, the critical coupling rate is slightly shifted when the interaction strength is of the same order as the potential depth. Apart from this, a finite atom interaction will increase the quantum depletion N_{qntm}.

A study of the phase diagram on the mean-field level has also been performed in reference [234] . By considering a shallow optical lattice, the authors effectively described the

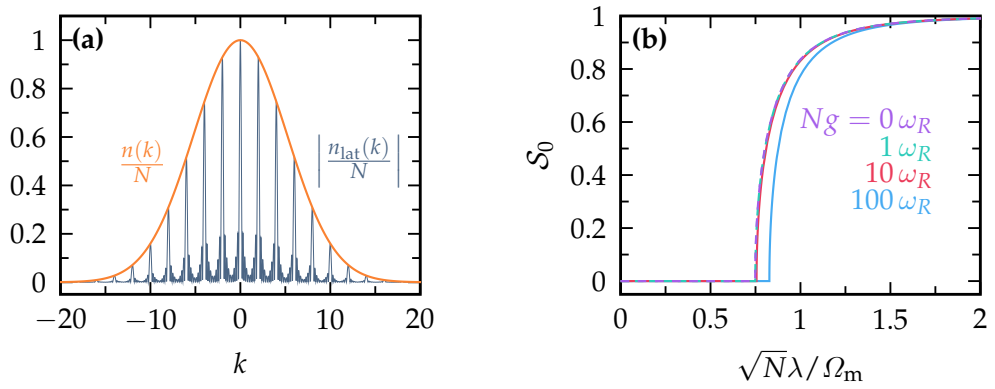

FIGURE 6.13: (a) A comparison of the momentum distribution $n(k)$ for a single site and $n_{\mathrm{lat}}(k)$ for a lattice with $L = 10$ site below the critical coupling rate $\lambda \leq \lambda_{\mathrm{c}}$. Here, we have chosen $Ng = 0$. (b) The steady state order parameter $\mathcal{S}_0$ as a function of the atom-membrane coupling is compared for different atom-atom interactions. The colors indicate different Ng. The other parameters are $V = 200\,\omega_R$, $\Omega_{\mathrm{m}} = 100\,\omega_R$, and $\Gamma_{\mathrm{m}} = 20\,\omega_R$.

atomic condensate by a Bose–Hubbard model. After an adiabatic elimination of the membrane motion, the mechanical amplitude α enters in the nearest-neighbor hopping rate J and the on-site energy. This gives rise to different MI and SF regions when the effective atom-membrane coupling is varied in the displaced phase. However, it is important to realize that this statement only holds in the condensate regime of weak interactions. If, however, the interactions are very strong such that Mott physics in the lattice occurs, the outcome might be different. Consequently, different approaches have to be taken.

Finally, let us note that one of the main features of this phase transition was the creation of a shifted lattice above the critical coupling. In the next chapter, we will show that a similar NQPT occurs in the internal coupling scheme which offers larger tunability.

CHAPTER 7

Changing the Order of a Quantum Phase Transition

Above a critical intensity of the coupling laser, a nonequilibrium quantum phase transition to a symmetry-broken phase emerges which is characterized by a sizeable occupation of the high-energy internal states and a displaced membrane. The order of this NQPT can be changed by tuning the atomic transition frequency. In this chapter, we present the results which have been partially published in:

N. Mann, A. Pelster, and M. Thorwart, "Tuning the Order of the Nonequilibrium Quantum Phase Transition in a Hybrid Atom-Optomechanical System", arXiv:1810.12846 (2018).

In this chapter, we show that the *internal* state coupling scheme also allows for a NQPT. As a novel additional feature, the order of this PT can be readily tuned by changing the atomic transition frequency. Thus, a first- and second-order NQPT can be realized in the same physical set-up and this, by only changing a directly accessible parameter. We show this for the *membrane-in-the-middle-setup* [159]. In a first step, we adiabatically eliminate the light field, which reveals an effective coupling between the membrane and the transition between two states in the atom gas.

7.1 Effective Description of the Internal State Coupling Scheme

In order to obtain the effective description of the dynamics for the reduced system, we start with the linearized Hamiltonian given in equation (5.46). In the same fashion as in the preceding chapter, we derive the equations of motion within in a QSDE approach. Hence, we start by expanding the time evolution operator to lowest order in the time delay δt. It follows that the relevant terms are given by

$$|\psi(t_0+\delta t)\rangle \simeq \left\{1 - i\int_{t_0}^{t_0+\delta t} dt\, H_{\text{isc}}^{\text{lin}}(t)_I - \int_{t_0}^{t_0+\delta t} dt \int_{t_0}^{t} ds\, H_{\text{isc}}^{\text{lin}}(t)_I H_{\text{isc}}^{\text{lin}}(s)_I\right\} |\psi(t_0)\rangle\,. \tag{7.1}$$

Again, we assume that the initial state $|\psi(t_0)\rangle = |\psi(t_0)\rangle_{\text{a+m}} \otimes |\text{vac}\rangle_{\text{l}}$ factorizes in a product state, where $|\psi(t_0)\rangle_{\text{a+m}}$ is an arbitrary state in the atom-membrane subspace and $|\text{vac}\rangle_{\text{l}}$

the vacuum state of the photon field. By making use of the relations $b_{\mu,\omega}(t)_I|\psi(t_0)\rangle = 0$ and $b_{\mu,\omega}(t)_I b^\dagger_{\mu,\omega}(t')_I|\psi(t_0)\rangle = \left[b_{\mu,\omega}(t)_I, b^\dagger_{\mu,\omega}(t')_I\right]|\psi(t_0)\rangle$ with $\mu \in \{-,+\}$, indicating the field polarization σ_μ, we evaluate the lowest-order terms in equation (7.1). The first-order term is reduced to the expression

$$\begin{aligned}\Big\{-iH_{\mathrm{isc},0}\delta t - i\lambda_{\mathrm{m}}[a+a^\dagger][\delta B^\dagger(t_0)+\mathrm{H.c.}] - i\lambda_\pm \int dz\, \left[\Psi^\dagger_+(z)\Psi_-(z)\delta C_+(t_0,z)+\mathrm{H.c.}\right] \\ - i\lambda_{\mathrm{a}}\int dz\, \Psi^\dagger_+(z)\Psi_+(z)\left[\delta C_-(t_0,z)+\mathrm{H.c.}\right]\Big\}|\psi(t_0)\rangle\,,\end{aligned} \tag{7.2}$$

with the noise increment operators for the different polarized photon fields

$$\delta B(t) = \int_t^{t+\delta t} ds \sum_\mu \int \frac{d\omega}{\sqrt{2\pi}}\, b_{\mu,\omega}(s)_I\,, \tag{7.3a}$$

$$\delta C_\mu(t,z) = \int_t^{t+\delta t} ds \int \frac{d\omega}{\sqrt{2\pi}}\, \sin(\omega_L z)\sin(\omega z + \Delta\phi_\omega) b_{\mu,\omega}(s)_I\,. \tag{7.3b}$$

Here, $\Delta\phi_\omega = \phi_\omega - \phi_{\omega_L}$ is the relative phase shift of the mode functions $u_\omega(z)$, see equation (5.8), between the field at frequency ω and at the laser frequency ω_L. In addition, we have defined the free atom-membrane Hamiltonian $H_{\mathrm{isc},0} = H_{\mathrm{m}} + H_{\mathrm{a}}$. The last term in equation (7.1) on the right-hand side has several contributions. The unitary atom-membrane coupling terms are given by the expression

$$i(a+a^\dagger)\int dz\, \sin(2\omega_L z)\Big\{\frac{\lambda}{2}\left[\Psi^\dagger_+(z)\Psi_-(z)+\Psi^\dagger_-(z)\Psi_+(z)\right] + \lambda_{\mathrm{ex}}\Psi^\dagger_+(z)\Psi_+(z)\Big\}\delta t|\psi(t_0)\rangle \tag{7.4}$$

with the coupling constants $\lambda = \lambda_{\mathrm{m}}\lambda_\pm/2$ and $\lambda_{\mathrm{ex}} = \lambda_{\mathrm{m}}\lambda_{\mathrm{a}}/2$. The second coupling term scaling with λ_{ex} is identical to the previously discussed motional coupling, however, with the exception that it only couples to the $|+\rangle$ internal state. Moreover, long-range interaction with a dissipative character due to the complex interaction potential $\mathcal{G}(z,z')$ given in equation (6.6) is induced by the field elimination according to the terms

$$-\frac{i}{4}\int dz dz'\, \Psi^\dagger_+(z)\left\{\lambda^2_\pm \Psi_-(z)\mathcal{G}(z,z')\Psi^\dagger_-(z') + \lambda^2_{\mathrm{a}}\Psi_+(z)\mathcal{G}(z,z')\Psi^\dagger_+(z')\right\}\Psi_+(z')\delta t|\psi(t_0)\rangle\,. \tag{7.5}$$

The radiation pressure on the membrane leads to momentum diffusion included by the term $-(\lambda^2_{\mathrm{m}}/2)(a+a^\dagger)^2\delta t|\psi(t_0)\rangle$. The last contribution of the second-order term induces the mixed dissipative terms

$$-2(a+a^\dagger)\int dz\left\{\frac{\lambda}{2}\sin^2(\omega_L z)\left[\Psi^\dagger_+(z)\Psi_-(z)+\mathrm{H.c.}\right] + \lambda_{\mathrm{ex}}\sin^2(\omega_L z)\Psi^\dagger_+(z)\Psi_+(z)\right\}\delta t|\psi(t_0)\rangle\,. \tag{7.6}$$

Finally, by taking the limit $\delta t \to 0$, the quantum stochastic differential equation for the wave function follows. With the same assumptions as for the motional coupling scheme, we

find the QSSE in Ito form

$$d|\psi\rangle = \left\{ -iH_{\rm isc}^{\rm eff} - \frac{1}{2}\left[\lambda_{\rm m}(a+a^\dagger) + \int dz\, \sin^2\omega_L z\left(\lambda_\pm \Psi_+^\dagger\Psi_- + \lambda_\pm\Psi_-^\dagger\Psi_+ + \lambda_{\rm a}\Psi_+^\dagger\Psi_+\right)\right]^2\right\} dt|\psi\rangle$$
$$- i\left\{\lambda_{\rm m}(a+a^\dagger)dB^\dagger + \lambda_{\rm a}\int dz\,\Psi_+^\dagger\Psi_+ dC_-^\dagger + \lambda_\pm\int dz\,\Psi_-^\dagger\Psi_+ dC_+^\dagger + {\rm H.c.}\right\}|\psi\rangle\,. \tag{7.7}$$

Again, we have defined the differential noise increment operators according to $dB^\dagger(t) = B^\dagger(t+dt) - B^\dagger(t)$ and $dC_\mu^\dagger(t,z) = C_\mu^\dagger(t+dt,z) - C_\mu^\dagger(t,z)$. Here, the effective Hamiltonian is given by

$$H_{\rm isc}^{\rm eff} = \Omega_{\rm m}a^\dagger a + \sum_{\tau=\pm}\int dz\,\Psi_\tau^\dagger(z)\left[\tau\frac{\Omega_{\rm a}}{2} - \frac{\partial_z^2}{2m} - \frac{V}{2}\sin(2\omega_L z) + \frac{1}{2}\sum_{\tau'=\pm} g_{\tau\tau'}\Psi_{\tau'}^\dagger(z)\Psi_{\tau'}(z)\right]\Psi_\tau(z)$$
$$- (a+a^\dagger)\int dz\,\sin(2\omega_L z)\left\{\frac{\lambda}{2}\left[\Psi_+^\dagger(z)\Psi_-(z) + \Psi_-^\dagger(z)\Psi_+(z)\right] + \lambda_{\rm ex}\Psi_+^\dagger(z)\Psi_+(z)\right\}$$
$$+ \frac{1}{4}\int dz dz'\,{\rm Re}[\mathcal{G}(z,z')]\Psi_+^\dagger(z')\left[\lambda_{\rm a}^2\Psi_+(z')\Psi_+^\dagger(z) + \lambda_\pm^2\Psi_-(z')\Psi_-^\dagger(z)\right]\Psi_+(z)\,, \tag{7.8}$$

which defines the mediated atom-membrane coupling in the internal state coupling scheme. Note that the Hamiltonian (7.8) involves two different interaction processes. On the one hand, the membrane couples to the internal state of the atomic ensemble, which scales with λ and induces transitions between the state $|+\rangle$ and $|-\rangle$. On the other hand, a term which couples the membrane to the motion of the atoms in the state $|+\rangle$ arises due to the driving of the transition between the auxiliary state $|{\rm e}\rangle$ and the $|+\rangle$ state. This term scales with the strength $\lambda_{\rm ex}$. In fact, $\lambda_{\rm ex}$ and λ are not independent of each other due to the nature of the coupling as $\lambda_{\rm ex}/\lambda = \mu_+/\mu_-$. We will therefore choose the parametrization

$$\lambda_{\rm ex} = \chi\lambda\,. \tag{7.9}$$

For our following purpose, we derive the quantum Langevin equation from the QSSE (7.7) by introducing new fluctuating forces ξ_μ which correspond to fluctuations of the corresponding polarized photon fields. With the only non-zero autocorrelation functions of the field fluctuations satisfying $\langle\xi_\mu(t)\xi_{\mu'}(s)\rangle = \delta_{\mu\mu'}\delta(t-s)$, the quantum Langevin equations are given by

$$i\partial_t a = \left[a, H_{\rm isc}^{\rm eff}\right] - \lambda_{\rm m}\sum_{\mu=+,-}\xi_\mu\,, \tag{7.10a}$$
$$i\partial_t\Psi_-(z) = \left[\Psi_-(z), H_{\rm isc}^{\rm eff}\right] - \lambda_\pm\sin^2(\omega_L z)\Psi_+(z)\xi_+\,, \tag{7.10b}$$
$$i\partial_t\Psi_+(z) = \left[\Psi_+(z), H_{\rm isc}^{\rm eff}\right] - \lambda_\pm\sin^2(\omega_L z)\Psi_-(z)\xi_+ - \lambda_{\rm a}\sin^2(\omega_L z)\Psi_+(z)\xi_-\,. \tag{7.10c}$$

7.2 Mean-Field Description of a First- and Second-Order Phase Transition

In analogy to the extended GPE (6.17) of the motional interaction scheme, we assume that the atoms are prepared at low temperatures such that a large fraction occupies the ground state and a condensate is formed. At weak atom-membrane coupling, i.e., $\lambda \ll \Omega_\mathrm{m}, \Omega_\mathrm{a}$, the combined system dynamics is subject to the set of coupled mean-field equations of motion

$$i\partial_t\alpha = [\Omega_\mathrm{m} - i\Gamma_\mathrm{m}]\alpha - \sqrt{N}\lambda\chi \int dz\, \cos(2z)|\psi_+|^2 - \sqrt{N}\lambda \int dz\, \cos(2z)\mathrm{Re}\left(\psi_+^*\psi_-\right)\,, \tag{7.11a}$$

$$\begin{aligned} i\partial_t\psi_- = &\left[-\frac{\Omega_\mathrm{a}}{2} - \omega_R\partial_z^2 - \frac{V}{2}\cos(2z) + N\sum_{\tau=\pm} g_{\tau-}|\psi_\tau|^2\right]\psi_- \\ &- \frac{\sqrt{N}\lambda}{2}(\alpha+\alpha^*)\cos(2z)\psi_+\,, \end{aligned} \tag{7.11b}$$

$$\begin{aligned} i\partial_t\psi_+ = &\left[\frac{\Omega_\mathrm{a}}{2} - \omega_R\partial_z^2 - \frac{V}{2}\cos(2z) + N\sum_{\tau=\pm} g_{\tau+}|\psi_\tau|^2\right]\psi_+ \\ &- \frac{\sqrt{N}\lambda}{2}(\alpha+\alpha^*)\cos(2z)\psi_- - \sqrt{N}\lambda\chi(\alpha+\alpha^*)\cos(2z)\psi_+\,, \end{aligned} \tag{7.11c}$$

where we have scaled and shifted the atom position variable $z \to z/\omega_L + \pi/2\omega_L$, such that the lattice minima for $V > 0$ are located at the positions $z_j = j\pi$ with $j \in \mathbb{Z}$. The atomic field operators $\Psi_\tau(z)$ and the membrane ladder operator a are replaced by their mean values, i.e., $\Psi_\tau(z) \simeq \sqrt{N}\psi_\tau(z)$ and $a \simeq \sqrt{N}\alpha$. The motional coupling of the excited internal state $|+\rangle$ to the membrane leads to an asymmetry in the coupling with the asymmetry parameter χ.

The extended GPE (7.11) is, in structure, very similar to its motional coupling equivalent in (6.17). There, the steady state at zero atom-membrane coupling is characterized by a non-displaced membrane and atomic condensate. Due to the structure of the interaction potential, this symmetry is spontaneously broken at the critical atom-membrane coupling λ_c, leading to a displacement of the membrane and atomic condensate in the mean-field ground state. In the following, we show that a similar behavior occurs also in the *internal* coupling scheme, but with different characteristics. In addition, fundamentally new effects emerge, which are discussed in the subsequent section.

7.2.1 Single Mode Approximation and Cumulant Expansion

For a sufficiently deep optical lattice $V \gg \omega_R$, the condensate profile is well described by a sum of Gaussians residing in the individual lattice wells at $z_j = j\pi$. When the overlap between neighboring sites is small, the problem reduces to an effective single-site problem. It is then reasonable to make the ansatz

$$\psi_\tau(t,z) = \gamma_\tau(t)\left(\frac{1}{\pi\sigma_\tau(t)^2}\right)\exp\left(-\frac{z^2}{2\sigma_\tau(t)^2} + i\eta_\tau(t)z^2\right)\,, \tag{7.12}$$

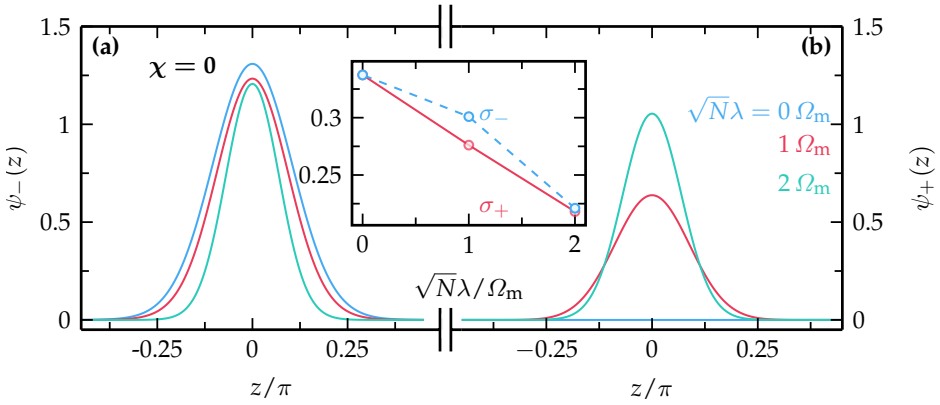

FIGURE 7.1: The steady-state condensate profile for the internal state (a) $|-\rangle$ and (b) $|+\rangle$ is shown for different values of the atom-membrane coupling, as indicated in panel (b). Here, a symmetric coupling with $\chi = 0$ is considered. The solid curves show the result obtained by using the imaginary time evolution of the extended GPE (7.11). The inset shows the condensate profile width of the corresponding internal state obtained via a Gaussian fit to the condensate profile. Other parameters used are $V = 100\,\omega_R$, $gN = \omega_R$, $\Omega_a = 50\,\omega_R$, $\Omega_m = 100\,\omega_R$ and $\Gamma_m = 10\,\omega_R$.

with $\tau = +, -$ and a constant number of atoms $|\gamma_-(t)|^2 + |\gamma_+(t)|^2 = 1$, the individual condensate widths $\sigma_\tau(t)$ and corresponding phases $\eta_\tau(t)$. In order to reduce the number of parameters, we here restrict to the special case $g_{\tau\tau'} \equiv g$. However, we note that for a binary BEC, this actually corresponds to a delicate regime as the ground state is either a miscible or immiscible state[1]. In fact, a mixture of the condensate profiles associated with the two different internal states is energetically preferred to the unmixed case for the underlying problem. Already from equation (7.11a), we can see that a maximally mixed condensate maximizes the effective coupling between the atoms and the membrane. This will eventually lead to a minimization of the effective nonequilibrium potential, which we will derive in the following.

But before, let us justify this ansatz. Therefore, we numerically determine the steady state of the extended GPE (7.11) by using an imaginary time evolution with the Crank–Nicolson scheme as described in appendix C. Due to the periodicity of the potential, we use periodic boundary conditions and evaluate the steady state within the interval from $-\pi/2$ to $\pi/2$. In figure 7.1, the condensate profile in a single potential well is shown for the symmetric coupling case $\chi = 0$ and different coupling constants λ, see the color coding in figure 7.1(b). The panels (a) and (b) show the condensate profile of the internal states $|-\rangle$ and $|+\rangle$, respectively, as a function of the position z. The well minimum is located at $z = 0$. In addition, we consider the case $\mu_+ = \mu_-$ that corresponds to $\chi = 1$ and show the numerically calculated condensate profile in figure 7.2. Again, the profile of the state $|-\rangle$ is shown in panel (a) and that of the internal state $|+\rangle$ is shown in panel (b). Moreover, the insets compare the individual widths σ_- and σ_+ obtained from a Gaussian fit to the condensate profile according to equation 7.12. The deviations between the individual widths are

[1]The immiscible state is characterized by a condensate profile where atoms in different internal states avoid each other and the overlap between the wave functions $\psi_\pm(z)$ is minimal. In the miscible phase, on the other hand, the condensate profile of different internal states is mixable.

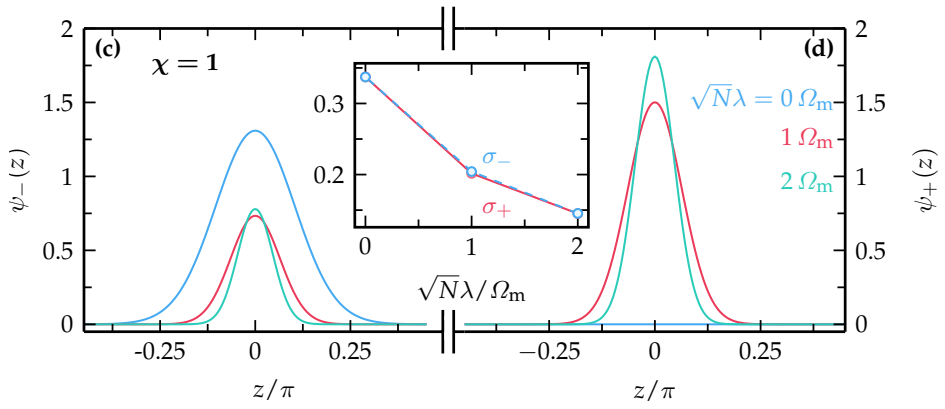

FIGURE 7.2: The steady-state condensate profile for the internal state (a) $|-\rangle$ and (b) $|+\rangle$ is shown for different atom membrane coupling rates, as indicated in panel (b). Here, a asymmetric coupling with $\chi = 1$ is considered. The solid curves show the result obtained by using the imaginary time evolution of the extended GPE (7.11). The inset shows the condensate profile width of the corresponding internal state obtained via a Gaussian fit to the condensate profile. Other parameters used are $V = 100\,\omega_R$, $gN = \omega_R$, $\Omega_a = 50\,\omega_R$, $\Omega_m = 100\,\omega_R$ and $\Gamma_m = 10\,\omega_R$.

negligible in most cases and slightly increase only in the vicinity of the critical point $\lambda \gtrsim \lambda_c$. Consequently, we can approximate the condensate profiles by a unified condensate width $\sigma = \sigma_- = \sigma_+$ and phase $\eta = \eta_- = \eta_+$, which drastically simplifies our description.

Next, we perform a cumulant expansion of the equations (7.11) in order to determine the dynamics of the respective variational parameters. That is, we calculate the (i) zeroth and (ii) second cumulants by multiplying equations (7.11b) and (7.11b) (i) with $\psi_0(z) = e^{-z^2/2\sigma^2 - i\eta z^2}/(\pi\sigma^2)^{1/4}$ as well as (ii) with $(z^2 - \sigma^2/2)\psi_0(z)$ and integrate then over z. This leads to five independent equations of motion of which one is given by $\dot{\sigma} = 4\omega_R\eta\sigma$. By defining the effective potential

$$\begin{aligned} E[\alpha,\gamma_-,\gamma_+,\sigma] =& \Omega_m|\alpha|^2 + \frac{\Omega_a}{2}\left(|\gamma_+|^2 - |\gamma_-|^2\right) + \frac{\omega_R}{2\sigma^2} - \frac{V}{2}e^{-\sigma^2} + \frac{Ng}{\sqrt{8\pi}\sigma} \\ & - \sqrt{N}\lambda(\alpha+\alpha^*)\left(\chi|\gamma_+|^2 + \mathrm{Re}\{\gamma_+^*\gamma_-\}\right)e^{-\sigma^2}, \end{aligned} \tag{7.13}$$

the equations of motion are given in a compact way

$$\dot{\alpha} = -i\partial_{\alpha^*}E - \Gamma_m\alpha\,, \tag{7.14a}$$

$$\dot{\gamma}_\tau = -i\partial_{\gamma_\tau^*}E\,, \tag{7.14b}$$

$$(4\omega_R)^{-1}\ddot{\sigma} = -\partial_\sigma E\,. \tag{7.14c}$$

Due to the damping, the variational parameters will eventually equilibrate to a steady-state configuration. Consequently, the steady-state profile is obtained by setting the time derivatives to zero and solving the set of equations for α_0, $\gamma_{\tau,0}$ and σ_0. The last term in equation (7.13) illustrates that a maximally mixed atomic condensate minimizes the effective potential energy.

7.2.2 Nonequilibrium Potential and Steady-State Configuration

From the steady state of the set of equations (7.14) follows the relation for the membrane amplitude

$$\alpha_0(\gamma,\sigma) = \frac{\sqrt{N}\lambda}{\Omega_\mathrm{m} - i\Gamma_\mathrm{m}}\left[\chi\gamma^2 + \gamma\sqrt{1-\gamma^2}\right] e^{-\sigma^2}\,. \tag{7.15}$$

Assuming that both occupation parameters γ_τ are real-valued and by using the normalization condition $\gamma_-^2 + \gamma_+^2 = 1$, we have introduced $\gamma \equiv \gamma_+$. With the relation for $\alpha_0(\gamma,\sigma)$, the energy potential $E[\alpha, \sqrt{1-\gamma^2}, \gamma, \sigma]$ can be expressed in terms of the condensate variational parameters

$$E[\gamma,\sigma] = -\frac{\Omega_\mathrm{a}}{2}\left[1-2\gamma^2\right] - \frac{N\lambda^2}{\Omega_\mathrm{m}'}\left[\chi\gamma^2 + \gamma\sqrt{1-\gamma^2}\right]^2 e^{-2\sigma^2} + \frac{\omega_R}{2\sigma^2} + \frac{Ng}{\sqrt{8\pi}\sigma} - \frac{V}{2}e^{-\sigma^2}\,, \tag{7.16}$$

where we have defined the primed mechanical frequency $\Omega_\mathrm{m}' = \Omega_\mathrm{m} + \Gamma_\mathrm{m}^2/\Omega_\mathrm{m}$.

The steady-state configuration $(\alpha_0, \gamma_0, \sigma_0)$ is characterized by a global minimum of the nonequilibrium potential $E_\mathrm{min} = E[\gamma_0, \sigma_0]$ according to the equations (7.14). The defining equations for these steady-state values are given by

$$V e^{-\sigma_0^2}\sigma_0 + \frac{4N\lambda^2}{\Omega_\mathrm{m}'}\left[\chi\gamma_0^2 + \gamma_0\sqrt{1-\gamma_0^2}\right]^2 e^{-2\sigma_0^2}\sigma_0 = \frac{\omega_R}{\sigma_0^3} + \frac{Ng}{\sqrt{8\pi}\sigma_0^2}\,, \tag{7.17a}$$

$$\gamma_0\left[N\lambda^2\left(\chi\gamma_0 + \sqrt{1-\gamma_0^2}\right)\left(2\chi\gamma_0\sqrt{1-\gamma_0^2} + 1 - 2\gamma_0^2\right) - N\lambda_\Omega^2 e^{2\sigma_0^2}\right] = 0\,, \tag{7.17b}$$

where we have defined the coupling rate[2] $\sqrt{N}\lambda_\Omega = \sqrt{\Omega_\mathrm{m}'\Omega_\mathrm{a}}$. Equation (7.17b) suggests the solution $\gamma_0 = 0$, which either minimizes or maximizes the nonequilibrium potential E and, hence, it is either a possible steady-state value or not. In order to answer this question, one has to consider the second derivative of E with respect to the atomic polarization variable γ at $\gamma = 0$. Instead, we first minimize the effective nonequilibrium potential with respect to σ and study the energy $E(\gamma) = E[\gamma, \sigma_0(\gamma)]$.

Figure 7.3 shows the normalized energy surface $\mathcal{E}(\gamma)$, which is defined according to equation (6.31), as a function of γ and the coupling constant λ. The dashed curves indicate the global minimum γ_0 of the potential energy. In the two panels (a) and (b), we consider the symmetric coupling regime, i.e., $\chi = 0$, with atomic transition frequencies $\Omega_\mathrm{a} = 50\,\omega_R$ and $\Omega_\mathrm{a} = 5000\,\omega_R$, respectively. Below a certain value of the coupling strength $\lambda \leq \lambda_\mathrm{c}$, the potential is minimized for $\gamma = 0$ and the system equilibrates to a completely polarized state, where all atoms reside in the energetically lower internal state $|-\rangle$. At the critical point $\lambda = \lambda_\mathrm{c}$, the system undergoes a nonequilibrium quantum phase transition that is characterized by a non-vanishing polarization variable $\gamma_0 \neq 0$. Interestingly, the behavior of the order parameter γ in the vicinity of the critical point differs in (a) and (b). For $\Omega_\mathrm{a} = 50\,\omega_R$ in (a), we find a continuous transition of the order parameter γ_0 at $\lambda = \lambda_\mathrm{c}$. In the limit of

[2] The definition of the coupling rate λ_Ω is in correspondence to the previously defined atom-membrane coupling rate λ_V of the motional coupling scheme. We will later see that λ_Ω approximates the critical coupling rate in the regime of a continuous phase transition within a rather deep optical lattice, just as λ_V approximated the critical coupling in the external state coupling setup.

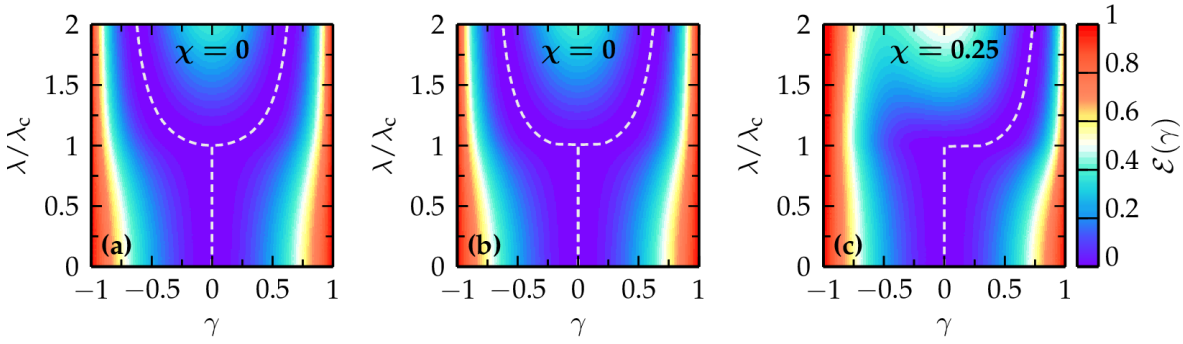

FIGURE 7.3: The normalized potential surface $\mathcal{E}(\gamma)$ is shown as a function of the atomic polarization parameter γ and the atom-membrane coupling strength λ. The dashed white curves show the steady-state configuration. In panel (a) and (b), a symmetric coupling ($\chi = 0$) is considered with $\Omega_a = 50\,\omega_R$ and $\Omega_a = 5000\,\omega_R$, respectively. In (a), the system exhibits a second-order phase transition, whereas the system undergoes a first-order phase transition in (b). In panel (c) is considered the asymmetric coupling regime with $\chi = 0.25$ and $\Omega_a = 50\,\omega_R$. Here, the system always exhibits an *asymmetric* first-order phase transition, characterized by a single favored atomic polarization. The other parameters throughout all panels are $V = 100\,\omega_R$, $gN = \omega_R$, $\Omega_m = 2\,\Omega_a$ and $\Gamma_m = 0.1\,\Omega_m$.

a large atom-membrane coupling strength, the bistable order parameter saturates to $\gamma_0 = \pm 1/\sqrt{2}$, which corresponds to the two states $(|-\rangle \pm |+\rangle)/\sqrt{2}$. The behavior of the order parameter suggests that, in this regime, the system exhibits a second-order NQPT with the critical behavior $\gamma_0 \sim (\lambda - \lambda_c)^{1/2}$ with the mean-field exponent $1/2$. In contrast, the order parameter shows a jump at the critical point λ_c in (b) for the larger transition frequency of $\Omega_a = 5000\,\omega_R$, indicating that the system also features a discontinuous phase transition.

Moreover, in figure 7.3(c) is shown an example of an *asymmetric* first-order NQPT for the same parameters as before, but with $\chi = 0.25$ and $\Omega_a = 50\,\omega_R$. This regime is characterized by a preferred atomic polarization $\gamma_0 > 0$ above the threshold λ_c. The branch $\gamma < 0$, which also locally minimizes the energy potential for $\lambda \geq \lambda_c$, is energetically raised compared to the steady-state solution.

In the case of a second-order NQPT, we label the critical coupling by λ_{s2}. Then, an implicit definition of λ_{s2} is found by inserting $\sigma_0^2 = \log(\lambda_{s2}/\lambda_\Omega)$ (see footnote 3) in equation (7.17a). Note that this equation relates the critical point of the continuous phase transition to the previously defined coupling rate λ_Ω via $\lambda_{s2} = \lambda_\Omega e^{\sigma_0^2}$. Hence, we find the implicit equation for the critical coupling rate

$$\omega_R + \frac{Ng}{\sqrt{8\pi}}\sqrt{\log\frac{\lambda_{s2}}{\lambda_\Omega}} = V\left(\frac{\lambda_\Omega}{\lambda_{s2}}\right)\left(\log\frac{\lambda_{s2}}{\lambda_\Omega}\right)^2 . \tag{7.18}$$

Yet, in the event of a symmetric or asymmetric first-order NQPT, such an implicit definition of the corresponding critical coupling rate can not be found on the basis of the set of equations (7.17). However, a procedure to find the critical points can be defined by performing a Landau expansion of the effective nonequilibrium potential $E(\gamma)$. Moreover, Landau theory allows to classify the order of the phase transition by evaluating the Landau expansion

[3] This width is a possible solution of equation (7.17b) as the term in the brackets vanishes.

coefficients of the present nonequilibrium potential.

7.2.3 Landau Expansion of the Nonequilibrium Potential

In order to verify whether figure 7.3(b) really shows a first-order phase transition, we expand the nonequilibrium potential $E(\gamma)$ around the order parameter $\gamma_0 = 0$. Due to the asymmetry in the coupling, the Taylor expansion takes in general the form $E(\gamma) = a_0 + \sum_{n\geq 2} a_n \gamma^n$, allowing also odd orders in n. In order to fix the condensate width to its value $\sigma_0(\gamma)$, we define the auxiliary function

$$F[\sigma,\gamma] = Ve^{-\sigma^2}\sigma + \frac{4N\lambda^2}{\Omega'_{\mathrm{m}}}\left[\chi\gamma^2 + \gamma\sqrt{1-\gamma^2}\right]^2 e^{-2\sigma^2}\sigma - \frac{\omega_R}{\sigma^3} - \frac{Ng}{\sqrt{8\pi}\sigma^2}\,, \tag{7.19}$$

which is nothing else but the first derivative of the nonequilibrium potential with respect to σ. Hence, the width is fixed by the condition $F[\sigma_0(\gamma),\gamma] = 0$. In the following, we omit the γ-dependence of σ_0 and, since the Landau expansion is performed around $\gamma = 0$, the equilibrium value is understood as $\sigma_0 \equiv \sigma_0(\gamma = 0)$. The zeroth- and second-order expansion coefficients are determined straightforwardly to

$$a_0 = -\frac{\Omega_{\mathrm{a}}}{2} + \frac{\omega_R}{2\sigma_0^2} - \frac{V}{2}e^{-\sigma_0^2} + \frac{Ng}{\sqrt{8\pi}\sigma_0}\,, \tag{7.20a}$$

$$a_2 = \Omega_{\mathrm{a}}\left[1 - \left(\frac{\lambda}{\lambda_{\mathrm{s2}}}\right)^2\right]. \tag{7.20b}$$

Note that in order to evaluate a_2, we have used that $F[\sigma_0, 0] = 0$ and $(\partial_\gamma F[\sigma,\gamma])_{\sigma=\sigma_0,\gamma=0} = 0$. To evaluate the higher-order Landau coefficients, we first perform the derivatives of the steady-state width σ_0 with respect to the order parameter γ. This is done by means of the theorem of implicit functions for which we use the auxiliary function $F[\sigma,\gamma]$, given in equation (7.19). For instance, the first derivative is given by the expression $\sigma_0' = (\partial\sigma_0/\partial\gamma)_{\gamma=0} = -(\partial_\gamma F[\sigma,\gamma])/(\partial_\sigma F[\sigma,\gamma])|_{\sigma=\sigma_0,\gamma=0}$. Keeping this in mind, we find the implicit derivatives

$$\sigma_0' = 0\,, \tag{7.21a}$$

$$\sigma_0'' = -8\Omega_{\mathrm{a}}\left(\frac{4\omega_R}{\omega_\sigma^2}\right)\left(\frac{\lambda}{\lambda_{\mathrm{s2}}}\right)^2\sigma_0\,, \tag{7.21b}$$

$$\sigma_0''' = 6\chi\sigma_0''\,, \tag{7.21c}$$

$$\sigma_0^{(4)} = \left(\frac{3-12\sigma_0^2}{\sigma_0}\right)(\sigma_0'')^2 - (12-6\chi^2)\sigma_0''\,, \tag{7.21d}$$

where we have defined the frequency of the atomic breathing mode

$$\omega_\sigma^2 = 4\omega_R\left[\frac{3\omega_R}{\sigma_0^4} + \frac{Ng}{\sqrt{2\pi}\sigma_0^3} + V(1-2\sigma_0^2)e^{-\sigma_0^2}\right]. \tag{7.22}$$

With these relations, the Landau coefficients $a_n = (\partial_\gamma^n E/n!)_{\gamma=0}$ up to sixth-order are given in the compact form

$$a_3 = -2\Omega_\mathrm{a}\left(\frac{\lambda}{\lambda_{\mathrm{s}2}}\right)^2 \chi\,, \tag{7.23a}$$

$$a_4 = \Omega_\mathrm{a}\left(\frac{\lambda}{\lambda_{\mathrm{s}2}}\right)^2 \left[1+\sigma_0\sigma_0'' - \chi^2\right]\,, \tag{7.23b}$$

$$a_5 = \Omega_\mathrm{a}\left(\frac{\lambda}{\lambda_{\mathrm{s}2}}\right)^2 \left[1+4\sigma_0\sigma_0''\right]\chi\,, \tag{7.23c}$$

$$a_6 = \frac{\Omega_\mathrm{a}}{6}\left(\frac{\lambda}{\lambda_{\mathrm{s}2}}\right)^2 \left[\left(1-4\sigma_0^2\right)\left(\sigma_0''\right)^2 - 12\sigma_0\left(1-3\chi^2\right)\sigma_0''\right]\,. \tag{7.23d}$$

As the second derivative of the width σ_0'' is always smaller than zero, the sixth-order expansion coefficient consequently fulfills $a_6 > 0$ for any set of parameters other than $\lambda = 0$. Hence, in order to describe a first-order nonequilibrium quantum phase transition in the symmetric coupling regime ($\chi = 0$), it is sufficient to consider the Landau coefficients up to sixth-order.

7.2.3.1 The Symmetric Coupling Regime

For a symmetric atom-membrane coupling ($\chi = 0$), the odd Landau coefficients vanish, since $a_{2n+1} \sim \chi$ for all $n \in \mathbb{N}$. This fact is intuitive as the nonequilibrium potential is symmetric in γ for $\chi = 0$, i.e., $E(\gamma) = E(-\gamma)$. Hence, the Landau expansion takes the form

$$E(\gamma) = a_0 + a_2\gamma^2 + a_4\gamma^4 + a_6\gamma^6 + \mathcal{O}(\gamma^8)\,. \tag{7.24}$$

In order to quantify the order of the phase transition, we have to look at the sign of the expansion coefficient a_4. The phase transition is continuous when $a_4 > 0$ and discontinuous for $a_4 < 0$ at the critical point. Indeed, the coefficient exhibits a point at which it changes its sign. From equation (7.23b), it directly follows that this point is given by the relation $1 + \sigma_0\sigma_0'' = 0$. For $a_4 = 0$, the phase transition occurs for $a_2 = 0$, or, in other words, when $\lambda = \lambda_{\mathrm{s}2}$. Hence, we can insert this expression for the atom-membrane coupling rate to find the relation

$$\Omega_\mathrm{c} = \frac{\omega_\sigma^2}{32\omega_R\sigma_0^2} = \frac{\omega_\sigma^2}{32\omega_R\log(\lambda_{\mathrm{s}2}/\lambda_\Omega)}\,, \tag{7.25}$$

which defines a critical atomic transition frequency, or alternatively a critical potential depth V_c or atomic interaction strength Ng_c. Below $\Omega_\mathrm{a} \leq \Omega_\mathrm{c}$, the phase transition is continuous and becomes discontinuous for transition frequencies satisfying $\Omega_\mathrm{a} > \Omega_\mathrm{c}$. This fact is depicted in the two panels of figure 7.4. In 7.4(a), it is shown that by altering either the potential depth V or the atomic transition frequency Ω_a, the order of the phase transition can be tuned from second- (blue region below dashed curve) to first-order (orange region). Alternatively, by changing the atomic interaction strength Ng, the order may also be tuned, which is shown in figure 7.4(b).

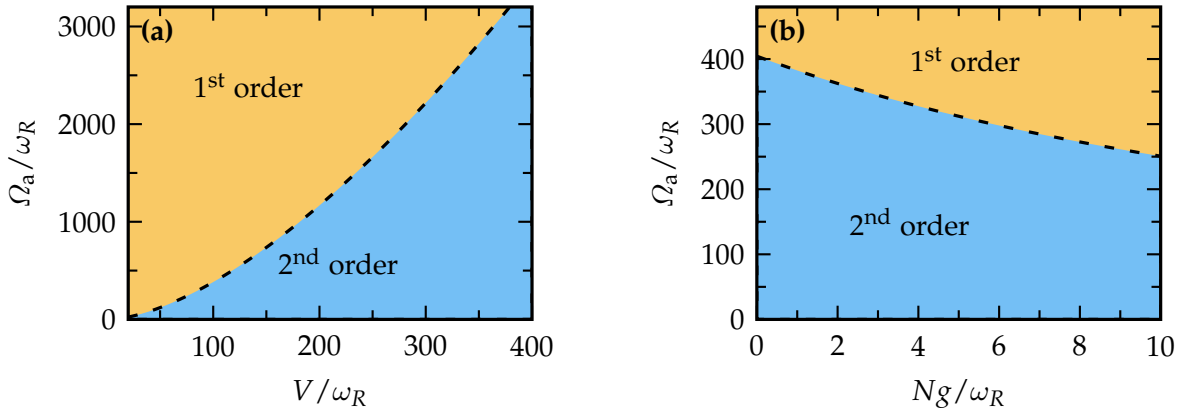

FIGURE 7.4: The phase diagram of the NQPT is shown as a function of the atomic transition frequency Ω_a and (a) the lattice depth V or (b) the interaction strength Ng. While the phase transition is a continuous PT in the blue regions, it is a discontinuous PT in the orange regions. The dashed curves show the critical transition frequency $\Omega_a = \Omega_c$ according to equation (7.25). The fixed parameter in (a) is the interaction strength $Ng = \omega_R$ and in (b) the potential depth $V = 100\,\omega_R$.

In the second-order regime, the critical coupling λ_{s2} is implicitly given by equation (7.18). In order to define the critical coupling rate λ_{s1} in the first-order regime, we make use of the Landau expansion. By taking the Landau expansion up to sixth-order, the nonequilibrium potential $E(\gamma)$ exhibits 3 minima on the real axis if $a_4 < 0$. The three local minima are located at

$$\gamma_1 = 0\,, \qquad \gamma_{2,3}^2 = -\frac{a_4}{3a_6} + \sqrt{\left(\frac{a_4}{3a_6}\right)^2 - \frac{a_2}{3a_6}}\,, \tag{7.26}$$

if $a_2 > 0$. The local minimum at $\gamma = 0$ has a value of $E(0) = a_0$ and the critical coupling rate λ_{s1} is found by equating $E(\gamma_{2,3})|_{\lambda=\lambda_{s1}} = a_0$. After some tedious algebra, this leads to the defining relation for the critical coupling rate in the first-order regime

$$13 a_2 a_6|_{\lambda=\lambda_{s1}} = 4 a_4^2|_{\lambda=\lambda_{s1}}\,, \tag{7.27}$$

which has to be solved on the surface $F[\sigma_0, 0] = 0$. With the definitions of the expansion coefficients in (7.27), we find the relation

$$52\left[1-\left(\frac{\lambda_{s1}}{\lambda_{s2}}\right)^2\right]\left[2(1-4\sigma_0^2)\left(\frac{\lambda_{s1}}{\lambda_{s2}}\right)^2 + \frac{3\omega_\sigma^2}{4\omega_R\Omega_a}\right]\sigma_0^2 = 3\left[\frac{\omega_\sigma^2}{4\omega_R\Omega_a} - 8\left(\frac{\lambda_{s1}}{\lambda_{s2}}\right)^2\sigma_0^2\right]^2. \tag{7.28}$$

By inserting the critical transition frequency Ω_c in this expression, we can further simplify this equation and find that the critical coupling rate for the discontinuous NQPT follows from

$$13\left[1-\left(\frac{\lambda_{s1}}{\lambda_{s2}}\right)^2\right]\left[\left(\log^{-1}\frac{\lambda_{s2}}{\lambda_\Omega} - 4\right)\left(\frac{\lambda_{s1}}{\lambda_{s2}}\right)^2 + 12\frac{\Omega_c}{\Omega_a}\right] = 24\left[\frac{\Omega_c}{\Omega_a} - \left(\frac{\lambda_{s1}}{\lambda_{s2}}\right)^2\right]^2, \tag{7.29}$$

from which we can conclude that $\lambda_{s1} < \lambda_{s2}$. In addition, we recover $\lambda_{s1} = \lambda_{s2}$ in the limit $\Omega_a = \Omega_c$.

7.2.3.2 The Asymmetric Coupling Regime

In the case of asymmetric coupling ($\chi \neq 0$), the Landau coefficients of odd order are finite. This breaks the symmetry in the nonequilibrium potential with respect to $\gamma = 0$, in other words, $E(\gamma) \neq E(-\gamma)$. In order to determine the critical coupling rate λ_{a1}, we consider the Landau expansion up to fourth order

$$E(\gamma) = a_0 + a_2\gamma^2 + a_3\gamma^3 + a_4\gamma^4 + \mathcal{O}(\gamma^5)\,. \tag{7.30}$$

Hence, we restrict to the case $a_4 > 0$. Then, the nonequilibrium potential $E(\gamma)$ below the critical point exhibits two local minima which are located at

$$\gamma_1 = 0\,, \qquad \gamma_2 = -\frac{3a_3}{8a_4} + \sqrt{\left(\frac{3a_3}{8a_4}\right)^2 - \frac{a_2}{2a_4}}\,. \tag{7.31}$$

For any set of parameters in the asymmetric coupling regime, we find that $\gamma_2 \neq \gamma_1 = 0$. Hence, the order parameter exhibits a jump at the critical point when the value of the nonequilibrium potential $E(\gamma_2)$ at γ_2 becomes smaller than $E(0)$ and a discontinuous NQPT occurs.

In a similar fashion as before, we equate $E(\gamma_2) = a_0$ and find the defining relation for the critical atom-membrane coupling strength according to

$$4a_2a_4\big|_{\lambda=\lambda_{\mathrm{a1}}} = a_3^2\big|_{\lambda=\lambda_{\mathrm{a1}}}\,. \tag{7.32}$$

Again, this equation has to be solved under the restriction that $F[\sigma_0, 0] = 0$. It is straightforward to show that λ_{a1} has to be smaller than λ_{s2}.

Note that if $a_4 < 0$, the expansion to fourth order is not sufficient anymore. This is for example the case when $\chi \geq 1 + \sigma_0\sigma_0''$ or $\Omega_{\mathrm{a}} \geq \Omega_{\mathrm{c}}$. Then, terms up to sixth-order have to be taken into account and an analytic expression for the local extrema cannot be found. Consequently, the calculation of the critical coupling rate can no longer be reduced to an equation like (7.32).

7.2.4 Hysteresis in the First-Order Regime

A characteristic feature of a first-order phase transition is the existence of hysteresis when the atom-membrane coupling λ is tuned adiabatically. In terms of the nonequilibrium potential, this is included by the existence of two or more local minima. At a certain coupling rate, these local minima become dynamically unstable and eventually turn into a maximum. At this point, the system jumps to the neighboring local minimum and remains there until this minimum becomes unstable. In the following, we consider the two generic cases of a symmetric and asymmetric coupling to discuss this effect.

In order to describe the hysteretic behavior, we take the equations of motion (7.14) with $\gamma(t) = \gamma_+(t)$ and adiabatically alter the atom-membrane coupling strength. Thus, we obtain for each λ a long-time solution $\gamma_\infty = \lim_{t\to\infty}\gamma(t)$ which becomes time independent. In

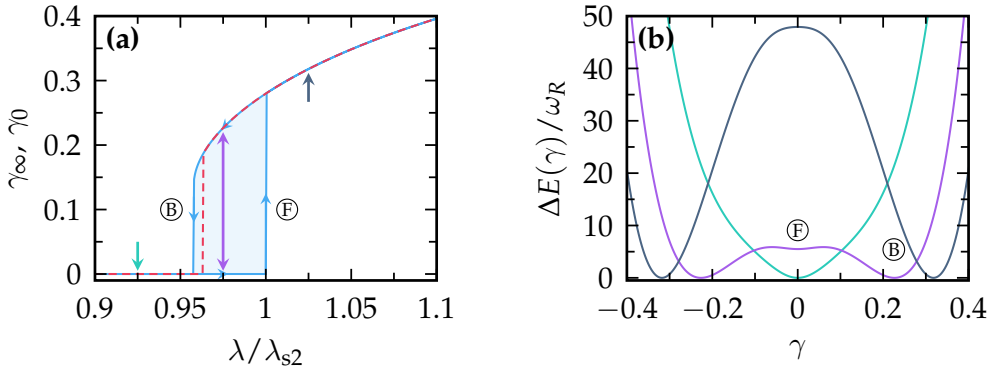

FIGURE 7.5: (a) Hysteresis curve (γ_∞, solid) shown as a function of the coupling parameter λ for the symmetric first-order phase transition. The dashed curve shows the stationary polarization γ_0. (b) Curves of the effective nonequilibrium potential $\Delta E(\gamma) = E(\gamma) - E(\gamma_0)$ are shown for a coupling strength below and above the turning points, $\lambda \leq \lambda_B$ and $\lambda \geq \lambda_F$, and in the coexistence area $\lambda_B < \lambda < \lambda_F$. The colors of the potential curves in (b) mark the associated configurations pointed to by the colored arrows in (a). The circled letters indicate the minimum of the forward (F) and backward (B) path. The parameters were chosen as in figure 7.3(b) according to $\Omega_\mathrm{a} = 5000\,\omega_R$, $V = 100\,\omega_R$, $gN = \omega_R$, $\Omega_\mathrm{m} = 2\,\Omega_\mathrm{a}$ and $\Gamma_\mathrm{m} = 0.1\,\Omega_\mathrm{m}$.

figure 7.5(a) and 7.6(a), we show the hysteresis for the symmetric and asymmetric ($\chi = 0.25$) first-order phase transition, respectively. On the forward path, the coupling strength λ is adiabatically increased and the system is initially placed in the minimum at $\gamma = 0$. The system stays there until it becomes unstable at $\lambda = \lambda_F$ and jumps to the adjacent minimum at $\gamma \neq 0$. This point is defined by $a_2 = 0$ and coincides with the critical coupling rate λ_{s2} in the symmetric regime. Afterwards, the steady-state solution $\gamma_0 \neq 0$ is followed as λ increases.

On the backward path, the system follows the steady-state minimum at $\gamma_0 \neq 0$ until this point becomes dynamically unstable at λ_B and jumps to the solution at $\gamma_\infty = 0$. For the symmetric case in 7.5(a), this jumping point is given by the relation $3a_2a_6 - a_4^2 = 0$, whereas it is given by the relation $32a_2a_4 - 9a_3^2 = 0$ for the asymmetric case 7.6(a).

In the picture of potential energy surfaces, the reason of the hysteresis behavior is the existence of multiple stable local minima at $\gamma = 0$ and $\gamma \neq 0$ in the coexistence region $\lambda_B \leq \lambda \leq \lambda_F$ as indicated in figure 7.5(b). Here, the forward and backward minima are indicated by the circled capital letters F and B, respectively. The same argumentation applies to the *asymmetric* first-order phase transition. The structure of the effective potential surface is shown in figure 7.6(b) for three different values of the atom-membrane coupling λ. The colors of the potential curves in (b) mark the associated configurations pointed to by the colored arrows in (a).

7.3 Outlook: Experimental Realization

Current state-of-the-art experiments use the motional coupling scheme [131, 132]. As we have shown in Chapter 6, the occurring phase transition is always of second-order as both

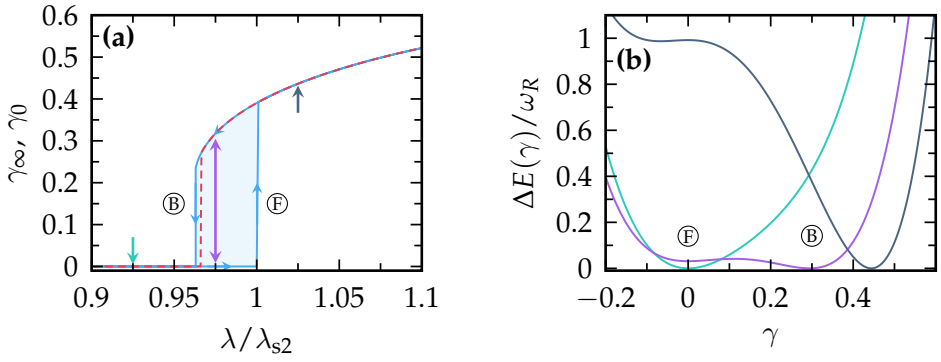

FIGURE 7.6: (a) Hysteresis curve (γ_∞, solid) shown as a function of the coupling parameter λ for the asymmetric first-order phase transition with $\chi = 0.25$. The dashed curve shows the stationary polarization γ_0. (b) Curves of the effective nonequilibrium potential $\Delta E(\gamma) = E(\gamma) - E(\gamma_0)$ are shown for a coupling strength below and above the turning points, $\lambda \leq \lambda_B$ and $\lambda \geq \lambda_F$, and in the coexistence area $\lambda_B < \lambda < \lambda_F$. Again, different colors correspond to different values of the atom-membrane coupling that are indicated by the same colored arrows in (a). The circled letters indicate the minimum of the forward (F) and backward (B) path. The parameters were chosen as in figure 7.3(c) according to $\Omega_\mathrm{a} = 50\,\omega_R$, $V = 100\,\omega_R$, $gN = \omega_R$, $\Omega_\mathrm{m} = 2\,\Omega_\mathrm{a}$ and $\Gamma_\mathrm{m} = 0.1\,\Omega_\mathrm{m}$.

relevant energy scales are related to the potential depth, see equation (6.39) and the discussion below. In that sense, the internal-state coupling scheme overcomes this limitation. Then, the transition between the first- and second-order is observable by either measuring the membrane eigenfrequency or the condensate width σ_0. In the case of the first-order NQPT, these quantities exhibit a discontinuous behavior which appears as a jump at the critical point. Another possible measure to observe the phase transition is the condensate polarization $\gamma_0\,(\gamma_\infty)$ which can detect the NQPT in a straightforward manner.

Concerning realistic experimental parameters, typical configurations operate with a membrane of a frequency $\Omega_\mathrm{m} \simeq 70\,\omega_R$ [130, 132]. Then, for an atomic transition frequency $\Omega_\mathrm{a} \simeq 20\,\omega_R$ and $\lambda \simeq \lambda_\mathrm{ex}$, the critical coupling constant is estimated to be $\sqrt{N}\lambda_\mathrm{c} \simeq 29\,\omega_R$. Such a coupling may be reached by increasing the cavity finesse or the laser power of these experiments by an overall factor of 10. Current setups accomplish the effective atom-membrane coupling by utilizing ^{87}Rb atoms. These atoms can readily be used to realize the internal state coupling scheme. For this, the internal states $|\tau = +, -, \mathrm{e}\rangle$ may be chosen as the hyperfine states $|-\rangle = |5^2S_{1/2}, F = 2, m_f = 2\rangle$, $|-\rangle = |5^2S_{1/2}, F = 2, m_f = 0\rangle$, and $|\mathrm{e}\rangle = |5^2P_{1/2}, F = 2, m_f = 1\rangle$.

Clearly, the *internal* state coupling scheme is superior to the *motional* coupling scheme from the perspective of storing quantum information. When encoded in discrete atomic states rather than in continuous, motional states, the quantum information is less fragile to fluctuations. Finally, let us note that the asymmetry parameter χ can be tuned by applying an additional laser field perpendicular to the coupling beam which drives the transition $|-\rangle$ to $|+\rangle$. This gives rise to an additional term of the form $\delta(\gamma_+^*\gamma_- + \mathrm{c.c.})$ in the potential energy (7.13). By compensating an additional force on the membrane that scales with $\sqrt{N}\lambda$, tuning the parameter δ allows for an indirect variation of χ.

Measuring the offset of a second-order phase transition is experimentally challenging as

all observables change continuously with the control parameter (here, the atom-membrane coupling strength λ). In contrast to this, the detection of the quantum critical point for a first-order phase transition is often easier to achieve, since the relevant measurable quantities exhibit a jump at this very point. In addition to this, dissipative first-order phase transitions have recently been proposed as an interesting tool for quantum sensing [235].

In the next chapter, we will discuss another possible application for the coupling of an atomic gas to the motion of a nanomechanical oscillator. We will show that the mechanical mode can be squeezed by the back-action of internal excitations of the atoms in the gas and that this effect is enhanced by finite particle interactions in the condensate.

CHAPTER 8

Enhanced Mechanical Displacement Squeezing Induced by Atomic Interactions

A Bogoliubov approach reveals that the internal excitations form a fluctuating environment of quasi-particle excitations for the mechanical mode with a gapped spectral density. Nanomechanical squeezing arises due to quasi-particle excitations in the interacting atom gas when the mechanical frequency is close to resonance with the internal atomic transitions. This nanomechanical squeezing is enhanced by finite atom-atom interactions. The results presented in this chapter have been partially published in:

N. Mann and M. Thorwart, "Enhancing nanomechanical squeezing by atomic interactions in a hybrid atom-optomechanical system", Physical Review A **98**, 063804 (2018).

In the preceding chapters, we have studied the nonequilibrium quantum phase transition in the mean-field regime. While it was found that tuning the interaction strength can lead to a change of the NQPT from a first- to second-order phase transition, the effect of the interaction led to no qualitative change in the features of the PT. In this chapter, we will investigate the atom-optomechanical system, with the aim to determine possible effects beyond the mean field approach of a finite atom-atom interaction.

For symmetric coupling ($\chi = 0$), the effective Hamiltonian of the hybrid system in the internal state coupling scheme takes the form

$$\begin{aligned} H =& \Omega_{\mathrm{m}} a^{\dagger} a + \sum_{\tau=\pm} \int dz\, \Psi_{\tau}^{\dagger}(z) \left[\tau \frac{\Omega_{\mathrm{a}}}{2} - \omega_R \partial_z^2 - \frac{V}{2} \cos(2z) + \frac{1}{2} \sum_{\tau'=\pm} g_{\tau\tau'} \Psi_{\tau'}^{\dagger}(z) \Psi_{\tau'}(z) \right] \Psi_{\tau}(z) \\ & - \frac{\lambda}{2} (a^{\dagger} + a) \int dz\, \cos(2z) \left[\Psi_{+}^{\dagger}(z) \Psi_{-}(z) + \Psi_{-}^{\dagger}(z) \Psi_{+}(z) \right] . \end{aligned} \tag{8.1}$$

The aim of this chapter is to identify a relevant feature induced by finite particle-particle interactions in the atomic condensate. It is well known that squeezed states can be generated

by such nonlinearities [152, 153], such as particle interactions. In addition to this, engineering the environment of an optomechanical setup can produce a squeezed-vacuum reservoir and a transfer of squeezing to the movable mirror may occur [149]. For this purpose, we describe the atom gas by a two-species Bose–Hubbard model. Under the assumption of not too strong local atom-atom interactions, the quartic interaction terms are reduced to terms that are quadratic in the bosonic ladder operators. This allows us to analytically solve the problem and study the effect of finite moderately strong interactions beyond the mean-field level.

8.1 Extended Bose–Hubbard Model for an Atom-Optomechanical System

In the following, we assume a deep optical lattice for which we can expand the atomic field operator $\Psi_\tau(z) = \sum_{j=1}^{L} w(z-z_j)c_{j\tau}$ in terms of Wannier functions $w(z-z_j)$ at the lattice sites $z_j = j\pi$. Moreover, $c_{j\tau}$ is the bosonic ladder operator which annihilates an atom in the internal state $\tau = +,-$ on site j and we consider a total number of L sites. Within this ansatz, the effective Hamiltonian is reduced to a two-species Bose-Hubbard model extended by the additional bosonic mode of the membrane vibration

$$\begin{aligned} H_{\text{lat}} =& \Omega_{\text{m}} a^\dagger a + \frac{\Omega_{\text{a}}}{2} \sum_{j=1}^{L} \sum_{\tau=\pm} \tau c_{j\tau}^\dagger c_{j\tau} - J \sum_{j=1}^{L-1} \sum_{\tau=\pm} \left(c_{j\tau}^\dagger c_{j+1\tau} + \text{H.c.} \right) + \frac{U}{2} \sum_{j=1}^{L} \sum_{\tau,\tau'=\pm} c_{j\tau}^\dagger c_{j\tau'}^\dagger c_{j\tau'} c_{j\tau} \\ & - \frac{\Lambda}{\sqrt{2\Omega_{\text{m}}}} (a + a^\dagger) \sum_{j=1}^{L} \left(c_{j+}^\dagger c_{j-} + \text{H.c.} \right) . \end{aligned} \tag{8.2}$$

For convenience, we assume only the leading order terms such as the on-site interaction, nearest-neighbor hopping and on-site coupling of the atoms to the membrane. In addition, we consider a state-independent interaction $g \equiv g_{\tau\tau'}$, such that the local Hubbard interaction strength is given by

$$U = g \int dz \, |w(z)|^4 . \tag{8.3}$$

Moreover,

$$J = \int dz \, w(z-z_j) \left[\omega_R \partial_z^2 + \frac{V}{2} \cos(2z) \right] w(z-z_{j\pm1}) \tag{8.4}$$

is the nearest-neighbor hopping rate and the effective atom-membrane coupling is rescaled to

$$\Lambda = \lambda \sqrt{\frac{\Omega_{\text{m}}}{2}} \int dz \, \cos(2z) |w(z)|^2 . \tag{8.5}$$

In the non-interacting case ($U = 0$ and $\Lambda = 0$), the Hamiltonian (8.2) is diagonalized via Fourier transformation of the bosonic ladder operators. By introducing new operators

in momentum space $c_{k\tau} = \sum_{j=1}^{L} e^{-ijk} c_{j\tau}/\sqrt{L}$, the Hamiltonian (8.2) can be written as

$$H_{\text{lat}} = \Omega_{\text{m}} a^\dagger a + \sum_{k\tau} \epsilon_{k\tau} n_{k\tau} + \frac{U}{2L} \sum_{kpq} \sum_{\tau\tau'} c^\dagger_{k+q\tau} c^\dagger_{p-q\tau'} c_{p\tau'} c_{k\tau} - \Lambda q_{\text{m}} \sum_{k} \left(c^\dagger_{k+} c_{k-} + \text{H.c.} \right) , \quad (8.6)$$

with the atomic energy dispersion $\epsilon_{k\tau} = \tau\Omega_{\text{a}}/2 - 2J\cos(k)$, $n_{k\tau} = c^\dagger_{k\tau} c_{k\tau}$ and the membrane displacement operator $q_{\text{m}} = (a + a^\dagger)/\sqrt{2\Omega_{\text{m}}}$. The sum over the spatial momentum index k runs in equidistant steps of size $2\pi/L$ from $-\pi$ to π and $\tau = \pm$

Already, the original effective Hamiltonian (8.2) at zero atom-membrane coupling exhibits a rich quantum phase diagram [236] with different types of Mott and superfluid phases, which immediately leads to the questions: What is the effect of an atomic condensate in different phases on the membrane and what happens at the phase boundary when the membrane is coupled to the condensate? Yet, in order to simplify this problem, we will refrain to the special case of weak to moderate atom-atom interactions beyond the pure mean-field regime. Hence, Mott physics will not be treated in the following and we assume in addition a weak atom-membrane coupling such that $\Omega_{\text{m}}, \Omega_{\text{a}} \gg NU/L, \lambda$, where N is the total number of atoms. In this limit, it is possible to apply a Bogoliubov approximation in the mean-field ground state with quantum numbers $(k, \tau) = (0, -)$.

8.1.1 Bogoliubov Approximation

In the Bogoliubov prescription, we isolate the fundamental mode ($k = 0$, $\tau = -$) and treat the remaining modes as non-interacting among each other. These excited modes form a dissipative bath for the zero mode and, hence, we associate

$$c_{0-}, c^\dagger_{0-} \simeq \sqrt{n_{0-}} , \quad (8.7a)$$

$$c^\dagger_{0-} c^\dagger_{0-} c_{0-} c_{0-} = n_{0-}(n_{0-} - 1) , \quad (8.7b)$$

$$n_{0-} = N - n_{0+} - \sum_{k\neq 0} \sum_{\tau} n_{k\tau} , \quad (8.7c)$$

in a particle conserving manner via the relation (8.7c). For the first relation to be acceptable, a larger number of atoms $N \gg 1$ is required to occupy the ground state. By inserting these relations in the Hamiltonian (8.6), and expanding the terms to leading order in N, we find

$$\begin{aligned} H^B =& \Omega_{\text{m}} a^\dagger a + E_0 N + (\Omega_{\text{a}} + nU) c^\dagger c + \sum_{k\neq 0,\tau} (\epsilon_{k\tau} - \epsilon_{0-} + nU)\, c^\dagger_{k\tau} c_{k\tau} - \sqrt{2N\Omega_{\text{a}}}\Lambda q_{\text{m}} q_{\text{a}} \\ & - \Lambda q_{\text{m}} \sum_{k\neq 0} \left(c^\dagger_{k+} c_{k-} + \text{H.c.} \right) + \frac{nU}{2} \sum_{k\neq 0} \left(c_{-k-} c_{k-} + \text{H.c.} \right) , \end{aligned} \quad (8.8)$$

with the replacement $c \equiv c_{0+}$ and the atomic displacement operator $q_{\text{a}} = (c + c^\dagger)/\sqrt{2\Omega_{\text{a}}}$. The mean-field ground state energy is given by $E_0 = \epsilon_{0-} + nU/2$ and $n = N/L$ is the particle density. In addition, the atomic transition frequency is slightly modified by the atom-atom interaction strength to $\Omega_{\text{a}} + nU \simeq \Omega_{\text{a}}$.

In order to diagonalize the excited modes, we introduce new quasi-particle modes[1] $d_{k\tau}$ according to

$$d_{k-} = \phi_k c_{k-} + \theta_k c^\dagger_{-k-} \,, \tag{8.9}$$

and $d_{k+} = c_{k+}$. The coefficients are given by the expressions

$$\phi_k = \sqrt{(\epsilon_{k-} - \epsilon_{0-} + nU + \omega_{k-})/2\omega_{k-}} \,, \tag{8.10a}$$

$$\theta_k = \sqrt{(\epsilon_{k-} - \epsilon_{0-} + nU - \omega_{k-})/2\omega_{k-}} \,. \tag{8.10b}$$

With these coefficients, the new defined modes fulfill bosonic commutation relations since $\phi_k^2 - \theta_k^2 = 1$. Moreover, the mode frequencies are given by

$$\omega_{k-} = (\epsilon_{k-} - \epsilon_{0-}) \sqrt{1 + \frac{2nU}{\epsilon_{k-} - \epsilon_{0-}}} \,, \tag{8.11a}$$

$$\omega_{k+} = \epsilon_{k+} - \epsilon_{0-} + nU \,. \tag{8.11b}$$

By inserting these relations, the effective Hamiltonian in the Bogoliubov prescription takes its final form

$$\begin{aligned} H^B =& \Omega_\mathrm{m} a^\dagger a + \Omega_\mathrm{a} c^\dagger c + \sum_{k\neq 0,\tau} \omega_{k\tau} d^\dagger_{k\tau} d_{k\tau} - \sqrt{2N\Omega_\mathrm{a}} \Lambda q_\mathrm{m} q_\mathrm{a} \\ & - \Lambda q_\mathrm{m} \sum_{k\neq 0} \left(\phi_k d^\dagger_{k-} d_{k+} + \theta_k d_{k-} d_{-k+} + \mathrm{H.c.} \right) \,. \end{aligned} \tag{8.12}$$

We observe that the coupling to the quasi-particle modes involves two different processes: The first process induces transition of quasi-particles between the states $|-\rangle$ and $|+\rangle$. The second process involves the annihilation (creation) of two particles in different internal states. The latter process is induced by particle collisions, where two atoms deplete out of the condensate state. This is only present at finite $U > 0$ because $4\theta_k^2 \simeq \sqrt{nU/J}$.

8.1.2 Fluctuations Induced by Quasi-Particle Excitations

Under these considerations, the coupling of the membrane to the excited modes appears in a similar structure as two-phonon processes studied in open two-state dynamics [237]. Within an Euklidean path integral formalism, the harmonic quasi-particle modes can be integrated out and an analytic solution for the resulting effective action can be obtained. In this approach, thermodynamic observables are expressed as sums involving bosonic Matsubara frequencies $\nu_n = 2\pi n/\beta$ with the inverse temperature $\beta = 1/T$. The corresponding influence action of the quasi-particle modes acting on the eigenmodes $\boldsymbol{q}(\cdot) = (q_1(\cdot), q_2(\cdot))$

[1] This transformation also refers to the Bogoliubov transformation. For more details on the idea and assumptions in order to find the appropriate transformation coefficients see appendix D.

takes the form

$$S_{\text{infl}}[\boldsymbol{q}(\cdot)] = -\sum_{s,s'=1}^{2} \Lambda_s \Lambda_{s'} \int_0^\beta d\rho \int_0^\rho d\varsigma\, k(\rho-\varsigma) q_s(\rho) q_{s'}(\varsigma)\,. \tag{8.13}$$

The kernel is given by $k(\rho) = \int d\omega\, G(\omega) D_\omega(\rho)$, where $D_\omega(\rho) = 2n(\omega)\cosh(\omega\rho) + e^{-\omega\rho}$ is the free boson propagator in imaginary time and

$$G(\omega) = \sum_{k\neq 0} \left\{ \phi_k^2 [n(\omega_{k-}) - n(\omega_{k+})]\delta(\omega - \Delta_k) + \theta_k^2 [n(\omega_{k-}) + n(\omega_{k+}) + 1]\delta(\omega - \Omega_k) \right\} \tag{8.14}$$

is the spectral density of the effective harmonic bath of the quasi-particle modes. Moreover, we have defined $\Omega_k = \omega_{k-} + \omega_{k+}$, $\Delta_k = \omega_{k+} - \omega_{k-}$ and the displacement coordinates q_s, which are the eigenmodes of the two bilinearly coupled harmonic oscillators. The eigenmodes are obtained via the unitary transformation

$$\begin{pmatrix} q_1 \\ q_2 \end{pmatrix} = \begin{pmatrix} \cos\zeta & -\sin\zeta \\ \sin\zeta & \cos\zeta \end{pmatrix} \begin{pmatrix} q_{\text{m}} \\ q_{\text{a}} \end{pmatrix} \tag{8.15}$$

with the angle

$$\tan\zeta = \left(\Omega_{\text{a}}^2 - \Omega_{\text{m}}^2 + \text{sgn}(\Omega_{\text{m}} - \Omega_{\text{a}}) \sqrt{[\Omega_{\text{m}}^2 - \Omega_{\text{a}}^2]^2 + 8N\Lambda^2\Omega_{\text{a}}} \right) / \sqrt{8N\Omega_{\text{a}}}\Lambda\,, \tag{8.16}$$

leading to an effective rescaling of the coupling constants in the influence action with $\Lambda_1 = \Lambda\cos\zeta$ and $\Lambda_2 = \Lambda\sin\zeta$.

At zero temperature, in the limit of a large lattice, and under the restriction $nU \ll J$ (see footnote 2), the sum over the spatial momenta can be approximated by an integral and the spectral density takes the form[3]

$$G_{T=0}(\omega) \simeq \frac{2L}{\pi} \left(\frac{nU}{4J}\right)^2 \frac{4J}{|\sin\kappa(\omega)|} \frac{1}{(\omega - \Omega_{\text{a}} - nU)^2}\,, \tag{8.17}$$

where $\kappa(\omega) = 2\sin^{-1}\sqrt{(\omega - \Omega_{\text{a}} - nU)/8J}$. From this expression, we find that the coupling to the quasi-particle excitations scales with the number of states, namely $\sqrt{L}\Lambda$, rather than the number of particles $\sqrt{N}\Lambda$, as it is the case for the zero momentum coupling.

The zero temperature spectral density exhibits two singularities at $\omega_{\text{min}} = \Omega_{\text{a}} + nU$ and $\omega_{\text{max}} = \Omega_{\text{a}} + nU + 8J$ and is only defined between these two frequencies. Here $8J$ equals twice the bandwidth $4J$ of the energy dispersion. In the vicinity of these singularities, the spectral density behaves as $G_{T=0}(\omega_{\text{min}} + \delta\omega) \sim (\delta\omega)^{-5/2}$ and $G_{T=0}(\omega_{\text{max}} - \delta\omega) \sim (\delta\omega)^{-1/2}$. Figure 8.1 shows examples of the zero temperature spectral density in (a) and at a finite temperature $\beta\Omega_{\text{a}} = 1000$ in (b) for different values of the interaction strength nU. The cosine energy dispersion (8.11) leads to a very flat density of states in the vicinity of the smallest and largest excitation frequency. As a consequence, the spectral density exhibits

[2] This condition is needed to assure a low condensate depletion.

[3] A detailed derivation of the zero temperature spectral density can be found in the appendix E.1.

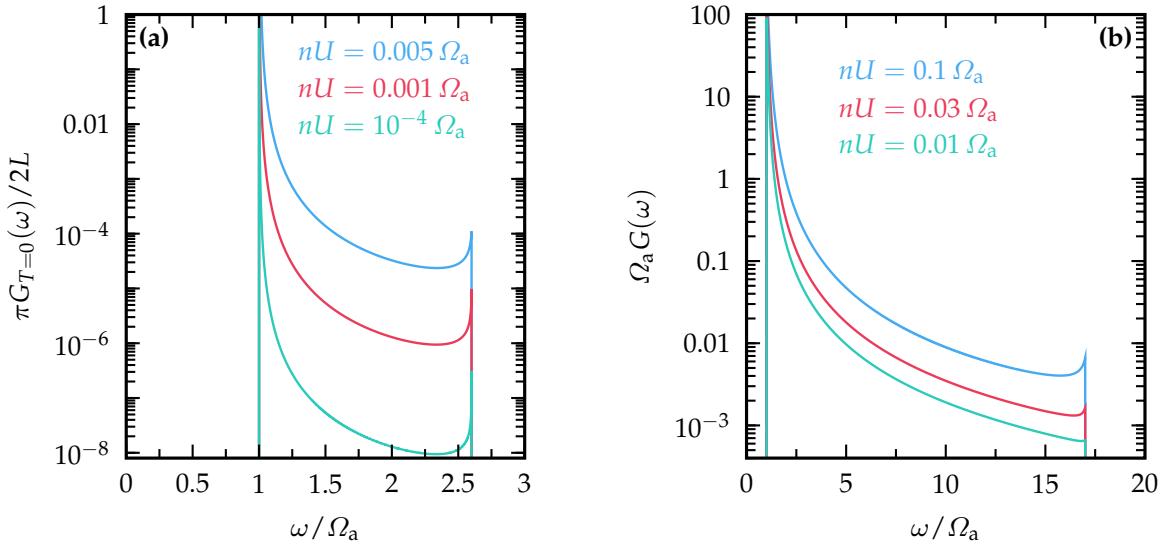

FIGURE 8.1: (a) The approximated zero temperature spectral density $G_{T=0}(\omega)$ of the Bogoliubov modes is shown for $J = 0.2\,\Omega_a$ with different atomic interaction strengths nU, indicated in the plot. (b) The spectral density $G(\omega)$ of equation (8.14) is shown for the inverse temperature $\beta\Omega_a = 1000$, $J = 2\,\Omega_a$, $L = 1000$ and various interaction strengths nU. In each case, the spectral density exhibits two singularities, one close to $\omega \simeq \Omega_a$ and the other shifted by $8J$ to higher frequencies. Only in between these two singularities, the spectral density is defined.

van Hove-type singularities at the minimal frequency $\omega = \omega_{\min}$ and the maximal frequency $\omega = \omega_{\max}$.

8.2 Quantum Squeezing of the Nanomembrane

In order to estimate the effect of weak atom-atom interactions on the membrane displacement variance $\langle q_m^2 \rangle$, we determine the partition function of the reduced system. It is obtained via the imaginary time path integral $Z(\beta) = \int \mathcal{D}\boldsymbol{q}(\cdot)\, \exp\{-S_{\text{eff}}[\boldsymbol{q}(\cdot)]\}$ with the effective action

$$S_{\text{eff}}[\boldsymbol{q}(\cdot)] = \frac{1}{2}\sum_{s=1}^{2}\int_0^\beta d\rho\, \left[\dot{q}_s^2(\rho) + \Omega_s^2 q_s^2(\rho)\right] + S_{\text{infl}}[\boldsymbol{q}(\cdot)]\,, \tag{8.18}$$

and the frequencies of the two harmonic oscillators $\Omega_1^2 = \Omega_m^2 + 2\sqrt{2N\Omega_a}\Lambda\tan\zeta$ and $\Omega_2^2 = \Omega_a^2 - 2\sqrt{2N\Omega_a}\Lambda\tan\zeta$. By using the influence action of equation (8.13), the displacement variance of the membrane can be determined by the first derivative of the logarithm of the partition function[4] $\langle q_m^2 \rangle = -(\beta\Omega_m)^{-1}\partial_{\Omega_m} \ln Z$. Then, quantum mechanical squeezing occurs when $\langle q_m^2 \rangle \leq 1/2\Omega_m$.

In figure 8.2(a) is shown the variance of the membrane position displacement (solid) as a function of the atomic transition frequency Ω_a. As a consequence of two-mode squeezing, the variance is strongly suppressed in the vicinity of the resonance condition when $\Omega_m \lesssim \Omega_a$. On the contrary, the atomic displacement variance shows the opposite behavior, such that both constituents exchange their role at $\Omega_m = \Omega_a$, and the atomic state is strongly

[4]The analytic evaluation of the partition function is discussed in the appendix E.2.

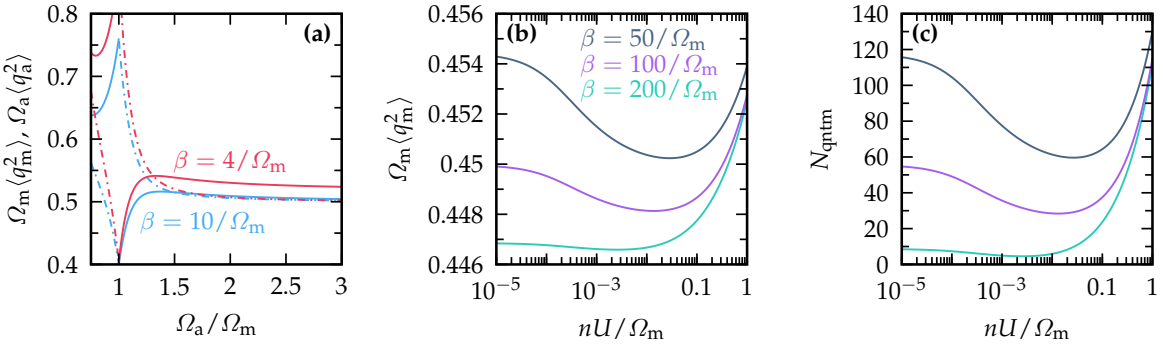

FIGURE 8.2: (a) The variances of the membrane displacement $\langle q_m^2\rangle$ (solid) and the associated atomic displacement of the internal states $\langle q_a^2\rangle$ (dash-dotted) is shown in dependence of the atomic frequency Ω_a at the interaction strength $nU = 0.5\Omega_m$. The other parameters chosen are $L = 200$, $N = 10^6$, $\Lambda = 2\times10^{-4}\,\Omega_m^{3/2}$ and $J = 0.1\,\Omega_m$. In addition, panels (b) and (c) show the membrane displacement variance and the number of particles depleted from the condensate as a function of the atom-atom interaction strength nU/Ω_m, respectively. The parameter chosen for panels (b) and (c) are $J = 0.5\,\Omega_m$, $\Omega_a = 1.04\,\Omega_m$, $L = 200$, $N = 10^3$ and $\Lambda = (0.015/\sqrt{2})\,\Omega_m^{3/2}$. The different colors mark different inverse temperatures which are indicated in panel (a) and (b).

squeezed near the resonance when $\Omega_a \lesssim \Omega_m$. As a matter of consequence, only when quasi-particle excitations above the spectral gap are possible, squeezing of the nanomembrane displacement mode may occur. Note that for the chosen set of parameters in figure 8.2(a), the effect of the quasi-particle excitations is negligibly small, due to the scaling $\sim\sqrt{L}\Lambda$.

In order to see an impact of finite atom-atom interactions on the nanomembrane observables, the effective coupling strength $\sqrt{L}\Lambda$ has to be enhanced. Interestingly, we find that these atom-atom interactions may have a positive effect for achieving a squeezed mechanical state, which is shown in figure 8.2(b) for different inverse temperatures β. By increasing the atom-atom interaction strength nU, the variance of the membrane displacement $\langle q_m^2\rangle$ initially decreases and finally grows again. This leads to an optimal value of nU for which the membrane displacement variance has a minimum, reaching maximal quantum mechanical squeezing. However, the position and magnitude of the minimal variance depends on temperature and is dominated by two processes: First, the dominant process in the weak interaction limit is due to differences of the thermal excitation of the states with the same momentum, but opposite internal state, leading to a scaling $\sim n(\omega_{k-}) - n(\omega_{k+})$ in the spectral density. The second, predominant process for rather strong atomic interactions compared to the thermal energy scale are excitations of Bogoliubov quasi-particles. These excitations are induced by the interaction, leading to a scaling with $(nU)^2[n(\omega_{k-}) + n(\omega_{k+}) + 1]$.

As a consequence of the optomechanical coupling, the squeezing of the membrane variance is also reflected in the number of depleted atoms $N_{qntm} = \sum_{k\neq0,\tau}\langle d_{k\tau}^\dagger d_{k\tau}\rangle$ which are excited from the mean-field ground state. The number of depleted particles is shown in figure 8.2(c) as a function of the interaction strength, for which a similar behavior as the membrane position variance is observed. Hence, squeezing is maximal when the atomic depletion is minimal.

In the following chapter, we will again return to the subject of nonequilibrium quantum

phase transitions. We provide a rigorous guide line, describing how the spectrum of the collective excitations are determined for the internal state coupling scheme. We will further show that a modified version of the Gaussian ansatz (6.23) can also be applied to the nonequilibrium Dicke model of equation (4.14).

CHAPTER 9

Generalizations of the Cumulant Expansion and Multi-Orbital Ansatz

Collective excitations in the vicinity of a quantum critical point show a characteristic behavior. For instance, a second-order QPT associated with a spontaneous symmetry breaking exhibits a mode softening of the low-energy excitation. In this chapter, we will first derive linearized equations of motion for the excitation modes of the internal-state coupling scheme. Second, we apply a two-site Gaussian ansatz to the nonequilibrium Dicke model describing a BEC which is coupled to the optical mode of a cavity.

9.1 Excitation Spectrum and Generalized Cumulant Expansion for a Multi-Species Condensate

In chapter 7, we have derived the mean-field equations of motion for the population amplitude γ, the condensate width σ and the membrane amplitude α. These mean-field equations in the Gaussian ansatz (7.14) lack an essential feature which becomes important when determining the collective excitation spectrum. As a matter of fact, it is not possible to describe individual excitations of the breathing mode for the fraction of the condensate in either of the internal states $|-\rangle$ or $|+\rangle$. Especially when the relevant energy scales[1] are of the same order, in combination with a weakly damped membrane, a stabilization analysis may not provide the correct excitation spectrum. This is especially the case, for the scenarios considered in figure 7.3(a) and (c). However, we can still utilize an adapted Bogoliubov ansatz in the manner of equation (6.57) with a universal width in order to avoid a tedious derivation with different widths σ_τ and phases η_τ.

In the following, we outline the procedure and explain how the excitations out of the mean-field steady state can be found. It is convenient to introduce the new field operators

$$\Psi_N(t,z) = \sqrt{1-\gamma_0^2}\Psi_-(t,z) + \gamma_0\Psi_+(t,z)\,, \tag{9.1a}$$

$$\Psi_\gamma(t,z) = -\gamma_0\Psi_-(t,z) + \sqrt{1-\gamma_0^2}\Psi_+(t,z)\,, \tag{9.1b}$$

[1] It means when the membrane frequency Ω_m, the atomic transition frequency Ω_a and the breathing mode frequencies are of similar magnitude.

where the first field contains the mean-field steady state, and the latter describes excitations out of this steady state via internal transitions. For simplicity, we set our focus on the special case of a symmetric coupling $\chi = 0$ and non-interacting atoms with $g = 0$. Then, the equations of motion for the newly introduced operators and the membrane ladder operator are reduced to

$$\begin{aligned} i\partial_t a =&[\Omega_\mathrm{m} - i\Gamma_\mathrm{m}]a - \frac{\lambda}{2}\int dz\, \cos(2z)\Big[(1-2\gamma_0^2)(\Psi_N^\dagger\Psi_\gamma + \Psi_\gamma^\dagger\Psi_N) \\ &+ 2\gamma_0\sqrt{1-\gamma_0^2}(\Psi_N^\dagger\Psi_N - \Psi_\gamma^\dagger\Psi_\gamma)\Big] + i\xi_\mathrm{th}\,, \end{aligned} \tag{9.2a}$$

$$\begin{aligned} i\partial_t\Psi_N =& \left[-\frac{\Omega_\mathrm{a}}{2}(1-2\gamma_0^2) - \omega_R\partial_z^2 - \frac{V}{2}\cos(2z) - \lambda\gamma_0\sqrt{1-\gamma_0^2}(a+a^\dagger)\cos(2z)\right]\Psi_N \\ &+ \left[\Omega_\mathrm{a}\gamma_0\sqrt{1-\gamma_0^2} - \frac{\lambda}{2}(1-2\gamma_0^2)(a+a^\dagger)\cos(2z)\right]\Psi_\gamma\,, \end{aligned} \tag{9.2b}$$

$$\begin{aligned} i\partial_t\Psi_\gamma =& \left[\frac{\Omega_\mathrm{a}}{2}(1-2\gamma_0^2) - \omega_R\partial_z^2 - \frac{V}{2}\cos(2z) + \lambda\gamma_0\sqrt{1-\gamma_0^2}(a+a^\dagger)\cos(2z)\right]\Psi_\gamma \\ &+ \left[\Omega_\mathrm{a}\gamma_0\sqrt{1-\gamma_0^2} - \frac{\lambda}{2}(1-2\gamma_0^2)(a+a^\dagger)\cos(2z)\right]\Psi_N\,, \end{aligned} \tag{9.2c}$$

where we have also neglected the fluctuating forces induced by the light field. The mean-field steady state $\Psi_- \simeq \sqrt{(1-\gamma_0^2)N}\psi_0$, $\Psi_+ \simeq \gamma_0\sqrt{N}\psi_0$ is completely included in the field operator Ψ_N. Hence, we can make the ansatz

$$\Psi_N(t,z) \simeq \left[\sqrt{N}\psi_0(z) + d_\sigma(t)\psi_2(z)\right]e^{-i\mu t}\,, \tag{9.3a}$$

$$\Psi_\gamma(t,z) \simeq \left[d_\gamma(t)\psi_0(z) + d_\rho(t)\psi_2(z)\right]e^{-i\mu t}\,, \tag{9.3b}$$

where the orbitals $\psi_n(z)$ have been defined in equation (6.58). Moreover, we assume the linear displacement $a(t) = \sqrt{N}\alpha_0 + d_\alpha(t)$. Next, we derive the equations of motion for the operators d_i with $i \in \{\alpha,\gamma,\sigma,\rho\}$ in the fashion of section 6.3. In order to derive the equation for d_γ, equation (9.2c) is multiplied by $\psi_0(z)$ and the space coordinate is integrated out. To find the equation for d_σ and d_ρ, we multiply equation (9.2b) and (9.2c) by $\psi_2(z)$ and integrate over space, respectively. After a linearization to lowest order in the ladder operators, the linearized equations of motion result in

$$i\partial_t d_\alpha = (\Omega_\mathrm{m} - i\Gamma_\mathrm{m})d_\alpha - \Lambda_{\alpha\gamma}(d_\gamma + d_\gamma^\dagger) + \Lambda_{\alpha\sigma}(d_\sigma + d_\sigma^\dagger) + \Lambda_{\alpha\rho}(d_\rho + d_\rho^\dagger) + i\xi_\mathrm{th}\,, \tag{9.4a}$$

$$i\partial_t d_\gamma = \Omega_\gamma d_\gamma - \Lambda_{\alpha\gamma}(d_\alpha + d_\alpha^\dagger) + \Lambda_{\gamma\sigma}d_\sigma\,, \tag{9.4b}$$

$$i\partial_t d_\sigma = \Omega_\sigma d_\sigma + \Lambda_{\alpha\sigma}(d_\alpha + d_\alpha^\dagger) + \Lambda_{\gamma\sigma}d_\gamma + \Lambda_{\sigma\rho}d_\rho\,, \tag{9.4c}$$

$$i\partial_t d_\rho = \Omega_\rho d_\rho + \Lambda_{\alpha\rho}(d_\alpha + d_\alpha^\dagger) + \Lambda_{\sigma\rho}d_\sigma\,, \tag{9.4d}$$

where the mode frequencies reduce to

$$\Omega_\gamma = \Omega_\mathrm{a}\left(1-2\gamma_0^2\right) + 2\sqrt{N}\lambda\gamma_0\sqrt{1-\gamma_0^2}(\alpha_0+\alpha_0^*)e^{-\sigma_0^2}\,, \tag{9.5a}$$

$$\Omega_\sigma = \frac{2\omega_R}{\sigma_0^2} + \widetilde{V}\left(2-\sigma_0^2\right)\sigma_0^2 e^{-\sigma_0^2}\,, \tag{9.5b}$$

$$\Omega_\rho = \Omega_\mathrm{a}\left(1-2\gamma_0^2\right) + \frac{2\omega_R}{\sigma_0^2} + V\left(2-\sigma_0^2\right)\sigma_0^2 e^{-\sigma_0^2} + \left(\widetilde{V}-V\right)\left(1-2\sigma_0^2+\sigma_0^4\right)e^{-\sigma_0^2}\,. \tag{9.5c}$$

In addition, we have defined the effective lattice depth $\widetilde{V} = V + 4\Omega_\mathrm{a}(\lambda/\lambda_\Omega)^2\gamma_0^2(1-\gamma_0^2)e^{-\sigma_0^2}$. The coupling constants between the individual atomic modes and the membrane mode are given by

$$\Lambda_{\alpha\gamma} = \frac{\sqrt{N}\lambda}{2}\left(1-2\gamma_0^2\right)e^{-\sigma_0^2}\,, \tag{9.6a}$$

$$\Lambda_{\alpha\sigma} = \sqrt{2N}\lambda\gamma_0\sqrt{1-\gamma_0^2}\sigma_0^2 e^{-\sigma_0^2}\,, \tag{9.6b}$$

$$\Lambda_{\alpha\rho} = \frac{\sqrt{2N}\lambda}{2}\left(1-2\gamma_0^2\right)\sigma_0^2 e^{-\sigma_0^2}\,, \tag{9.6c}$$

$$\Lambda_{\gamma\sigma} = \frac{\sqrt{2N}\lambda}{2}\left(1-2\gamma_0^2\right)(\alpha_0+\alpha_0^*)\sigma_0^2 e^{-\sigma_0^2}\,, \tag{9.6d}$$

$$\Lambda_{\sigma\rho} = \Omega_\mathrm{a}\gamma_0\sqrt{1-\gamma_0^2} - \frac{\sqrt{N}\lambda}{2}\left(1-2\gamma_0^2\right)(\alpha_0+\alpha_0^*)\left(1-4\sigma_0^2+2\sigma_0^4\right)e^{-\sigma_0^2}\,. \tag{9.6e}$$

In addition, we have used the steady-state equations (7.17) in order to show that there occurs no direct coupling between the two excited modes described by d_γ and d_ρ.

In similarity to the previous approach, we define the excitation vector $\boldsymbol{x} = (d_\alpha, d_\gamma, d_\sigma, d_\rho, d_\alpha^\dagger, d_\gamma^\dagger, d_\sigma^\dagger, d_\rho^\dagger)$ and rewrite the Bogoliubov–de Gennes equation (9.4) in terms of a vector-matrix product $i\dot{\boldsymbol{x}} = \boldsymbol{M}\boldsymbol{x} + i\boldsymbol{\xi}$. Then, the collective excitation spectrum is given by the complex eigenvalues of the linear stability matrix $\boldsymbol{M}$. The collective excitation spectrum ν_i is shown in figure 9.1 for the case of a weakly damped vibrational mode. In (a), the excitation frequencies $\omega_i = \mathrm{Re}(\nu_i)$ are shown. Below the critical coupling rate $\lambda < \lambda_\mathrm{c}$, the breathing modes (red, green) are constant, while the low energy excitation frequency (purple) exhibits a roton-type behavior and monotonically decreases to zero according to $\omega_i \simeq \Omega_\mathrm{a}\sqrt{1-(\lambda/\lambda_\mathrm{c})^2}$. Simultaneously, the high energy excitation frequency (blue) increases monotonically. Above the threshold $\lambda > \lambda_\mathrm{c}$, the roton-type mode frequency increases again. Eventually, this mode frequency saturates to Ω_m and the membrane mode decouples from the atomic transition modes, coupling only to the atomic breathing mode via $\Lambda_{\alpha\sigma}$. In addition, the other mode frequencies monotonically increase and exhibit avoided energy crossings when close to another frequency. This behavior is a direct consequence of the comparably weak membrane damping rate $\Gamma_\mathrm{m} = \omega_R$. In addition, we show the corresponding decay rates $\gamma_i = -\mathrm{Im}(\nu_i)$ in figure 9.1(b). In the vicinity of the avoided crossings in (a), the initially small decay rates are significantly increased, which indicates a strong mixing of the membrane mode and the atomic modes. In fact, such a mixing can induce entanglement between the membrane and the atomic modes as it was shown in figure 6.8.

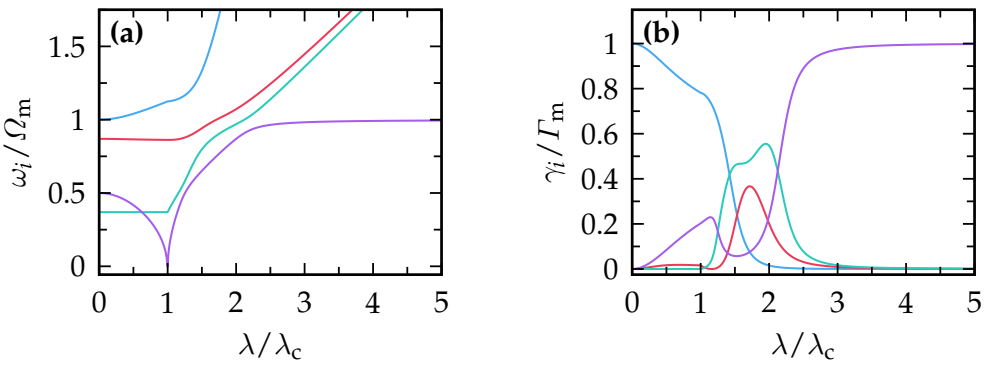

FIGURE 9.1: (a) The four collective excitation frequencies $\omega_i = \mathrm{Re}(\nu_i)$ are shown as a function of the atom-membrane coupling rate λ/λ_c in the weak damping limit. The different colors correspond to different eigenmodes. Note that the energy difference between the green and red curve in the non-displaced phase ($\alpha_0 = 0$) is Ω_a. (b) In addition, the corresponding collective decay rates are shown. The parameters used are $V = 100\,\omega_R$, $\Omega_m = 100\,\omega_R$, $\Gamma_m = \omega_R$, $\Omega_a = 50\,\omega_R$, and $g = 0$, $\chi = 0$. We note that due to the weak membrane damping, most of the energy crossings are avoided, which is also reflected in the rich structure of the collective decay rates.

9.2 Modified Expansion for the Nonequilibrium Dicke Model

Another possible application of the Gaussian ansatz is offered by the well-known Dicke model. It is realized by a bosonic condensate in an optical lattice that is placed inside an optical cavity with transversal optical pumping. The time evolution of this hybrid system follows the set of equations (4.14), given by

$$i\partial_t a = \left[-\Delta_C + U_0 \int dz\, \cos^2(z)\Psi^\dagger(z)\Psi(z) - i\kappa\right]\alpha + \eta \int dz\, \cos(z)\Psi^\dagger(z)\Psi(z)\,, \tag{9.7a}$$

$$i\partial_t \Psi(z) = \left[-\omega_R\partial_z^2 + \left(V_{cl} + U_0 a^\dagger a\right)\cos^2(z) + \eta(a + a^\dagger)\cos(z) + g\Psi^\dagger(z)\Psi(z)\right]\Psi(z)\,, \tag{9.7b}$$

where we introduced an additional conservative optical lattice with depth V_{cl}. This classical lattice can be realized by a far off-resonant dipole trap (FORT) [114]. This FORT can be experimentally accomplished by a laser whose frequency is detuned by only very few spectral ranges from the cavity frequency. Close to the cavity center, the cavity potential and FORT field very well coincide, such that the same periodicity of the potential can be assumed. In order to describe the essential feature of the phase transition, one has to consider at least two lattice sites, because the NQPT leads to an imbalanced occupation between even and odd lattices sites. In the two-dimensional experimental realization [115, 117, 201], this is manifested in a checkerboard pattern. Hence, we consider the minimum of two lattice sites. In the presence of a sufficiently deep classical potential (with depth V_{cl}), the condensate profile in each lattice well is described by a Gaussian. The two-mode functions which satisfy $\int dz\, \psi_i(z)\psi_j^*(z) = \delta_{ij}$ are then given by

$$\psi_\pm(z) = \left(\frac{\delta_\pm^2}{4\pi\sigma^2}\right)^{1/4}\left(e^{-z^2/2\sigma^2} \pm e^{-(z-\pi)^2/2\sigma^2}\right), \tag{9.8}$$

with a stationary width σ, the normalization constants $\delta_\pm = 1 \pm e^{-\rho}$ and the overlap exponent $\rho = \pi^2/4\sigma^2$. Note that in order for equation (9.8) to be an appropriate variational ansatz for the condensate profile, we assume that $V_{\mathrm{cl}} < 0$. Then, the condensate field operator takes the form

$$\Psi(z) = d_+\psi_+(z) + d_-\psi_-(z)\,, \tag{9.9}$$

where $d_\pm$ are bosonic ladder operators which satisfy the usual bosonic commutation relations, i.e., $\left[d_i, d_j^\dagger\right] = \delta_{ij}$. The equations of motion have to be solved in the subspace $d_+^\dagger d_+ + d_-^\dagger d_- \equiv N$, where N is the total number of atoms.

Within this ansatz, the equation of motion for the cavity mode operator simplifies to

$$i\partial_t a = (-\Delta_C + U_+ n_+ + U_- n_- - i\kappa)a + \eta'\left(d_+^\dagger d_- + d_-^\dagger d_+\right)\,, \tag{9.10}$$

with the effective atom-light field coupling $\eta' = \eta e^{-\sigma^2/4}\sqrt{1+\coth(\rho)}/\sqrt{2}$ and $U_\pm$ defined below. Here, $n_\pm = d_\pm^\dagger d_\pm$ is the number of atoms in the $j = \pm$ orbital. In order to derive the equation of motion for the atomic mode operator d_+ (d_-), we have to multiply equation (9.7b) by ψ_+ (ψ_-) and integrate over the space variable z. Then, the individual equations of motion can be brought to the form

$$i\partial_t d_+ = \Omega\tanh(\rho/2)d_+ + \eta'\left(a^\dagger + a\right)d_- + U_+ n_a d_+ + g_+ n_+ d_+ + g' d_+^\dagger d_- d_-\,, \tag{9.11a}$$

$$i\partial_t d_- = \Omega\coth(\rho/2)d_- + \eta'\left(a^\dagger + a\right)d_+ + U_- n_a d_- + g_- n_- d_- + g' d_-^\dagger d_+ d_+\,, \tag{9.11b}$$

where we have defined the following constants

$$\Omega = \frac{\omega_R}{2\sigma^2}\rho + \frac{V_{\mathrm{cl}}}{2}e^{-\sigma^2}\,, \tag{9.12a}$$

$$U_+ = \frac{U_0}{2}\left[1 + e^{-\sigma^2}\tanh(\rho/2)\right]\,, \tag{9.12b}$$

$$U_- = \frac{U_0}{2}\left[1 + e^{-\sigma^2}\coth(\rho/2)\right]\,, \tag{9.12c}$$

$$g_+ = g'\Big(\left[1 + \operatorname{sech}(\rho/2)\right]\left[2 - \tanh(\rho/2) - \operatorname{sech}(\rho/2)\right] - 2\Big)\,, \tag{9.12d}$$

$$g_- = \frac{g'}{2}\Big(\left[1 - \tanh(\rho/4)\right]^2 - 2\Big)\,, \tag{9.12e}$$

and $g' = g/\sqrt{8\pi}\sigma$. Here, we note that the overlap exponent $\rho > 0$ is approaching infinity, when the overlap between the Gaussians in the left and right well is becoming smaller. Hence, $\coth(\rho) > \tanh(\rho)$ will always be satisfied, such that the lowest energy state is actually given by the $j = +$ orbital (when interactions are neglected). Moreover, $n_a = a^\dagger a$ is the number of photons in the cavity. In the following, we perform a stationary mean-field analysis of this problem.

Therefore, we assume $d_+(t) \simeq \sqrt{N}\gamma_+(t)$, $d_-(t) \simeq \sqrt{N}\gamma_-(t)$, and $a(t) = \sqrt{N}\alpha(t)$, with the complex variational parameters $\gamma_\pm(t)$, $\alpha(t)$. In fact, within this ansatz, the dynamics of

the photon amplitude and the atomic polarization are determined by the equations

$$\dot{\alpha} = -i\partial_{\alpha^*} E - \kappa\alpha\,, \tag{9.13a}$$

$$\dot{\gamma}_\tau = -i\partial_{\gamma_\tau^*} E\,. \tag{9.13b}$$

In addition, we have defined the effective energy functional according to $E = E[\alpha, \gamma_-, \gamma_+, \sigma]$ with

$$\begin{aligned} E =& -\Delta_C'|\alpha|^2 + \frac{\omega_R}{2\sigma^2}(1-\rho) + \left[\Omega + \frac{NU_0}{2}|\alpha|^2 e^{-\sigma^2}\right]\left[\tanh(\rho/2)|\gamma_+|^2 + \coth(\rho/2)|\gamma_-|^2\right] \\ &+ \sqrt{\frac{N}{2}}\eta(\alpha+\alpha^*)\sqrt{1+\coth(\rho)}(\gamma_+^*\gamma_- + \gamma_-^*\gamma_+) + \frac{Ng}{\sqrt{8\pi}\sigma}\mathrm{Re}\left([\gamma_-^*\gamma_+]^2 + 2|\gamma_+|^2|\gamma_-|^2\right) \\ &+ \frac{Ng}{2\sqrt{8\pi}\sigma}\left[1+\mathrm{sech}(\rho/2)\right]\left[2-\mathrm{sech}(\rho/2)-\tanh(\rho/2)\right]|\gamma_+|^4 \\ &+ \frac{Ng}{4\sqrt{8\pi}\sigma}\left[2+\{1-\tanh(\rho/4)\}^2\right]|\gamma_-|^4\,, \end{aligned} \tag{9.14}$$

with the shifted cavity detuning $\Delta_C' = \Delta_C - NU_0/2$. Then, the stationary solution for the variational parameters (α_0, $\gamma_{-,0}$, $\gamma_{+,0}$, σ_0) is found via the relations

$$\partial_{\alpha^*} E = -i\kappa\alpha\,, \tag{9.15a}$$

$$\partial_{\gamma_-^*} E = 0\,, \tag{9.15b}$$

$$\partial_{\gamma_+^*} E = 0\,, \tag{9.15c}$$

$$\partial_\sigma E = 0\,. \tag{9.15d}$$

By inserting the solution for α_0 of equation (9.15a) in the effective potential $E[\alpha, \gamma_\tau, \sigma]$ and using the normalization condition $|\gamma_+|^2 + |\gamma_-|^2 = 1$, the steady state problem reduces to a minimization problem of the energy functional $E[\gamma, \sigma] \equiv E[\alpha_0(\gamma, \sigma), \gamma, \sigma]$, with $\gamma \equiv \gamma_-$.

Figure 9.2(a) and (b) show the energy functional as a function of the atomic parameter γ and the atom-field coupling strength η for different values of the classical lattice depth V_{cl}. For a better comparison, the energy functional is scaled according to $\mathcal{E}(\gamma) = [E(\gamma) - E(\gamma_0)] \,/\, \max_{\bar{\gamma}}[E(\bar{\gamma}) - E(\gamma_0)]$. Below a certain value of η, the system relaxes to a steady state with $\gamma = 0$, which is indicated by the dashed curves in (a) and (b). Moving away from this minimum at a fixed η, the effective potential steadily increases with γ until it reaches a global maximum roughly around $\gamma = \pm 1/\sqrt{2}$. At $\gamma = \pm 1$, local minima appear which are energetically raised with respect to the minimum $\mathcal{E}(0)$. Above a critical threshold $\sqrt{N}\eta_c$, the initial minimum at $\gamma = 0$ turns into a (local) maximum and the steady state occupation γ_0 splits into two branches, indicating the nonequilibrium quantum phase transition. Hence, the atom-field coupling is the important parameter that tunes the phase transition. In 9.2(a) the phase transition appears to be continuous, while it appears to be discontinuous for the deeper lattice in 9.2(b). Beyond the critical point, γ_0 quickly saturates to $\gamma_0 \simeq \pm 1/\sqrt{2}$.

In addition to the investigation of the energy surface, we show in figure 9.2(c) the positive steady state solution γ_0 as a function of the pump strength η. Here, the results are shown for various atomic interaction strengths that are indicated by the color bar and a

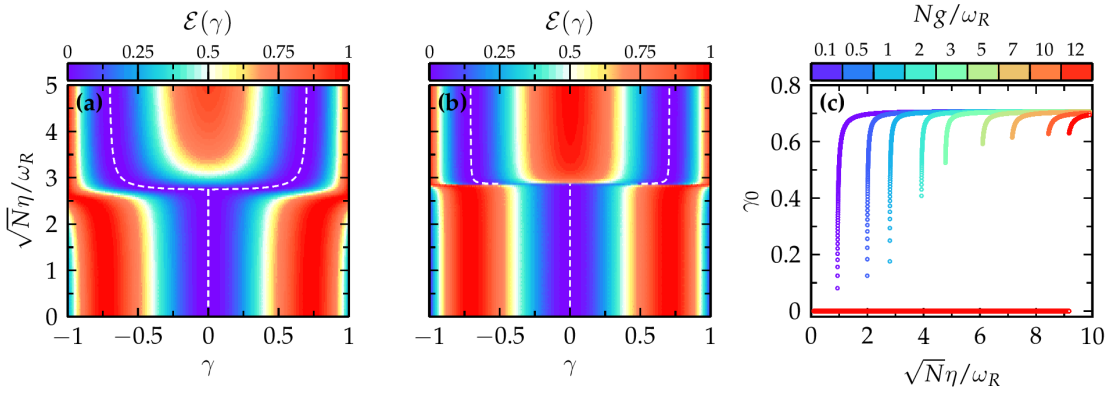

FIGURE 9.2: (a), (b) The scaled energy potential is shown as a function of the atomic density order parameter γ and the atom-field coupling η for interacting atoms with $Ng = \omega_R$. Different classical potential depths $V_{\mathrm{cl}} = -10\,\omega_R$ and $V_{\mathrm{cl}} = -20\,\omega_R$ have been considered in the panels (a) and (b), respectively. Below a critical coupling strength the potential surface exhibits a single minimum at $\gamma = 0$ (indicated by the dashed lines). At the critical point, this minimum turns into a maximum and two new minima are formed at $\gamma \neq 0$. Note that there are two other minima at $\gamma = \pm 1$ below the critical point. However, these local minima are energetically higher than the global minimum at $\gamma = 0$ since $\coth(x) \geq \tanh(x)$ for $x > 0$. (c) The stationary value of the atomic parameter γ_0 is tracked as a function of the coupling constant $\sqrt{N}\eta/\omega_R$ with the lattice depth $V_{\mathrm{cl}} = -15\,\omega_R$. Here, only the positive solution $\gamma_0 > 0$ is shown. Different colors correspond to different atom interactions. Other parameters used are $\Delta_C = -10\,\omega_R$, $\kappa = \omega_R$ and $NU_0 = -\omega_R$.

classical lattice depth $V_{\mathrm{cl}} = -15\,\omega_R$ has been considered. The critical point roughly scales with the square root of the interaction strength $\sqrt{Ng}$. On the one hand, we find that for rather strongly interacting atoms, the phase transition appears to be discontinuous which is an indicator for the importance of Mott physics. On the other hand, for rather weakly interacting atoms, the imbalance between the occupancy of odd and even sites grows seemingly in a continuous manner. However, we have to emphasize that these indicators are by far no criterion to deduce whether the phase transition really is of first- or second-order. On the basis of a Landau expansion of the effective potential $E[\gamma, \sigma]$ around $\gamma = 0$, this notion can be clarified. Moreover, we are aware of the existence of two possible PTs in this system, one from the normal phase to the self-organized superfluid phase and another from the normal phase to the self-organized Mott phase. For instance, the two PTs have been investigated in reference [116], where a slightly modified setup without the FORT has been considered. Yet, to which extent these different phase transitions influence the presented mean-field analysis has to be examined. This, however, we leave as an open question for further investigations.

Chapter 10

Summary

In this thesis, the effects of quantum statistical fluctuations and the resulting nonequilibrium dynamics in different physical situations have been investigated.

Thermal and Nonequilibrium Fluctuations

In the first scenario, we have considered a molecular complex which is affected by thermal fluctuations that induce geometrical variations of its dipole moments, leading to a chiral effect which is not present in the isolated molecule. We have determined the linear and 2D optical chiral spectra for the dimer system whose static dipole moments are orthogonal with a connecting vector parallel to one of the dipole moments. In other words, the dimer is achiral in its equilibrium configuration, no chiral signal is expected, and the dipolar coupling vanishes. Yet, geometrical fluctuations are shown to induce finite average dipolar couplings between the two dipole moments which causes a rather fast energy transfer as experimentally observed. This fast energy transfer can be unambiguously assigned to angular fluctuations around its orthogonal equilibrium configuration by investigating the chiral signals. As long as the dimer configuration fluctuates around an orthogonal equilibrium configuration, the linear chiral spectrum vanishes, but is non-zero for non-orthogonal configurations. In fact, the nonlinear 2D spectrum also vanishes when chiral fluctuations are absent, however, it has a finite signal when angular fluctuation are present. In turn, this signal can be utilized to experimentally accurately determine the autocorrelation times, which may be used to measure correlation times that are otherwise hardly accessible.

The second scenario falls within the same scope of qualitatively new effects induced by fluctuations. Therein, we analyzed the real-time dynamics of a quantum two-state system under the action of nonequilibrium quantum statistical fluctuations by taking the point of view of electronic quantum transport through a single-level quantum dot that is coupled to the quantum two-state system. When a finite transport voltage is applied, a nonequilibrium electron current flows so that the quantum two-level system is exposed to nonequilibrium fluctuations. Under the assumption of weak dot-lead electronic tunneling, a diagrammatic perturbation method is utilized on the basis of sequential charge tunneling. The electronic degrees of freedom can be integrated out such that the quantum dissipative dynamics of the two-state system itself can be directly studied. We have concentrated on the relaxation and dephasing processes at long times by calculating the smallest non-zero eigenvalues of

the underlying Liouville operator. In the regime of sequential tunneling processes, the action of the quantum noise is sufficiently weak such that the unperturbed energy spectrum of the dot-plus-two-level-system is a useful starting point. Since the eigenvalues of the Liouvillian rate matrix can easily be evaluated numerically, we have straightforward access to the nonequilibrium quantum relaxation and dephasing rates as a function of all model parameters. We find a rich structure in both of these observables, which can consistently be traced back to the unperturbed energy spectrum. Furthermore, an analysis in terms of Heisenberg–Langevin equations of motion allows us to extract the autocorrelation function of the nonequilibrium quantum statistical noise in the limit of a Markovian approximation. The zero-temperature limit allows us to obtain a simple spectral decomposition of the frequency components of the nonequilibrium noise under the action of a static DC voltage. Likewise, a generalized nonequilibrium fluctuation relation follows, which reproduces the well-known equilibrium fluctuation-dissipation theorem at zero transport voltage. A generalization to time-periodic AC voltages is also provided, such that a generalized driven fluctuation relation results, involving all higher harmonics.

Parametric Resonance for Driven Ultracold Atoms

This investigation is followed by a study of a driven one-dimensional Bose–Hubbard model with a periodically modulated harmonic trap. This system describes a gas of interacting bosonic atoms in a lattice which is placed in a parametrically modulated trapping potential. Within this model, the interplay of strong atomic interactions in the Mott state of the lattice and the external parametric drive can be investigated. We have analyzed the parametric resonance condition in the mean-field regime of weak atomic interactions. In the presence of the lattice, the dynamics of the condensate width is governed by the Mathieu equation. The resonance frequency of the condensate is shifted to lower values as the atomic interaction is increased. Moreover, the stability diagram of stable and unstable dynamics is inherited from the Mathieu equation but is altered due to the interaction. We compare numerically exact results, obtained by the time-evolving block decimation algorithm, which expands the wave-function in terms of matrix product states, in the transient regime with the aim to check the resonance condition predicted by our mean-field ansatz. Although the mean-field approach becomes invalid for stronger interaction, a good agreement is found. We note that for even stronger interactions, the formation of a local Mott-insulator region in which the movement of the atoms also in the presence of the driving becomes completely suppressed, leading to a breakdown of our mean-field approach. Finally, we have demonstrated that the global parametric modulation yields site-dependent hopping amplitudes which can be controlled by the external drive. Interestingly, locating the onset of the instability allows us, in principle, to determine the atom interaction strength. Thus, dynamically probing quantum many-body systems with a periodic modulation of the global harmonic confinement provides a diagnostic tool, which warrants an experimental realization in the realm of ultracold Bose gases.

Nonequilibrium Quantum Phase Transitions in Hybrid Systems

Finally, we put our focus on a rather new type of quantum hybrid systems. We have shown that a hybrid atom-optomechanical system possesses a nonequilibrium quantum phase transition between phases of different collective behavior. The interaction between the atomic condensate and the optomechanical part is realized in two different ways which allow to couple either the center-of-mass motion of the condensate or a certain transition between the internal states of the atoms to the vibrational motion of a membrane in an optical resonator. According to the type of coupling, these schemes are labeled *motional* and *internal* coupling scheme.

In the first coupling approach, the steady state of an ultracold atomic condensate in an optical lattice, whose motion is coupled to a single mechanical vibrational mode of a spatially distant membrane, has been analyzed based on an extended Gross–Pitaevskii like mean field approach. The coupling between both parts occurs via the light field of a common laser. Below the critical effective atom-membrane coupling λ_c , the atoms in the combined atom-membrane ground state are symmetrically distributed around their lattice minima. At the quantum critical point, this $\mathbb{Z}_2$ symmetry is spontaneously broken and a nonequilibrium quantum phase transition to a symmetry-broken state occurs in which the atomic center-of-mass and membrane displacements are all either positive or negative. Near the critical point of the nonequilibrium quantum phase transition, the lowest excitation mode shows roton-type characteristics, a mode softening of the excitation frequency and a bifurcation of the decay rate, accompanied by a strong atom-membrane entanglement. This variational ansatz was further generalized, which allows us to include fluctuating forces generated by the light field and environment.

In the second coupling approach, where the membrane is coupled to an internal state transition of the atoms in the gas, we have shown that this hybrid atom-optomechanical system also undergoes a nonequilibrium quantum phase transition between phases of different collective behavior. Most interestingly, the order of the phase transition can be tuned in a straightforward manner. Our investigation is based on an extended Gross–Pitaevskii-like mean-field approach with a time-dependent Gaussian variational ansatz. Mediated by the light field of a common laser, the atom-membrane coupling is tuned by changing the laser intensity. Below a critical coupling λ_c , all the atoms occupy the energetically lower atomic internal state $|-\rangle$ and at the critical point a nonequilibrium quantum phase transition occurs. This phase is characterized by a sizeable steady-state occupation of the energetically higher atomic internal state $|+\rangle$ and a constantly displaced membrane. Its order is determined by a state-dependent atom-membrane coupling and the size of the atomic transition frequency. For an asymmetric coupling, $\chi \neq 0$, we have shown that an asymmetric first-order phase transition occurs with a preferred polarization. Instead, for a symmetric coupling, $\chi = 0$, the phase transition is continuous for transition frequencies below a critical value Ω_c and discontinuous above. Moreover, the first-order transition is accompanied by hysteresis. The crossover between the first- and second-order phase transition is observable by tuning readily accessible parameters in the internal state coupling scheme.

Within the *internal* coupling scheme, we have further investigated the effect of finite

atom-atom interactions in the two-component atom gas on the nanomechanical vibrational state of the nanomembrane. In the zero temperature limit, the spectral density of the quasi-particle excitations induced by atomic interactions can be determined within a Bogoliubov approach. We isolate the fundamental mode and treat the higher modes in the limit that they are non-interacting as a harmonic bath. The spectral density of the latter is gapped and exhibits a two peak structure with a dominant peak at the atomic transition frequency and a reduced peak at the largest attainable frequency in the reduced atomic system. We show that, even at finite temperature, the quasi-particle excitations can be used to enhance the two-mode squeezing of the displacement variance of the nanomembrane, thereby creating highly nontrivial quantum many-body states that involve a squeezed nanomechanical mode and an interacting atom gas coupled in a hybrid optomechanical setup. Squeezing of the nanomembrane displacement only occurs when quasi-particle excitations are possible above the spectral gap.

Finally, we have shown that even the Gaussian ansatz in the time-dependent variational perturbation theory with a unified condensate profile width for atoms in the energetically lower and higher internal state is capable of describing individual breathing mode excitations in a straightforward manner. This approach may be used to determine correlation functions and quantum entanglement in the steady-state regime. In addition, a modified variational multi-mode ansatz is applied to the nonequilibrium Dicke model, which readily allows one to study the nonequilibrium Dicke phase transition. A promising application of this description is to find relations between the number of photons dissipated out of the cavity and the condensate parameters. For instance, this would allow non-destructive measurements of the condensate width rather than usual methods which rely on time-of-flight measurements.

Appendix A

First-Order Integral Kernel of the Diagrammatic Perturbation Series

To determine the dynamics of the quantum dot and the stationary current, we have to evaluate the integral $I_\alpha^\pm(\omega)$ of equation (2.43). However, in order to find an analytical solution to this integral, for instance by using the residue theorem, the integrand has to approach zero faster than $1/E$ as E is sent to $\pm\infty$. In fact, this is only satisfied for one of these limits since $\lim_{E\to\pm\infty} f_\alpha^\pm(E) = 0$, while in the other limit $\lim_{E\to\mp\infty} f_\alpha^\pm(E) = 1$.

To circumvent this contradiction, we introduce a Lorentzian cut-off weight function $D_\alpha(z) = \omega_c^2/[(z-\mu_\alpha)^2+\omega_c^2]$ with the cut-off frequency (or band width) ω_c. Then, we can replace the integral $\int dE \to \int dE\, D_\alpha(E)$. By choosing the cut-off frequency ω_c large in comparison to the relevant energies in the system, the integrand remains almost unchanged on the real axis and we can close the integration path over the upper or lower complex half plane. In practice, we choose the path according to figure A.1 and average over the contributions from contour A and contour B. Here, the dots indicate the poles of the integrand, which are given by $z_0 = \omega + i0^+, z_\pm = \mu_\alpha \pm \omega_c$. In addition, the Fermi-Dirac distribution has poles at $z = \mu_\alpha + \nu_n$ with the fermionic Matsubara frequencies $\nu_n = i\pi(2n+1)/\pi$, which are located on the dotted line. Hence, the integral $I_\alpha^\pm(\omega)$ is given by the contour integral

$$\begin{aligned} I_\alpha^\pm(\omega) =& \frac{1}{2}\left[\oint_A dz\, g(z) + \oint_B dz\, g(z)\right] \\ =& i\pi\left[\sum_{\mathrm{Im}(z)>0} \mathrm{Res}(g,z) - \sum_{\mathrm{Im}(z)<0} \mathrm{Res}(g,z)\right], \end{aligned} \tag{A.1}$$

with the function $g(z) = if_\alpha^\pm(z)D_\alpha(z)/(\omega - z - i0^+)$.

By inserting the residues of the function $g(z)$, the integral is evaluated to be

$$\begin{aligned} I_\alpha^\pm(\omega) =& -\pi D_\alpha(\omega)\left[f_\alpha^\pm(\omega) + \frac{\omega-\mu_\alpha}{2i\omega_c} \pm \frac{i}{2}\tan(\beta\omega_c/2)\right] \\ & \pm (\pi/\beta) D_\alpha(\omega) \sum_{n=0}^{\infty}\left(\frac{1}{\omega-\mu_\alpha-\nu_n} - \frac{1}{\omega+\nu_n}\right) \\ & \pm (\pi/\beta) D_\alpha(\omega) \sum_{n=0}^{\infty}\left(\frac{1}{\nu_n - i\omega_c} - \frac{1}{\nu_n + i\omega_c}\right). \end{aligned} \tag{A.2}$$

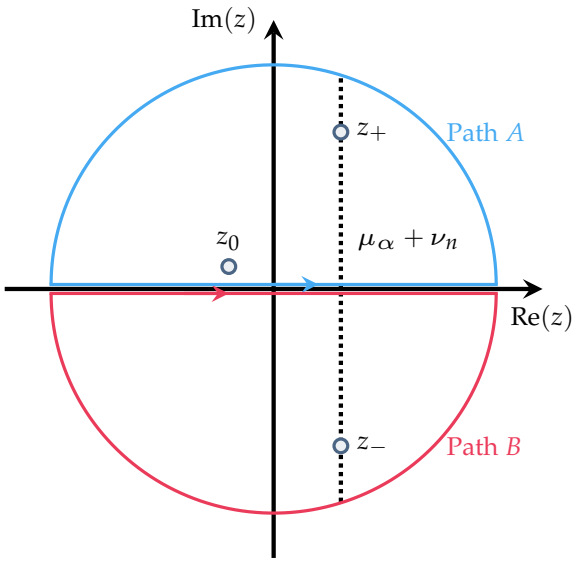

FIGURE A.1: The contours A and B in the complex plane are illustrated. The circles indicate the positions of the singularities of the function $g(z)$ for the case $\omega < 0$ and $\mu_\alpha > 0$. The singularities of the Fermi-Dirac distribution are located on the vertical dotted line.

The sum over the Matsubara frequencies can be reduced to a simple analytic expression by making use of the properties of the digamma function $\psi_0(z)$, where $\psi_0(z_1) - \psi_0(z_2) = \sum_{n=0}^{\infty}[(n+z_1)^{-1} - (n+z_2)^{-1}]$. Finally, we consider a very large cut-off frequency ω_c, such that the weight function satisfies $D_\alpha(\omega) \simeq 1$. Then, the integral simplifies

$$I_\alpha^{\pm}(\omega) = -\pi f_\alpha^{\pm}(\omega) \pm i \log(\beta\omega_c/2\pi) \pm \frac{1}{2i}\left[\psi_0\left(\frac{1}{2} + \frac{i\beta}{2\pi}[\omega - \mu_\alpha]\right) + \psi_0\left(\frac{1}{2} - \frac{i\beta}{2\pi}[\omega - \mu_\alpha]\right)\right], \tag{A.3}$$

where we have further used the asymptotic expansion $\psi_0(x+1) = \log(x) + \mathcal{O}(x^{-1})$ of the digamma function. In addition, we have used the identity

$$i\pi \tan(\beta\omega_c/2) = \psi_0\left(\frac{1}{2} - \frac{\beta\omega_c}{2\pi}\right) - \psi_0\left(\frac{1}{2} + \frac{\beta\omega_c}{2\pi}\right). \tag{A.4}$$

We note that due to the structure of the super-operators $\boldsymbol{W}$ and $\boldsymbol{W}^I$, many of the contributions include terms of the form $\sim I_\alpha^{\pm}(\omega) + [I_\alpha^{\pm}(\omega')]^*$ or $\sim I_\alpha^{\pm}(\omega) + I_\alpha^{\mp}(\omega')$ such that these expressions under the summation over all terms become independent of the choice of ω_c.

Appendix B

Numerical Solution to Inhomogeneous First-Order Differential Equations

Suppose that one wants to find the solution to the differential equation

$$\partial_t \boldsymbol{x}(t) = \boldsymbol{M}\boldsymbol{x}(t) + \boldsymbol{y}(t)\,, \tag{B.1}$$

where $\boldsymbol{x}$ and $\boldsymbol{y}$ are both n-dimensional vectors and $\boldsymbol{M}$ is a $n \times n$ matrix. In terms of analytic expressions, the solution is simply given by

$$\boldsymbol{x}(t) = e^{\boldsymbol{M}t}\boldsymbol{x}(0) + \int_0^t ds\, e^{\boldsymbol{M}(t-s)}\boldsymbol{y}(s)\,. \tag{B.2}$$

However, the numerical solution of the analytic expression is rather tedious. The problem arises from the matrix exponential in (B.2) in combination with the fact that $\boldsymbol{M}$ is, in general, non-normal. Hence, the matrix $\boldsymbol{M}$ has different left and right eigenvectors $\boldsymbol{\ell}^{(i)}$ and $\boldsymbol{r}^{(i)}$, respectively, which are biorthogonal according to the scalar product $(\boldsymbol{\ell}^{(i)}, \boldsymbol{r}^{(j)}) = \sum_{k=1}^{n} \ell_k^{(i)} r_k^{(j)} = \delta_{ij}$. The right eigenvectors are defined as column vectors satisfying

$$\boldsymbol{M}\boldsymbol{r}^{(i)} = m_i \boldsymbol{r}^{(i)}\,, \tag{B.3}$$

where the left eigenvectors are defined as row vectors satisfying

$$\boldsymbol{\ell}^{(i)}\boldsymbol{M} = m_i \boldsymbol{\ell}^{(i)}\,, \tag{B.4}$$

with the same eigenvalues m_i. It is then easier to express the evolution vector $\boldsymbol{x}$ in terms of the left eigenvectors. That is, one defines the quasi-normal mode by $q_i(t) = \sum_{k=1}^{n} \ell_k^{(i)} x_k(t)$. By multiplying equation (B.2) with $\boldsymbol{\ell}^{(i)}$ from the left, we arrive at the expression

$$q_i(t) = e^{m_i t} q_i(0) + \int_0^t ds\, e^{m_i(t-s)} p_i(s)\,, \tag{B.5}$$

with $p_i(t) = (\boldsymbol{\ell}^{(i)}, \boldsymbol{y}(t)) = \sum_{k=1}^{n} \ell_k^{(i)} y_k(t)$. The original vector is then reproduced via $\boldsymbol{x}(t) = \sum_i q_i(t)\boldsymbol{r}^{(i)}$.

The left and right eigenvector decomposition is easily found with the usual numerical packages, such as LAPACK (Linear Algebra Package) for instance. The only delicate point is the biorthogonality condition $\boldsymbol{\ell}^{(i)}\boldsymbol{r}^{(j)} = \delta_{ij}$. Numerical methods usually choose the orthonormal sets independently according to the conditions $\boldsymbol{r}^{(i)\dagger}\boldsymbol{r}^{(j)} = \delta_{ij}$ and $\boldsymbol{\ell}^{(i)}\boldsymbol{\ell}^{(j)\dagger} = \delta_{ij}$. In general, such an evaluation is not compatible up to a matrix $\boldsymbol{C}$, i.e., $(\boldsymbol{\ell}^{(i)}, \boldsymbol{r}^{(j)}) = C_{ij}$, with the biorthogonality condition. In many cases, this matrix is diagonal and the eigenvectors can simply be scaled by a factor of the norm. On the other hand, when this is not the case, one can do the following.

By forming matrices $\boldsymbol{L}$ and $\boldsymbol{R}$ with the left and right eigenvectors, respectively, the inner product becomes

$$\boldsymbol{LR} = \boldsymbol{C}\,. \tag{B.6}$$

In order to arrive at the expression $\boldsymbol{LR} = \mathbf{1}$, one can do a LU decomposition (lower-upper) of the matrix $\boldsymbol{C} = \boldsymbol{C}_L\boldsymbol{C}_U$. Here, $\boldsymbol{C}_L$ is a lower triangular matrix and $\boldsymbol{C}_U$ is a upper triangular matrix. Then,

$$\boldsymbol{C}_L^{-1}\boldsymbol{LR}\boldsymbol{C}_U^{-1} = \mathbf{1} \tag{B.7}$$

suggests the new biorthonormal vectors

$$\boldsymbol{L}' = \boldsymbol{C}_L^{-1}\boldsymbol{L} \tag{B.8a}$$

$$\boldsymbol{R}' = \boldsymbol{R}\boldsymbol{C}_U^{-1}\,. \tag{B.8b}$$

Appendix C

The Crank–Nicolson Scheme

In general, the Gross–Pitaevskii equation for an atomic ensemble in one dimension is given by

$$i\partial_t \psi(t,z) = \left[-\frac{\partial_z^2}{2m} + V(t,z) \right] \psi(t,z)\,, \tag{C.1}$$

where the potential $V(t,z)$ includes the particle-particle interaction $gN|\psi(t,z)|$ and m is the mass of a single atom. In order to formulate a numerical scheme, let us denote the state after the n-th time step in discretized space by

$$\psi_j^n = \psi(n\delta t, z_0 + j\delta z)\,, \tag{C.2}$$

with the grid spacing δz and the time step δt. By using the equivalent description for the potential $V_j^n = V(n\delta t, z_0 + j\delta z)$, the equation of motion in the Crank–Nicolson scheme reads

$$i\frac{\psi_j^{n+1} - \psi_j^n}{\delta t} = -\frac{\psi_{j+1}^{n+1/2} - 2\psi_j^{n+1/2} + \psi_{j-1}^{n+1/2}}{2m\delta z^2} + V_j^n \psi_j^{n+1/2}\,, \tag{C.3}$$

where $\psi_j^{n+1/2} = (\psi_{j+1}^{n+1} + \psi_j^n)/2$. This average is essential for the Crank–Nicolson scheme. In comparison to a *backward time centered scheme* and *forward time centered scheme*, where only the updated state ψ_j^{n+1} or the initial state ψ_j^n on the right-hand side are taken into account, the error is reduced by one order of magnitude to $\mathcal{O}(\delta t^3)$ for the non-interacting case $g = 0$.

To find an equation which relates the updated state ψ_j^{n+1} to the initial state ψ_j^n, we introduce a vector notation for the condensate function. The relation between the old and the new vector can then be written in terms of a matrix-vector multiplication according to

$$\boldsymbol{\psi}^{n+1} = \left(1 + \tfrac{i}{2}\boldsymbol{H}_{CN}^n \delta t\right)^{-1} \left(1 - \tfrac{i}{2}\boldsymbol{H}_{CN}^n \delta t\right) \boldsymbol{\psi}^n\,, \tag{C.4}$$

with the discretized Hamiltonian at time step n

$$\boldsymbol{H}_{CN}^n = -\frac{1}{2m\delta z^2} \begin{pmatrix} -2 & 1 & & & \Delta_{BC} \\ 1 & -2 & 1 & & \\ & 1 & \ddots & \ddots & \\ & & \ddots & \ddots & 1 \\ \Delta_{BC} & & & 1 & -2 \end{pmatrix} + \begin{pmatrix} V_1^n & & & & \\ & V_2^n & & & \\ & & V_3^n & & \\ & & & V_4^n & \\ & & & & \ddots \end{pmatrix}. \tag{C.5}$$

Here, the parameter Δ_{BC} is either 0 or 1 for open boundary conditions or periodic boundary conditions, respectively. By expanding the matrix product, one finds the replacement $(1 + i\boldsymbol{H}^n_{CN}\delta t/2)^{-1}(1 - i\boldsymbol{H}^n_{CN}\delta t/2) = \boldsymbol{Q}^{-1} - 1$, where $\boldsymbol{Q} = (1 + i\boldsymbol{H}^n_{CN}\delta t/2)/2$. With this relation, equation (C.4) reduces to

$$\boldsymbol{\psi}^{n+1} = \boldsymbol{Q}^{-1}\boldsymbol{\psi}^n - \boldsymbol{\psi}^n\,, \tag{C.6}$$

which is the basis equation for the numerical time evolution.

In order to calculate the ground state or steady state for a given problem, the Crank–Nicolson scheme can be used in imaginary time. Hence, the time step has to be exchanged by $\delta t \to -i\delta\tau$. Then, the ground state can be estimated via equation (C.6) with the matrix $\boldsymbol{Q}_{im} = (1 + \boldsymbol{H}^n_{CN}\delta\tau/2)/2$. Due to the non-unitary time evolution, the state ψ has to be normalized after each time step.

Appendix D

Bogoliubov Transformation

In order to diagonalize the Hamiltonian of the excited modes

$$H^B_{\text{exc}} = \sum_{k\neq 0}\sum_{\tau=\pm}\left(\epsilon_{k\tau} - \epsilon_{0-} + nU\right) c^\dagger_{k\tau} c_{k\tau} + \frac{nU}{2}\sum_{k\neq 0}\left(c_{-k-}c_{k-} + \text{H.c.}\right), \tag{D.1}$$

we rewrite it in terms of a vector matrix product

$$H^B_{\text{exc}} = \sum_{k\neq 0}\begin{pmatrix} c^\dagger_{k-} & c_{-k-}\end{pmatrix}\begin{pmatrix} E_k & nU \\ nU & E_{-k}\end{pmatrix}\begin{pmatrix} c_{k-} \\ c^\dagger_{-k-}\end{pmatrix} + \sum_{k\neq 0}\omega_{k+}c^\dagger_{k+}c_{k+}, \tag{D.2}$$

with $E_k = \epsilon_{k-} - \epsilon_{0-} + nU$. The second term is already diagonal. For the first term, we make the ansatz given in equation (8.9). Imposing canonical commutation relations for the quasi-particle operators d_{k-} leads to the relations

$$\phi_k\phi^*_k - \theta_k\theta^*_k = 1, \tag{D.3a}$$

$$\phi_k\theta_{-k} - \phi_{-k}\theta_k = 0. \tag{D.3b}$$

Under these restrictions, the eigenvalue problem reduces to

$$\begin{pmatrix} E_k & nU \\ -nU & -E_{-k}\end{pmatrix}\begin{pmatrix}\phi_k \\ \theta_k\end{pmatrix} = \omega_{k-}\begin{pmatrix}\phi_k \\ \theta_k\end{pmatrix}, \tag{D.4}$$

which includes a non-hermitian matrix. In general, the eigenvalues of this matrix can become complex, but since $\epsilon_{k-} - \epsilon_{0-} > 0$, this is not possible here. Moreover, these eigenvalues always appear in pairs with $\omega_{k-} = -\omega^*_{k-}$, where only one of the corresponding eigenvectors can fulfill the orthonormalization conditions (D.3). Consequently, we find that only the eigenvalues $\omega_{k-} = (\epsilon_{k-} - \epsilon_{0-})\sqrt{1 + 2nU/(\epsilon_{k-} - \epsilon_{0-})}$ and their corresponding eigenvectors (8.10) allow canonical commutation relations for the quasi-particle modes.

Appendix $\mathcal{E}$

Path Integral Formalism and Displacement Variance

In order to find an analytic solution to our problem of equation (8.12), we will integrate out the Bogoliubov quasi-particle modes. This is done in a path integral formalism for which an analytical solution for two bilinearly coupled harmonic oscillators interacting with a harmonic 'bath' can be written down explicitly. Hence, we define the interaction Hamiltonian according to

$$H_I^B = (\Lambda_1 q_1 + \Lambda_2 q_2) \sum_{k\neq 0} \left(\phi_k d_{k-}^\dagger d_{k+} + \theta_k d_{k-} d_{-k+} + \text{H.c.} \right) . \tag{E.1}$$

In this context, we follow the description of reference [237], which addresses a similar structure of the coupling Hamiltonian, yet in the context of two-phonon processes in a Caldeira–Leggett model.

E.1 The Influence Functional and Spectral Density of Quasi-Particle Excitations at Zero Temperature

The influence functional in imaginary time, describing the membrane-atom coupling to the excited modes, takes the form

$$\mathcal{F}[\boldsymbol{q}(\cdot)] = \exp\left(-S_{\text{infl}}[\boldsymbol{q}(\cdot)]\right) = Z_{\text{ex}}^{-1} \int \mathcal{D}\boldsymbol{x} \, \exp\left(-S_{\text{ex}}[\boldsymbol{x}] - S_I[\boldsymbol{q},\boldsymbol{x}]\right) , \tag{E.2}$$

where $\boldsymbol{x}$ and $\boldsymbol{q}$ denote the $2(L-1)$ component vector of the Bogoliubov modes and the mixed coordinates q_1 and q_2 of equation (8.15). Moreover, $Z_{\text{ex}} = \operatorname{tr} e^{-\beta \sum_{k\neq 0} (\omega_{k-} n_{k-} + \omega_{k+} n_{k+})}$ is the free partition function of the excited atomic modes at $k \neq 0$ and $S_{\text{ex}}[\boldsymbol{x}]$ is the corresponding action.

In order to integrate out the Bogoliubov modes, it is essential for the coupling Hamiltonian to fulfill $\langle H_I^B \rangle_\beta = 0$ in the zero coupling limit $\Lambda = 0$ with $\langle \cdot \rangle_\beta = Z_{\text{ex}}^{-1} \int \mathcal{D}\boldsymbol{x}\, e^{-S_{\text{ex}}}(\cdot)$. Then, the right-hand side of equation (E.2) can be considerably simplified in two steps. First, we expand the exponential

$$Z_{\text{ex}}^{-1} \int \mathcal{D}\boldsymbol{x} \, \exp\left(-S_{\text{ex}}[\boldsymbol{x}] - S_I[\boldsymbol{q},\boldsymbol{x}]\right) = \sum_n \frac{1}{n!} \langle (-S_I[\boldsymbol{q},\boldsymbol{x}])^n \rangle_\beta \tag{E.3}$$

and observe that only even terms in n contribute to the sum. By reordering the terms under the sum, it can be shown [237] that the only relevant contribution is the correlator $\langle H_I^B[\boldsymbol{q}(\rho)]H_I^B[\boldsymbol{q}(\varsigma)]\rangle_\beta$. Then, the influence action is simply given by the expression

$$S_{\text{infl}}[\boldsymbol{q}(\cdot)] = -\int_0^\beta d\rho \int_0^\rho d\varsigma \, \langle H_I^B[\boldsymbol{q}(\rho)]H_I^B[\boldsymbol{q}(\varsigma)]\rangle_\beta \,. \tag{E.4}$$

The correlator can be evaluated exactly and we find the expression

$$\begin{aligned}\langle H_I^B[\boldsymbol{q}(\rho)H_I^B[\boldsymbol{q}(\varsigma)]\rangle_\beta = \left[\sum_{s=1}^{2} \Lambda_s q_s(\rho)\right]\left[\sum_{s'=1}^{2} \Lambda_{s'} q_{s'}(\varsigma)\right] \sum_{k\neq 0} \{\phi_k^2[n(\omega_{k-}) - n(\omega_{k+})]D_{\Delta_k}(\rho-\varsigma) \\ +\theta_k^2[n(\omega_{k-}) + n(\omega_{k+}) + 1]D_{\Omega_k}(\rho-\varsigma)\}\end{aligned} \tag{E.5}$$

with the frequencies $\Omega_k = \omega_{k+} + \omega_{k-}$ and $\Delta_k = \omega_{k+} - \omega_{k-}$, and the free boson propagator $D_\omega(\rho)$. With this in mind, we may write the influence action according to equation (8.13).

At zero temperature, the spectral density of the quasi-particle excitations reduces to

$$G_{T=0}(\omega) = \sum_{k\neq 0}\left(\frac{\epsilon_{k-} - \epsilon_{0-} + nU - \omega_{k-}}{2\omega_{k-}}\right)\delta(\omega - \Omega_k) \simeq \sum_{k\neq 0}\left[\frac{nU}{4J\sin^2(k/2)}\right]^2 \delta(\omega-\Omega_k)\,, \tag{E.6}$$

where we have expanded the quasi-particle eigenfrequencies ω_{k-} to second order in nU, and used that $\epsilon_{k-} - \epsilon_{0-} = 4J\sin^2(k/2)$. Using that the delta distribution, composed with a smooth function $g(x)$, follows $\delta(g(x)) = \delta(x-x_0)/|g'(x_0)|$, when $g(x)$ has only the root $g(x_0) = 0$ in the interval of integration, we may rewrite the delta distribution in equation (E.6). For this, we define $g(k) = \omega - \Omega_k \simeq \omega - \Omega_\text{a} - nU - 8J\sin^2(k/2)$ and expand it to lowest order in nU. The momentum, for which $g(\kappa(\omega)) = 0$, is given by the expression $\kappa(\omega) = 2\sin^{-1}\sqrt{\omega - \Omega_\text{a} - nU)/8J}$, and the derivative with respect to k is simply $g'(k) = -4J\sin(k)$. Inserting these expressions in equation (E.6), the spectral density is approximated by

$$G_{T=0}(\omega) \simeq \left(\frac{nU}{4J}\right)^2 \sum_{k\neq 0}\frac{\delta[k-\kappa(\omega)]}{4J|\sin(k)|\sin^4(k/2)}\,. \tag{E.7}$$

By replacing the summation over the momenta k with an integral, i.e., $\sum_{k\neq 0} \to \frac{L}{2\pi}\int_0^{2\pi} dk$, we arrive at the expression for the zero temperature spectral density, given in equation (8.17).

E.2 Analytic Solution for the Path Integral

The path integral with the effective action $S_\text{eff}[\boldsymbol{q}(\cdot)]$, given in equation (8.18), can be evaluated in a closed analytic expression. Therefore, we expand the path $\boldsymbol{q}(\rho) = \bar{\boldsymbol{q}}(\rho) + \boldsymbol{y}(\rho)$ around its extremal, classical path $\bar{\boldsymbol{q}}(\rho)$ with the quantum-mechanical deviation $\boldsymbol{y}(\rho)$. By

inserting this ansatz in the effective action, we find

$$S_{\text{eff}}[\boldsymbol{q}(\cdot)] = S_{\text{eff}}[\bar{\boldsymbol{q}}(\cdot)] + \frac{1}{2}\int_0^\beta d\rho\, \boldsymbol{y}^T(\rho)\boldsymbol{K}\boldsymbol{y}(\rho)\,, \tag{E.8}$$

where the matrix $\boldsymbol{K}$ is defined according to

$$K_{ss'}y_{s'}(\rho) = \delta_{ss'}\left(\Omega_s^2 - \partial_\rho^2\right) y_s(\rho) - 2\Lambda_s\Lambda_{s'}\int_0^\beta d\varsigma\, k(\rho-\varsigma)y_s(\varsigma)\,. \tag{E.9}$$

The extremal path fulfills the relation $\partial_{\boldsymbol{q}} S_{\text{eff}}[\boldsymbol{q}]|_{\boldsymbol{q}=\bar{\boldsymbol{q}}} = 0$. Via a Fourier expansion of the kernel $k(\rho) = \sum_{n=-\infty}^{\infty}\hat{k}_n e^{i\nu_n\rho}/2$ and the deviations $y_s(\rho)\sum_{n=-\infty}^{\infty}\hat{y}_{sn}e^{i\nu_n\rho}/2$, with bosonic Matsubara frequencies $\nu_n = 2\pi n/\beta$, the effective action takes the form

$$S_{\text{eff}}[\boldsymbol{q}(\cdot)] = S_{\text{eff}}[\bar{\boldsymbol{q}}(\cdot)] + \frac{1}{2\beta}\sum_{s,s'=1}^{2}\sum_{n=-\infty}^{\infty}\hat{y}_{sn}\left[\delta_{ss'}(\Omega_s^2+\nu_n^2) - 2\Lambda_s\Lambda_{s'}\hat{k}_n\right]\hat{y}_{s'n}\,. \tag{E.10}$$

By performing the integration over the deviations, the partition function reduces to the expression

$$Z(\beta) = \mathcal{N}\frac{e^{-S_{\text{eff}}[\bar{\boldsymbol{q}}]}}{\sqrt{D_0}}\prod_{n>0}\frac{1}{D_n} \tag{E.11}$$

where $\mathcal{N}$ is a universal normalization constant, which drops out when evaluating expectation values. The denominators D_n are given by

$$D_n = \left(\Omega_1^2+\nu_n^2\right)\left(\Omega_2^2+\nu_n^2\right) - 2\Lambda^2\hat{k}_n(\Omega_1^2\sin^2\zeta + \Omega_2^2\cos^2\zeta + \nu_n^2)\,, \tag{E.12}$$

where $\Lambda^2 = \Lambda_1^2 + \Lambda_2^2$ is the atom-membrane coupling strength. Moreover, the Fourier expansion coefficients of the kernel are given by the expression

$$\hat{k}_n = \sum_{p\neq 0}\left\{\frac{\phi_p^2\Delta_p}{\Delta_p^2+\nu_n^2}[n(\omega_{p+}) - n(\omega_{p-})] + \frac{\theta_p^2\Omega_p}{\Omega_p^2+\nu_n^2}[n(\omega_{p+}) + n(\omega_{p-}) + 1]\right\}. \tag{E.13}$$

References

[1] A. Einstein, Annalen der Physik **322**, 549 (1905).

[2] H. B. Callen and T. A. Welton, Physical Review **83**, 34 (1951).

[3] R. Kubo, Reports on Progress in Physics **29**, 255 (1966).

[4] R. Kubo, Journal of the Physical Society of Japan **12**, 570 (1957).

[5] M. Campisi, P. Hänggi, and P. Talkner, Review of Modern Physics **83**, 771 (2011).

[6] P. Hauke, M. Heyl, L. Tagliacozzo, and P. Zoller, Nature Physics **12**, 778 (2016).

[7] S. Pappalardi, A. Russomanno, A. Silva, and R. Fazio, Journal of Statistical Mechanics: Theory and Experiment **2017**, 053104 (2017).

[8] K. Funo, M. Ueda, and T. Sagawa, in *Thermodynamics in the Quantum Regime*, Vol. 195, edited by F. Binder, L. A. Correa, C. Gogolin, J. Anders, and G. Adesso, Fundamental Theories of Physics (Springer International Publishing, Basel, 2019).

[9] D. J. Evans, E. G. D. Cohen, and G. P. Morriss, Physical Review Letters **71**, 2401 (1993).

[10] G. Gallavotti and E. G. D. Cohen, Journal of Statistical Physics **80**, 931 (1995).

[11] C. Jarzynski, Physical Review Letters **78**, 2690 (1997).

[12] G. E. Crooks, Physical Review E **60**, 2721 (1999).

[13] C. Jarzynski, Journal of Statistical Physics **98**, 77 (2000).

[14] T. Hatano and S. Sasa, Physical Review Letters **86**, 3463 (2001).

[15] E. H. Trepagnier, C. Jarzynski, F. Ritort, G. E. Crooks, C. J. Bustamante, and J. Liphardt, Proceedings of the National Academy of Sciences **101**, 15038 (2004).

[16] U. Seifert, Physical Review Letters **95**, 040602 (2005).

[17] R. Kawai, J. M. R. Parrondo, and C. V. den Broeck, Physical Review Letters **98**, 080602 (2007).

[18] M. Esposito, U. Harbola, and S. Mukamel, Review of Modern Physics **81**, 1665 (2009).

[19] D. J. Evans and D. J. Searles, Physical Review E **50**, 1645 (1994).

[20] D. J. Evans and D. J. Searles, Physical Review E **53**, 5808 (1996).

[21] D. J. Evans and D. J. Searles, Advances in Physics **51**, 1529 (2002).

[22] C. Jarzynski, Annual Review of Condensed Matter Physics **2**, 329 (2011).

[23] U. Seifert, Reports on Progress in Physics **75**, 126001 (2012).

[24] C. Jarzynski, Physical Review E **56**, 5018 (1997).

[25] J. Liphardt, S. Dumont, S. B. Smith, I. Tinoco, and C. Bustamante, Science **296**, 1832 (2002).

[26] D. Collin, F. Ritort, C. Jarzynski, S. B. Smith, I. Tinoco Jr, and C. Bustamante, Nature **437**, 231 (2005).

[27] T. Sagawa, "Second law-like inequalities with quantum relative entropy: an introduction", in *Lectures on Quantum Computing, Thermodynamics and Statistical Physics* (World Scientific, Singapore, 2012).

[28] A. M. Alhambra, L. Masanes, J. Oppenheim, and C. Perry, Physical Review X **6**, 041017 (2016).

[29] A. Alemany, A. Mossa, I. Junier, and F. Ritort, Nature Physics **8**, 688 (2012).

[30] K. Hayashi, H. Ueno, R. Iino, and H. Noji, Physical Review Letters **104**, 218103 (2010).

[31] T. B. Batalhão, A. M. Souza, L. Mazzola, R. Auccaise, R. S. Sarthour, I. S. Oliveira, J. Goold, G. De Chiara, M. Paternostro, and R. M. Serra, Physical Review Letters **113**, 140601 (2014).

[32] S. An, J.-N. Zhang, M. Um, D. Lv, Y. Lu, J. Zhang, Z.-Q. Yin, H. T. Quan, and K. Kim, Nature Physics **11**, 193 (2015).

[33] M. Naghiloo, D. Tan, P. M. Harrington, J. J. Alonso, E. Lutz, A. Romito, and K. W. Murch, arXiv:1703.05885 (2017).

[34] A. Larkin and Y. N. Ovchinnikov, Journal of Experimental and Theoretical Physics **28**, 1200 (1969).

[35] N. Tsuji, T. Shitara, and M. Ueda, Physical Review E **97**, 012101 (2018).

[36] N. Tsuji, T. Shitara, and M. Ueda, Physical Review E **98**, 012216 (2018).

[37] N. Tsuji and M. Ueda, arXiv:1807.11683 (2018).

[38] E. P. Wigner and M. M. Yanase, Proceedings of the National Academy of Sciences **49**, 910 (1963).

[39] T. Förster, Annalen der Physik **437**, 55.

[40] P. Nalbach, I. Pugliesi, H. Langhals, and M. Thorwart, Physical Review Letters **108**, 218302 (2012).

[41] F. Šanda and S. Mukamel, The Journal of Chemical Physics **135**, 194201 (2011).

[42] J. König, H. Schoeller, and G. Schön, Physical Review Letters **76**, 1715 (1996).

[43] J. König, J. Schmid, H. Schoeller, and G. Schön, Physical Review B **54**, 16820 (1996).

[44] M. Rigol and M. Srednicki, Physical Review Letters **108**, 110601 (2012).

[45] J. M. Deutsch, Physical Review A **43**, 2046 (1991).

[46] M. Srednicki, Physical Review E **50**, 888 (1994).

[47] C. Kollath, A. M. Läuchli, and E. Altman, Physical Review Letters **98**, 180601 (2007).

[48] M. Rigol, V. Dunjko, and M. Olshanii, Nature **452**, 854 (2008).

[49] M. Rigol, Physical Review Letters **103**, 100403 (2009).

[50] M. Rigol, Physical Review A **80**, 053607 (2009).

[51] L. F. Santos and M. Rigol, Physical Review E **81**, 036206 (2010).

[52] L. F. Santos and M. Rigol, Physical Review E **82**, 031130 (2010).

[53] C. Neuenhahn and F. Marquardt, Physical Review E **85**, 060101 (2012).

[54] E. Khatami, G. Pupillo, M. Srednicki, and M. Rigol, Physical Review Letters **111**, 050403 (2013).

[55] S. Sorg, L. Vidmar, L. Pollet, and F. Heidrich-Meisner, Physical Review A **90**, 033606 (2014).

[56] L. D'Alessio, Y. Kafri, A. Polkovnikov, and M. Rigol, Advances in Physics **65**, 239 (2016).

[57] A. Lazarides, A. Das, and R. Moessner, Physical Review E **90**, 012110 (2014).

[58] A. Russomanno, G. E. Santoro, and R. Fazio, Journal of Statistical Mechanics: Theory and Experiment **2016**, 073101 (2016).

[59] L. D'Alessio and M. Rigol, Physical Review X **4**, 041048 (2014).

[60] M. Bukov, L. D'Alessio, and A. Polkovnikov, Advances in Physics **64**, 139 (2015).

[61] F. Schmitt, P. S. Kirchmann, U. Bovensiepen, R. G. Moore, L. Rettig, M. Krenz, J.-H. Chu, N. Ru, L. Perfetti, D. H. Lu, M. Wolf, I. R. Fisher, and Z.-X. Shen, Science **321**, 1649 (2008).

[62] R. Yusupov, T. Mertelj, V. V. Kabanov, S. Brazovskii, P. Kusar, J.-H. Chu, I. R. Fisher, and D. Mihailovic, Nature Physics **6**, 681 (2010).

[63] S. Hellmann, M. Beye, C. Sohrt, T. Rohwer, F. Sorgenfrei, H. Redlin, M. Kalläne, M. Marczynski-Bühlow, F. Hennies, M. Bauer, A. Föhlisch, L. Kipp, W. Wurth, and K. Rossnagel, Physical Review Letters **105**, 187401 (2010).

[64] T. Rohwer, S. Hellmann, M. Wiesenmayer, C. Sohrt, A. Stange, B. Slomski, A. Carr, Y. Liu, L. M. Avila, M. Kalläne, S. Mathias, L. Kipp, K. Rossnagel, and M. Bauer, Nature **471**, 490 (2011).

[65] M. Rini, R. Tobey, N. Dean, J. Itatani, Y. Tomioka, Y. Tokura, R. W. Schoenlein, and A. Cavalleri, Nature **449**, 72 (2007).

[66] D. J. Hilton, R. P. Prasankumar, S. Fourmaux, A. Cavalleri, D. Brassard, M. A. El Khakani, J. C. Kieffer, A. J. Taylor, and R. D. Averitt, Physical Review Letters **99**, 226401 (2007).

[67] M. Liu, H. Y. Hwang, H. Tao, A. C. Strikwerda, K. Fan, G. R. Keiser, A. J. Sternbach, K. G. West, S. Kittiwatanakul, J. Lu, S. A. Wolf, F. G. Omenetto, X. Zhang, K. A. Nelson, and R. D. Averitt, Nature **487**, 345 (2012).

[68] J. Demsar, R. D. Averitt, A. J. Taylor, V. V. Kabanov, W. N. Kang, H. J. Kim, E. M. Choi, and S. I. Lee, Physical Review Letters **91**, 267002 (2003).

[69] J. Graf, C. Jozwiak, C. L. Smallwood, H Eisaki, R. A. Kaindl, D.-H. Lee, and A. Lanzara, Nature Physics **7**, 805 (2011).

[70] C. L. Smallwood, J. P. Hinton, C. Jozwiak, W. Zhang, J. D. Koralek, H. Eisaki, D.-H. Lee, J. Orenstein, and A. Lanzara, Science **336**, 1137 (2012).

[71] R. Matsunaga, Y. I. Hamada, K. Makise, Y. Uzawa, H. Terai, Z. Wang, and R. Shimano, Physical Review Letters **111**, 057002 (2013).

[72] D. Fausti, R. I. Tobey, N. Dean, S. Kaiser, A. Dienst, M. C. Hoffmann, S. Pyon, T. Takayama, H. Takagi, and A. Cavalleri, Science **331**, 189 (2011).

[73] R. Mankowsky, A. Subedi, M. Först, S. O. Mariager, M. Chollet, H. T. Lemke, J. S. Robinson, J. M. Glownia, M. P. Minitti, A. Frano, M. Fechner, N. A. Spaldin, T. Loew, B. Keimer, A. Georges, and A. Cavalleri, Nature **516**, 71 (2014).

[74] W. Hu, S. Kaiser, D. Nicoletti, C. R. Hunt, I. Gierz, M. C. Hoffmann, M. Le Tacon, T. Loew, B. Keimer, and A. Cavalleri, Nature Materials **13**, 705 (2014).

[75] S. Kaiser, C. R. Hunt, D. Nicoletti, W. Hu, I. Gierz, H. Y. Liu, M. Le Tacon, T. Loew, D. Haug, B. Keimer, and A. Cavalleri, Physical Review B **89**, 184516 (2014).

[76] M. Först, A. D. Caviglia, R. Scherwitzl, R. Mankowsky, P. Zubko, V. Khanna, H. Brom-berger, S. B. Wilkins, Y.-D. Chuang, W. S. Lee, W. F. Schlotter, J. J. Turner, G. L. Dakovski, M. P. Minitti, J. Robinson, S. R. Clark, D. Jaksch, J.-M. Triscone, J. P. Hill, S. S. Dhesi, and A. Cavalleri, Nature Materials **14**, 883 (2015).

[77] R. Singla, G. Cotugno, S. Kaiser, M. Först, M. Mitrano, H. Y. Liu, A. Cartella, C. Manzoni, H. Okamoto, T. Hasegawa, S. R. Clark, D. Jaksch, and A. Cavalleri, Physical Review Letters **115**, 187401 (2015).

[78] M. Mitrano, A. Cantaluppi, D. Nicoletti, S. Kaiser, A. Perucchi, S. Lupi, P. Di Pietro, D. Pontiroli, M. Riccò, S. R. Clark, D. Jaksch, and A. Cavalleri, Nature **530**, 461 (2016).

[79] R. Citro, E. G. D. Torre, L. D'Alessio, A. Polkovnikov, M. Babadi, T. Oka, and E. Demler, Annals of Physics **360**, 694 (2015).

[80] C. Zerbe and P. Hänggi, Physical Review E **52**, 1533 (1995).

[81] M. Thorwart, P. Reimann, and P. Hänggi, Physical Review E **62**, 5808 (2000).

[82] A. Polkovnikov, K. Sengupta, A. Silva, and M. Vengalattore, Review of Modern Physics **83**, 863 (2011).

[83] In, *Quantum Gas Experiments: Exploring Many-Body States*, Vol. 3, edited by P. Törmä and K. Sengstock, Fundamental Theories of Physics (Imperial College Press, London, 2014).

[84] T. Langen, R. Geiger, and J. Schmiedmayer, Annual Review of Condensed Matter Physics **6**, 201 (2015).

[85] J. Eisert, M. Friesdorf, and C. Gogolin, Nature Physics **11**, 124 (2015).

[86] A. Eckardt, Review of Modern Physics **89**, 011004 (2017).

[87] Y. Castin and R. Dum, Physical Review Letters **79**, 3553 (1997).

[88] J. J. García-Ripoll, V. M. Pérez-García, and P. Torres, Physical Review Letters **83**, 1715 (1999).

[89] F. K. Abdullaev and J. Garnier, Physical Review A **70**, 053604 (2004).

[90] P. L. Kapitza, in *Collected Papers of P.L. Kapitza*, Vol. 2, edited by D. T. Haar (Pergamon Press, London, 1965).

[91] D. Jaksch, V. Venturi, J. I. Cirac, C. J. Williams, and P. Zoller, Physical Review Letters **89**, 040402 (2002).

[92] S. E. Pollack, D. Dries, R. G. Hulet, K. M. F. Magalhães, E. A. L. Henn, E. R. F. Ramos, M. A. Caracanhas, and V. S. Bagnato, Physical Review A **81**, 053627 (2010).

[93] H. Saito and M. Ueda, Physical Review Letters **90**, 040403 (2003).

[94] S. E. Pollack, D. Dries, M. Junker, Y. P. Chen, T. A. Corcovilos, and R. G. Hulet, Physical Review Letters **102**, 090402 (2009).

[95] W. Cairncross and A. Pelster, The European Physical Journal D **68**, 106 (2014).

[96] A. Eckardt and M. Holthaus, Physical Review Letters **101**, 245302 (2008).

[97] A. Zenesini, H. Lignier, D. Ciampini, O. Morsch, and E. Arimondo, Physical Review Letters **102**, 100403 (2009).

[98] A. Rapp, X. Deng, and L. Santos, Physical Review Letters **109**, 203005 (2012).

[99] T. Wang, X.-F. Zhang, F. E. A. d. Santos, S. Eggert, and A. Pelster, Physical Review A **90**, 013633 (2014).

[100] M. Holthaus, Journal of Physics B: Atomic, Molecular and Optical Physics **49**, 013001 (2016).

[101] N. Goldman and J. Dalibard, Physical Review X **4**, 031027 (2014).

[102] G. Tang, S. Eggert, and A. Pelster, New Journal of Physics **17**, 123016 (2015).

[103] T. Posske, B. Trauzettel, and M. Thorwart, Physical Review B **96**, 195422 (2017).

[104] C. Sträter, S. C. L. Srivastava, and A. Eckardt, Physical Review Letters **117**, 205303 (2016).

[105] H. Lignier, C. Sias, D. Ciampini, Y. Singh, A. Zenesini, O. Morsch, and E. Arimondo, Physical Review Letters **99**, 220403 (2007).

[106] J. Struck, C. Ölschläger, R. Le Targat, P. Soltan-Panahi, A. Eckardt, M. Lewenstein, P. Windpassinger, and K. Sengstock, Science **333**, 996 (2011).

[107] J. Struck, C. Ölschläger, M. Weinberg, P. Hauke, J. Simonet, A. Eckardt, M. Lewenstein, K. Sengstock, and P. Windpassinger, Physical Review Letters **108**, 225304 (2012).

[108] F. Meinert, M. J. Mark, K. Lauber, A. J. Daley, and H.-C. Nägerl, Physical Review Letters **116**, 205301 (2016).

[109] N. Goldman, J. C. Budich, and P. Zoller, Nature Physics **12**, 639 (2016).

[110] L. D'Alessio and A. Polkovnikov, Annals of Physics **333**, 19 (2013).

[111] T. Kuwahara, T. Mori, and K. Saito, Annals of Physics **367**, 96 (2016).

[112] N. Mann, "Driven Bose-Hubbard Model Beyond the Mean-Field Approximation", Master Thesis (Universität Hamburg, Germany, 2015).

[113] D. Nagy, G. Szirmai, and P. Domokos, The European Physical Journal D **48**, 127 (2008).

[114] C. Maschler, I. Mekhov, and H. Ritsch, The European Physical Journal D **46**, 545 (2008).

[115] K. Baumann, C. Guerlin, F. Brennecke, and T. Esslinger, Nature **464**, 1301 (2010).

[116] M. R. Bakhtiari, A. Hemmerich, H. Ritsch, and M. Thorwart, Physical Review Letters **114**, 123601 (2015).

[117] J. Klinder, H. Keßler, M. Wolke, L. Mathey, and A. Hemmerich, Proceedings of the National Academy of Sciences **112**, 3290 (2015).

[118] S. Gupta, K. L. Moore, K. W. Murch, and D. M. Stamper-Kurn, Physical Review Letters **99**, 213601 (2007).

[119] S. Ritter, F. Brennecke, K. Baumann, T. Donner, C. Guerlin, and T. Esslinger, Applied Physics B **95**, 213 (2009).

[120] B. Öztop, M. Bodyuh, O. E. Müsecaplıoğlu, and H. E. Türeci, New Journal of Physics **14**, 085011 (2012).

[121] R. Mottl, F. Brennecke, K. Baumann, R. Landig, T. Donner, and T. Esslinger, Science **336**, 1570 (2012).

[122] J. Léonard, A. Morales, P. Zupancic, T. Donner, and T. Esslinger, Science **358**, 1415 (2017).

[123] H. Keßler, J. Klinder, B. P. Venkatesh, C. Georges, and A. Hemmerich, New Journal of Physics **18**, 102001 (2016).

[124] J. K. Asbóth, P. Domokos, H. Ritsch, and A. Vukics, Physical Review A **72**, 053417 (2005).

[125] W. Lu, Y. Zhao, and P. F. Barker, Physical Review A **76**, 013417 (2007).

[126] T. Salzburger and H. Ritsch, New Journal of Physics **11**, 055025 (2009).

[127] K. Hammerer, M. Wallquist, C. Genes, M. Ludwig, F. Marquardt, P. Treutlein, P. Zoller, J. Ye, and H. J. Kimble, Physical Review Letters **103**, 063005 (2009).

[128] B. Vogell, K. Stannigel, P. Zoller, K. Hammerer, M. T. Rakher, M. Korppi, A. Jöckel, and P. Treutlein, Physical Review A **87**, 023816 (2013).

[129] A. Jöckel, A. Faber, T. Kampschulte, M. Korppi, M. T. Rakher, and P. Treutlein, Nature Nanotechnology **10**, 55 (2015).

[130] H. Zhong, G. Fläschner, A. Schwarz, R. Wiesendanger, P. Christoph, T. Wagner, A. Bick, C. Staarmann, B. Abeln, K. Sengstock, et al., Review of Scientific Instruments **88**, 023115 (2017).

[131] A. Vochezer, T. Kampschulte, K. Hammerer, and P. Treutlein, Physical Review Letters **120**, 073602 (2018).

[132] P. Christoph, T. Wagner, H. Zhong, R. Wiesendanger, K. Sengstock, A. Schwarz, and C. Becker, New Journal of Physics **20**, 093020 (2018).

[133] A. Schliesser, R. Rivière, G. Anetsberger, O. Arcizet, and T. J. Kippenberg, Nature Physics **4**, 415 (2008).

[134] C. Genes, D. Vitali, and P. Tombesi, Physical Review A **77**, 050307 (2008).

[135] H. Ian, Z. R. Gong, Y.-X. Liu, C. P. Sun, and F. Nori, Physical Review A **78**, 013824 (2008).

[136] K. Hammerer, M. Aspelmeyer, E. S. Polzik, and P. Zoller, Physical Review Letters **102**, 020501 (2009).

[137] M. Wallquist, K. Hammerer, P. Rabl, M. Lukin, and P. Zoller, Physica Scripta **T137**, 014001 (2009).

[138] M. Paternostro, G. De Chiara, and G. M. Palma, Physical Review Letters **104**, 243602 (2010).

[139] C. Genes, H. Ritsch, M. Drewsen, and A. Dantan, Physical Review A **84**, 051801 (2011).

[140] D. Hunger, S. Camerer, M. Korppi, A. Jöckel, T. W. Hänsch, and P. Treutlein, Comptes Rendus Physique **12**, 871 (2011).

[141] Y.-D. Wang and A. A. Clerk, Physical Review Letters **108**, 153603 (2012).

[142] D. Vitali, S. Gigan, A. Ferreira, H. R. Böhm, P. Tombesi, A. Guerreiro, V. Vedral, A. Zeilinger, and M. Aspelmeyer, Physical Review Letters **98**, 030405 (2007).

[143] M. Asjad, S. Zippilli, and D. Vitali, Physical Review A **93**, 062307 (2016).

[144] J.-Q. Liao and L. Tian, Physical Review Letters **116**, 163602 (2016).

[145] T. P. Purdy, P.-L. Yu, R. W. Peterson, N. S. Kampel, and C. A. Regal, Physical Review X **3**, 031012 (2013).

[146] A. Kronwald, F. Marquardt, and A. A. Clerk, New Journal of Physics **16**, 063058 (2014).

[147] K. Jähne, C. Genes, K. Hammerer, M. Wallquist, E. S. Polzik, and P. Zoller, Physical Review A **79**, 063819 (2009).

[148] A. Mari and J. Eisert, Physical Review Letters **103**, 213603 (2009).

[149] W.-J. Gu, G.-X. Li, and Y.-P. Yang, Physical Review A **88**, 013835 (2013).

[150] H. Tan, G. Li, and P. Meystre, Physical Review A **87**, 033829 (2013).

[151] A. Kronwald, F. Marquardt, and A. A. Clerk, Physical Review A **88**, 063833 (2013).

[152] M. Kitagawa and M. Ueda, Physical Review A **47**, 5138 (1993).

[153] D. J. Wineland, J. J. Bollinger, W. M. Itano, and D. J. Heinzen, Physical Review A **50**, 67 (1994).

[154] J. L. Sørensen, J. Hald, and E. S. Polzik, Physical Review Letters **80**, 3487 (1998).

[155] J. Hald, J. L. Sørensen, C. Schori, and E. S. Polzik, Physical Review Letters **83**, 1319 (1999).

[156] A. Banerjee, Physical Review A **54**, 5327 (1996).

[157] A. Kuzmich, K. Mølmer, and E. S. Polzik, Physical Review Letters **79**, 4782 (1997).

[158] J. Hald, J. L. Sørensen, C. Schori, and E. S. Polzik, Journal of Modern Optics **47**, 2599 (2000).

[159] B. Vogell, T. Kampschulte, M. T. Rakher, A. Faber, P. Treutlein, K. Hammerer, and P. Zoller, New Journal of Physics **17**, 043044 (2015).

[160] N. N. Bogolyubov, *On Some Statistical Methods in Mathematical Physics*, in Russian (Ukrainian Academy of Sciences, Kiew, 1945).

[161] U. Weiss, *Quantum Dissipative Systems*, 4th ed. (World Scientific, Singapore, 2012).

[162] A. J. Leggett, S. Chakravarty, A. T. Dorsey, M. P. A. Fisher, A. Garg, and W. Zwerger, Reviews of Modern Physics **59**, 1 (1987).

[163] H. Grabert, P. Schramm, and G.-L. Ingold, Physics Reports **168**, 115 (1988).

[164] R. Kubo, M. Toda, and N. Hashitsume, *Statistical Physics II: Nonequilibrium Statistical Mechanics*, 2nd ed., Vol. 31 (Springer, Berlin, 1991).

[165] D. Giulini, E. Joos, C. Kiefer, J. Kupsch, I.-O. Stamatescu, and H.-D. Zeh, *Decoherence and the Appearance of a Classical World in Quantum Theory*, 2nd ed. (Springer, Berlin, 2003).

[166] S. R. de Groot and P. Mazur, *Non-equilibrium Thermodynamics* (Dover, New York, 1984).

[167] R. L. Stratonovich, *Nonlinear Nonequilibrium Thermodynamics I* (Springer, Berlin, 1992).

[168] R. Zwanzig, *Nonequilibrium Statistical Mechanics* (Oxford University Press, Oxford, 2001).

[169] P. Hänggi and H. Thomas, Physics Reports **88**, 207 (1982).

[170] D. Bercioux, R. Egger, P. Hänggi, and M. Thorwart, New Journal of Physics **17**, 020201 (2015).

[171] P. Mukhopadhyay, P. Wipf, and D. N. Beratan, Accounts of Chemical Research **42**, 809 (2009).

[172] M. Quack, J. Stohner, and M. Willeke, Annual Review of Physical Chemistry **59**, 741 (2008).

[173] F. J. Devlin, P. J. Stephens, C. Österle, K. B. Wiberg, J. R. Cheeseman, and M. J. Frisch, The Journal of Organic Chemistry **67**, 8090 (2002).

[174] H. Langhals, S. Poxleitner, O. Krotz, T. Pust, and A. Walter, European Journal of Organic Chemistry **2008**, 4559.

[175] D. Beljonne, C. Curutchet, G. D. Scholes, and R. J. Silbey, The Journal of Physical Chemistry B **113**, 6583 (2009).

[176] S. Mukamel, *Principles of Nonlinear Optical Spectroscopy* (Oxford University Press, New York, 1995).

[177] A. J. Leggett, S. Chakravarty, A. T. Dorsey, M. P. A. Fisher, A. Garg, and W. Zwerger, Reviews of Modern Physics **67**, 725 (1995).

[178] M. Grifoni and P. Hänggi, Physics Reports **304**, 229 (1998).

[179] A. Mitra and A. J. Millis, Physical Review B **72**, 121102 (2005).

[180] D. Segal, D. R. Reichman, and A. J. Millis, Physical Review B **76**, 195316 (2007).

[181] G. Vidal, Physical Review Letters **91**, 147902 (2003).

[182] G. Vidal, Physical Review Letters **93**, 040502 (2004).

[183] A. J. Daley, C. Kollath, U. Schollwöck, and G. Vidal, Journal of Statistical Mechanics: Theory and Experiment **2004**, P04005 (2004).

[184] V. M. Pérez-García, H. Michinel, J. I. Cirac, M. Lewenstein, and P. Zoller, Physical Review Letters **77**, 5320 (1996).

[185] S. M. Forghani and T. G. Ritto, Nonlinear Dynamics **86**, 1561 (2016).

[186] M. Aidelsburger, S. Nascimbene, and N. Goldman, Comptes Rendus Physique **19**, 394 (2018).

[187] P. Hauke, O. Tieleman, A. Celi, C. Ölschläger, J. Simonet, J. Struck, M. Weinberg, P. Windpassinger, K. Sengstock, M. Lewenstein, and A. Eckardt, Physical Review Letters **109**, 145301 (2012).

[188] Z.-F. Xu, L. You, and M. Ueda, Physical Review A **87**, 063634 (2013).

[189] T. D. Kühner and H. Monien, Physical Review B **58**, R14741 (1998).

[190] F. E. A. dos Santos and A. Pelster, Physical Review A **79**, 013614 (2009).

[191] T. Vojta, "Quantum and classical phase transitions in electronic systems", Habilitation Thesis (Technische Universität Chemnitz, 1999).

[192] M. Vojta, Reports on Progress in Physics **66**, 2069 (2003).

[193] E. A. Guggenheim, The Journal of Chemical Physics **13**, 253 (1945).

[194] W. Nolting, *Theoretical Physics 8* (Springer, Berlin, 2000).

[195] M. Campostrini, A. Pelissetto, P. Rossi, and E. Vicari, Physical Review E **65**, 066127 (2002).

[196] M. H. Anderson, J. R. Ensher, M. R. Matthews, C. E. Wieman, and E. A. Cornell, Science **269**, 198 (1995).

[197] K. B. Davis, M.-O. Mewes, M. R. Andrews, N. J. van Druten, D. S. Durfee, D. M. Kurn, and W. Ketterle, Physical Review Letters **75**, 3969 (1995).

[198] D. Nagy, G. Szirmai, and P. Domokos, Physical Review A **84**, 043637 (2011).

[199] D. Nagy and P. Domokos, Physical Review Letters **115**, 043601 (2015).

[200] M.-J. Hwang, P. Rabl, and M. B. Plenio, Physical Review A **97**, 013825 (2018).

[201] K. Baumann, R. Mottl, F. Brennecke, and T. Esslinger, Physical Review Letters **107**, 140402 (2011).

[202] D. Nagy and P. Domokos, Physical Review A **94**, 063862 (2016).

[203] E. Hodby, O. M. Maragò, G. Hechenblaikner, and C. J. Foot, Physical Review Letters **86**, 2196 (2001).

[204] I. Bloch, Nature Physics **1**, 23 (2005).

[205] T. Kippenberg and K. Vahala, Science **321**, 1172 (2008).

[206] M. Aspelmeyer, S. Gröblacher, K. Hammerer, and N. Kiesel, Journal of the Optical Society of America B **27**, A189 (2010).

[207] M. Aspelmeyer, T. J. Kippenberg, and F. Marquardt, Reviews of Modern Physics **86**, 1391 (2014).

[208] L. Tian and P. Zoller, Physical Review Letters **93**, 266403 (2004).

[209] K. Hammerer, K. Stannigel, C. Genes, P. Zoller, P. Treutlein, S. Camerer, D. Hunger, and T. W. Hänsch, Physical Review A **82**, 021803 (2010).

[210] G. Raithel, W. D. Phillips, and S. L. Rolston, Physical Review Letters **81**, 3615 (1998).

[211] C. W. Gardiner and P. Zoller, *Quantum Noise* (Springer, Berlin, 2000).

[212] M. S. Kim, L. Allen, and R. Loudon, Physical Review A **50**, 3614 (1994).

[213] J. P. Gordon and A. Ashkin, Physical Review A **21**, 1606 (1980).

[214] T. W. Hänsch and A. L. Schawlow, Optics Communications **13**, 68 (1975).

[215] S. Camerer, M. Korppi, A. Jöckel, D. Hunger, T. W. Hänsch, and P. Treutlein, Physical Review Letters **107**, 223001 (2011).

[216] D. J. Wilson, V. Sudhir, N. Piro, R. Schilling, A. Ghadimi, and T. J. Kippenberg, Nature **524**, 325 (2015).

[217] M. Poggio, C. L. Degen, H. J. Mamin, and D. Rugar, Physical Review Letters **99**, 017201 (2007).

[218] C. M. Caves, K. S. Thorne, R. W. P. Drever, V. D. Sandberg, and M. Zimmermann, Rev. Mod. Phys. **52**, 341 (1980).

[219] V. B. Braginsky, Y. I. Vorontsov, and K. S. Thorne, Science **209**, 547 (1980).

[220] M. Tsang and C. M. Caves, Physical Review X **2**, 031016 (2012).

[221] B. Julsgaard, A. Kozhekin, and E. S. Polzik, Nature **413**, 400 (2001).

[222] W. Wasilewski, K. Jensen, H. Krauter, J. J. Renema, M. V. Balabas, and E. S. Polzik, Physical Review Letters **104**, 133601 (2010).

[223] C. B. Møller, R. A. Thomas, G. Vasilakis, E. Zeuthen, Y. Tsaturyan, M. Balabas, K. Jensen, A. Schliesser, K. Hammerer, and E. S. Polzik, Nature **547**, 191 (2017).

[224] K. Zhang, W. Chen, M. Bhattacharya, and P. Meystre, Physical Review A **81**, 013802 (2010).

[225] Z. Wang, J. Lian, J.-Q. Liang, Y. Yu, and W.-M. Liu, Physical Review A **93**, 033630 (2016).

[226] N. Aggarwal, S. Mahajan, and A. B. Bhattacherjee, Journal of Modern Optics **60**, 1263 (2013).

[227] J. Lian, N. Liu, J.-Q. Liang, G. Chen, and S. Jia, Physical Review A **88**, 043820 (2013).

[228] X. Zhao, N. Liu, X. Bai, and J.-Q. Liang, Annals of Physics **378**, 448 (2017).

[229] L. Santos, G. V. Shlyapnikov, and M. Lewenstein, Physical Review Letters **90**, 250403 (2003).

[230] S. Giovanazzi and D. H. J. O'Dell, The European Physical Journal D **31**, 439 (2004).

[231] G. Adesso, A. Serafini, and F. Illuminati, Physical Review A **70**, 022318 (2004).

[232] M. Eghbali-Arani and V. Ameri, Quantum Information Processing **16**, 47 (2016).

[233] A. Schliesser and T. J. Kippenberg, in *Advances in atomic, molecular, and optical physics*, Vol. 58, Advances In Atomic, Molecular, and Optical Physics (Academic Press, 2010), p. 207.

[234] C. Gao and Z. Liang, Physical Review A **99**, 013629 (2019).

[235] M. Raghunandan, J. Wrachtrup, and H. Weimer, Phys. Rev. Lett. **120**, 150501 (2018).

[236] E. Altman, W. Hofstetter, E. Demler, and M. D. Lukin, New Journal of Physics **5**, 113 (2003).

[237] F. Napoli, M. Sassetti, and U. Weiss, Physica B: Condensed Matter **202**, 80 (1994).

Acknowledgements

At this point, I would like to take the opportunity to thank all those without whom the work presented in this thesis would not have been possible. I have been very fortunate to be encouraged by and to work with different people during the process of this PhD.

I owe a special thanks to Prof. Michael Thorwart for providing me with the chance to be a part of his group, his constant support and motivation. I would like to kindly thank Prof. Axel Pelster for many fruitful discussions, his assistance, many questions, and suggestions. I am indebted to Prof. Masahito Ueda for giving me the opportunity to be a guest in his group at the Tokyo University and many interesting discussion.

I have to thank Reza Bakhtiari who was almost always my first contact person during the first half of my phD. Beyond academic topics, I would like thank all my colleagues during the last years for many interesting conversations during lunch or coffee break.

Ein großer Dank gebührt meiner Familie, insbesondere meinen Eltern und Großeltern für ihren finanziellen und mentalen Support in den Jahren meines Studiums.

最後に、本論文の作成にあたって妻の理解と協力に心から感謝します。